University of Southampton Research Repository

UNIVERSITY OF SOUTHAMPTON

Magnetic Retrieval of Prosthetic Heart Valves for redo-TAVI

by

Oguz Can Eren (ORCID: 0000-0002-2665-3611)

A thesis submitted in partial fulfillment for the
degree of Doctor of Philosophy

in the
Faculty of Engineering and Physical Sciences
Aeronautical and Astronautical Engineering
Computational Engineering and Design Group

March 2023

UNIVERSITY OF SOUTHAMPTON

ABSTRACT

FACULTY OF ENGINEERING AND PHYSICAL SCIENCES
AERONAUTICAL AND ASTRONAUTICAL ENGINEERING
COMPUTATIONAL ENGINEERING AND DESIGN GROUP

Doctor of Philosophy

by Oguz Can Eren (ORCID: 0000-0002-2665-3611)

With increasing life expectancy and the low durability of bioprosthetic valve replacements, the number of patients requiring multiple redo aortic valve replacements are on the rise. For patients unable to undergo open heart surgery, the only current option for redo valve replacement is the Valve-in-Valve (ViV) method which minimally invasively deploys a new prosthetic inside the failed one. The number of ViV procedures a patient can undergo are limited due to the shrinking of the aortic annulus with each additional prosthesis as smaller aortic annuli result in a larger reduction of blood pressure across the valve, decreasing blood output to the body.

To alleviate this problem, a novel prosthetic valve system, e-TAVI, was designed that allowed for the removal of the degenerated valve prosthesis and the deployment of a new one minimally invasively. The e-TAVI system comprises a three component system: (i) a **holding member** anchored inside the aortic root; (ii) an **exchangeable valve** that could be engaged to and disengaged from this holding member via (iii) a **dedicated catheter**. The method of engagement between the components incorporated ferromagnetic regions on the exchangeable valve and electromagnets in the catheter. The three components were designed and modelled computationally and simulations were performed to assess crimping, deployment, engagement, and removal of an exchangeable valve.

The crimping of the exchangeable valve frame via the catheter electromagnets resulted in the radially inward crushing of the frame forming a star-shaped axial profile. The force required to reduce the diameter of the frame in this manner was lower than its outward radial force, demonstrating an advantageous trade-off for the exchangeable valve frame design. Larger ferromagnetic regions, wider struts and shorter cell height on the frame resulted in larger removal force requirements. Smaller ferromagnetic regions and smaller catheter electromagnets resulted in a higher required current through the catheter to achieve this required force.

The re-sheathing of the exchangeable valve following crimping via the catheter electromagnets was not possible with contact between the electromagnets and ferromagnetic

regions being unable to resist the shear force. This showed the need for an additional mechanical engagement between the catheter and the exchangeable frame to achieve full retrieval of the exchangeable valve in the e-TAVI system.

Contents

List of Figures

List of Tables

Declaration of Authorship

I, Oguz Can Eren, declare that this thesis and the work presented in it are my own and has been generated by me as the result of my own original research.

Magnetic Retrieval of Prosthetic Heart Valves for redo-TAVI

I confirm that:

1. This work was done wholly or mainly while in candidature for a research degree at this University;

2. Where any part of this thesis has previously been submitted for a degree or any other qualification at this University or any other institution, this has been clearly stated;

3. Where I have consulted the published work of others, this is always clearly attributed;

4. Where I have quoted from the work of others, the source is always given. With the exception of such quotations, this thesis is entirely my own work;

5. I have acknowledged all main sources of help;

6. Where the thesis is based on work done by myself jointly with others, I have made clear exactly what was done by others and what I have contributed myself;

Signed:

Date:

Acknowledgements

I would like to extend my utmost thanks to:

My supervisors, *Prof. Neil W. Bressloff* and *Prof. Dr. Nick Curzen*, for their help, support and time spent in aiding me from the formation of this PhD research up until the final dot in this thesis;

My partner, *Isil*, and our cat, *Muhittin*, for alleviating my stress, anxiety, and despondence through the past 4 years with their love and cuddles;

My *friends* and *colleagues* for all their advice and support during my PhD;

And, most of all, my dear *Mother* and *Father* for their unwavering and unconditional support throughout my life, for which I remain eternally grateful.

Without you, this thesis would not have been possible.

Abbreviations

BE - Balloon-expandable

BVD - Bioprosthetic valve dysfunction

BVF - Bioprosthetic valve fracture

CAD - Computer aided design

CAE - Computer aided engineering

CoCr - Cobalt chromium

COF - Chronic outward force

EOA - Effective orifice area

e-TAVI - exchangeable-TAVI

FEA - Finite element analysis

Fr - French (catheter inner diameter unit)

LBB - Left bundle branch

LCC - Left coronary cusp

NCC - Non-coronary cusp

PCT - Patent cooperation treaty

PET - Polyethylene terephthalate

RCC - Right coronary cusp

RF - Radial force

RRF - Radial resistive force

SAVR - Surgical aortic valve replacement

SE - Self-expanding

SVD - Structural valve deterioration

TAVI - Transcatheter aortic valve implantation

TAV-in-TAV - Transcatheter aortic valve in transcatheter aortic valve

TOE - Trans-oesophagal echocardiography

VHD - Valvular heart disease

ViV - Valve-in-Valve

Chapter 1

Introduction

This chapter provides an introduction to the rest of the thesis. Firstly, a brief background and description of the PhD research is given, followed by the aims and main objectives. The contents of each chapter is also detailed.

1.1 PhD Research Overview

Valvular Heart Disease (VHD), referring to a myriad of conditions that hinder the function of heart valves, affects one in eight patients older than 75 [1]. Most prevalent among these conditions is Aortic Stenosis (AS) where the aortic valve becomes calcified and loses function [2]. With increasing life expectancy, the prevalence of AS represents a growing health problem.

The treatment of AS can involve either surgical aortic valve replacement (SAVR) or, increasingly, transcatheter aortic valve implantation (TAVI). In SAVR the patient undergoes open heart surgery where the diseased valve is excised, and a replacement is sutured in its place. TAVI, however, is a minimally invasive procedure where a replacement valve is deployed via catheter inside the diseased valve without excision. TAVI was initially developed and approved for use in high-risk patients that were unable to undergo open-heart surgery. However, recent studies and comparison trials against SAVR have shown a justification in utilising TAVI for younger, lower risk patients as well. This led to the approval of TAVI in lower-risk patient groups in the US and Europe [3]. This recent approval is expected to continue the trend of patients with lower surgical risk scores being selected for TAVI instead of SAVR [4].

One of the biggest challenges of VHD treatment is the durability of replacement valves where onset of valve deterioration tends to occur within 7 to 8 years after implantation with freedom from deterioration decreasing substantially after 10 to 15 years [5, 6]. This problem is amplified further when considering increasing life expectancy and younger

recipients where it becomes likely a patient will need multiple valve replacements over their lifetime. The total number of valve replacement procedures (including SAVR and TAVI) have also increased over the years from 67,321 in 2012 to 130,617 in 2019 in the US, furthering the number of patients at risk of prosthesis degeneration [7]. A redo valve replacement can be performed surgically where the failed prosthesis is excised but this becomes increasingly high-risk as the patient gets older. An alternative is to deploy a second valve inside the failed one through TAVI. This method is called Valve-in-Valve (ViV) and presents a different challenge in terms of decreasing effective blood flow area through the valve.

1.2   Aims & Objectives

Against this background, the main aim of this PhD research was to computationally design and demonstrate the feasibility of a new valve system that facilitated multiple, minimally invasive valve replacements without sacrificing blood flow area through the valve. The research question was: *What kind of valve frame structure, engagement method and delivery system are sufficient to develop a three component valve system that can be engaged and disengaged to facilitate valve exchange?*

The objectives to achieve this aim and answer the research question were:

- to design an engagement mechanism between a catheter and a valve that allows for the removal of a deployed valve via a catheter *in vivo*;

- to design an engagement mechanism that enables rapid engagement (< 30 s) between the valve and catheter;

- to design a holding member that the valve can be deployed into, providing further anchoring and limiting tissue contact between the valve and the aortic wall;

- to design a valve frame that has sufficient radial strength to ensure secure anchoring within the aorta, resisting axial forces up to 11 N;

- to design a valve that can be delivered via a catheter, where the valve can be constricted radially inward to a diameter below 8 mm to fit within a catheter and then expand radially outward without fracturing;

- to design a valve that has the smallest frame profile possible while achieving the other objectives to minimise the amount of inorganic material implanted in the body.

1.3   Thesis Outline

This thesis contains eleven chapters and three appendices, aiming to detail the progress throughout the PhD research and discuss the results. A brief description of the contents of each chapter is below.

Chapter 1 - Introduction to the thesis including a summary of the rationale behind the PhD research.

Chapter 2 - Clinical background to the function of heart valves and valvular heart disease.

Chapter 3 - Description of current treatments of valvular heart disease. Most commonly implanted commercial prostheses and associated problems are also discussed through clinical evidence.

Chapter 4 - Causes of valve prosthesis failure and analysis of redo valve replacement procedures, with a focus on the Valve-in-Valve method.

Chapter 5 - Description of the concept of exchangeable-TAVI (e-TAVI), the novel valve system developed through the PhD research, followed by the main tasks.

Chapter 6 - The methodology used in the crimping and unsheathing simulations performed in this thesis including mesh resolution, time increment and assemblies.

Chapter 7 - Detailing the methods and process of designing the exchangeable valve frame, particularly in terms of the removal process.

Chapter 8 - Description and discussion of the development of the electromagnets on the e-TAVI catheter.

Chapter 9 - Design and computational development of the holding member, particularly in terms of axial anchoring.

Chapter 10 - Discussion on how the results in this thesis will affect the future development of the e-TAVI system.

Chapter 11 - Concluding remarks with future work in the development of e-TAVI.

Appendix A - Computational modelling of the parts used in the simulations.

Appendix B - Mesh and step size dependency simulations.

Appendix C - Derivation of the simple electromagnetic force equation.

Chapter 2

Valvular Heart Disease

This chapter gives a clinical background to valvular heart disease to build towards the treatments of valvular heart disease. A brief summary of how the human heart and heart valves function is given, followed by a description of how valvular disease can occur and is diagnosed.

2.1   Heart and the Aortic Valve

The human heart is mostly made up of cardiac muscle tissue and consists of four chambers: the right and left atria, and the right and left ventricles (Figure 2.1). The purpose of the heart is to pump blood through the vascular system. This is achieved through a cycle of contractions and relaxations of the cardiac muscle, called the cardiac cycle (Figure 2.2). The cycle does not have a beginning per se, but it is common to envision a fully relaxed state with the atria filling with blood as the start. With that, the steps of the cardiac cycle are can be described as follows.

1. The atria relax, increasing in volume and filling with blood. The right atrium fills with de-oxygenated blood from the vena cavas while the left atrium fills with oxygenated blood from the pulmonary vein. This occurs during the region labelled *rapid inflow* and *diastasis* in Figure 2.2 [2].

2. The atria contract decreasing atrial volume and creating a pressure gradient between the atria and their corresponding ventricles. Blood flows from right atrium to right ventricle and from left atrium to left ventricle. This occurs during the region labelled *atrial systole* in Figure 2.2 [2].

3. The ventricles contract decreasing ventricular volume and creating a pressure gradient between the ventricles and the arteries leading out of the heart. De-oxygenated blood flows from the right ventricle to the pulmonary artery while

4

HEAD AND UPPER EXTREMITY

Superior
vena cava

Aorta

Pulmonary artery

Lungs

Right atrium

Pulmonary
valve

Pulmonary
vein

Tricuspid
valve

Left atrium

Mitral valve

Right ventricle

Aortic valve

Inferior
vena cava

Left
ventricle

TRUNK AND LOWER EXTREMITY
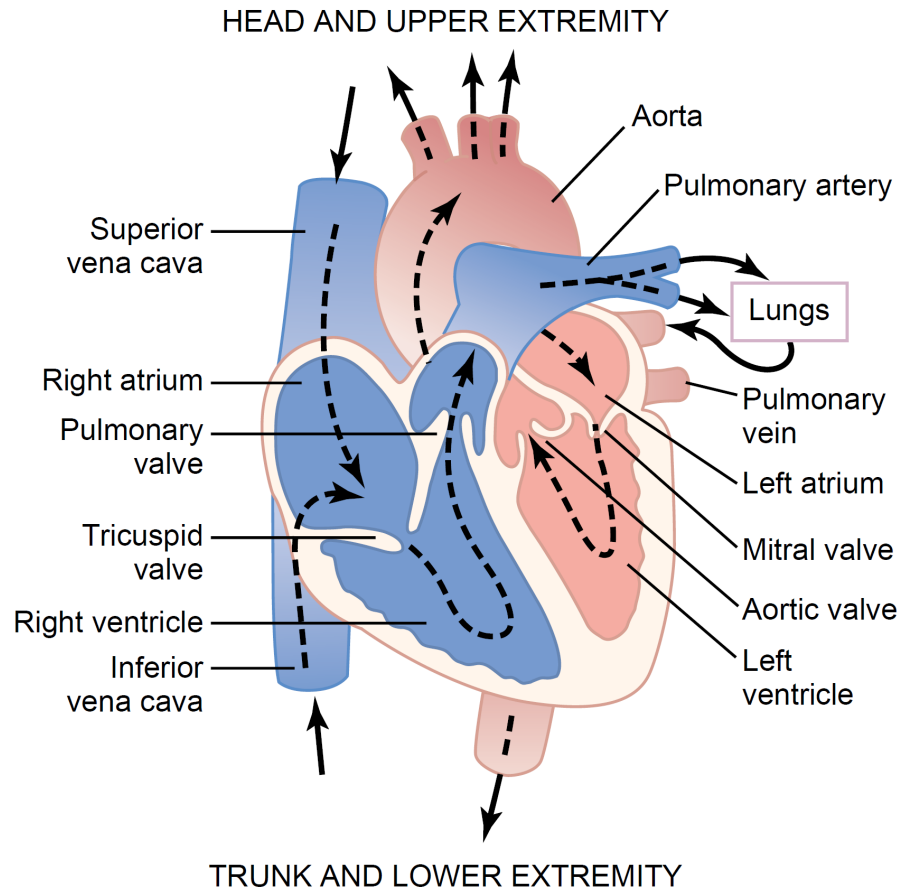
FIGURE 2.1: Graphical representation of the human heart. The dashed lines and arrows show the direction of blood flow. All valves, chambers, arteries and veins of the heart are also labelled [2].

oxygenated blood flows from the left ventricle to the aorta and through that to the entire body. Simultaneously the atria relaxes. This occurs during the region labelled *isovolumic contraction* and *ejection* in Figure 2.2 [2].

4. The ventricles relax, decreasing ventricular pressure and completing the cycle to a fully relaxed state. This occurs during the region labelled *isovolumic relaxation* Figure 2.2 [2].

Indispensable to the correct direction of blood flow through the cardiac cycle are the heart valves situated at the entrance and exit to each ventricle [2]. These are:

- the tricuspid valve: situated between the right atrium and the right ventricle;

- the pulmonary valve: situated between the right ventricle and the pulmonary artery;

- the mitral valve: situated between the left atrium and the left ventricle;

- the aortic valve: situated between the left ventricle and the aorta.
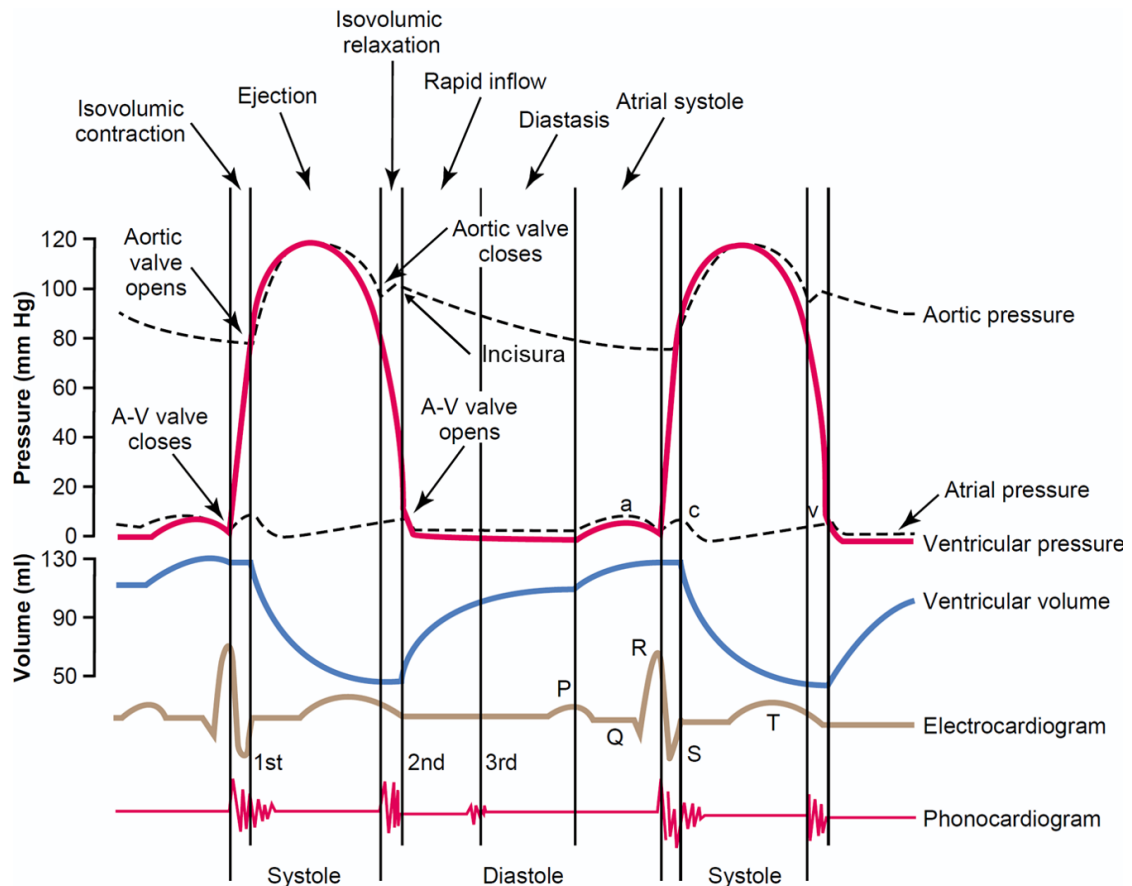
FIGURE 2.2: Wiggers diagram showing a healthy human cardiac cycle. Of interest are how the aortic pressure and ventricular pressure change over the cardiac cycle as these relate to the forces over the aortic valve [2].

The function of these valves is to prevent blood flow in the reverse direction. In order to achieve this, each valve only allows blood to flow through in one direction. To illustrate, when the ventricles contract the pressure inside the ventricles increases. This creates a pressure gradient between the ventricles and the arteries, as described above in the cardiac cycle, but it also creates a pressure gradient between the ventricles and the atria. This gradient forces blood to flow from the ventricles back into the atria but this flow is prevented by the closing of the tricuspid and mitral valves. Similarly, the pulmonary and aortic valves accomplish the same function between the heart, and the pulmonary artery and aorta respectively. The aortic valve forms the focus of the e-TAVI procedure discussed in this thesis.

The opening and closing of the valves is a passive process, driven by the pressure gradient and valve anatomy [2]. Figure 2.3 shows the structure of the aortic valve in a planar view. The three cusps, or leaflets, are pushed radially outward by blood flow from the left ventricle to the aorta but they snap shut when flow reverses. The points at which the cusps are connected, overlapping, to the aortic wall are called commissures, of which there are three [8]. The ring of aortic wall tissue holding the leaflets is thicker than the

surrounding tissue and is referred to as the aortic annulus, separating the left ventricle from the aorta [8].

Another area of interest in Figure 2.3 is the coronary arteries, the entrance to which is behind the right coronary and left coronary cusps. These arteries supply blood to the cardiac muscle and hence any blockage can lead to severe heart muscle malfunction [8, 9].
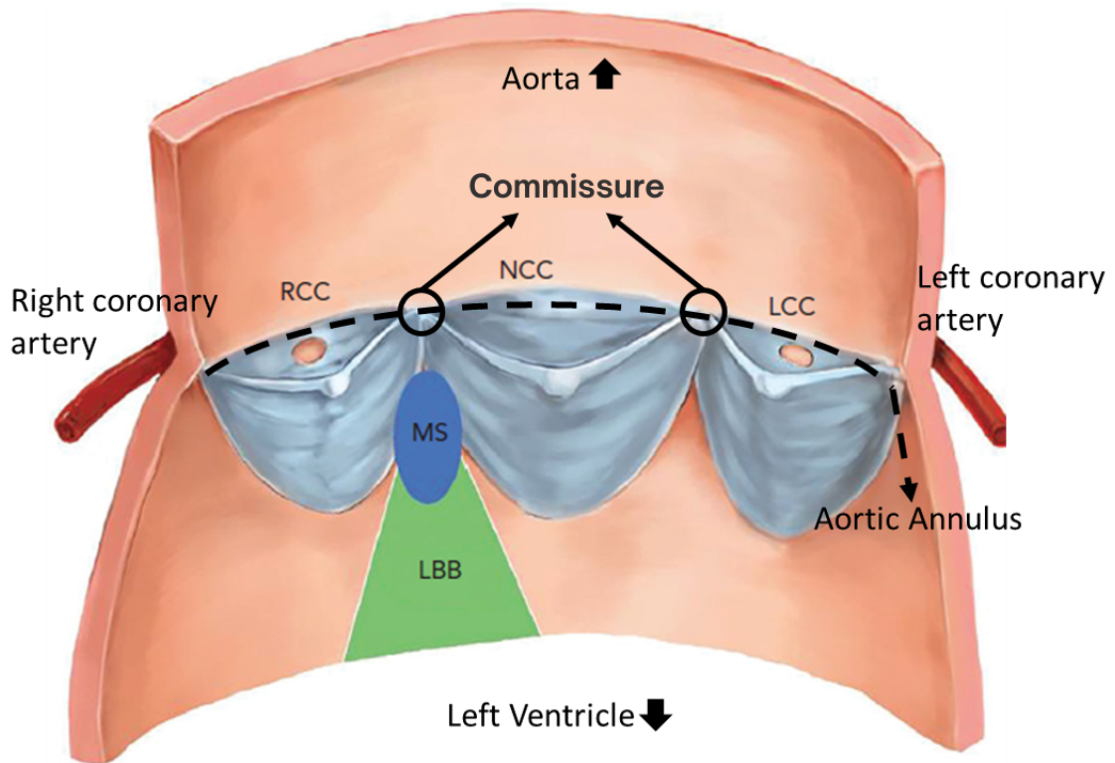
FIGURE 2.3: A graphical representation of the aortic root, cut open and planar. The three leaflets and the coronary arteries are shown. The commissures and the aortic annulus are also labelled. RCC: right coronary cusp, NCC: non-coronary cusp, LCC: left coronary cusp, MS: membranous septum , LBB: left bundle branch [9].

The motion of the aortic root also contributes to the opening and closing of the aortic valve. During the isovolumic contraction phase, the aortic root undergoes circumferential expansion, effectively preparing to accommodate the large volume of blood about to be ejected from the left ventricle [10, 11]. This expansion improves transvalvular heamodynamics and minimises damage to the leaflets caused by turbulent flow [10, 12]. Prior to diastole, the aortic root undergoes a shape change from conical to cylindrical which negates the velocity gradient across the root. This negation reverses the pressure gradient across the valve, initiating the closure of the leaflets [10, 11]. In addition to this expansion, the aortic root also tilts between systole and diastole. During systole this tilting motion aligns the ascending aorta with the left ventricular outflow tract, effectively resulting in a straight cylinder which improves the ejection of blood [10, 13]. The reverse is true during diastole which likely decreases the amount of stress experienced by the leaflets [10, 12].

2.1.1 Forces on the Aortic Valve

With the contraction of the left ventricle, there is a pressure increase until the aortic valve is pushed open. Following this, the pressure increase in the left ventricle, while the ventricular muscles are still contracting, is much slower because blood immediately flows out through the open valve. The blood flow into the arteries increases the aortic pressure to 120 mmHg. Next, at the end of systole, a so called incisura (shown in Figure 2.2) occurs as the aortic valve closes. This is caused by a short period of backflow through the valve as the pressure in the left ventricle drops below that of the aortic pressure, followed by a sudden stop of backflow as the leaflets snap shut. The aortic pressure then decreases slowly throughout diastole to 80 mmHg [2].

The pressure curves of the right ventricle and pulmonary artery follow a similar profile to that of the aorta but the magnitude of pressure is about six times less [2]. This is due to the left ventricle muscles being stronger as they need to pump blood through the entire vascular system as opposed to just the lungs. The higher pressures experienced by the aortic valve causes it to undergo the most stress through a patient's lifetime [14]. The high pressure in the aorta at the end of systole causes the aortic valve to snap into the closed position as opposed to the softer closure of the other valves. This rapid closure and ejection subject the edges of the valve to greater mechanical abrasion. Also, the cross-sectional opening of the aortic valve is smaller than the others, causing blood flow velocity to be higher through the valve, increasing the shear stress on the cusps [15].

Blood pressure and flow through the valve are the two components causing stress to the aortic valve. Quantifying these forces and stresses is of interest to better understand the function and failure of the aortic valve. In vivo studies using markers to estimate a canine aortic valve's membrane stress from displacement have found the maximum stress on the leaflets in the circumferential direction to be 2.4 kPa during normal valve function [16]. A finite element study of a human aortic valve found the maximum principle stress to be 2.19 kPa, similar to the canine study, under healthy valve function [17]. The peak wall shear stress due to blood flow through the valve was found to be 0.07 kPa, during systole with a peak flow velocity of 1.2 m/s [18]. The highest force on the valve is due to the blood pressure during diastole, which is approximately 6.01 N in the axial direction for an average valve cross-sectional area of 4.52 cm^2 [19]. When the valve is in the closed position, the pressure in the aorta exerts this force on the entire surface of the valve facing the aortic arch. This is a crucial value as any prosthetic replacements of the aortic valve must be able to function under this load. The valve designs in this thesis were hence evaluated on the maximum axial force they could resist before dislodging.
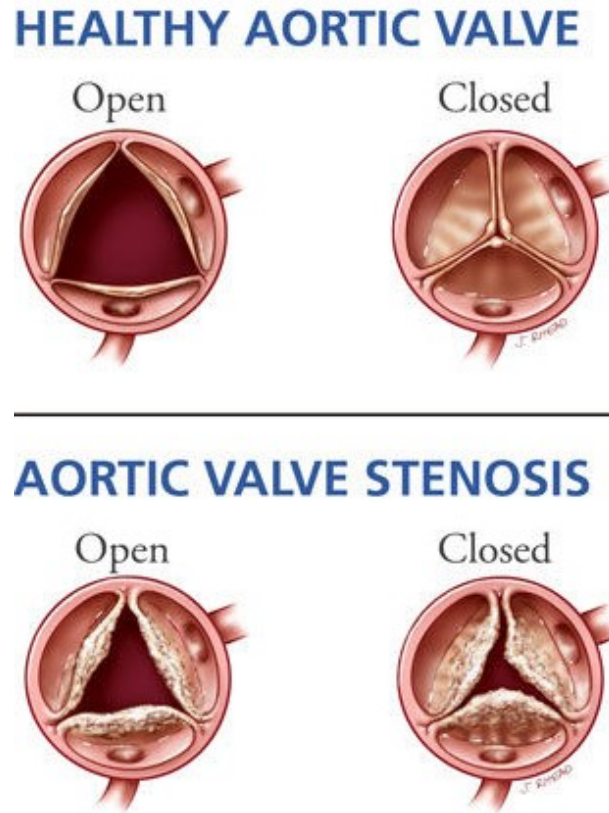
FIGURE 2.4: Representations of the open and closed position of a healthy aortic valve (top) and a stenosed aortic valve (bottom). The deceased leaflets are unable to open or close properly [20].

2.2 Calcification and Loss of Valve Function

Valvular Heart Disease (VHD) is a term given to any condition that hinders the function of the heart valves. This hindrance is most commonly due to calcification around the leaflets which impairs the valve from opening and closing fully; though other problems such as tears in the leaflets, thrombi formation, or congenital leaflet defects can also hinder valve function [2]. When the valve is unable to open fully the cross-sectional area that blood can flow through decreases, increasing the pressure drop across the valve, and hence lowering blood outflow. This is called stenosis, or aortic stenosis when referring specifically to the aortic valve [2]. When the valve is unable to close fully there is some reverse flow of blood, again decreasing the total blood output. This is called regurgitation. Usually, diseased valves exhibit both conditions as the deformation caused by the plaque formation on the leaflets affects both the closed and open positions of the valve [2]. This is illustrated in Figure 2.4 where both the open and closed positions of the stenosed valve are irregular.

While the exact biomechanical process is not understood fully, it has been observed that the amount of calcification is related to the amount of stress experienced by the valve

[21, 22]. Due to the higher stresses it experiences, the aortic valve is the most common valve to be diseased [21, 22]. Its location also means that any reduction in its blood output directly decreases the amount of blood supplied to the body, making any loss of function critical to patient health. As valve function deteriorates, total blood output of the heart decreases causing symptoms such as shortness of breath, lethargy, palpitations, chest discomfort and swelling which is usually the stage at which diagnosis occurs [23, 24].

VHD is diagnosed through echo-cardiography which uses sound waves to visualise the valve of interest. Figure 2.5 shows an example image from a transesophogeal echo of the aortic valve. The leaflets of the aortic valve are visible in the image and are used in identifying the presence of stenosis by visually assessing whether the valve is able to open fully. Blood flow through the valve is visualised by using Doppler ultrasound, which allows the diagnosis of regurgitation by assessing whether there is any backflow into the left ventricle during diastole [23]. Following diagnosis, the severity of valve function loss is assessed to determine treatment options, including valve replacement, if necessary.
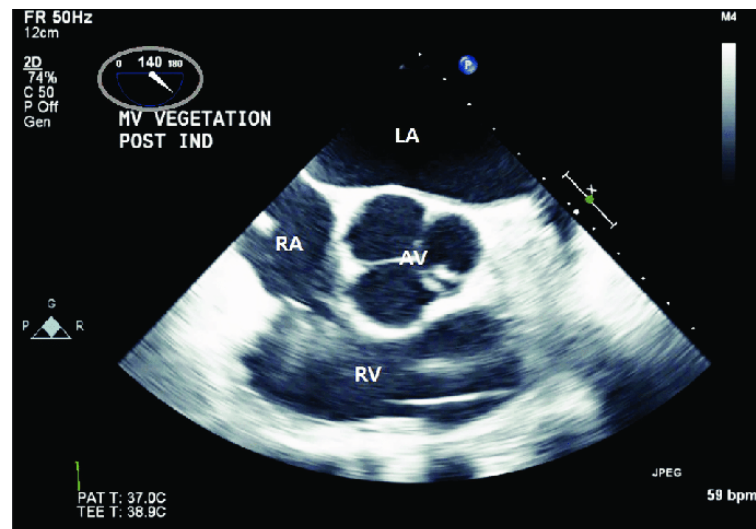
FIGURE 2.5: Transesophageal echocardiographic aortic valve short-axis view. AV: aortic valve, LA: left atrium, RA: right atrium, RV: right ventricle [25].

2.3 Summary

The purpose of this chapter was to give a brief background to the anatomy of the aortic valve and explain valvular heart disease to describe the current methods of treatment in the subsequent chapter. The important points from this chapter are summarised below.

- Heart valves are integral to the function of the human heart by only allowing one-way blood flow.

- The aortic valve experiences the largest amount of force, and hence stress, through its regular function.

- Due to the higher stresses it experiences, VHD is most prevalent in the aortic valve.

- Loss of aortic valve function due to VHD decreases the blood supply to the body, necessitating replacement in severe cases.

Chapter 3

Treatment of Valvular Heart Disease

Severe stenosis and/or regurgitation of the aortic valve can limit blood output from the heart to such an extent that intervention becomes necessary. Currently, this is performed through the implantation of a prosthetic heart valve, taking over the function of the diseased native valve. There are two methods of valve implantation: surgical aortic valve replacement (SAVR) and transcatheter aortic valve implantation (TAVI). Following an overview of these methods, the main commercially available valves are described followed by the problems and recent developments associated with SAVR and TAVI.

An overview followed by commercial products, problems, and recent developments of both procedures are discussed in this chapter.

3.1 Surgical Aortic Valve Replacement (SAVR)

3.1.1 Overview

The SAVR procedure consists of performing open heart surgery on the patient, excising the degenerated valve out of the body and suturing in a replacement prosthetic heart valve. Firstly, an incision, approximately 25 cm long, is made in the patient's chest to access the heart [26]. The patient is connected to a cardiopulmonary bypass device and their heart is stopped. The aorta is either completely or partially cut through above the valvular annulus, depending on the type of prosthesis used. The calcified native valve is then cut out from the aorta. The prosthesis is sutured into the aortic annulus (or in between the two cut ends of the aorta if it was severed completely) and the cut into the aorta is closed. Finally, the heart is restarted and the chest incision is sutured. The

patient must stay in hospital for about a week and a full recovery takes two to three months [26].

3.1.2   Commercial Products

There are two main types of prosthetic valves for SAVR: mechanical valves and bio-prosthetic valves. Bioprosthetic valves are further divided into stented and stentless valves.

3.1.2.1   Mechanical Heart Valves

The first prosthetic heart valve, implanted in 1952 by Charles A. Hufnagel, was a mechanical valve design called caged-ball valve [27]. This design consisted of a silicone elastomer ball placed inside a metal cylindrical cage. Figure 3.1 illustrates this valve. The ball either moved towards the mouth of the cage and blocked the passage of blood or moved towards the other end, allowing blood to flow. This movement was dominated by the pressure gradient across the valve, in the same way native valves function. The general structure of the prosthetic valve, however, was vastly different than the native heart valves. It lacked any kind of leaflets and was made up of a metal cage and a plastic ball.

FIGURE 3.1: The caged-ball valve consisting of an elastomer ball which was the first prosthetic heart valve to be developed [23].

Improvements were made to mechanical heart valves over the years and the current state of the art are bileaflet mechanical heart valves [27]. These valves consist of two semi-circular tilting disks that tilt open 90 degrees, and close horizontally to control the flow of blood. Figure 3.2 shows the On-X (CryoLife Inc, Kennesar, USA) bileaflet mechanical valve. This design is more like the native heart valve than the ball and cage model, and this increase in similarity has been the trend over the years [23, 27].

The inorganic materials used in mechanical valves ensure they have excellent durability and most patients implanted with a mechanical valve do not experience a loss in

FIGURE 3.2: The On-X (CryoLife Inc, Kennesar, USA) bileaflet mechanical valve. [28].

valve function in their lifetime [23, 27]. Blood coming into contact with this inorganic material, however, can cause blood clots to form on the surface of the valve, leading to thrombi formation on the prosthesis [27]. These thrombi can either hinder valve function by blocking the aortic annulus, or get detached and become emboli causing blockages elsewhere in the vascular system [23]. To remedy this, patients with a mechanical valve need to use anti-coagulants daily throughout their lifetime to prevent these thrombi from forming. Aside from the discomfort and cost of taking medicine every day, this can lead to other health risks such as decreased blood clotting in other parts of the body and hence a higher risk of bleeding [23, 27]. The risk of thrombi formation on mechanical valves is compounded by the difference in their structure to the native valve. The different structure changes the complex blood flow patterns around the aortic root, leading to blood stasis in certain regions. This blood stasis can, in turn, contribute to the clotting around the valve [29].

3.1.2.2 Bioprosthetic Heart Valves

Bioprosthetic valves are in part made up of organic valve tissue from animals (i.e. xenografts), most commonly pigs or cows. Valves consisting of only the leaflets from an animal valve attached to an inorganic frame are called stented bioprosthetic valves. Valves that purely consist of tissue from animals and no inorganic support structure are called stentless bioprosthetic valves. Figure 3.3 shows the Perimount Magna (Edwards Lifesciences Corp, Irvine, USA) valve, the first stented bioprosthesis designed for the aortic valve [30]. Bovine pericardium leaflets, treated with glutaraldehyde to limit xenograft rejection and preserve their structure, are mounted on a cobalt-chromium frame [30]. The frame is covered with a polyester fabric and the sewing ring is made of silicone rubber [30]. Figure 3.4 shows the stentless Toronto valve (St. Jude Medical, Little Canada, USA), one of the first products in stentless bioprostheses [31]. The prosthesis is an entire porcine aortic valve covered on the outer surface with Dacron fabric

and is sutured between the left ventricle and the arching aorta, replacing the entire native aortic root [32].

FIGURE 3.3: The Perimount Magna (Edwards Lifesciences Corp, Irvine, USA) stented bioprosthetic valve [30].

FIGURE 3.4: The Toronto (St. Jude Medical, Little Canada, USA) stentless bioprosthetic valve [33].

Due to the materials from which they are made and their closer resemblance to the native valve in terms of their structure and function, both types of bioprosthetic valves do not necessitate lifetime use of anticoagulants, although some medication is necessary to ensure xenograft acceptance following implantation [23]. However, the animal leaflets present in both valve types are also susceptible to several forms of dysfunction, just like the human native leaflets. This causes the durability of bioprosthetic valves to be much less than that of their mechanical counterparts where one out of three bioprostheses undergo structural degeneration within 10-15 years of implantation [23, 34].

3.1.3 Problems

The main problem with SAVR is that many patients with VHD are unable to undergo cardiopulmonary bypass due to their comorbidities. VHD usually becomes severe enough to merit a valve replacement in older patients, and patients with other cardiovascular problems [35]. These groups have a high-risk of death if they were to undergo open-heart surgery [35].

Even for patients able to undergo a sternotomy, the recovery period from the operation can be up to six months [26]. Following successful recovery the anticoagulant use necessitated by mechanical valves and the low durability of the bioprosthetic valves represent further problems associated with SAVR.

3.1.4 Recent Developments

While the total number of aortic valve replacements in the USA has increased by 63,296 between 2012 and 2019, the number of SAVR procedures have largely remained the same. There were 62,655 SAVR operations in the USA in 2012 compared to 57,626 in 2019 [7]. This discrepancy is due to the increase in the minimally invasive method, transcatheter aortic valve implantation (TAVI).

Recent developments in SAVR try to address the high risk of open heart surgery. Sutureless surgical valves are in development which can be implanted in the patient with no or minimal suturing by the surgeon, decreasing the operation time [36]. This can then allow higher risk patients to undergo SAVR with this method as they can better tolerate the shorter amount of time under cardiopulmonary bypass. Another path of development is the minimally invasive surgery, using similar sutureless valves, to limit the extent of damage caused by the sternotomy by making a smaller incision [36]. Both these developments reflect a trend of SAVR trying to mimic the attributes of transcatheter aortic valve implantation, described in the next section.

3.2 Transcatheter Aortic Valve Implantation (TAVI)

Transcatheter aortic valve implantation (TAVI) is a minimally invasive method of implanting a crimpable, stented bioprosthetic valve in a patient.

3.2.1 Procedure Overview

The procedure consists of crimping a stented valve on a catheter which is then inserted into an artery (most commonly the transfemoral artery) and guided to the aortic root

[37]. The valve is then deployed in the aortic annulus, either through balloon expansion or simply unsheathing depending on whether the prosthetic valve is balloon-expandable (BE) or self-expanding (SE), respectively. The positioning of the valve is controlled using trans-oesophagal echocardiography (TOE) and angioplastic fluoroscopy where radio-opaque regions on the valve are visible in real time [23].
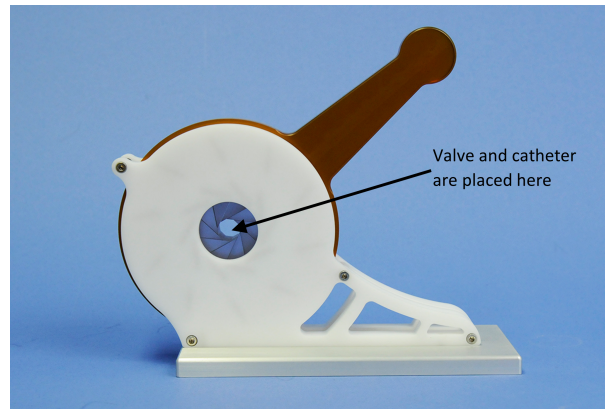
FIGURE 3.5: Crimping tool used for crimping BE valves onto balloon catheters [38]. The 12 rectangular prisms (in blue) within the circular opening move radially inwards as the handle is pressed down. The valve prosthetic and the balloon catheter are placed within this opening and the motion of the prisms collapses the frame such that it wraps around the catheter.

For BE valves, the prosthetic to be implanted is crimped onto its appropriate catheter using a dedicated heart valve crimping device. This crimping device and its function is described in Figure 3.5. The valve prosthetic is sanitised and placed inside the crimping device with the delivery catheter and the handle is pressed downwards to collapse and prepare the valve for deployment. For SE valves, the delivery catheters are supplied with the valve already crimped onto the catheter via a compression loading system. This compression loading system is depicted in Figure 3.6. The SE valve is crimped via its passage through the inflow cone and is inserted into a capsule on the delivery catheter. The opening and closing of this capsule is controllable through a knob on the catheter handle to receive the valve in the open position, and then close to prevent the expansion of the frame [39, 40].

FIGURE 3.6: Compression loading system used for crimping SE valves onto catheters. (1) Inflow tube (straight tube) (2) Outflow cone (3) Outflow cap (4) Outflow tube (tube with flared ends) (5) Inflow cone [39].

The catheter is then ready to be guided to the aortic root. This is most commonly done through the femoral artery (the transfemoral method), although transapical and

transaortic methods also exist [41]. Figure 3.7 shows representations of different deployment methods. An incision is made to gain entry to the preferred artery and a guidewire is pushed through to reach the aortic root, using TOE for guidance. Alongside the guidewire, a pacing wire and a contrast agent injector also need to be placed near the aortic valve. The catheter then follows the guidewire and is moved inside the native aortic valve. The interventionalist needs to align the fluoroscopic markers on the crimped prosthetic with different anatomical features (depending on the valve) visible through fluoroscopy, to ensure correct 3D alignment of the prosthesis within the annulus [41].
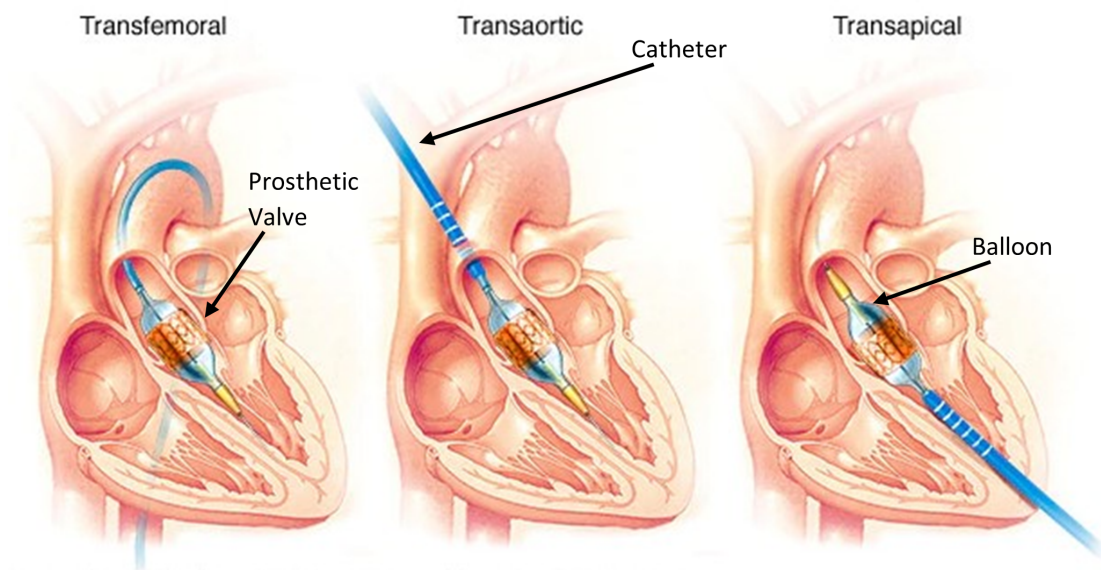
FIGURE 3.7: Representation of the three delivery methods of TAVI using a BE valve. In all images the delivery is at the step where the TAVI valve is fully expanded by the balloon. The catheter positions indicate the differences in the delivery methods. [42]

When the interventionalist is satisfied with the position, rapid ventricular pacing is used to effectively stop blood flow and native leaflet movement [41, 43]. The prosthetic valve is then expanded into the aortic annulus, anchoring in place and squishing the native leaflets between the aortic wall and the prosthesis. Pacing is removed and contrast agent is injected to visualise blood flow through the heart and assess new valve function [41, 43]. There is a limit on the duration of rapid pacing a patient can tolerate as blood flow is effectively stopped during this time. On average, rapid pacing episodes of 30 seconds are used during TAVI deployment [43]. If valve function is satisfactory, the catheter and other wires are removed, and the incision is closed. The patient is likely to be discharged after a single day stay at the hospital and is expected to be fully recovered in one month, although, in transapical and transaortic methods, these times can be longer [37, 44].

There are two main types of TAVI valves on the market, differentiated by their method of deployment after crimping: balloon-expandable (BE) and self-expanding (SE) valves.

3.2.2 Balloon-Expandable Prosthetic Valves

Balloon-expandable (BE) TAVI valves were the first TAVI valves to be developed [45]. Structurally these valves consist of a metal frame - usually made of stainless steel or a cobalt-chromium (CoCr) alloy - to which the organic leaflets are mounted [45, 46]. The leaflets - typically manufactured from bovine or porcine pericardial tissue - are fixed, as in the surgical bioprosthetic case, to limit immune response and preserve their structural integrity. In more recent iterations, these valves also include inner and outer skirts made of polyethylene terephthalate (PET) fabric for better sealing around the prosthesis and radio-opaque markers for positioning in vivo [46].

FIGURE 3.8: The Edwards Commander balloon-catheter delivery system (Edwards Lifesciences, California, US) used in the deployment of SAPIEN 3 valves. The image shows the balloon and the SAPIEN 3 mounted on it in the expanded position [47].

These TAVI valve frames undergo plastic deformation during crimping and require external work to then expand into their functional position. This is achieved by crimping the valve onto a balloon catheter, similar to a balloon angioplasty catheter (Figure 3.8). When the crimped valve is in the correct position in the aorta, the balloon is inflated pushing the frame radially outwards and expanding the valve. The metal frame again undergoes plastic deformation as it expands to become anchored into the aortic annulus, trapping the native leaflets.

3.2.2.1 SAPIEN Series

Currently the SAPIEN 3 valve (Edwards Lifesciences, California, US), is the most commonly implanted BE valve in the world [46]. SAPIEN 3 has performed well in studies with paravalvular regurgitation as low as 3.5% at 30 days [37]. In a comparison with its predecessor, SAPIEN XT, the newer model has shown significantly lower rates of regurgitation (15.9%) and was non-inferior in pacemaker rates (9.8%) and 30-day mortality (5%) [37, 45]. The latest version, SAPIEN 3 Ultra, improved upon the annular sealing properties of the valve due to its higher outer skirt, with a mild paravalvular regurgitation rate of 18.7% compared to SAPIEN 3's 43.0% [48].

The structure of the SAPIEN series have evolved through the versions shown in Figure 3.9. The Edwards SAPIEN valve has a rhombus cell shape in the middle section while the top and bottom circle of cells lack two struts each that would complete the rhombus.
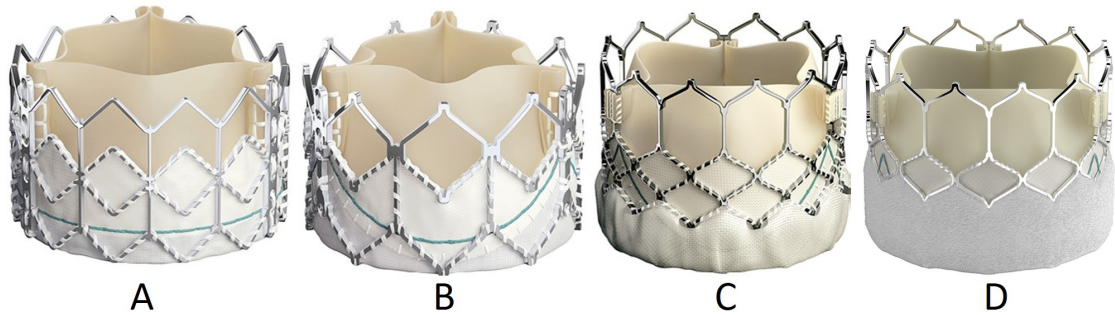
FIGURE 3.9: The four evolutions of the SAPIEN valve series: (A) SAPIEN, (B) SAPIEN XT, (C) SAPIEN 3, (D) SAPIEN 3 Ultra [45, 48].

This lack of struts is to decrease the amount of non-biological materials on the valve and hence decrease thrombogenicity. However, the frame should also have the required radial strength to anchor the valve against the aortic wall and that is why the middle cells have full rhombus structures. SAPIEN XT uses an even larger cell size and fewer struts. It also has circular fillets at the top vertices to improve the crimping and expanding process. Finally, SAPIEN 3 and SAPIEN 3 Ultra have small, rhombus-like cells lining the skirt with large cells on top. These cells on top are larger in order to minimise the risk of coronary obstruction. Strut size is thinner than the other models but there are more cells in total and the circular fillets can be seen in the top and bottom vertices of all cells. SAPIEN 3 Ultra has a higher outer skirt for better annular sealing. The exact dimensions of the frame are not provided by Edwards Lifesciences, but 0.3 mm is used in the literature for the strut width and the strut thickness in simulations, generally determined from scans of the SAPIEN XT [45, 49]. The strut width of SAPIEN 3 was also estimated in literature to be 0.3 mm based on unfolded images of the frame available on the Edwards Lifesciences website [50].

Figure 3.10 shows an image of the SAPIEN 3 with prominent features labelled for reference. The trend of the SAPIEN frame design evolution is towards thinner struts, coarser cell density at the aortic end to reduce coronary occlusion, and denser cells at the left ventricle to improve anchoring. Thinner struts increase the biocompatibility of the frame, due to less contact surface area between the struts and the aortic wall tissue, but weaken the overall structure both in terms of radial strength and resistance to fracture during crimping and expansion. The increased likelihood of fracture is mitigated by the nipple-like crowns on the vertices of the cells where the largest strain occurs during crimping and expansion. These crowns first appear on some of the vertices in the SAPIEN XT model and proliferate to all cell vertices in SAPIEN 3 Ultra, demonstrating the satisfactory outcome of this design addition. The weaker radial strength of the frame is mitigated by the denser cells in the lower region which overlap with the aortic annulus after deployment. The denser cells ensure the outward radial force around these regions are higher compared to the rest of the frame because they align with the aortic annulus, which is the ideal anchoring spot being the narrowest and hardest part of the aortic root.
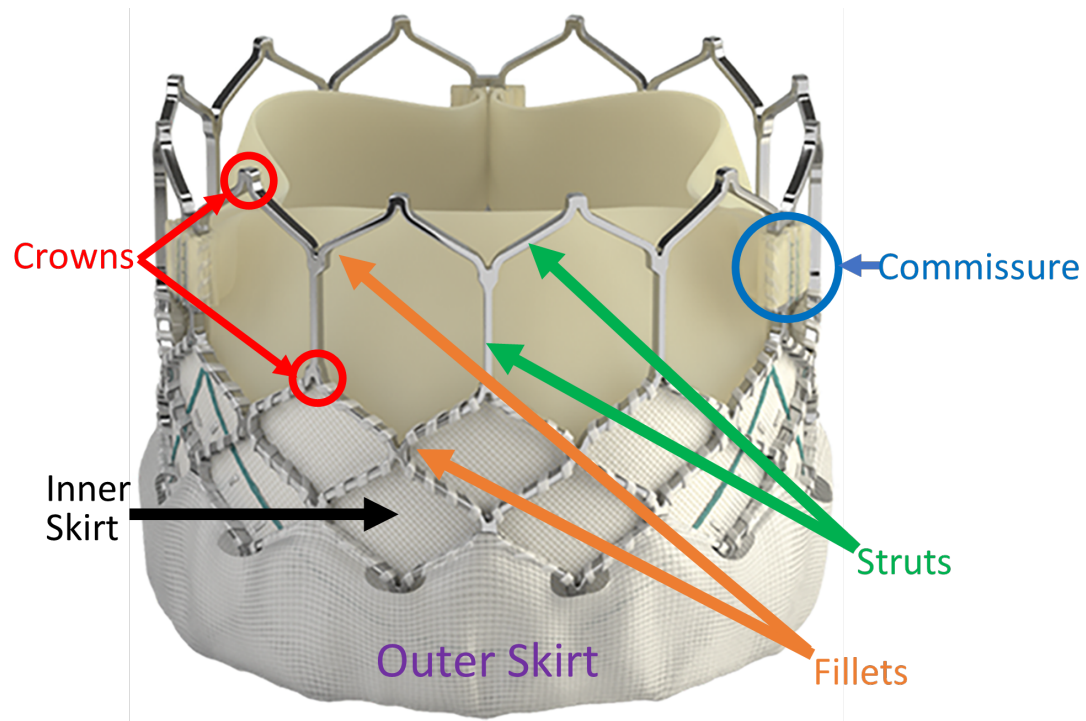
FIGURE 3.10: Representation of SAPIEN 3 with features of interest annotated: struts, commisssure, crowns, fillets, inner and outer skirts [45].

Further anchoring in the axial direction (reverse direction to blood flow) is provided by the coarser cells on the top region conforming to the increasing diameter of the aortic arch in the supra-annular section. The larger cells deform relatively easily, the vertical struts bending radially outward to conform to the aortic wall. The SAPIEN and SAPIEN XT variants include these vertical struts across the height of the frame for conformance across the aortic root, but the latter two designs limit them to the supra-annular end. This change in design coincides with the addition of the outer skirt around the lower section where vertical struts were removed in the SAPIEN 3 and Ultra, effectively removing the need for strut conforming by reducing paravalvular leakage through the skirts.

3.2.3 Self-Expanding Prosthetic Valves

Self-expanding (SE) valves are also made up of stent-like frames with animal leaflets sutured to the struts. The difference is that these frames are made of Nitinol, a nickel-titanium, shape memory alloy. Shape memory alloys can be deformed into another shape under a certain temperature but retain their original ("remembered") shape when the temperature threshold is exceeded. Above this threshold value, Nitinol exhibits superelasticity where it can undergo a large amount of deformation but returns to its original shape when the stress is removed. SE valves are manufactured such that they exhibit superelasticity at 37° C [51]. They are crimped onto a catheter at room temperature and sheathed. When the catheter is inserted into the body the expansion of the valve

is prevented by the sheath until the aortic root is reached, where the delivery system allows for the unsheathing of the valve. An intermediate step in this unsheathing is shown in Figure 3.11. When unsheathed, the valve springs into its original shape, exerting a radially outward force which pushes the diseased native leaflets out and anchors the prosthetic in place [37].
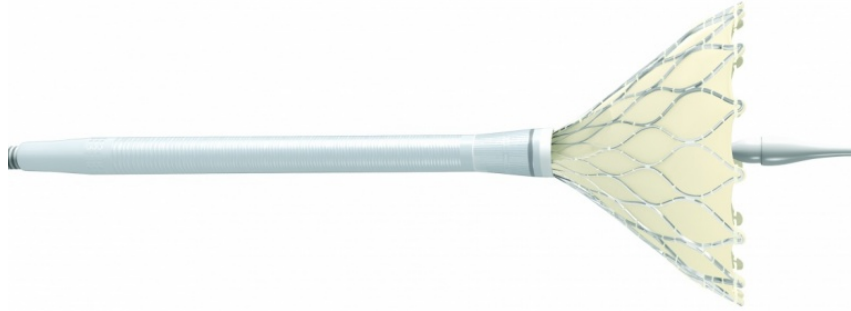
FIGURE 3.11: Representation of the delivery catheter of the CoreValve series (Medtronic PLC, Minneapolis, USA), just as the valve is half unsheathed [40].

3.2.3.1 Radial Force of BE and SE TAVI valves

The radial force (RF) of a TAVI valve is an important characteristic of all TAVI valves because it determines the ability of the valve to anchor within the aorta. It refers to the force a valve frame exerts along every radius when compressed around the circumference [52]. For a BE valve, this force is equivalent to the force required to plastically deform the frame in the radial direction after deployment. Hence, the radially outward force exerted by a BE valve is equivalent to the radially inward force required to crimp the frame.

SE valves, however, present an RF profile in the form of a loop where radial force intensity is higher during crimping and lower during expansion. This behaviour is called stress hysteresis and implies that the RF exerted by a SE valve depends on its incrementally-previous compression state [52]. To capture this difference, the radial force during expansion of a SE valve is referred to as the chronic outward force (COF) and the radial force during crimping is called resistive radial force (RRF) [53]. Figure 3.12 shows a typical hysteresis loop of an SE valve with regions of COF and RRF labelled. The anchoring of an SE valve is hence dependant on its COF and the SE valve designs in this thesis were evaluated through the COF they exhibit.
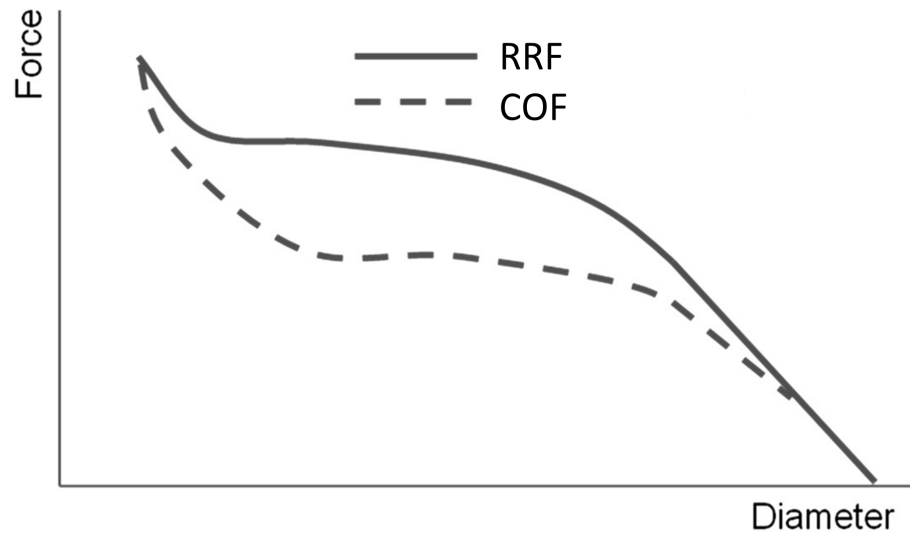
FIGURE 3.12: A typical hysteresis loop of an SE valve. RRF = radial resistive force, COF = chronic outward force. [52]

3.2.3.2 CoreValve Series

The CoreValve range (Medtronic PLC, Dublin, Ireland) is the leading SE TAVI valve in the world [37]. The first generation CoreValve (Figure 3.13, left) exhibited 5.0% 30-day all-cause mortality, 5.2% device failure, and 8.0% paravalvular leakage. These outcomes were improved in the second generation Evolout R (Figure 3.13, middle) which exhibited 3.4%, 3.5%, and 6.4% in the same respective variables [54]. The latest model, Evolut PRO, shown in Figure 3.13 on the right, has performed even better in studies, with all-cause mortality at 30 days at 3.2%, paravalvular regurgitation of 3.8%, and an average pressure gradient of 7.5 mmHg [55–57].

Structurally, all three generations in Figure 3.13 have vertically elongated rhombus-like cells with curved struts. The middle section of the valve frame is narrower than the top and bottom parts which improves anchoring in the aortic annulus and prevents the valve from moving axially along the aorta. The leaflets sit higher (towards the arching aorta) inside the frame compared to the aortic annulus. This means that the patient's new functional aortic valve following CoreValve implantation is further along the aorta than the native valve [37]. This positioning is referred to as supra-annular deployment. The two anchor points on the top part of the frame allow the interventionalist to reposition or re-sheath the valve until it is fully deployed. The larger cell size on the top also decreases the risk of coronary obstructions and allows for future catheter access into the coronary arteries [37].

Again, the addition of skirts features across the device generations where Evolut R has a higher inner skirt than CoreValve, and Evolut Pro contains an additional outer skirt. This coincides with the improvement in paravalvular regurgitation across the design evolution. SE valves in general exhibit larger paravalvular regurgitation compared to
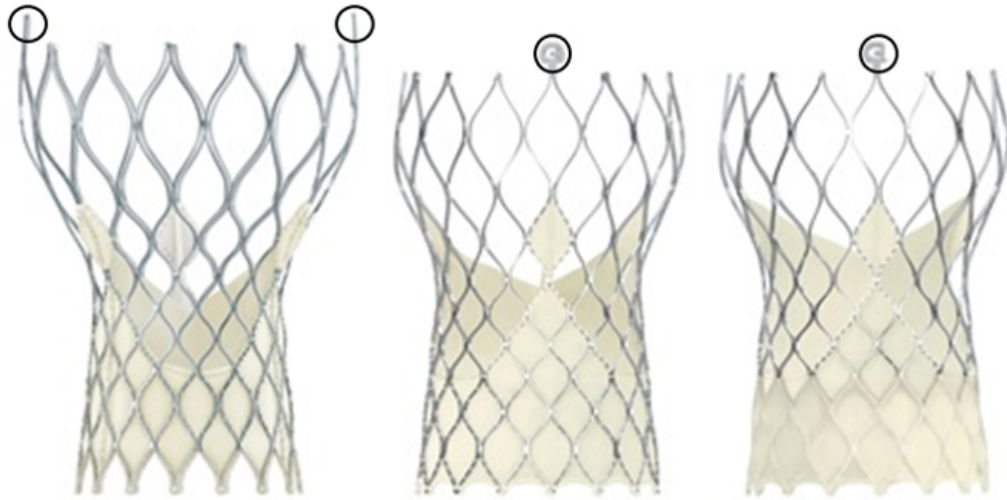
FIGURE 3.13: The three evolutions of the CoreValve series: CoreValve (left), Evolut R (middle) and Evolut Pro (right). The black circles show the anchor points on the frames where the delivery system attaches to, and can reposition the frame through, during deployment [39].

BE valves. In a meta-analysis of 9 studies consisting of 5910 patients, the rate of paravalvular regurgitation of CoreValve was 15.75% compared to 3.93% for SAPIEN valves [58]. This is because the COF of SE valves are lower than the radial force of BE valves. For example, a 26 mm SAPIEN XT exhibits 101.2 N of radial force at a crimped diameter of 23 mm, compared to 9.5 N COF of a 26 mm CoreValve at the same crimp diameter [53]. Although positive in terms of anchoring, the greater radial force of BE valves put them in a higher risk of aortic root rupture [59].

In addition to the enhancement provided by the outer skirt, the trend with decreasing strut width, particularly between the first two generations, contributes to greater conformance after deployment, as thinner struts deform easier under contact with the aortic wall. Another interesting design evolution is the decreased difference in radius between the middle and the ends of the frame. Due to lower COF compared to BE counterparts, most SE frames have an hourglass-like shape that improves anchoring in the axial direction. The upper end of the frame lodges in the supra-annular region of the aortic arch, resisting the maximum force on the valve applied during diastole in the direction of the left ventricle. The decrease in radius variance along the height of the frame over the generations shows that the COF of the frame is mostly sufficient for anchoring. Finally, the nipple-like crowns in the high-strain regions of cell vertices seen in latter generations of SAPIEN are also present in all CoreValve generations.

3.2.3.3   ACURATE Neo

The ACURATE Neo (Boston Scientific Corporation, Marlborough, USA) prosthesis (Figure 3.14) is a self-expanding valve which is deployed in a two-step deployment where

<small>FIGURE 3.14: The ACURATE Neo (Boston Scientific Corporation, Marlborough, USA) self-expanding valve [60].</small>

the upper, larger crowns provide supra-annular anchoring and cap the native leaflets. The extruding arches in the middle are referred to as the stabilisation arches and contribute to axial self-alignment of the frame.

1-year follow-up studies of the ACURATE Neo through transfemoral access showed favourable results with 8% mortality out of 1000 patients [60]. Pacemaker implantation rate was 9.9% and severe paravalvular leakage occurred in 3.6% of patients [60].

3.2.3.4 Allegra Valve

<small>FIGURE 3.15: The NVT Allegra Valve (New Valve Technology, Muri, Switzerland) [61].</small>

The NVT Allegra (New Valve Technology, Muri, Switzerland) transcatheter heart valve (Figure 3.15) is a self-expanding TAVI prosthesis which was designed to avoid haemodynamic compromise and facilitate correct positioning during the step-wise implantation phase of the prosthesis [61]. The variable cell size distribution along the height of the frame allows easier access to the coronaries. Different levels of COF due to this variable cell size enhance the anchoring and conformation of the prosthesis within the native aortic annulus [61]. Using a three-step release mechanism, the delivery process allows a controlled positioning of the NVT Allegra prosthesis without interfering with the left ventricular outflow [61]. As long as the prosthesis is attached to the catheter system and until 70% of complete unsheathing, the transcatheter heart valve can easily be recaptured and fully retrieved [61].

Only 30-day follow up studies with small patient cohorts (n = 27 and n = 21) have been completed with the Allegra valve [61, 62]. Permanent pacemaker implantation was needed in 23.8% of the patients and one death was recorded [61, 62]. The mean transvalvular pressure gradient was decreased from 48.0 ± 21 mmHg to 8.9 ± 3 mmHg following implantation [61].

3.2.3.5 Portico Valve

FIGURE 3.16: The Portico valve (St. Jude Medical, Little Canada, USA) [63].

The Portico valve (St. Jude Medical, Little Canada, USA) (Figure 3.16) is a self-expanding bioprosthetic aortic valve. A porcine pericardium cuff attached at the annular level of the frame is intended to provide sealing within the native aortic annulus. The high compliance of the frame due to its thinner struts further reduces paravalvular leaks. The large cells allow easy access to the coronary arteries in case of percutaneous coronary revascularization after implantation.

At 30-day follow-up of Portico valve implantation, all cause mortality was at 2.7% [63]. Only a single case of severe paravalvular regurgitation was observed out of 73 patients [63]. Pacemaker implantation rate stood at 12% and the mean transvalvular pressure gradient was 6.9 ± 3.2 mmHg [63].

3.2.4 Comparison Between SE TAVI Devices

The design choices and features of the commercial SE TAVI valves are largely similar across the different brands. Figure 3.17 depicts the four SE valves investigated side-by-side. The cell shape is consistent between the Allegra, Evolut Pro and Portico valves, with the Acurate Neo also holding very similar cells in its bottom ring. This implies that this cell shape provides feasible structures for SE valves.

	Allegra	Evolut Pro	Portico	Acurate Neo
Valve Height (mm)	41.3	45	50	50
Cell Quantity (circumferential)	15	15	9	12
Cell Quantity (height)	3	5	2.5	~1.5 - 2
Type of Leaflet	Bovine	Porcine	Bovine	Porcine
Leaflet Fixation Process	Elimination of phospholipid layer, reduction of glutaraldehyde free bonds	Glutaraldehyde-fixed, anti-mineralization treatment of alpha-amino oleic acid	Linx™ Anticalcification Treatment	BioFix™ anti-calcification process

FIGURE 3.17: Comparison between the relevant design parameters of Allegra [62], Evolut Pro [64], Portico [65] and Acurate Neo [60].

The valve height looks to be inversely related to the density of cells on the valve frame. Portico and Acurate Neo contain the least frame material across the four valves and are also the highest. This is most likely due to the larger supra-annular anchoring required for these valves since their COF is lower due to less material. Allegra and Evolut Pro contain a larger amount of cells and hence require less height for anchoring. The number of circumferential cells for each valve is divisible by three, which is required to mount a tri-leaflet valve within the frame symmetrically.

All four valves also include a varying radius across their height, although this is less pronounced in Allegra and Acurate Neo compared to Evolut Pro and Portico. The number of cells across the height of the device are different in all valves, as well.

Across the four devices, the leaflets are made from either bovine or porcine pericardium tissue. There are conflicting results in literature in terms of which tissue performs better in a valve prosthetic [66]. Several studies have compared bovine and porcine leaflet valves in terms of their post-operative mortality, durability, and haemodynamics

[67–70]. However, the results of these studies were confounded by the difference in the design and structure of the corresponding prosthetic valves the leaflets were mounted to [66]. As represented by both tissues being used in the commercial valves in Figure 3.17, there is no consensus on which type of leaflets is better. There is also a market size consideration in using bovine leaflets as opposed to porcine leaflets due to some patients refusing to be implanted with pig tissue due to religious reasons. This might be a contributing factor to certain valves using bovine tissue in their products.

The exact process of leaflet fixation to preserve the tissue's structure and limit calcification for the four valves in Figure 3.17 is not readily available to the public. The leaflets for all devices are glutaraldehyde fixed to prevent tissue degradation, reduce antigenicity and improve durability [71]. However, this fixation method can result in the stiffening of the leaflets via mineralization when in contact with blood [71–73]. To limit this mineralization, the leaflets undergo anti-calcification treatments prior to valve assembly [73]. The main purpose of these treatments is broadly as described below the Allegra valve in Figure 3.17, namely the elimination of the phospholipid layer and reduction of glutaraldehyde free bonds on the leaflet surface [62]. Information on how this is achieved for the Allegra valve is not available publicly. The Evolut Pro valve utilises an alpha-amino oleic acid treatment as an anti-mineralization measure [64]. The Linx anticalcification treatment involves ethanol treatment of the glutaraldehyde fixed leaflets [65]. There is also no further information on the BioFix anticalcification process used in Acurate Neo [60].

3.2.5 History and Recent Trends

TAVI was first implemented in 2002 as an alternative to SAVR for high-risk patients who could not undergo open heart surgery [74]. The initial trials comparing TAVI and SAVR all focused on high risk patients unable to undergo heart surgery and TAVI was only approved for use in high-risk patients with severe aortic stenosis. Over the years it has had a high rate of success and more TAVI operations are happening each year. From 2012 to 2019 the number of TAVI procedures per year has increased from 4,666 to 72,991 in the US [7]. In 2018, the number of TAVI procedures surpassed the number of SAVR operations for the first time in the US [7].

Since its development, there have been many studies that compare the TAVI method to the surgical method. The evidence shows overwhelmingly that TAVI is a better option for high-risk elderly patients with comorbidities. In a study in Japan with a total patient cohort of 16775 patients, it was found that the ratio of in-hospital mortality between TAVI and SAVR was 0.36 (in favour of TAVI) in all patients [75].

Many patients with severe aortic stenosis, however, are intermediate or low risk [76]. As TAVI is a minimally invasive alternative to SAVR with faster recovery period, there

has been a trend worldwide towards using TAVI for lower risk patients as well. In the latest PARTNER 3 and CoreValve Low-risk trials, which compared the efficacy of SAPIEN 3 and CoreValve Evolut Pro to SAVR in low-risk patients, both devices were found to be non-inferior to SAVR [3]. In August 2019, based on these clinical trials that showed non-inferiority of TAVI versus SAVR in low-risk patients, the FDA approved an "expanded indication of some TAVI devices to patients with severe aortic stenosis who are at low-risk for death or major complications during surgery" [3].

Following from these data and developments transcatheter valve interventions have become the outstanding option for patients under prohibitive risk from traditional surgical treatments, revolutionising the management of VHD, along with providing a minimally invasive alternative for patients at lower risk categories [77]. TAVI is now a proven and highly effective treatment for VHD which has a profound effect on both patients and healthcare systems [77]. With the degenerative nature of valvular heart disease, the ageing population will require an increase in TAVI implantation rates, coupled with the expected increase due to the inclusion of patients at low surgical risk who currently undergo SAVR [78].

3.3 Bioprosthetic Valve Dysfunction (BVD)
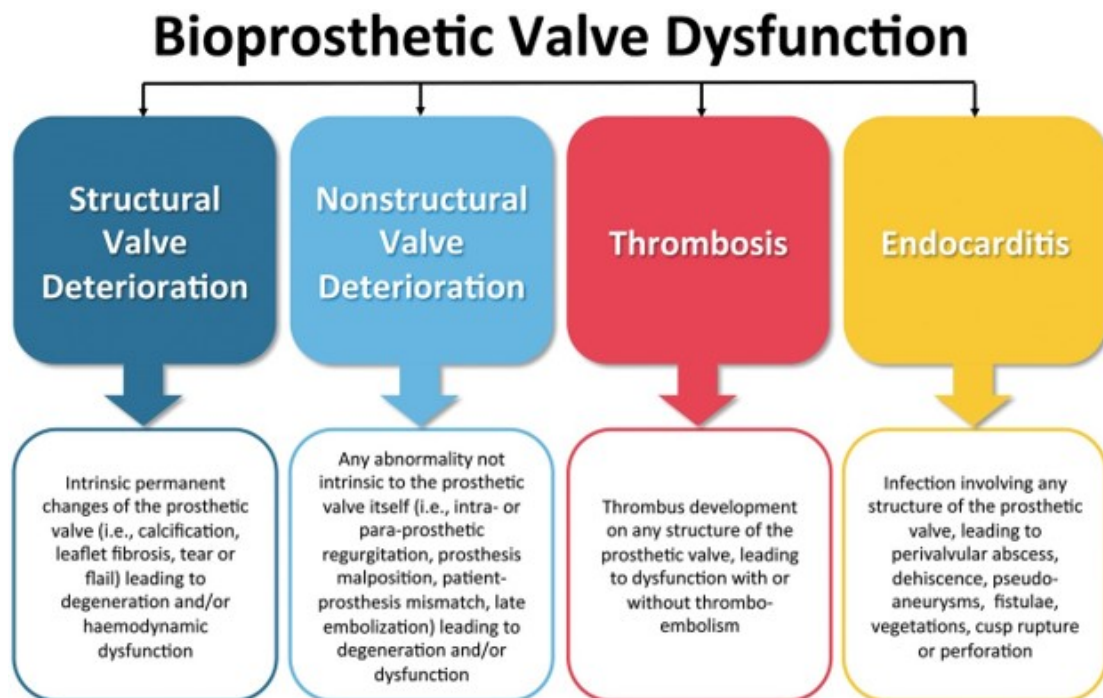
FIGURE 3.18: Causes of bioprosthetic valve dysfunction [79]

The function of bioprosthetic valve replacements have been widely demonstrated to be reduced over time due to several factors such as young age, highly active calcium metabolism, mechanical stress, and/or immunological responses to animal leaflets [80,

81]. In recent years, the causes of bioprosthetic valve dysfunction (BVD) were standardised based on consensus. Figure 3.18 shows the four main categories of BVD causes: structural valve deterioration (SVD), nonstructural valve deterioration, thrombosis and endocarditis. SVD relates to physical issues intrinsic to the prosthesis such as leaflet tear and calcification. Such changes in the prosthesis structure can result in dysfunction of the opening and closing of the valve leading to stenosis and regurgitation. Some examples of excised prosthesis with SVD are shown in Figure 3.19. Non-structural valve deterioration encompasses issues not intrinsic to the prosthesis but related to its implantation. These include problems such as valve malposition, paravalvular regurgitation and patient-prosthesis mismatch. Most non-structural valve issues are identified and remedied post-implantation, though untreated patient-prothesis mismatch is a strong indicator of future SVD [82]. Endocarditis is a rare but deadly bacterial infection of the inner lining of the heart and heart valves.[79]
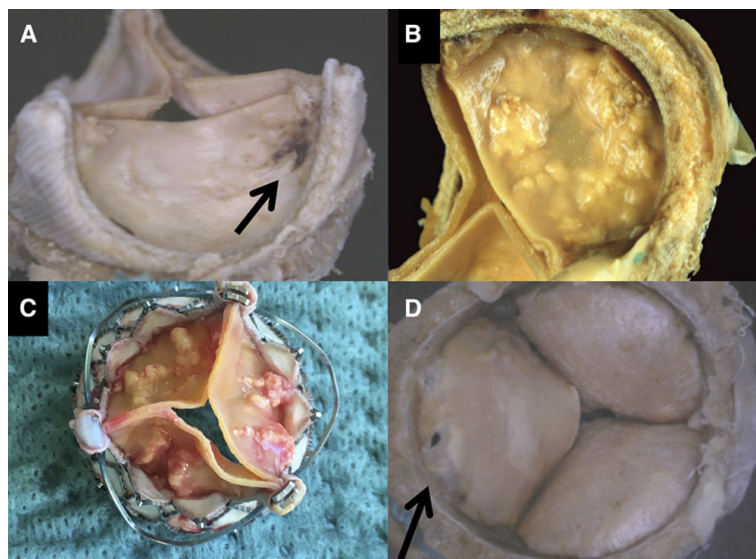
FIGURE 3.19: Examples of degenerated bioprostheses: (A) Carpentier-Edwards Perimount valve: leaflet tear, (B) Carpentier-Edwards Magna Ease valve: leaflet calcification, (C) Engager THV (Medtronic): leaflet restriction and calcification, (D) Carpentier-Edwards Perimount valve: leaflet tear (ventricular side) [83].

Thrombosis is the formation of blood clots on and around the prosthesis and can lead to functional impairment of the valve. These thrombi can also detach from the prosthesis to become emboli, leading to blockages in the vascular system. In particular, thrombosis occurs following the mineralization of the glutaraldehyde fixed animal leaflets [81]. With the mineralization of the leaflets, calcification and thrombi formation on the leaflets increases. The rate at which the the leaflets undergo mineralization is mostly associated with the stresses on the prosthetic valve [16, 80, 81]. Thrombosis is widely accepted as an indicator of subsequent SVD, particularly through the thickening of thrombosed cusps reducing their mobility.[84]

3.3.1 Incidence of SVD

SVD eventually leads to BVD and necessitates the replacement of the prosthesis. In this aspect, the incidence of SVD is directly related to the durability of a bioprosthetic valve replacement. Most of the long-term (> 10 years) durability data for bioprosthetic valves are based on SAVR valves since they have been in market for a longer. Table 3.1 and 3.2 list SVD and BVD rates from studies of SAVR and TAVI valves respectively.

TABLE 3.1: Medium and long-term studies that have investigated the durability of SAVR valves. Follow-up years are the maximum each study has investigated. Leaflet type refers to the leaflet tissue used in the valve. All valve leaflets were glutaraldehyde fixed but some had further anti-mineralization treatments. These are specified under the fixation column with either the anti-mineralization treatment specified or only-GA for valves that did not undergo such treatment. ThermaFix = Carpentier-Edwards trademarked anticalcification treatment. AOA = alpha-amino oleic acid treatment. SDS = sodium dodecyl sulfate. GA = glutaraldehyde NR = not reported.

Author / Trial	Follow-up (years)	Freedom from SVD (%)	BVD (%)	Leaflet Type	Fixation
Bourguignon et al.[6]	20	37.2	20	bovine	ThermaFix
Guenzinger et al.[85]	20	67	8.1	porcine	SDS
Forcillo et al.[86]	20	67	3.7	bovine	ThermaFix
David et al.[87]	20	63.4	7.6	porcine	only GA
Myken and Bech-Hansen[88]	20	61.1	5	porcine	SDS
Yankah et al.[89]	20	62.3	4.2	bovine	only GA
Jamieson et al.[90]	18	64	7.2	bovine	ThermaFix
Christ et al.[91]	15	44.1	48	porcine	only GA
Bach and Kon[92]	15	85.1	4.6	porcine	AOA
Mohammadi et al.[93]	15	62.6	27	porcine	AOA
Repossini et al.[94]	10	90.8	4	bovine	only GA
NOTION trial[95]	8	71.5	10.6	both	mixed
Johnston et al.[96]	6	NR	3.3	bovine	ThermaFix
Sénage et al.[97]	5	91.6	10.3	bovine	only GA

The stresses that the native aortic leaflets experience due to high blood pressure and velocity were discussed in Chapter 2. The same forces also act on both SAVR and TAVI bioprosthetic valve replacements. TAVI valve leaflets, however, undergo additional mechanical stress during the crimping and expansion procedure which can create further fenestration in the glutaraldehyde fixed leaflets [80]. The presence of heavily calcified native leaflets in the aortic annulus can also lead to non-circular expansions of the TAVI valve during deployment. These non-ideal deployments also put further stress on the leaflets [80].

These phenomena would point towards lower valve durability for TAVI devices but this is yet to be observed. Based on the data in Table 3.1 and 3.2 the average freedom from SVD for SAVR valves was 78.9% below 10 years, 69.3 % between 10 to 20 years, and 58% at 20 years. For TAVI, this was 89% at 5 years, 87.9% at 7 years, 89.5% at 8 years and 90.9% at 10 years. These results imply that TAVI valves undergo less

TABLE 3.2: Medium and long-term studies that have investigated the durability of TAVI valves. Follow-up years are the maximum each study has investigated. Leaflet type refers to the leaflet tissue used in the valve. All valve leaflets were glutaraldehyde fixed and had further anti-mineralization treatments of either ThermaFix or AOA. ThermaFix is a Carpentier-Edwards trademarked anticalcification treatment. AOA = alpha-amino oleic acid treatment. NR = not reported.

Author / Trial	Follow-up (years)	Freedom from SVD (%)	BVD (%)	Leaflet Type	Fixation
UK TAVI registry[98]	10	90.9	NR	both	both
Eltchaninoff et al.[99]	8	87.2	0.58	bovine	ThermaFix
Holy et al.[100]	8	NR	4.5	porcine	AOA
Testa et al.[101]	8	95.4	2.5	porcine	AOA
NOTION trial[95]	8	85.9	7.3	porcine	AOA
Deutsch et al.[102]	7	77.3	0.5	both	both
Barbanti et al.[103]	7	97.5	4.51	both	both
Panico et al.[104]	7	NR	3.1	porcine	AOA
Durand et al.[105]	7	88.8	1.9	both	both
Didier et al.[106]	5	87.6	NR	both	both
CoreValve high-risk trial[107]	5	90.5	NR	porcine	AOA

SVD compared to SAVR valves. However, the highest increase in the rate of SVD is observed more than 10 years after implantation for SAVR valves. Data for TAVI valve durability beyond 10 years is currently lacking in literature. PARTNER 3, CoreValve low-risk, Valve Durability Registry, and INDURE trials are currently ongoing and aim to follow TAVI patients up to 10 years after implantation. Since the stresses on the TAVI bioprostheses are larger than that of the SAVR bioprostheses it is likely that TAVI devices will exhibit similar or higher incidence of SVD in these trials.

SVD eventually requires the replacement of the prosthesis. This can be done through open-heart surgery where the degenerated prosthesis is excised and a new one is sutured in. This, however, is not possible for many high-risk patients.

3.3.2 Problems

Beyond the durability of bioprosthetic valves, there are other problems associated with TAVI. Firstly, the valve is initially not fixed in place with sutures but is rather anchored into the aorta and is held in place solely by the radial strength of the frame. As time passes, tissue builds up around the struts of the frame and strengthens this connection but during the first days after TAVI, the risk of malposition of the valve is high [108]. If the valve loses its position too much, paravalvular regurgitation gets too high and an intervention becomes necessary. In a study of 251 patients who underwent TAVI, paravalvular regurgitation was moderate/severe in 7.1% of cases(n = 18) [109].

Secondly, the native valves are not removed from the annulus and are instead squashed between the aortic wall and the stent frame. This causes a total decrease in the valvular

orifice through which blood can flow, decreasing the total output of blood from the heart. This area is called the Effective Orifice Area (EOA) and its decrease is related to a decrease in blood supply [23]. Alongside this, the degenerated, native leaflets can be damaged over time and chunks of tissue might be ripped out from them. This can cause blockages further down the vascular system [108].

Thirdly, there is the risk of coronary blockage where the degenerated, native leaflets can be pushed out and hinder blood flow into the coronary arteries which supply the heart. This can lead to serious conditions such as heart attacks. In a total of 142 patients 14 had either the right or left coronary ostium fully covered following TAVI [110].

Fourthly, patient-prosthesis mismatch is a prevalent problem. Patient-prothesis mismatch relates to the size of a prosthesis not matching with that of the patients aortic annulus. The fundamental reason for this is that estimating the aortic annulus diameter of a patient is non-trivial. In an ideal case, the resultant EOA of an implanted prosthesis would match the EOA of the healthy native valve. However, this EOA can only be estimated since the patient at the point of assessment already has reduced EOA due to valvular heart disease. Furthermore, the size data for commercial valves is non-standard, where a 23 mm prosthesis of one brand may have a different EOA compared to another brand. This discrepancy is increased in the case of TAVI valves where deployment uncertainties can result in a lower than expected EOA after implantation [23]. In current literature, the incidence of severe patient-prothesis mismatch ranges between 8-18% for TAVI valves [82]. Since patient-prothesis mismatch is a strong predictor of subsequent SVD, it contributes to the low durability of bioprosthetic valves [79].

Finally, there is considerable impact force on the aortic root during valve deployment. This can damage the Left Bundle Branch (LBB) located very close to the aortic annulus which can lead to conductance disturbances in the heart [111]. As a result of this some patients can develop arrhythmia [23]. Unfortunately, the exact reason for this interference is unknown and only some patients require a pacemaker implantation to remedy this effect. In a multi-centre study, 121 patients out of the whole cohort (n = 1151) had to be implanted with a pacemaker following TAVI [112].

3.4 Alternative Treatments

There are alternative options to treating valvular heart disease (VHD) without the implantation of a mechanical or bioprosthetic replacement heart valve. While used less extensively, these methods are utilised in certain patient populations successfully.

3.4.1 Aortic Valve Repair

Aortic valve repair is an alternative to prosthetic valve replacements for patients suffering from aortic insufficiency. This insufficiency results from aortic valve regurgitation caused by anatomical deformities of the leaflets and/or the aortic root. These deformities include unicuspid/bicuspid valves and, aortic root and ascending aorta dilation resulting in prolapsing leaflets [113]. The valve repair procedure aims to remodel the valve anatomy to achieve clinically satisfactory valve function through open heart surgery. The remodelling that needs to be done depends on the existing anatomy of the patient. For patients with unicuspid valves, the procedure involves the laceration of the single leaflet to generate a bicuspid valve [114]. For patients with bicuspid valves, the goal is to remodel the valve into a tricuspid valve [114]. The patient-specific anatomy of either the unicuspid or bicuspid valve can increase the complexity of the procedure depending on the symmetry of the existing leaflets and the presence or lack thereof of the commissures. For patients with leaflet prolapse due to dilations in the aortic root/ascending aorta, the procedure includes the restoration of the aortic diameter via suturing and subsequent correction of the prolapsing leaflet(s) with reference to the non-prolapsing leaflet(s) [113].

Aortic valve repair is not recommended on patients with moderate or severe calcification of the leaflets [113, 114]. Patients who are at high surgical risk are also unable to undergo this procedure. Hence, valve repair is mostly performed on younger patients. The high complexity of the procedure also prohibits its wide-spread use and it is mostly performed in high-volume centres [113]. Successful aortic valve repairs, however, exhibit comparable clinical outcomes to prosthetic valve replacements while avoiding long-term anticoagulant use [113, 114].

3.4.2 Ross Procedure

The Ross procedure, also called pulmonary autograft replacement, refers to the translocation of the pulmonary valve of a patient to the aortic valve position with the pulmonary valve being replaced with an allograft [115]. Mainly, the Ross procedure is performed on children and young adults due to the autograft being able to grow through the development of the patient [115]. With the lack of inorganic material and any type of stent, the procedure exhibits excellent haemodynamic outcomes [116]. However, the highly complex nature of the Ross procedure prohibits its use in many cases with high success rates mainly occurring in high volume centres [115]. In addition, the allograft replacing the pulmonary valve exhibits high rates of failure, necessitating additional complex re-operations in the patient's lifetime [115].

3.4.3 Polymer Valves

To address the issues of durability with bioprosthetic valves and the burden of anticoagulant treatment with mechanical valves, polymer valves are being developed. In these prosthetic heart valves, the leaflets are fabricated from advanced polymeric materials, mimicking the material properties of tissue leaflets with increased durability [117, 118]. The Tria valve (Foldax Inc, Salt Lake City, USA), shown in Figure 3.20, is one example of these new devices that have already undergone first-in-man trials [119]. Although initial results have been promising, the concept of polymer valves have existed for the past 60 years [117]. Many iterations have exhibited calcification and thrombosis in *in vivo* studies. Further studies are needed to assess the performance of the recent iterations of these valves over the medium and long term [117, 118].
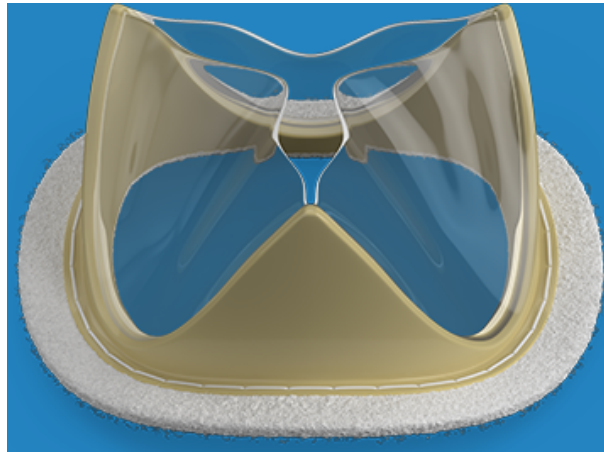
FIGURE 3.20: The Tria Valve Foldax Inc, Salt Lake City, USA). A recent polymer valve undergoing clinical trials. The leaflets of the valve is manufactured from a biopolymer named LifePolymer, a material created by Foldax [119].

3.5 Summary

The commercial valves described in this chapter formed the basis of the valve frame designs in this thesis. The cell shape and strut dimensions of SAPIEN and CoreValve series were used in the design of the BE and SE frames in this PhD research, as they had proven performance. The range of cell quantities, cell heights and strut widths of the SE valves determined the boundaries of the design space for these variables. Overall, the frame designs in this thesis aimed to emulate the commercial designs as much as possible while making necessary additions to allow for the exchange function of the e-TAVI system. Summary of the other important information in this chapter are listed below.

- Surgical aortic valve replacement (SAVR) and transcatheter aortic valve implantation (TAVI) are the two methods of valve replacement.

- Prosthetic valves for SAVR can be mechanical or bioprosthetic where mechanical valves are more durable but require lifetime anticoagulant use.

- All commercially available prosthetic valves for TAVI are bioprostheses and can be balloon-expandable (BE) or self-expanding (SE).

- Most commonly implanted TAVI valves are the SAPIEN series for BE and the CoreValve series for SE.

- Due to the high-risk of open heart surgery and proven efficacy of TAVI, increasing number of valve replacements are done through the TAVI method, even for lower-risk patients.

- Long-term durability of bioprostheses is becoming more important with the increase in number of valve replacements and decrease in patient risk profile.

Chapter 4

Redo Aortic Valve Replacements

This chapter contains the description and discussion of the Valve-in-Valve (ViV) and Transcatheter Aortic Valve-in-Transcatheter Aortic Valve (TAV-in-TAV) procedures, the minimally invasive methods for redo aortic replacements.

When a bioprosthetic valve, whether SAVR or TAVI, degenerates it eventually needs to be replaced. The current gold standard for a redo valve replacement is open heart surgery where the dysfunctioning prosthetic valve is excised and a new SAVR valve is sutured in [120–122]. However, many VHD patients with a degenerated prosthetic valve are at high risk of open heart surgery due to higher age and comorbidities [121]. For these inoperable patients, the only existing alternative treatment is the deployment of a TAVI valve within the failing bioprosthetic.

4.1   Valve-in-Valve (ViV)

The valve-in-valve (ViV) method is the minimally invasive alternative for redo valve replacements to open heart surgery when the degenerated valve is a SAVR valve. The procedure is named TAV-in-TAV when the degenerated valve is a TAVI valve.

4.1.1   Procedure Overview

The ViV and TAV-in-TAV procedures are identical to the TAVI procedure with the one difference being the deployment into a degenerated prosthesis instead of the native valve. Both BE and SE devices can be used. Figure 4.1 shows an illustration of ViV and Figure 4.2 shows different TAV-in-TAV scenarios.

Transfemoral, transaortic and transapical accesses can be used for ViV operations, with the transfemoral route being the most common [7]. The new replacement valve is

crimped onto a catheter and guided to within the degenerated valve. Alignment is achieved with respect to the degenerated prosthetic, rather than the native aortic valve, and the new valve is deployed. The deployed frame expands and pushes the degenerated leaflets of the prosthetic radially outwards. When fully expanded the new prosthetic anchors into the degenerated one and replaces its function.

FIGURE 4.1: Representation of a ViV operation using a CoreValve Evolut R inside a Perimount [123].
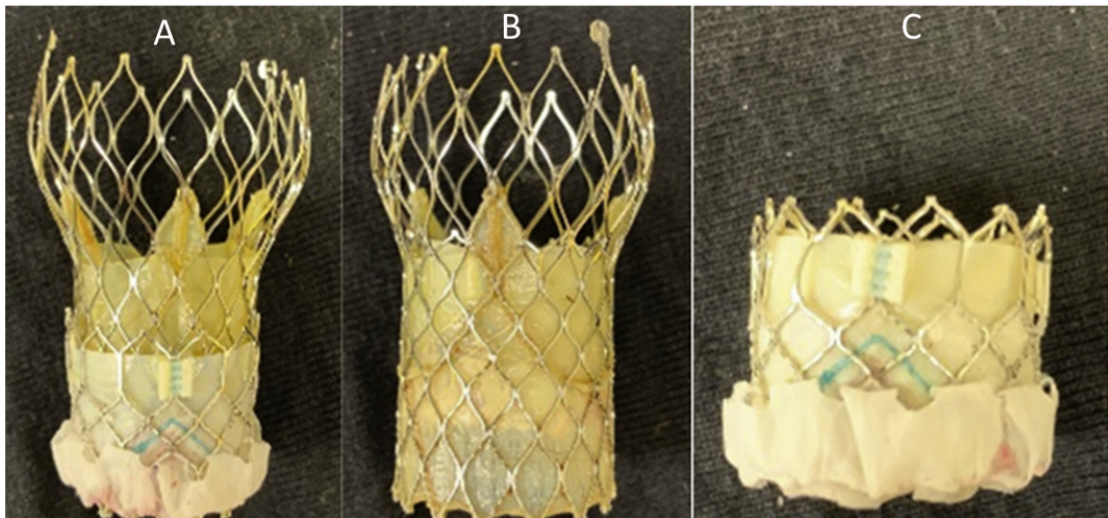
FIGURE 4.2: Ex-vivo TAV-in-TAV deployments: (A) CoreValve Evolut (23 mm) in SAPIEN 3 (23 mm), (B) SAPIEN 3 (23 mm) in CoreValve Evolut (26 mm), (C) SAPIEN 3 (23 mm) in SAPIEN 3 (23 mm) [124].

4.1.2 Clinical Data

4.1.2.1 Redo-SAVR versus ViV-TAVI

A large set of studies have been undertaken in which the performance of ViV-TAVI operations were compared to that of surgical redo operations. In this context, surgical redo refers to the removal of a degenerated prosthetic valve and the suturing of a

new surgical valve through open-heart surgery. The main aim in these studies was to determine whether ViV was non-inferior in terms of valvular function compared to the surgical method. Since the ViV operation is already advantageous compared to open heart surgery due to its inherent lower risk, showing that it is comparable in terms of function was crucial. Six multi-centre studies all concluded that ViV-TAVI is a feasible alternative to redo-SAVR for high-risk patients. A summary of these studies is given in Table 4.1. It can be seen that the two methods had very similar performances regarding mortality rates but ViV-TAVI had higher mean transaortic pressure gradients which was due to the decreased EOA caused by the presence of the previous device [120, 125, 126].

TABLE 4.1: Combined data from six studies comparing the performance of redo-SAVR vs ViV-TAVI

		Redo-SAVR	ViV-TAVI
Stankowski et al. [127]	30-day Mortality	7.5%	7.35%
	1-year Mortality	35%	30.9%
	Mean Gradient (mmHg)	19	16.8
	Pacemaker Implantation	5%	5.88%
Woitek et al. [128]	30-day Mortality	4.5%	4.76%
	1-year Mortality	9.91%	8.84%
	Mean Gradient (mmHg)	11.9	17.4
	Pacemaker Implantation	12.6%	13.6%
Sedeek et al. [129]	30-day Mortality	2.69%	2.22%
	1-year Mortality	18.8%	21.1%
	Mean Gradient (mmHg)	15	19
	Pacemaker Implantation	16.9%	5.56%
Deharo et al. [130]	30-day Mortality	7.25%	3.63%
	1-year Mortality	20.5%	23.7%
	Mean Gradient (mmHg)	-	-
	Pacemaker Implantation	5.72%	18.4%
Malik et al. [122]	30-day Mortality	4.93%	0.84%
	1-year Mortality	-	-
	Mean Gradient (mmHg)	-	-
	Pacemaker Implantation	6.34%	2.82%
Hirji et al. [131]	30-day Mortality	4.99%	2.80%
	1-year Mortality	-	-
	Mean Gradient (mmHg)	-	-
	Pacemaker Implantation	8.48%	10.9%

4.1.2.2 TAVI versus ViV-TAVI

Another important comparison was between ViV-TAVI and regular TAVI procedures. In this case, the effect of anchoring the TAVI valve to the native valves as opposed to a bioprosthetic valve was investigated. Relevant results from a study which compared these two procedures are given in Table 4.2. The mortality values are given in Hazard Ratio (HR) which is the ratio of the number of mortalities in the ViV-TAVI patients to

the number of mortalities in the normal TAVI group. A value of 0.5, for example. shows that only one patient in the ViV-TAVI group has died for every two patients in the TAVI group within the given time frame. Tuzcu et al. also concluded that ViV-TAVI is an acceptable option for high-risk patients and its performance is not vastly different from that of native valve TAVI. Although ViV-TAVI seems to be superior to normal TAVI in terms of mortality, the decreased EOA (which is the reason for the higher mean gradient) shows the disadvantage of this method. This difference was due to the constraint put on the deployment of the TAVI valve by the degenerated prosthetic valve. This constraint is less in the case of the native valve and hence the TAVI valve can be expanded further into the annulus, increasing the EOA [120].

TABLE 4.2: Results of study comparing the performances of regular TAVI and ViV-TAVI [120].

	TAVI	ViV-TAVI
30-day Mortality (Hazard Ratio)	0.50%	
1-year Mortality (Hazard Ratio)	0.65%	
Mean Gradient ($mmHg$)	9	16
Aortic Valve Area (cm^2)	1.8	1.3

A secondary paper investigated further into the results of Tuzcu et al.'s review in an attempt to identify further disadvantages of ViV TAVI compared to TAVI. The occurrence of coronary obstruction was found to be more common in ViV implants, concluded to be due to the presence of the leaflets from the failed prosthesis [132]. The mode of failure of the previous prosthesis can result in an imperfect deployment of the new valve [80]. This change in position is most likely related to the higher occurrence of coronary blockages. Also, the presence of the degenerated valve can cause under-expansion of the TAVI valve, further reducing the orifice area [132]. This irregular under-expansion may also cause durability issues through increased stress on the leaflets, though this still needs further investigation [23].

4.1.3 Problems

Problems associated with the ViV and TAV-in-TAV methods are mainly caused by the presence of the failed prosthetic valve, and range from sub-optimal valve function to life-threatening vascular blockages.

4.1.3.1 Pressure Gradient and Effective Orifice Area (EOA)

One of the biggest limitations of the ViV procedure is the post-procedural transvalvular gradients. This gradient refers to the rate of decrease in blood pressure over the prosthetic valve and is directly related to the EOA of the valve. When this gradient is above

20 mmHg the patient is at risk of insufficient blood supply from the heart and overworking of the cardiac muscle [41]. Out of three studies which investigated the performance of the ViV operation, the percentage of patients with high (>20 mmHg) transvalvular gradients were 44% (n = 47), 28.4% (n = 197) and 37.5% (n = 8) [133–135].

4.1.3.2   Coronary Ostia Blockage

Coronary obstruction is another risk in ViV operations. Most commonly, this occurs due to the leaflets of the degenerated valve which can fully or partially cover the coronary arteries after the deployment of the new valve. Factors such as short coronary ostia height (distance from the valve), and narrow aortic annuli are indicators for this issue [136]. The literature shows that this is not a very common issue where 3.5% of 202 patients, 2.3% of 1612 patients and 0.66% of 6688 patients had coronary obstruction in three separate studies [137]. However, it is a life-threatening complication where 30-day mortality of patients who experience it was 40.9% [137].

4.1.3.3   Permanent Pacemaker Implantation

The need for a permanent pacemaker is a problem associated with all kinds of valve implants. While the exact cause is unknown, it is thought that both the proximity of a metal frame to the conductive pathways of the heart and physical trauma during valve implantation could be the reason [138]. Eggbrecht et al. found that 11% of 47 patients who underwent ViV-TAVI required a pacemaker implantation [133]. Further to this, Hoyt et al. showed that ViV operations were associated with a much higher percentage of pacemaker implantation (VIV increased the likelihood from 17.4% to 62.5%) compared to TAVI, and concluded that this was most likely due to additional trauma suffered in the second deployment [138].

4.1.3.4   Multiple Valve Replacements

The feasibility of ViV, in terms of clinical satisfactory valvular function, decreases substantially with each new prospective implant due to decreasing EOA. Hence, there is a theoretical limit on the number of ViV operations that can be performed on a single patient [77, 78]. While this limit will vary between patients according to factors such as aortic annulus diameter, amount of valve calcification, and type of previous valve implant; the most in current literature is two concurrent ViV operations resulting in a total of three prostheses within the patient [139]. However, particularly due to the variation in aortic size across the population, many patients are not able to tolerate multiple ViV operations without the excision of the previous valve(s) through surgery.

Effectively, VHD patients with previous implants and smaller aortic areas are left with redo-SAVR as their only option in the event of prosthesis degeneration.
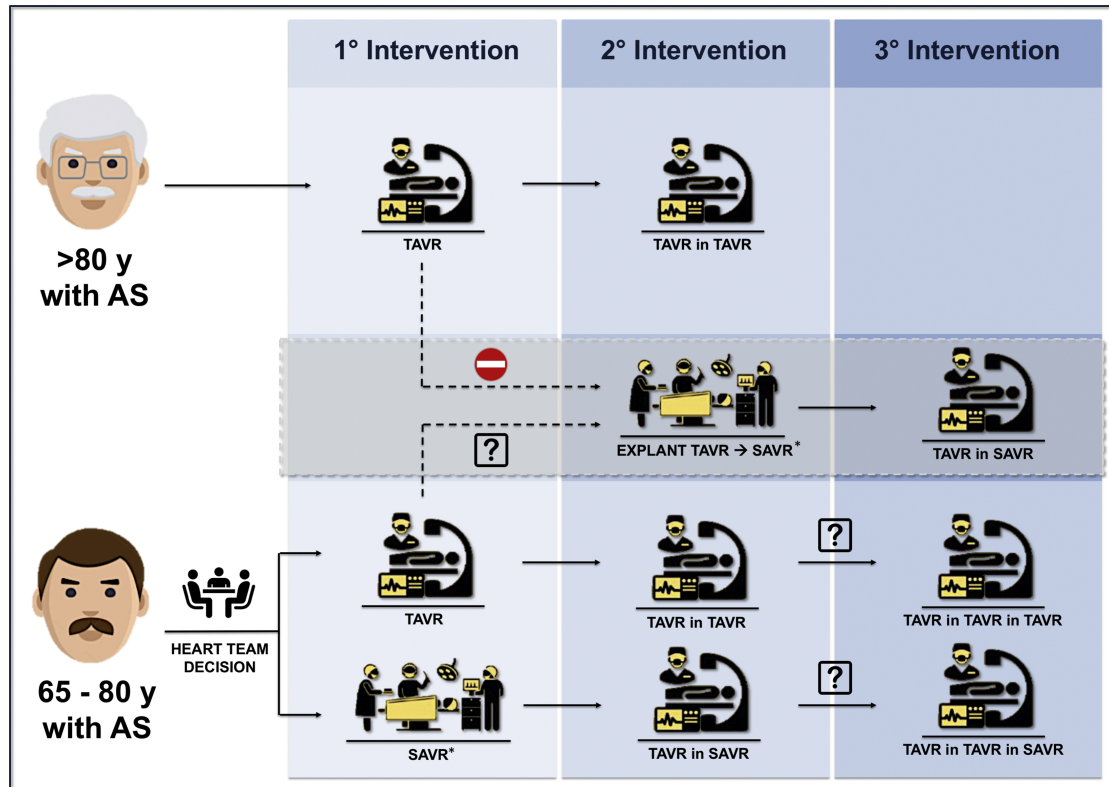
FIGURE 4.3: Potential treatment strategies in the lifetime management of patients with aortic stenosis [140].

Figure 4.3 portrays the possible lifetime treatment pathway of patients with aortic stenosis. For patients at high-risk of surgery, TAVI is the outstanding option. In the need of a second intervention for such a patient, TAV-in-TAV is the only possible option since removal of the valve through surgery will only increase in risk as the patient gets older. In such cases, the life expectancy of the patient will most likely be lower than the expected durability of the valve. For younger patients at lower risk groups, however, there is a high likelihood that secondary and tertiary valve replacements will be necessary. As shown in Figure 4.3, the first intervention determines the possible future treatment paths for the patient. Hence, the heart team must make a decision with foresight of future interventions and expected increase in surgical risk to the patient [140]. This decision also depends on anatomical factors such as aortic area which can limit the feasibility of ViV and TAV-in-TAV procedures. These uncertainties are portrayed in Figure 4.3 with question marks.

4.2   The Growing Need for Redo Valve Replacements

Even with the associated problems discussed above, ViV and TAV-in-TAV procedures are continuing to increase in number every year. In the US, in 2014, there were a total 305 ViV and TAV-in-TAV operations which increased to 4508 in 2019 [7]. Alongside this, the number of redo-SAVR surgeries increased slightly from 782 in 2012 to 840 in 2016 [141]. With the number of total valve replacements increasing over the years, it is not surprising that redo valve replacement numbers have also increased. The proportion of minimally invasive redo procedures has increased more rapidly than redo surgeries, showing that many patients with dysfunctional bioprostheses are either unable or unwilling to undergo open heart surgery.

With the increase in TAVI procedures, the proportion of bioprosthetic valves have increased, as all commercial TAVI valves are bioprosthetic. This is important for the future need for redo valve replacement as, unlike mechanical valves, bioprostheses exhibit SVD after implantation. In addition, TAVI has been approved for lower-risk patients and hence, the age profile of bioprosthetic valve recipients is also expected to decrease. Indeed, the risk profile of patients for TAVI in the US has decreased from 6.9% (30-day predicted risk of mortality score) to 4.4% between 2011 and 2019 [7]. This indicates that a larger number of valve recipients will be expected to live with a bioprosthetic valve for longer. This increases the number of patients which will belong in the third row pathway in Figure 4.3 where the first intervention in a younger patient is TAVI. The options for the secondary intervention in such a case are either TAV-in-TAV or explantation of the TAVI valve through open heart surgery, the latter of which might not be possible due to increased risk of surgery to the patient over time. With further reduction to the age and risk profile of patients recommended for TAVI, there will be an increase in patients that will require not one but multiple, minimally-invasive redo valve replacements over their lifetime. Thus, there is a growing need for redo valve replacements, both through the increase in the number of implanted bioprosthetic valves and the increase in expected survival time following implantation.

4.3   Recent Advances in ViV

The problems caused by the presence of the dysfunctional prosthesis in both ViV and TAV-in-TAV operations have formed the basis of two recent methods: bioprosthetic valve fracture (BVF) and bioprosthetic aortic scallop intentional laceration to prevent iatrogenic coronary artery obstruction (BASILICA) [142, 143]. BVF refers to the fracturing of an implanted SAVR frame via an angioplasty balloon prior to a ViV deployment. The fractured frame allows the TAVI valve to expand further within the dysfunctional valve, increasing EOA [143]. An example of BVF is shown in Figure 4.4a. BASILICA refers to the laceration of the leaflets on a dysfunctional prosthesis by an electrified wire prior

to the deployment of the TAVI valve. The lacerated leaflets decrease the probability of coronary obstruction [142]. The way these leaflet are lacerated are portrayed in Figure 4.4b, where the top image is prior to laceration and the bottom image is post-laceration.

(a) (b)
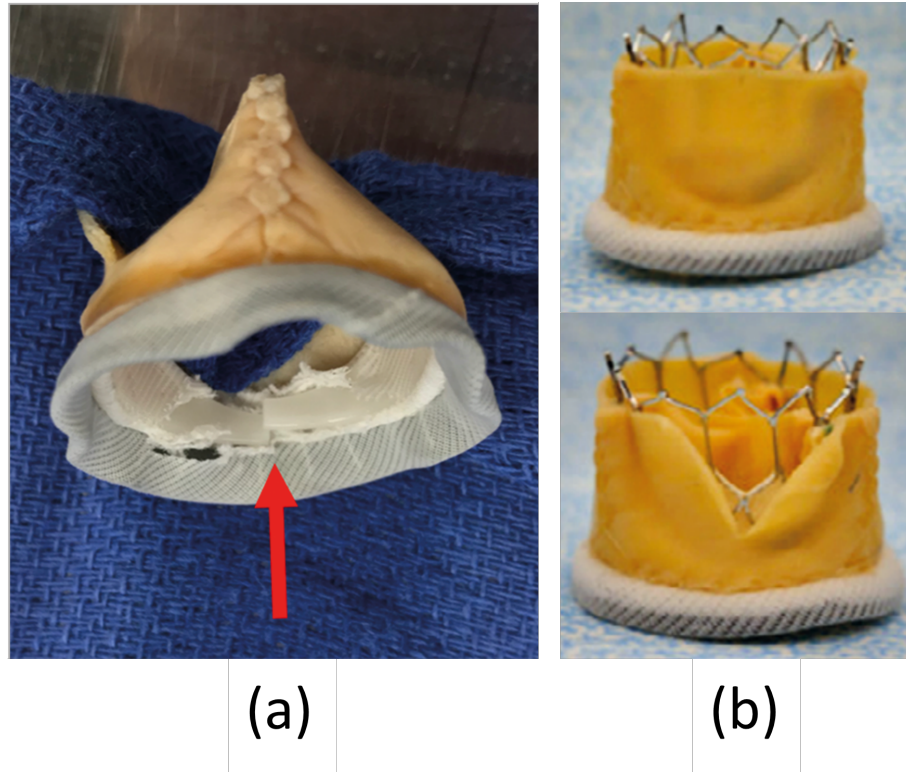
FIGURE 4.4: (a) Example of BVF of a Mitroflow valve (b) Example of BASILICA of a SAPIEN 3 in a Mitroflow valve [142].

Both methods attempt to reduce the profile of the dysfunctional prosthesis to improve ViV (or TAV-in-TAV) outcomes. However, in both cases the bulk of material consisting the dysfunctional valve still remains in the aorta, retaining a limit on redo replacements. Hence, the ability to remove the dysfunctional valve in the e-TAVI system exhibits an improvement to both these methods in terms of repeatability.

4.4   Summary

The problems identified in this chapter regarding the current state of the art in minimally invasive, redo valve replacements was the main motivation in developing an alternate procedure. The main cause of these problems was identified as the continued presence of the dysfunctional prosthesis following the replacement of its function by a new valve. Hence, the need of a new method of minimally invasive redo valve replacement where the dysfunctional prosthesis is removed prior to a new deployment was realised. Other important takeaways from this chapter are listed below.

- Bioprosthetic valves deteriorate within 10-20 years of implantation and need to be replaced, based on long-term durability studies of SAVR valves.

- For patients unable to undergo open heart surgery, a TAVI deployment within the dysfunctional valve is the only option.

- This ViV (or TAV-in-TAV) method is associated with worse outcomes compared to native TAVI, and puts a limit on multiple redo operations on a single patient due to decreasing EOA.

- With increasing aortic valve replacements and more bioprosthetic valves being used, more patients are expected to require multiple redo valve replacements in the future.

Chapter 5

A Novel Exchangeable Valve System

This chapter lists the problems associated with current methods of redo valve replacement followed by a description of e-TAVI, a novel valve system designed to alleviate these problems. Aims and objectives in the design of this new valve system are detailed, followed by preliminary design concepts.

5.1   Problems Identified in the Literature

The literature review identified several problems with the ViV and TAV-in-TAV methods:

- low durability of bioprosthetic valves;

- limit on concurrent treatments due to decreasing orifice area;

- increased pressure gradient post-procedure;

- risk of coronary ostia obstruction by the previous leaflets;

- damage to the conduction path of the heart leading to permanent pacemaker implantation.

With the increase in life expectancy combined with the low durability of bioprosthetic valves the future need for redo valve replacements are expected to increase [144]. For high-risk patients unable to undergo open heart surgery, ViV and TAV-in-TAV are the only current options for redo valve replacement, and there exists a limit on concurrent implantations within failed valves [145]. The pressure gradient and pacemaker implantation rate were even higher in ViV compared to TAVI due to the further decrease in EOA

due to the addition of a another valve inside the degenerated prosthetic valve [135]. The risk of coronary ostia blockage is also increased due to the leaflets of the degenerated valve [137].

5.2   Concept of exchangeable-TAVI

The problems associated with minimally invasive redo operations mostly stem from the presence of the previous failed bioprosthetic. Thrombosis, and subsequent SVD, is associated with the stresses on the leaflets and these stresses are increased when the valve is deployed non-circularly due to the calcified leaflets of this previous prosthesis around it. In addition, the physical presence of the previous valve constrain the diameter of the aortic annulus, leading to lower EOA and higher pressure gradients. This constraint can also cause non-ideal deployment scenarios leading to nonstructural valve deterioration such as paravalvular regurgitation and patient-prothesis mismatch. Coronary ostia are also most commonly blocked by the leaflets of a previous valve. The decreasing EOA due to the presence of the previous valve also limits the number of recurrent ViV operations that can be performed on a single patient. With the increased number of lower-risk patients implanted with degeneration-prone bioprosthetic valves, the need for multiple, repeated, minimally-invasive replacements will only increase. The recent advances in ViV - BVF and BASILICA methods - also identified and attempted to remedy the problems caused by the presence of the failed bioprosthetic, but the ability to completely remove a failed valve would be an improvement to both methods.

Following from this, the concept of a novel prosthetic valve replacement procedure was devised called e-TAVI, in which a previously failed exchangeable valve can be removed prior to the deployment of a new exchangeable valve. The e-TAVI valve system consists of three components:

1. a *holding member* deployed in the aortic annulus to push the native valve aside and to serve as an anchoring platform;

2. an *exchangeable valve* with attached leaflets that can mate with and be removed from the holding member;

3. a *dedicated catheter* that can attach to the exchangeable valve and remove it from the aorta.

Figure 5.1 portrays how the three e-TAVI components could look like when deployed, with magnetic attraction used for engagement between them. The holding member is situated in the aorta with magnetised bands facing radially inwards. Ferromagnetic regions on the exchangeable valve frame are attracted to these magnetised bands, serving
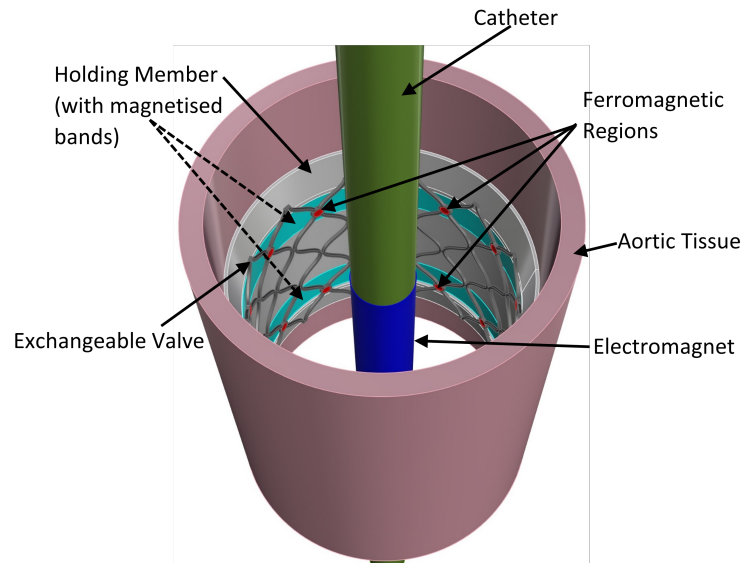
FIGURE 5.1: Conceptual image of e-TAVI with magnetic mating between the components. The image shows the holding member situated in the aorta with magnetised bands engaging with ferromagnetic regions on the exchangeable valve. The catheter holds an electromagnetic region to attach to the exchangeable valve. The skirt and leaflets on the exchangeable valve are not included in the image for clarity.

as an anchoring platform for the exchangeable valve. The catheter includes a region of electromagnets, shown simply as a cylinder in Figure 5.1, that can attract the ferromagnetic regions on the exchangeable valve for removal. In Figure 5.1, the catheter is positioned to attract the exchangeable valve and detach it from the holding member for its subsequent removal.

With the ability to remove a dysfunctional exchangeable valve *in vivo* and replace it with a new one, the identified problems regarding redo valve replacements can be alleviated. The removal of the failed valve can allow for multiple, minimally invasive valve replacements in a single patient, decrease the post-procedural pressure gradient by achieving a higher EOA and decrease the risk of coronary blockage.

The e-TAVI procedure can be divided into five steps, as depicted in Figure 5.2. Further description of these steps are:

1. The holding member is deployed within the aorta. In Figure 5.2, the holding member is portrayed as a surgically implanted component which is sutured into the aortic root through open heart surgery. Transcatheter holding members are also described in this thesis but surgical versions were deemed more feasible.

2. The initial exchangeable valve is deployed within the holding member via a catheter. The initial in this circumstance refers to the first e-TAVI replacement for a given patient (i.e. the first exchangeable valve deployed into the holding member). While the first two steps are described separately in Figure 5.2 to reflect the evolution of

the e-TAVI design concept as it occurred through this PhD research, there is scope for them to be combined. Since the patient is effectively without a functioning valve following the implantation of the holding member, the initial exchangeable valve should be delivered alongside the implantation of the holding member.

3. The initial exchangeable valve is detached from the holding member and crimped via its attraction to the e-TAVI catheter. This third step and the subsequent steps, 4 and 5, relate to the exchange process after the initial exchangeable valve has degenerated. The catheter in Figure 5.2 includes a new exchangeable valve to replace the old one, and a tapered sheath to remove the initial exchangeable valve. Removal elements on the catheter, such as electromagnets in Figure 5.1, overcome the engagement between the holding member and the exchangeable valve. Following this, the same removal elements exert a radially inward force on the exchangeable valve to reduce its radial profile such that it can be moved axially out from within the holding member.

4. A new exchangeable valve is deployed into the vacated holding member. In Figure 5.2, the new exchangeable valve is aligned within the holding member in the same axial motion described in Step 3. Whether this is plausible or not, the time between the completion of Step 3 and 4 must be minimised as the patient does not have a functioning valve between these two steps.

5. The crimped, old exchangeable valve is pulled into a tapered sheath for subsequent removal from the body.

5.2.1   Genesis of the e-TAVI Concept

The e-TAVI concept began from Prof. Dr. Nick Curzen's identification of the future "Russian Doll" issue facing the ViV method, through his profession as a cardiovascular interventionist. Curzen approached Prof. Dr. Neil Bressloff, who had experience with cardiovascular engineering research, to discuss the possibilities of solving this problem. From this discussion, a PhD position was published with the task of finding a solution to the challenges facing ViV procedures which would most likely need to be performed multiple times on a single patient in the coming years. While Bressloff and Curzen were thinking of a dedicated ViV prosthesis that maximised EOA and allowed for a larger number of ViV procedures on a single patient as the possible solution to the problem, Oguz Can Eren proposed a valve that could be exchanged minimally invasively. Eren proposed that the valve would have a permanent component deployed within the aorta and an exchangeable component able to be engaged to and disengaged from this permanent member. Alongside these, the new valve system would have a catheter capable of performing this engagement/disengagement between the two components to deliver and remove the valve. Eren also proposed that the engagement between these components

1) *Deployment of the holding member into the aorta.*

2) *Deployment of the exchangeable*

3) *Disengagement of the exchangeable valve from the holding member via the e-TAVI catheter.*

4) *Deployment of a new exchangeable valve.*

5) *Retrieval of the old exchangeable valve.*
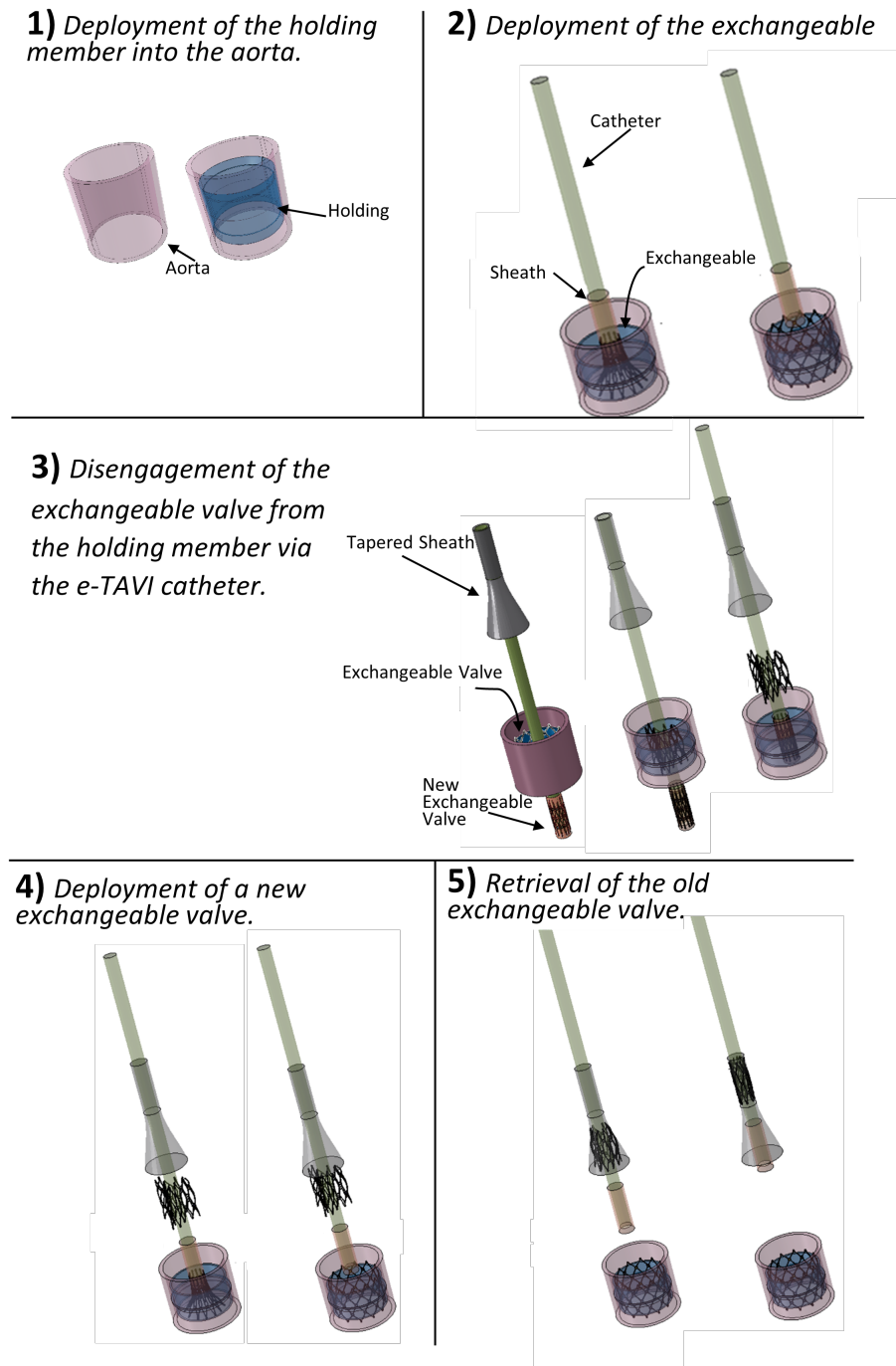
FIGURE 5.2: The five steps of the e-TAVI procedure. These steps include the initial deployment of the e-TAVI system where a holding member and an exchangeable valve is deployed within the aorta in steps 1 and 2. Steps 3, 4 an 5 relate to the exchange procedure where the previously deployed exchangeable valve is crimped, disengaged from the holding member and sheathed. Simultaneous to this removal, a new exchangeable valve is deployed in the holding member.

could be magnetic, based on his background in electronics engineering. Curzen and Bressloff agreed on this new approach to solving the "Russian Doll" problem and the focus of the PhD research became the design and development of this system.

Eren undertook the design, modelling, and simulation of this e-TAVI system components with weekly meetings with Bressloff discussing and deciding on design choices. Within these discussion, Bressloff proposed the idea of having a single catheter capable of both deploying a new valve and removing the existing valve. Hence, the contributions of Eren in the development of the e-TAVI system were the initial idea of having a novel three-component valve system allowing the exchange of a degenerated heart valve prosthesis, and the design and development of the exchangeable valve, holding member, and the engagement method between them, which are described in this thesis. Through the development of the exchangeable valve, methods of crimping the frame via a catheter was investigated and the multi-pronged crushing approach was identified as a result of the simulations performed as part of the PhD research. Throughout the research, Eren and Bressloff had discussions on the development process and which design to move forward with on a weekly basis with meetings including Curzen every six months. The input of Eren's supervisors guided the design and development of the e-TAVI system through these collaborative discussions, as should be in any PhD research.

5.2.2 Tasks

The following tasks were identified to design and develop the e-TAVI system and achieve the design objectives listed in Chapter 1:

- design of the exchangeable valve frame in terms of delivery method, material, cell shape and mating mechanism;

- parametric, computational modelling of the exchangeable valve frame with changeable design parameters for frame height, frame radius, strut width, strut thickness, and cell height;

- computational simulations of *in vivo* crimping of the exchangeable valve frame to design and develop the mating mechanism for optimising the removal process;

- analysis of the effects of cell height and strut width on COF and force required to remove to further develop the valve frame design;

- design and simulations of the removal mechanism on the catheter including the crimping of the exchangeable valve and subsequent re-sheathing;

- design and computational modelling of a holding member able to anchor in the aortic root, and provide the necessary platform to anchor the exchangeable valve in accordance with its COF;

- deployment simulations of the exchangeable valve into the holding member for anchoring analysis.

5.3 Intellectual Property

Following the invention of the e-TAVI concept, the opportunity for a patent application was realised. To evaluate the novelty of the concept, a search of the patent literature was performed around exchangeable aortic valve replacement systems. Relevant prior art is detailed below, though there was none that captured the entirety of the e-TAVI concept.

Vesely described a two part valve assembly with a permanent base member sutured in by open heart surgery and a replaceable member that could percutaneously be attached to and detached from the base member [146]. The replaceable member consisted only of a single ring and leaflets with three attachment points corresponding to 3 slots on the base member. Figure 5.3 shows a drawing of his concept. Vesely also maintained a separate patent on a TAVI valve removal tool. This consisted of a series of expandable and collapsible hooks on a stent frame. This frame could be expanded within a deployed TAVI valve, attach the hooks to struts on the valve, and collapse to crimp the valve with it [146].
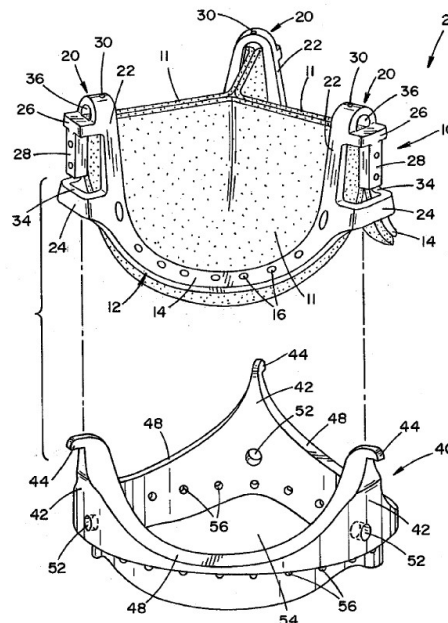
FIGURE 5.3: Conceptual drawing of Vesely's replaceable valve assembly [146].

Alonso described a two part surgical valve assembly that was sutured together [147]. The inner member hosting the leaflets could be cut free from the base member using a dedicated catheter. A replacement member could then be slotted on to the base member but still needed to be sutured in through open heart surgery. Hence, the purpose of this assembly was simply to speed up a redo-SAVR operation.

Garrison et al. described a two part TAVI assembly where a valve displacer was deployed first to move the native leaflets out of the way. The valve was then deployed on top

of the valve displacer. Certain mating mechanisms between them were discussed but no concept of exchange was mentioned [148]. Sharkawy et al. described a similar two part TAVI assembly consisting of a valve mechanism and fixation mechanism where the coupling between them were achieved by magnetism but still lacked any discussion of exchange [149].

Finally, Revuelta et al. invented a dedicated TAVI valve for replacing a degenerated prosthetic valve [150]. The new valve had hooks which could attach to the degenerated prosthesis's struts, increasing anchoring strength and reducing paravalvular leakage between the two prostheses.

As none of the patents above included a minimally-invasive exchange process, the novelty of the e-TAVI concept was realised. Consequently an Invention Information Form (IIF) on the e-TAVI concept was submitted to the University of Southampton in September 2020 and discussion with a patent attorney commenced in December 2020. A patent application was filed on March 2021 (UK Patent Application No 2103033.3) followed by an international PCT application (No:PCT/GB2022/050562) on March 2022. The patent, WO2022185063A1: A catheter, was published on September 2022 [151].

5.4 Engineering and Clinical Translation Pathway

The research in this thesis formed only the start of the design and development of the e-TAVI system. Looking broadly, the plans for the development and eventual clinical translation of the e-TAVI system can be described in the following steps, leading to a first-in-man trial:

1. Computational simulation of deployment and removal of the e-TAVI system.

2. Design and manufacture of a catheter system incorporating (i) magnetic elements to facilitate valve removal, (ii) a retrieval sheath, and (iii) a delivery sheath.

3. Final design and manufacture of prototypes for both the holding member and the exchangeable valve incorporating ferromagnetic regions.

4. Manufacture of complete exchangeable valve prototypes with leaflets and skirt.

5. *In vitro* testing of deployment and retrieval.

6. Computational modelling of the deployment and retrieval for exchangeable valves of all sizes in the diameter range 19-32 mm.

7. *In vitro* testing of durability and hydrodynamic performance

8. Biocompatibility and heamocompatability assesment

9. Preliminary pre-clinical study involving a small number (~5) of pig/sheep in an acute study.

10. Manufacture of 40 holding members, 40 catheters, and 80 exchangeable valves (i.e. two exchangeable valves per holding member) and subsequent 30-day and 6-month pre-clinical animal study using around 40 pigs/sheep

11. First-in-man clinical trial proposal submission

The manufacture of the components of the e-TAVI system is a crucial part of the future development of e-TAVI. Some conversation has taken place throughout this PhD research with companies who perform valve manufacture. These conversations were mostly focused on the manufacture of the exchangeable valve incorporating regions of ferromagnetic material. The exchangeable valve frame with the circular holes for the ferromagnetic regions can be manufactured via laser cutting of a Nitinol tube, in the same way that other self-expanding valve frames are manufactured. Some companies also manufacture the complete valve following laser cutting by suturing on leaflets and skirts which can be utilised in e-TAVI development since this suturing requires considerable skill. The addition of the ferromagnetic material to the holes present in the exchangeable valve can be achieved through biocompatible bonding agents or suturing. Step 3 in the above development pathway would assess the feasibility of different attachment methods. The design and manufacture of the catheter would most likely require additional partners with catheter design expertise. While the components and the required motion of these components on the catheter was designed in this thesis, the inner mechanisms of the catheter which would allow this motion via controllable knobs on the handle was not designed.

5.5   Summary

- A novel valve system named exchangeable-TAVI was conceptualised to address the growing need for minimally invasive redo valve replacements without sacrificing EOA.

- The e-TAVI system consisted of three components, the holding member, the exchangeable valve and a dedicated catheter, with the purpose of allowing the exchangeable valve to be replaced by a new one *in vivo* via the catheter.

- The PhD research aimed to computationally design and test the e-TAVI system, including the deployment, mating between holding member and the valve, removal of the exchangeable valve and retrieval via the catheter.

- The search of patent literature reiterated the novelty of the e-TAVI concept as there were no patents that discussed a minimally invasive exchange procedure.

Chapter 6

Methodology

This chapter details the generic setup of FEA simulations throughout the thesis, including mesh resolution, steps size, boundary conditions, and defined loads. This generic setup is the crimping and unsheathing simulations of the exchangeable valve frame which was a part of most of the simulations performed in this thesis. For those simulations that had differing or additional elements, the changes in methodology are described in the appropriate sections throughout the thesis.

6.1   Parts and Meshing

The part instances in most simulations in this thesis included a valve frame, a crimping cylinder and circular regions representing magnetic regions on the valve frame. The diameter of the crimping cylinder was decreased to crimp the frame and translated axially to unsheathe. Figure 6.1 shows an assembly of a simulation with these three parts with the aim of crimping and unsheathing the valve frame.

The mesh resolution of the parts in the simulations can have an effect on the results. To determine this effect, a mesh refinement study was undertaken as described in AP-PENDIX B. The goal of the refinement study was to identify the mesh resolution which produced negligible change in the solution results with further mesh refinement. The coarsest mesh that satisfied this condition was chosen since finer meshes cost increased computational time due to the larger number of equations to be solved.

The frame was meshed with hexahedral elements (C3D8R), with an edge length of 0.1 mm, following the mesh refinement study, resulting in at least three elements across a frame strut, as shown in Figure 6.2. The frame was divided into two partitions across the height of the device to allow for meshing with hexahedral elements using the Sweep meshing technique with the advancing front algorithm.
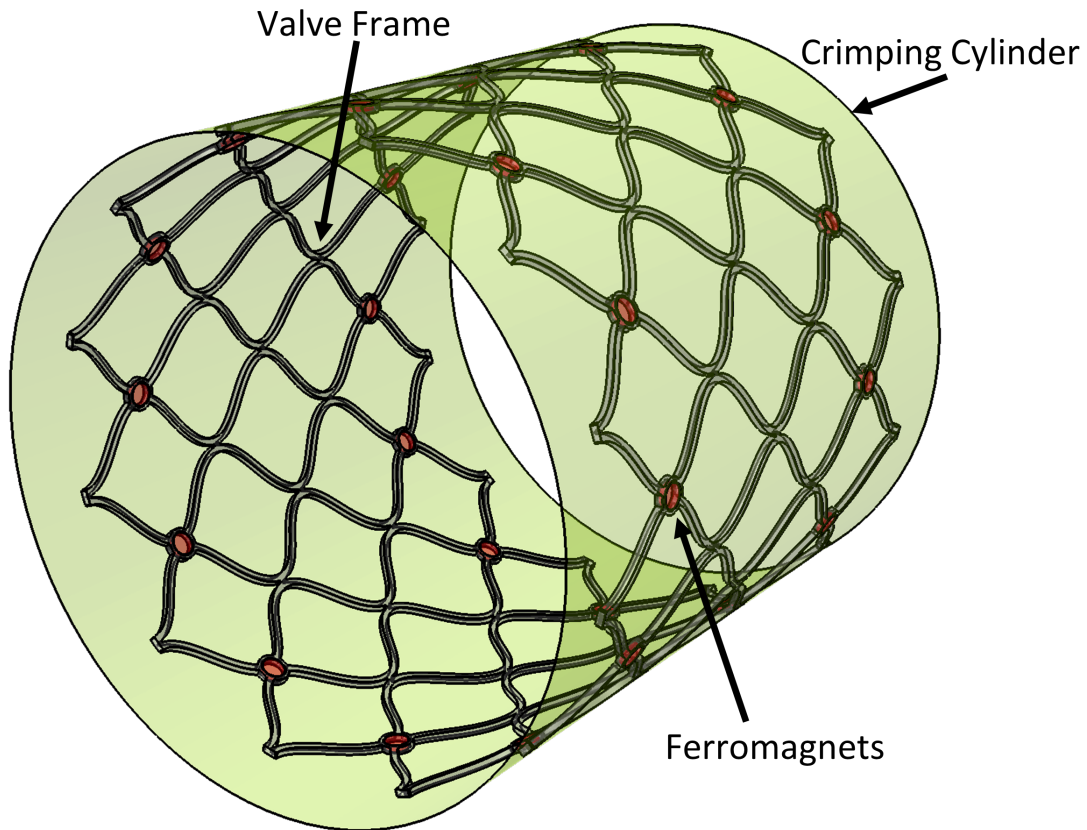
FIGURE 6.1: An assembly of the crimping and unsheathing simulations of the exchangeable valve frame.

Several computational studies in literature also found a mesh resolution consisting of three element across a frame strut to be sufficiently refined. Hopf et al. compared the influence of mesh size in crimping a CoreValve frame model with reduced-integration hexahedral elements (C3D8R) with one, two, three, and four elements across its strut, showing negligible difference between three and four elements in terms of displacement [152]. Luraghi et al. also discussed the mesh resolution with C3D8R elements of the crimping of a CoreValve device model, reporting less than 4% difference in terms of first principal stress during crimping between meshes with three and four elements across the strut [153]. Bianchi et al. also used three elements (C3D8R) across the strut for the crimping and deployment simulations of both SAPIEN and CoreValve devices, claiming this achieved mesh independence of the results, though the mesh refinement process was not explicitly stated [154]. Finotello et al. used meshes with three elements across a strut in the crimping and deployment simulations of Acurate Neo, Portico, CoreValve, and Evolut R, using reduced integration hexahedral elements as well [155].
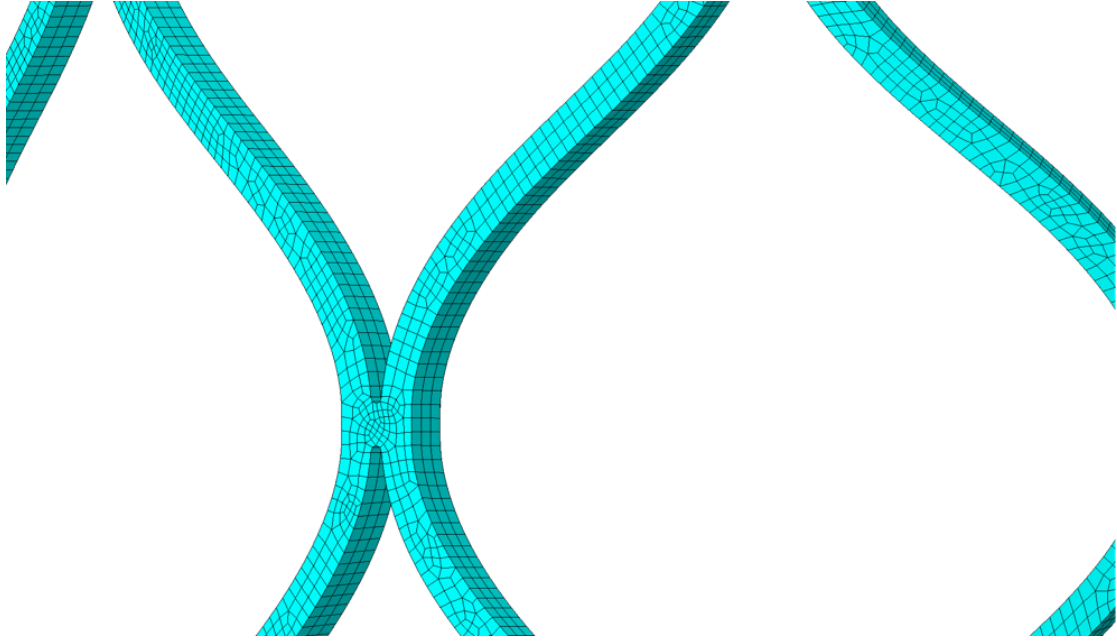
FIGURE 6.2: Close up view of the exchangeable valve frame mesh with a global seed size of 0.1 mm to achieve three elements across a strut. This resulted in a mesh with 92,712 elements for the exchangeable valve frame.

In this thesis, hexahedral elements with reduced integration were also used for their lower computational cost and higher tolerance, through the elements being less stiff, to large strain and deformations which occur during crimping simulations. Hour-glassing did not occur throughout the analyses as the mesh resolution was low enough to ensure this [152]. A comparison between the performance of full integration (C3D8) and reduced integration (C3D8R) elements was also performed and reported in APPENDIX B. Although the mesh with C3D8R elements predicted lower stresses than C3D8 elements (8 %) this was deemed tolerable when taking into account that the computational cost was 3.3 times higher.

In latter parts of the thesis, exchangeable valve frame designs with different strut widths were simulated. In these cases, the global seed size was always set as one-third of the strut width value to ensure three elements across a strut face.

The crimping cylinder part was generated in ABAQUS with a diameter 0.1 mm larger than the outer diameter of the exchangeable valve frame. The height of the cylinder was 5 mm longer on either end to ensure the end of the frame remained covered following its crimping. The crimping cylinder was meshed with quadrilateral 2D surface elements (SFM3D4R) in all simulations with a global seed size of 0.5 mm resulting in 13440 elements.

The magnetic regions on the frame were also generated in ABAQUS. They were meshed with the same elements (C3D8R) as the exchangeable valve frame with matching global seed size.

6.2 Sections and Material Models

The exchangeable valve frame was a self-expanding frame and hence had to be modelled as Nitinol. The superelastic material definition in ABAQUS was used to model this material. The properties of this material and how the constitutive material model was chosen is explained in Chapter 8. The parameters used are detailed in Table 6.1. The section assignment for the frame was as a homogeneous solid.

TABLE 6.1: Nitinol material parameters used in modelling the exchangeable valve frame.

	Nematzadeh et al. (2012) [156]
Density ($tonnes/mm^3$)	6.45×10^{-9}
Martensite Young's modulus (MPa)	18554
Austenite Young's modulus (MPa)	40000
Martensite Poisson's ratio	0.46
Austenite Poisson's ratio	0.46
Uniaxial transformation strain	0.040
Start of transformation stress during loading (MPa)	390
End of transformation stress during loading (MPa)	425
Start of transformation stress during unloading (MPa)	140
End of transformation stress during unloading (MPa)	135
Start of transformation stress during compression (MPa)	585
Reference Temperature	$37°C$
Loading	6.527
Unloading	6.527

The crimping cylinder was assigned a surface section with a density of 7×10^{-9} $tonnes/mm^3$.

The circular magnetic regions were assigned a homogeneous solid section with material properties based on neodymium magnets (N52 NdFeB Composite). The parameters defining this material is listed in Table 6.2

TABLE 6.2: Magnetic regions material properties (N52 NdFeB) [157].

Material Parameter	Value
Young's modulus	18554 MPa
Poisson's ratio	0.46
Magnetic Remanence (B_r)	1.45 T
Density	7.5×10^{-9} $tonnes/mm^3$

6.3 Steps

ABAQUS 2018 (Dassault Systèmes, Vélizy-Villacoublay, France) CAE software was used for all meshing and FEA simulations. This package contains two options for simulating

dynamic problems such as valve crimping and deployment: Implicit and Explicit. In this thesis, the Explicit analysis was used due to its superior complex contact solving algorithms and ability to model extremely fast events. The crimping of an SE valve frame through its contact with the crimping cylinder required the superior contact solver, and the self-expansion of the Nitinol frame when this contact was lost during unsheathing was a very fast event.

The main drawback of Explicit analysis over Implicit is the requirement for smaller time increments which greatly increases the computational cost of simulations. Unlike in Implicit analysis, there is no iterative step, following the system solution at each time increment, to ensure equilibrium within the internal forces of the system and retain simulation stability [158]. Unstable simulations can lead to an unbounded solution and cause convergence problems [158]. As such, in Explicit analyses, the time increment must be kept extremely small to ensure a stable simulation. The stability limit can be defined in terms of the time increment (Δt) satisfying the condition:

$$\Delta t << \frac{L}{c} \tag{6.1}$$

where L is the length of the smallest mesh element and c is the wave propagation speed. In order to decrease the time increment, and hence simulation time, the wave propagation speed must be decreased, which can be achieved through increasing the density of the part material. In ABAQUS this can be achieved through mass scaling where a target time increment is set and the mass is scaled accordingly [158]. A mass scaling analysis was performed (APPENDIX B) to determine the target time increment that provided stable results while minimising computational cost. As a result, a target time increment of 4E-7s was used in all simulations with semi-automatic mass scaling applied to the whole model. Automatic incrementation was used with global stable time estimation and the maximum time increment was not manually limited. The linear and bulk viscosity parameters were left at the default values of 0.06 and 1.2 respectively.

Following the identification of the target time increment, the step duration was determined as the shortest duration which ensured that the kinetic energy of the model was below 5% of the total internal energy to prevent unrealistic momentum from taking effect. This was 0.3s for the crimping and unsheathing simulations, and set individually for other simulations to ensure the same energy ratio.

6.4 Contact Interactions

The general contact algorithm was used to model contact interactions between the parts in the simulations. Self-contact was also defined on the parts through the general contact algorithm. As opposed to the alternative contact pair algorithm, the general contact

algorithm can enforce edge-to-edge contact for geometric feature edges, allows for each slave node to see contact with multiple faces per increment, and has built-in smoothing for element-based surfaces that is beneficial for modelling contact near corners [159]. The crimping of the frame involves edge-to-edge contact between the struts of the frame which needs to be enforced. Also, the nodes on the frame can contact multiple element faces on the cylinder in a single increment during crimping and expansion. Hence, the general contact algorithm was preferred over the contact pair algorithm. The contact between the parts was defined as frictionless and the hard contact pressure-overclosure relationship was used. In this contact model the surfaces do not transmit any contact pressure until there is contact between them (i.e. until the clearance between them is zero) [160]. The magnitude of contact pressure transmission is limitless when the surfaces are in contact [160]. The hard contact relationship also minimizes the penetration between the surfaces in contact through a constraint enforcement method. The penalty constraint method was used in this thesis with finite sliding.

Contact was defined between the surfaces of the frame and the surfaces of the crimping cylinder and ferromagnetic regions. Self-contact was defined for the valve frame and the ferromagnetic regions but not for the crimping cylinder.

6.5 Constraints

To represent the attachment of the ferromagnets to the frames, node-to-surface tie constraints were defined between each ferromagnet as the slave surface and the frame as the master surface. In a tie constraint, each node on the slave surface will have the same values for its degrees of freedom as those of its closest point on the master surface [161]. A position tolerance of 0.06 mm was also defined within the tie constraints which only tied the nodes on the ferromagnets that were within this tolerance of the frame. A problem with tie constraints is that they can cause localised, artificial stress spikes and oscillations around the constrained nodes [161]. Hence, the stress values around the ferromagnetic regions may be incorrect. This numerical inaccuracy applied to the stresses on the outer curved face of the ferromagnets and the inner circular faces across the thickness of the frame as these were the locations of the constrained nodes.

6.6 Boundary Conditions

The crimping and unsheathing simulations consisted of three steps: Crimp, Unsheathe, and Relax. These steps are depicted and explained in Figure 6.3.

In the Crimp step, a radially inward boundary condition was applied to all nodes on the crimping cylinder. This boundary condition is shown in Figure 6.3 in orange arrows.

Step 1 (Crimp):
Radially inwards boundary condition on the cylinder to crimp the frame.
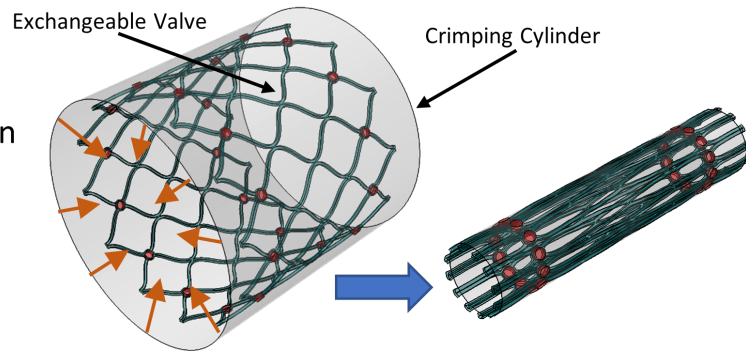
Step 2 (Unsheathe):
Axial boundary condition on the cylinder to uncover the frame while 3 nodes on the frame are constrained to move only in the radial direction.
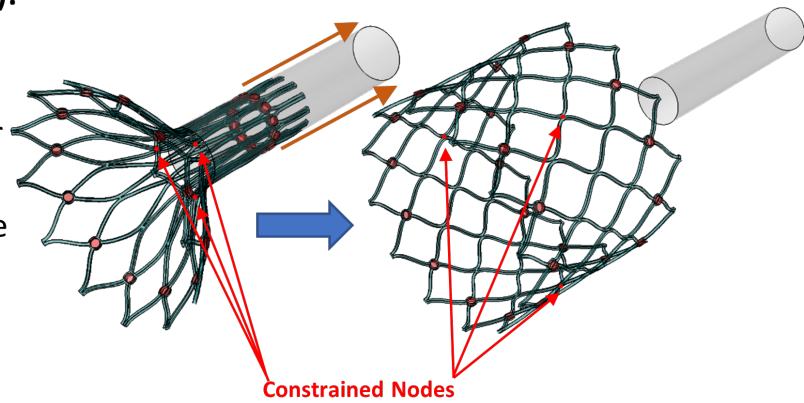
Step 3 (Relax):
Boundary condition on the 3 nodes of the frame is removed to allow the frame to relax into its final shape.
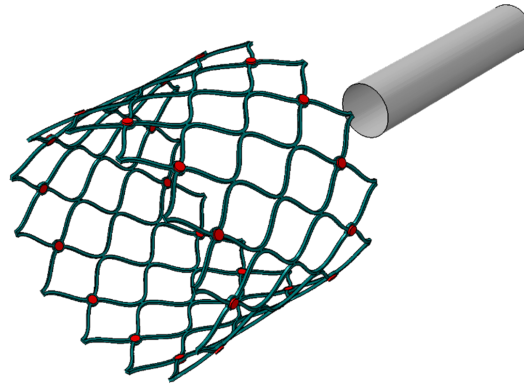
FIGURE 6.3: The three steps of the crimping and unsheathing simulations of the exchangeable valve frame with a cylindrical surface. The position and direction of the displacement boundary conditions are depicted as orange arrows. The radially constrained nodes are shown in red with red arrows pointing to their locations on the exchangeable valve frame.

The magnitude of this boundary condition determined the maximum crimped diameter of the frame. Initially, this final diameter was set to be 6 mm, representing an 18 Fr sheath. However, with the addition of ferromagnetic regions on to the exchangeable valve frame, this value was unfeasible. Hence, the target crimp diameter was updated to be 8 mm, representing a 24 Fr sheath. The cylinder was constrained in the axial and circumferential directions.

In the Unsheathe step, the boundary condition on the cylinder was converted to an axial

translation to uncover the frame through the step duration while it was constrained in the radial and circumferential directions. The magnitude of this boundary condition was 10 mm larger than the height of the valve frame to ensure that the frame was fully uncovered at the end of the step since the height of the frame would increase beyond its expanded height after crimping. Three nodes on the frame were constrained to move solely in the radial direction to prevent lateral and axial motion of the frame during unsheathing as it was observed that the frame would move axially with the crimping cylinder without this. These three nodes are marked in red in Figure 6.3 and labelled with red arrows. The position of these nodes were selected to be axially in the middle of the frame and the same distance apart circumferentially.

In the final Relax step, the boundary conditions on the three nodes of the frame was deactivated to allow the frame to settle into its final expanded shape. The contact definition between the cylinder and the frame was also deactivated.

A smooth step amplitude curve was defined to apply the boundary conditions in the simulations to avoid jumps in displacement across time increments. The amplitude definition had an amplitude of zero at the first time increment and an amplitude of one at the final time increment.

Gravity load was not defined in any of the finite element analyses in this thesis because the magnitude of force exerted on the prosthetic valves due to gravity are negligible compared to the magnitude of forces exerted by blood flow during systole and diastole. For example, the mass of the frame model in Figure 6.1 is 4.93×10^{-4} kg. For a gravitational acceleration of 9.82 m/s, this equates to a force magnitude of 4.84×10^{-3} N. This value is considerably smaller than the 6 N exerted on the valve during diastole and hence was neglected in the analyses in this thesis.

6.7 Summary

A few simulations performed in this thesis were different to the setups detailed in this chapter and are explained within their relevant chapter.

- ABAQUS/Explicit was used in all FEA simulations in this thesis.

- The global seed size for the exchangeable valve frame was set such that there were three elements across all faces of the frame struts, resulting in a value of 0.1 mm for most frame designs.

- The target time increment of the simulations was 4E-7s with step duration of 0.3s.

Chapter 7

Design and Development of
e-TAVI

The primary function of the e-TAVI system differentiating it from other TAVI valves
was the ability to minimally invasively exchange a degenerated valve with a new one.
Hence, the design and development around this exchangeability element of the system
was the main focus of this PhD research.

7.1 Design Requirements

The e-TAVI system was envisaged as comprising of three components: the exchangeable
valve, holding member and catheter. All three components had different but comple-
menting design requirements.

7.1.1 Design Requirements for the Exchangeable Valve

The exchangeable valve essentially had to perform all requirements of existing heart valve
prostheses with additional requirements for the exchange procedure. These requirements
for existing valves were:

- Hold three leaflets able to be opened and closed in response to blood flow in the
  aorta, achieving a transvalvular pressure gradient of below 20 mmHg while open
  and less than 30 cc of backflow while closed;

- Able to be crimped down to a diameter below 8 mm to fit inside a 24 Fr catheter
  and expand back to original dimensions when unsheathed;

- Exert sufficient outward radial force within the aorta to anchor against 11 N of axial force.

Additionally, the exchange procedure had the following requirements:

- Contain elements that are able to engage with the catheter where the engagement is sufficiently secure for the valve frame to be crimped *in vivo.*

7.1.2 Design Requirements for the Catheter

The catheter also had to perform all the requirements of a normal TAVI catheter with added requirements for the exchange procedure. These were:

- Have a low enough profile (24 Fr or below) to be able to move through the femoral artery, reaching the aorta, without damaging the patient's vessel walls or the catheter itself;

- Contain control elements on the handle than can unsheathe the valve prosthesis for deployment, capable of relative axial motion larger than 50 mm.

With the added requirements:

- Contain elements able to engage with the exchangeable valve. These elements must be able to move radially, *in vivo*, up to the radius of the exchangeable valve (13 mm) controlled from the handle. Elements must also be able to move axially relative to the catheter for sheathing of the exchangeable valve *in vivo.*

- Contain a controllable, tapered sheath that can be opened up to the full diameter of the exchangeable valve (26 mm) and closed back down.

7.1.3 Design Requirements for the Holding Member

The holding member did not perform a function that could be compared to an existing device. The design requirements for the holding member were:

- Securely anchor into the aorta, either via its outward radial force or suturing, to resist a minimum of 11 N of axial force;

- Have a radially inner surface with tribological qualities such that the outward radial force of the exchangeable valve exerted on this surface results in sufficient axial anchoring for the exchangeable valve (11 N).

- Contain elements able to engage with the exchangeable valve to increase anchoring strength and minimise paravalvular gaps between the exchangeable valve and the holding member,

- Have sufficient height to limit tissue contact between the exchangeable valve and the aortic wall to minimise tissue growth on the exchangeable valve.

7.1.4   Design Functionality Considerations

Further to these component based requirements, there were general design functionality considerations for the e-TAVI procedure as a whole. These were related to the ease with which the interventionist could perform the e-TAVI exchange procedure, including the removal and sheathing of a degenerated valve and the deployment of a new one. These included:

- The time between the removal of the degenerated valve and the deployment of a new one must be below 30 seconds as the patient is effectively without a valve during this interval. The 30 second limit is based on the maximum recommended pacing window during valve replacement procedures [43].

- The engagement elements on the catheter must be able to engage with the elements on the exchangeable valve with a very high success rate. The scenario where the contact between even a single one of the engagement pairs is lost after the exchange procedure has begun can have life-threatening dangers to the patient as the degenerated valve may not be able to be fully removed to deploy a new one while it also cannot be re-deployed back to its position to try again. Hence, the safety factor in terms of the strength of engagement between the catheter and the exchangeable valve must be very high through selecting a design capable of exerting a larger force than the minimum required to crimp the frame.

- The connection between the catheter and the exchangeable valve must also be easy to engage *in vivo*. The interventionist has limited vision inside the aorta in the form of a 2D x-ray image. Hence, the 3D alignment of engagement elements cannot be fine tuned manually via the interventionist. In addition, the engagement between the catheter and the exchangeable valve should ideally be accomplished without the need for pacing. This complicates the manoeuvring of the engagement elements further due to the presence of blood flow and leaflet in motion. Consequently, the ideal engagement mechanism would include some manner of self-manoeuvring and connection between the two components with minimal input necessary by the interventionist.

7.2 Development Flowchart

The development of some aspects of the e-TAVI components depended on the design of the other components. Hence there had to be an order to the design process, prioritising the components whose design would effect the design of others. Within this, the primary aspect of the e-TAVI system that had to be designed was the method of engagement between the three components which would influence the design of them all. Figure 7.1 shows the design and development flowchart of the e-TAVI system, where the crucial step of identifying the engagement method between the components depicted at the top.
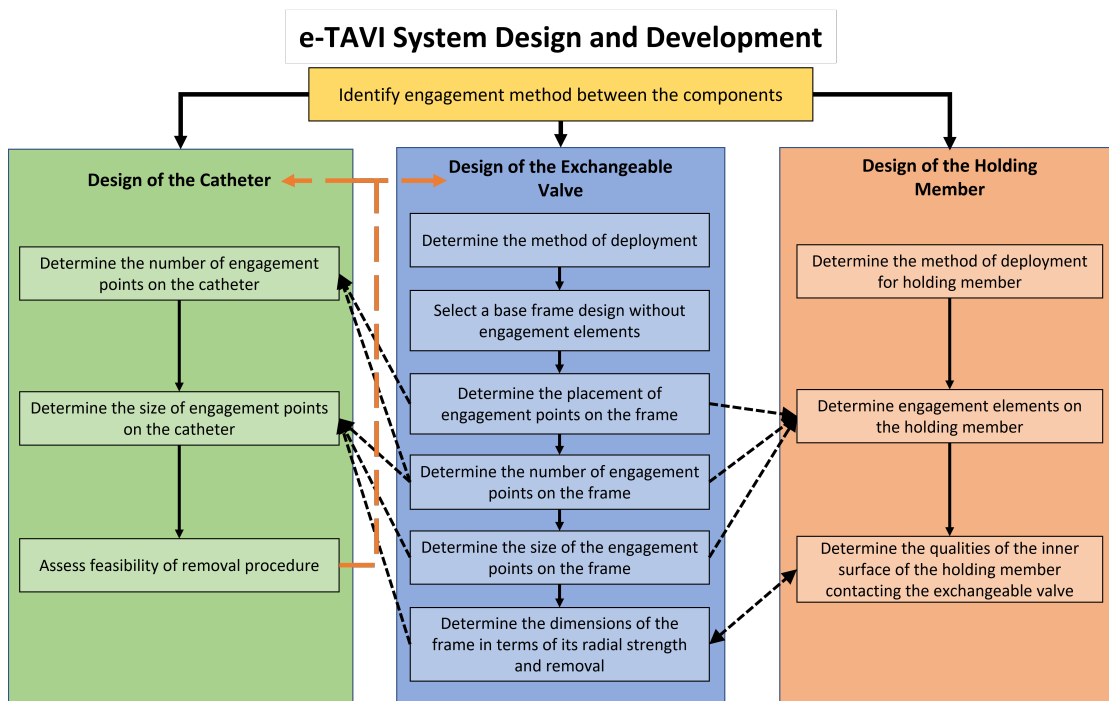
FIGURE 7.1: Design and development flowchart of the e-TAVI system. Continuous black lines signify the timeline within the development of the three components. Dashed black lines show how the design of certain aspects of a component influences that of the other components. The dashed orange lines depict the feedback direction resulting in possible design changes.

Of the three components, the design of the exchangeable valve was given priority due it being the active component performing the required valve function and its influence on the design of the other two components. The deployment method choices for the exchangeable valve were between balloon-expandable and self-expanding as these are the only two types of TAVI valves.

Following the choice of deployment method, the frame design of the exchangeable valve in terms of its cell shape and structure was attempted to be kept as similar to existing valve technologies. The reason for this was that these existing frame designs had clinically proven satisfactory function in terms of the design requirements stated in the previous

section, namely their radial force, ability to hold leaflets, crimpability and subsequent expansion, and haemodynamics. As the main focus of this PhD research was on the exchange process, starting from a frame design vastly differing from existing devices was not deemed efficient. Achieving an e-TAVI system where the components had as minimal additions to that of existing designs would be advantageous in terms of achieving a final design that had comparable clinical performance. In an ideal scenario, the e-TAVI exchangeable valve would exhibit the same clinical performance of existing devices with the added advantage of being exchangeable minimally invasively. Thus, in selecting a base frame design without engagement elements, similarity to existing devices was a consideration.

After the generation of a basic exchangeable valve frame, the goal was to add engagement elements to the frame to allow for the exchange process to take place. One of the main considerations in these additions was to retain the existing base frame structure as much as possible while allowing engagement elements of sufficient size, number and at appropriate positions to achieve removal. These design choices for the exchangeable valve influenced the requirements of the designs of the catheter and the holding member. Hence, these design choices were made in conjunction with the development of the other components. This is reflected in this thesis where some elements of the exchangeable valve design is resolved in the chapter describing the development of the e-TAVI catheter. Also, most aspects of the catheter and the holding member depended on the radial strength of the exchangeable valve frame.

Assessing the feasibility of the removal procedure consisted of simulating the crimping and sheathing of the deployed exchangeable valve design with the engagement elements of the catheter design. Conclusions were drawn in this thesis regarding how the results of these simulations would influence to future development of the e-TAVI components.

7.2.1   Limitations of Computational Modelling and Simulation

The development of the e-TAVI system in this thesis was purely based on computational work. The resources available to this PhD research did not allow for the manufacture and physical testing of the designs. The main objective of this research, then, was to computationally assess the feasibility of the e-TAVI system, determine how different design choices affected the exchangeability of the valve, and determine a future path in the development of the system which would include the manufacturing and bench testing of the components and procedure. Computational simulations do have limitations in that the numerical accuracy of the results are dependant on the material properties, solver choices, and interaction properties. The effect of these on the results in this thesis was mitigated through mesh refinement and mass scaling analyses, comparison of different material models, and using simulation parameters reported in literature which were validated against bench testing. However, the numerical accuracy of the results

in this thesis can still contain errors as they were not compared with bench testing of the specific corresponding designs. The conclusions drawn in this thesis are based on comparing the effect of different design parameters on the feasibility of the exchange process and hence retain their value in guiding the future development of the e-TAVI system.

7.3   Mating Concepts

The most important part of the e-TAVI design process was to determine the mating mechanism which would influence the design of all three components of the e-TAVI system. The important design aims for the mating mechanism were:

- ability to be engaged and disengaged *in vivo* via a catheter;

- sufficient mating strength between the holding member and the exchangeable valve against dislodging;

- facilitating complete exchange of the valve within a short time frame, beginning from the removal of the failed valve.

7.3.1   Slot Mating Concept

Initially, the mating mechanism was designed to be very basic: the physical slotting of the exchangeable valve into dedicated slots on the holding member. The holding member had slots lining its middle, following the struts of its frame. The bottom row of cells in the exchangeable valve were shaped such that they could be inserted into these slots with some force delivered via the catheter and then be locked in.

7.3.1.1   Design of Slot Concept Components

The design of both components was influenced heavily by the two TAVI market leaders, SAPIEN and CoreValve, as they had proven satisfactory clinical outcomes. The holding member was based on the SAPIEN series because it needed to provide anchoring in the aortic root. The cell shape of SAPIEN also lent itself to the formation of slots aligning the inner radius of the frame without drastically changing its structure. Figure 7.2 shows how these slots were formed as a radially inward extension of the struts. Rounded crowns were also added to the joints between the slots to prevent snagging during the insertion of the exchangeable valve. As per SAPIEN 3, the frame material was modelled as cobalt-chromium and the frame was balloon-expandable.
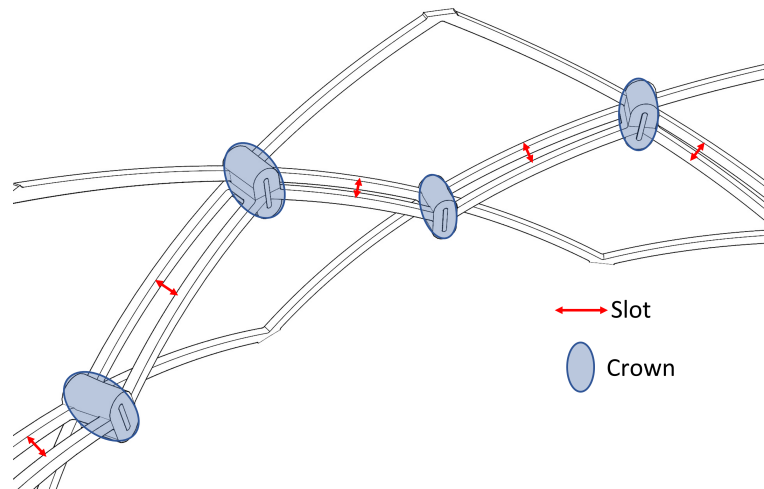
FIGURE 7.2: Illustration of the concept for the slotted holding member. Cells similar to the SAPIEN design with added slots are shown. The slots are labelled with red arrows showing the opening and the crowns are emphasized with blue ovals.

The exchangeable valve frame was based on the CoreValve series, which was driven by the need for valve re-capture. The re-crimping ability of commercial self-expanding valve platforms up until full deployment was promising for the possible re-capturing of the exchangeable valve. The same cell shape as CoreValve was used in the exchangeable valve frame, but cell size and frame radius were kept constant across the height of the device. The anchoring of the valve in the aorta would be partially provided by the engagement between the valve and the holding member, hence the supra-annular anchoring of CoreValve's hourglass shape was not needed. The connection points between the row of cells on one end of the frame (the leading end when crimped onto a catheter) were removed to allow for slotting into the holding member. Figure 7.3 shows the entire exchangeable valve frame with the removed connections between cells.
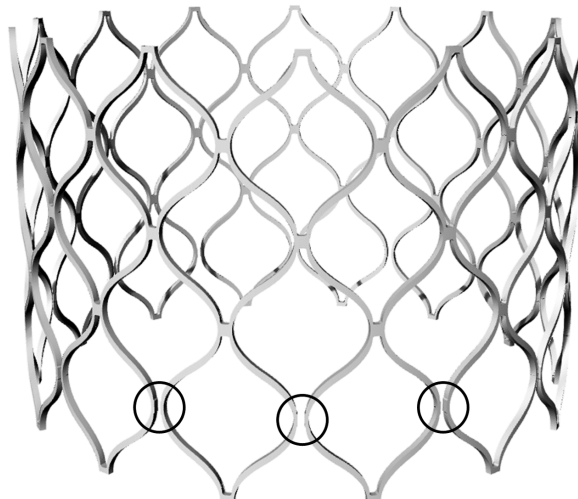
FIGURE 7.3: Illustration of the exchangeable valve frame. The connectors removed to form the slotting cells are circled in black.

7.3.1.2 Procedure of e-TAVI with the Slot Concept

During deployment, the exchangeable valve would be guided above the holding member and fully-unsheathed. This position is portrayed in Figure 7.4 where the exchangeable valve is positioned above the holding member. The catheter would remain connected to the exchangeable valve through similar connection tabs as the CoreValve devices, and be used to push the bottom row of cells into the slots on the holding member in the direction of the arrows in 7.4. The force would elastically deform the cells to push through the slots, and retain their original shape when through, to engage fully. Figure 7.5 shows a close-up view of the cells of the exchangeable valve moving into the slots on the holding member.
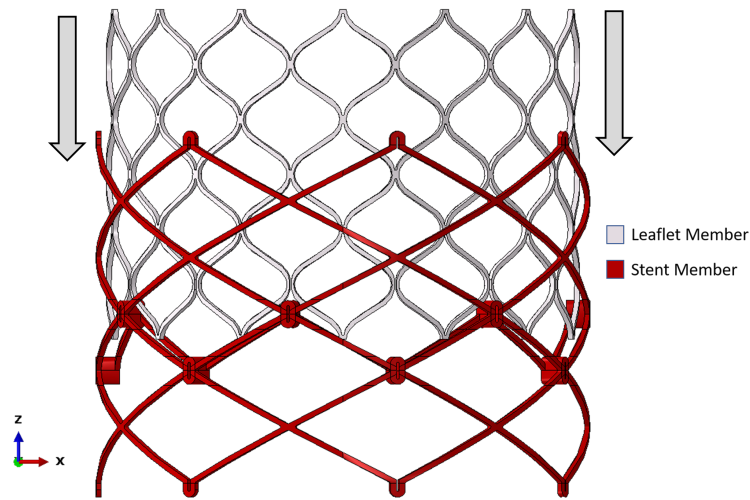
FIGURE 7.4: Position of the exchangeable valve above the holding member after unsheathing for the slot concept. The arrows show the direction of force that the catheter will apply to the exchangeable valve to push its cells through the slots on the holding member.
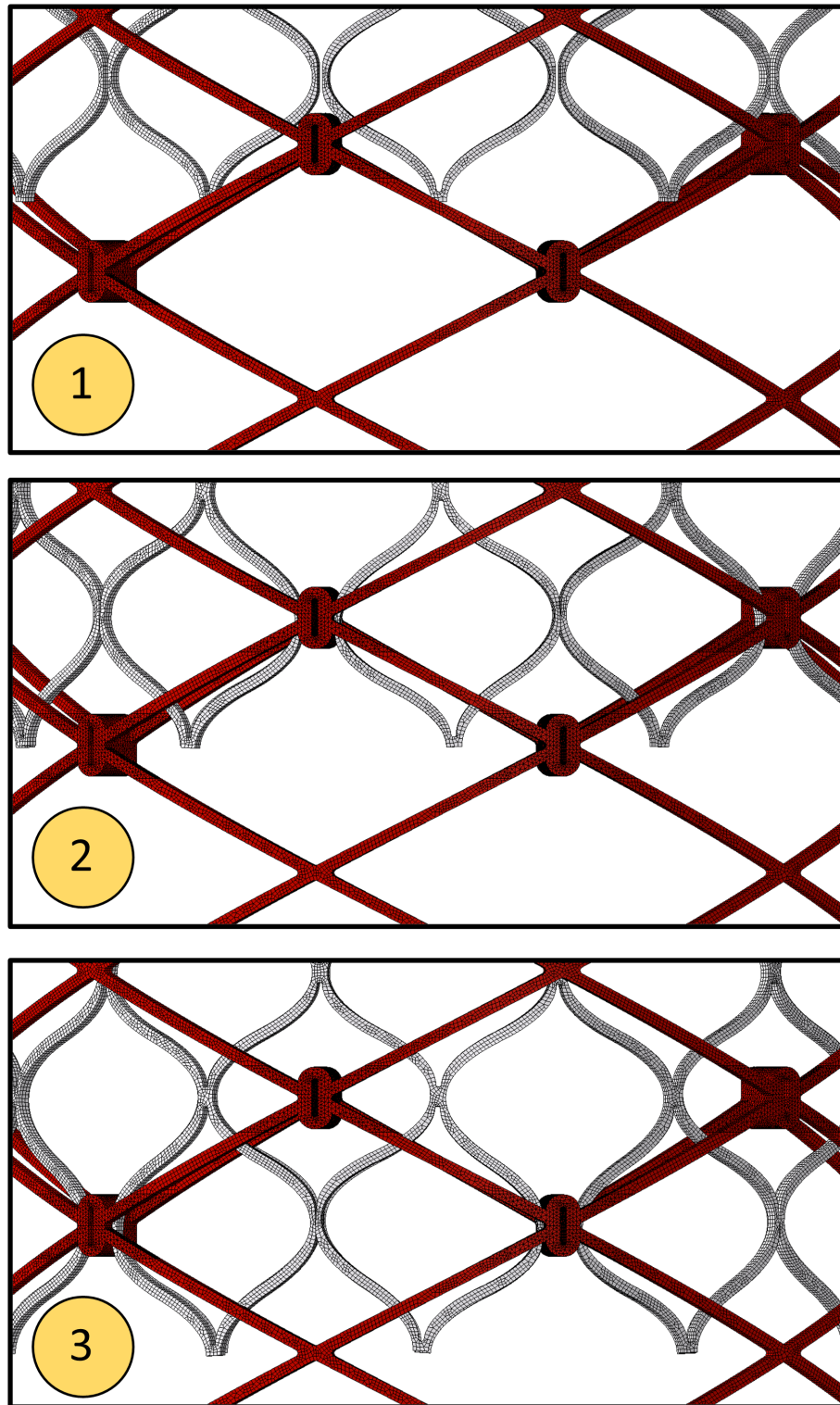
FIGURE 7.5: Close-up view of the engagement between the exchangeable valve and the holding member over three increments, showing the deformation of the cells as they slot in, particularly in the second step.

During removal, the delivery system would grab hold of the exchangeable valve and exert enough force to once again deform the cells and disengage the exchangeable valve from the holding member, moving in the opposite direction to the arrows in Figure 7.4. The

removed valve would then be pulled into the ascending aorta and a new exchangeable valve deployed via the same catheter. The removed valve would be re-crimped, exerting force through the same connection tabs, re-sheathed and removed from the body.

7.3.1.3   Methodology of Slot Concept Investigations

After the generation of computational models for the two components, the crimping, expansion and mating of both was simulated. The crimping and expansion simulations of the exchangeable valve was as described in Chapter 6. For the holding member, a balloon expansion simulation was set up. The frame was meshed with hexahedral elements and a crimping cylinder was used to crimp the frame onto a folded balloon model. The material properties of the frame were set to represent a CoCr valve frame with the parameters shown in Table 7.1.

Property	Value
Young's Modulus	232000 MPa
Poisson's Ratio	0.3
Yield Stress	379 MPa
Density	8.4×10^{-9} $tonnes/mm^3$

TABLE 7.1: Material properties of the slot concept holding member [50].

The balloon was meshed with shell elements with a shell thickness of 0.07 mm. The material properties of the balloon are given in Table 7.2, which were based on polyethylene terephthalate.

Property	Value
Young's Modulus	1000 MPa
Poisson's Ratio	0.3
Density	1.1×10^{-9} $tonnes/mm^3$

TABLE 7.2: Material properties of the balloon [50].

The target time increment of the balloon expansion simulations were 1×10^{-7} s with a step duration of 1 s. The simulation consisted of two steps. In the first step, the holding member frame was crimped on to the balloon via the crimping cylinder with a boundary condition of 11 mm in the radially inward direction. In the second step, the furled balloon was expanded with a pressure load of 2 MPa acting on the inner surface of the balloon. A parabolic amplitude curve was defined on this pressure load to expand and deflate the balloon in a single step. Boundary conditions were defined on either end of the balloon to pin these ends in place and achieve balloon expansion. Figure 7.6 depicts the assembly of the balloon expansion simulations of the slot concept holding member.
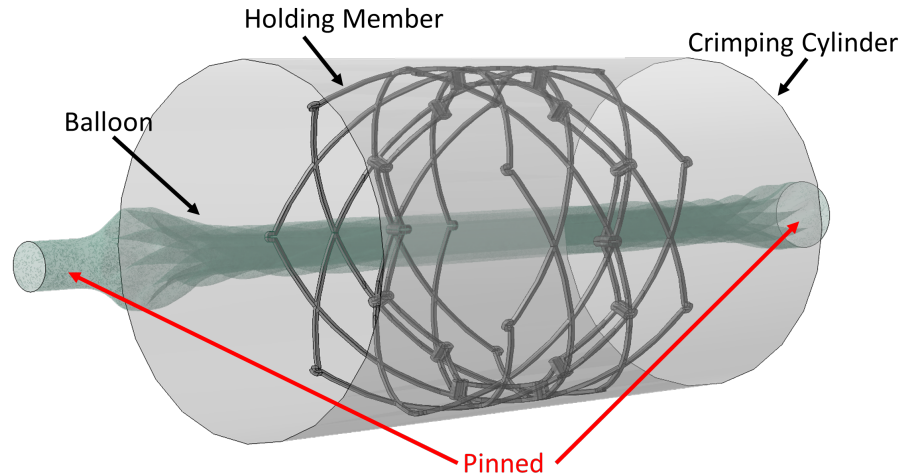
FIGURE 7.6: Assembly of the balloon expansion simulations

7.3.1.4 Results of Slot Concept Investigations

Figure 7.7 shows the crucial results from this simulation. Firstly, the balloon-expansion of the holding member following crimping resulted in a very deformed shape. Frame height was greatly reduced due to larger balloon expansion towards the ends of the frame compared to the middle. Referred to as dog-boning, this was due to the middle of the frame being harder to expand because of the slot features lining it. The slots were also deformed shut during balloon expansion. Generally, this BE holding member design was not feasible due to this increased stiffness around the slots. Secondly, the unsheathing of the exchangeable frame resulted in some cells on the leading end folding radially inward. While the rest of the frame returned to its original shape, the row of cells with cut connectors did not return to a circular shape, making it nearly impossible to align with the slots. Finally, successful mating could only achieved by beginning from an ideal deployment of both components and perfect alignment between the slots and corresponding cells. This ideal deployment and alignment were very unlikely due to the shapes of the expanded frames seen in Figure 7.7.

7.3.1.5 Discussion of Slot Concept Investigations

These results showed that there was a lot of uncertainty during deployment with this method: some of the target slotting areas could be smaller during holding member deployment, the position of the slotting cells on the exchangeable valve after deployment were variable, and the slotting cells must be guided very precisely to ensure successful mating. To alleviate this uncertainty, a mating mechanism that required minimal manual manoeuvring of the catheter for alignment and attachment was needed.
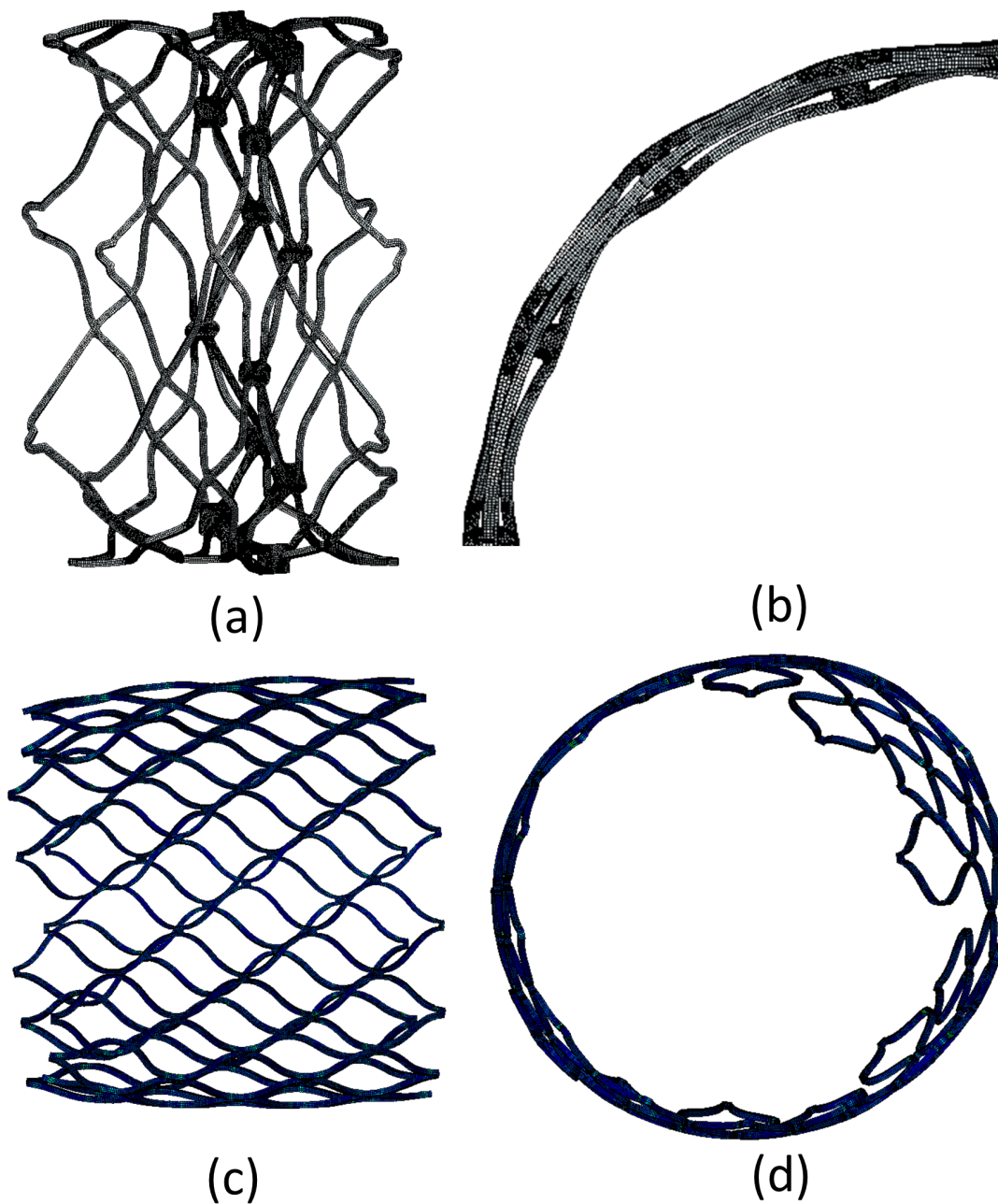
FIGURE 7.7: (a) Side view of the balloon expansion of the holding member showing an extremely distorted final shape. (b) Top-down view of the expansion of the holding member showing deformation of the slots. (c) Side and (d) top-down view of the unsheathed exchangeable valve showing the leading, slotting cells translated radially inwards from their ideal expanded position.

7.3.2 Magnetic Mating Concept

Following from the analysis on the slot exchange concept, the difficulty in aligning and engaging minuscule features on the exchangeable valve with the holding member *in vivo* was captured. Magnetic attraction was identified as a possible solution to these difficulties where magnetic elements on the exchangeable valve would be attracted to magnetic

elements on the holding member in close proximity *in vivo*. Further, the re-capturing and removal of the exchangeable valve, which necessitates a catheter securely grabbing a deployed exchangeable valve, could be better achieved with magnetic elements on the catheter engaging with the magnetic regions on the exchangeable valve.

In this magnetic mating concept, the holding member could be either a surgically implanted component, or a self-expanding frame. BE frames were not considered due to the unpredictability of the plastic deformation during deployment. The member could also comprise magnetic regions facing radially inward to complement the magnetic regions on the exchangeable valve. The exchangeable valve would be a self-expanding frame with additional magnetic regions to engage with both the holding member and the catheter. Figure 7.8 shows a conceptual deployment of a magnetic exchangeable valve into the magnetic regions of a surgical holding member.
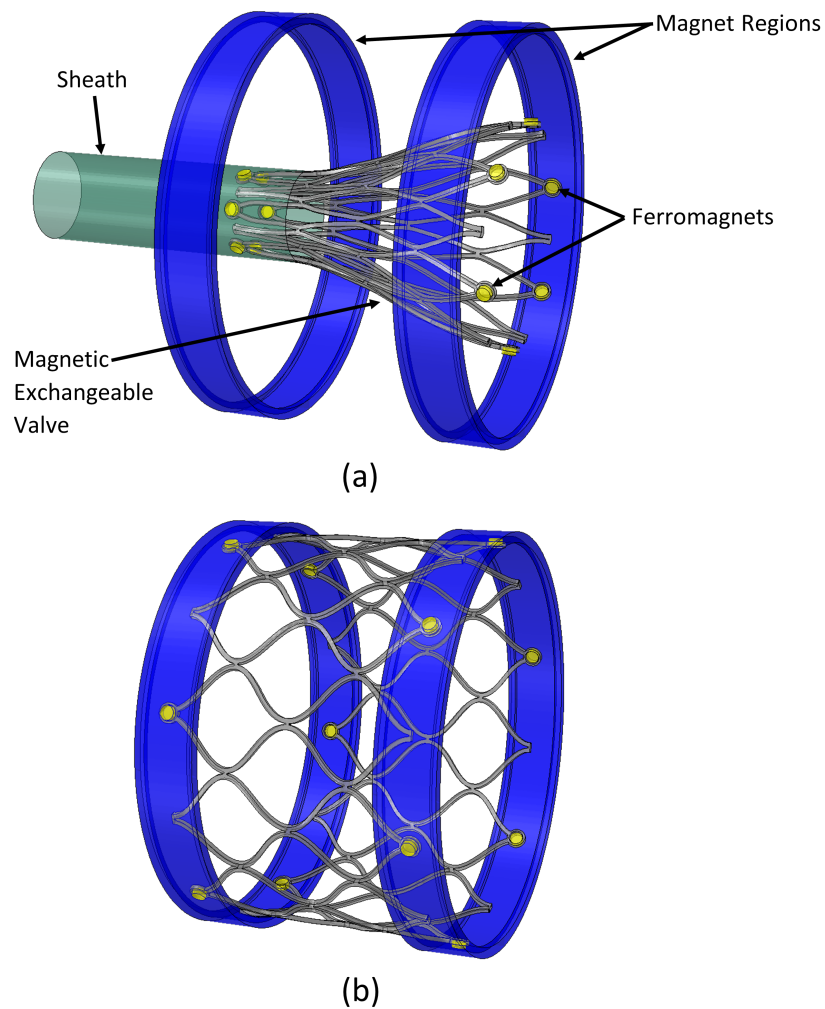
FIGURE 7.8: The concept of magnetic mating. Blue bands represent the magnetic regions of a holding member. The frame represents a SE exchangeable valve with the yellow cylinders portraying the magnetic regions. (a) Unsheathing of the exchangeable valve withing the holding member. (b) Mating between the magnetic regions of the exchangeable valve and holding member.

The catheter in the magnetic mating concept must hold magnetic regions that could be translated radially inward and outward to capture and remove the exchangeable valve from the holding member. It must also include features to crimp the removed exchangeable valve to fit through the vessels when the catheter is retracted. It could also include a delivery segment to deploy a new exchangeable valve in place of the removed one via the same catheter. Figure 7.9 portrays a concept model of this catheter holding electromagnets as the magnetic regions, placed on SE frames for radial movement. This radial movement could be controlled via the power wires to the electromagnets. The image also includes a tapered sheath to receive and crimp the removed valve, alongside a deployment section holding a new, crimped exchangeable valve.
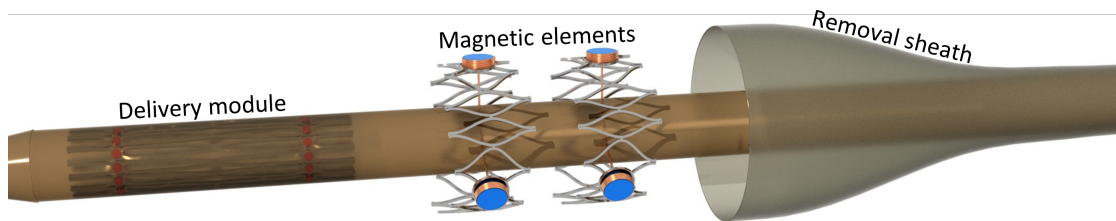
FIGURE 7.9: Representation of a e-TAVI catheter design with electromagnets as magnetic mating elements.

The rest of this thesis details the development of the three components of the e-TAVI system utilising the magnetic mating concept.

7.4 Summary

This chapter listed the design requirements of the e-TAVI system components and the framework of how the components would be developed. An initial slotted mating concept was described and the reasoning behind abandoning it and moving to a magnetic mating concept was given.

- The design requirements of the e-TAVI components included both requirements associated with regular TAVI valves and additional requirements for the exchangeability.

- The development process of the e-TAVI components was determined by how the design of the exchangeable valve affected the design requirements of the other components.

- A first e-TAVI design concept with a physical, slotting mating mechanism was concluded to be infeasible due to the difficulty of achieving the required precision for attachment and a magnetic mating concept was selected instead.

Chapter 8

Exchangeable Valve Design

This chapter explains the development of the exchangeable valve component of the e-TAVI system. Initial design choices are justified, the computational modelling process is described, and the investigations regarding the effect of various design parameters on radial strength and removal are discussed.

8.1   Frame Design

The exchangeable valve frame was designed as a SE device. Compared to the radial force of BE valves, SE valves exhibit lower COF and RRF [162]. This was advantageous for the e-TAVI removal process. Furthermore, the ability of repositioning the valve in current SE devices during unsheathing allowed for a more controlled deployment which would improve mating success.

8.1.1   Basic Self-Expanding Frame

The basic cell shape was kept the same as the CoreValve series due to its clinically proven performance. As exemplified in Figure 3.17 of Chapter 3, most other SE valves on the market (such as Allegra and Portico) also mimic this cell shape. The frame diameter was chosen as 26 mm, which is mid-size in most commercial valve series. A 26 mm valve is usually deployed into patients with aortic diameters ranging from 20 mm to 24 mm [39]. Since the mean aortic diameter in the population is 21 +- 1.8 mm for women and 23.1 +- 2 mm for men, this valve size was appropriate for the most amount of patients [163]. The strut width, number of horizontal and vertical cells, and valve height of the frame were varied throughout the thesis to assess their impact on the crimping and removal of the frame.

The CAD software Rhinoceros3D 5 (Robert McNeel & Associates, Seattle, USA) was used for the computational modelling. The functionality of writing python scripts to control the generation of the model was utilised to define the design parameters. Detailed below in Table 8.1, these parameters afforded the ability to make quick and easy design changes to the models.

TABLE 8.1: Design parameters for the basic exchangeable valve frame modelling script.

Design Parameter	Symbol	Initial Value
Valve height	h_v	24 mm
Outer valve radius	r_v	13.3 mm
Number of horizontal cells	N_{hor}	12
Number of vertical cells	N_{ver}	3
Strut thickness	t_{st}	0.3 mm
Strut width	w_{st}	0.3 mm
Fillet radius	r_f	0.1 mm
Width of gap between horizontal cells	w_{hgap}	0.1 mm
Width of gap between vertical cells	w_{vgap}	0.15 mm

Appendix A details the python script and steps used to generate the frame models. Figure 8.1 shows the basic frame produced through this script using the values in Table 8.1.
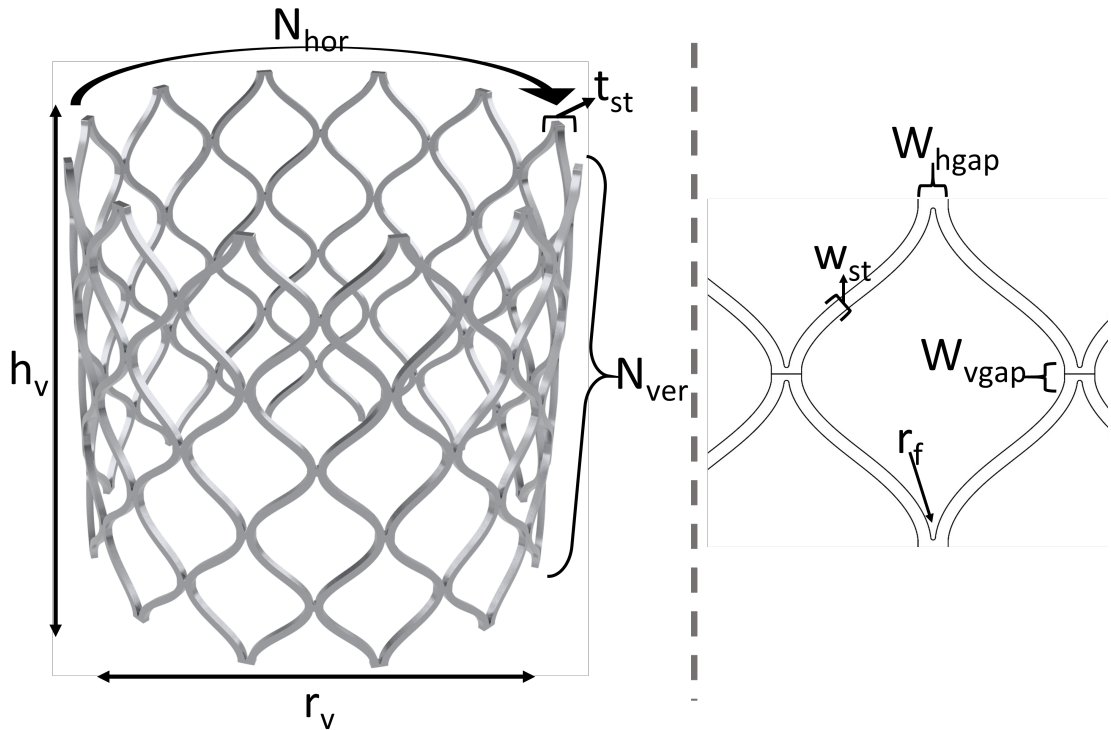
FIGURE 8.1: Base self-expanding, exchangeable valve frame design with the design parameters in Table 8.1 labelled.

8.1.2   Magnetic Elements on Frame

In the e-TAVI concept, the exchangeable valve frame had to contain magnetic elements for engagement with the other components of the system. Nitinol is not a ferromagnetic material so these magnetic regions had to be defined as separate regions on the basic frame made from a ferromagnetic material. An important consideration in the design of these additional features during the computational modelling and simulations was to preserve the existing base frame shape as much as possible. The reasoning behind preserving the existing base frame shape was stated in Chapter 7 as retaining the mechanical properties of commercial valves as much as possible.

The ideal addition for the ferromagnetic regions would have been completely preserving the struts of the basic frame and adding ferromagnetic material in between sections of the struts, following the same shape as the existing struts. However, this would drastically change the crimping and expansion behaviour of the frame as sections within the struts would no longer be made of Nitinol and hence would not exhibit shape memory and superelasticity. This would lead to portions of the frame being unable to expand and exert a radially outward force. Hence, the frame had to contain struts made of Nitinol that are continuous across its height. This meant that the ferromagnetic regions had to be additional elements to the fully Nitinol frame.

Magnetic coatings could have been a method of adding magnetic regions to the frame without changing the strut shapes. After manufacturing the frame, magnetic powder could be deposited on the surface around discrete sections of the struts. This method was not deemed feasible as the thickness of such a coating would be too small and hence the strength of the magnetic field produced by the removal elements on the catheter would need to be unrealistically large to achieve a meaningful amount of attractive force on the exchangeable valve frame.

Due to the infeasibility of the above methods, ferromagnetic material was designed to be attached to the frame structure as separate elements with the frame shape altered in such a way as to hold these elements. The self-expansion of the frame would be preserved as these ferromagnetic region holders would be surrounded by Nitinol struts. SE frames are manufactured through the laser cutting of a Nitinol tube. The composition of the Nitinol alloy must be precise to achieve the required superelasticity effects at the human body temperature. Hence, the ferromagnetic regions had to be designed as additional, discrete elements, attached to the frame after manufacture.
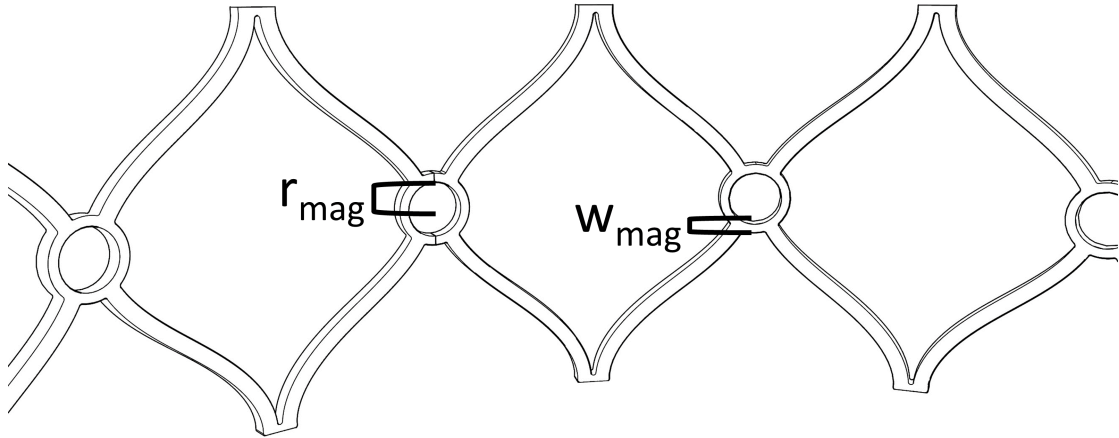
FIGURE 8.2: CoreValve cells with the magnets between them for the magnetic exchangeable valve frame.

The connectors between cells and the crowns on either end of the frame were identified as the ideal regions to add ferromagnetic holder regions that would result in minimal change in cell shape. These regions were shaped as circles to avoid sharp edges in the frame structure that could become high stress points during crimping. Figure 8.2 portrays a section of cells with the ferromagnetic regions added in between. The additional design parameters for these regions are listed in Table 8.2.

TABLE 8.2: Magnetic design parameters for the exchangeable valve modelling script.

Design Parameter	Symbol	Initial Value
Magnet radius	r_{mag}	0.5 mm
Width of strut around magnets	w_{mag}	0.15 mm
Magnet thickness	t_{mag}	1 mm
Number of magnets	N_{mag}	12 per ring

Figure 8.3 shows the generated magnetic exchangeable valve frame using the values in Tables 8.1 and 8.2.
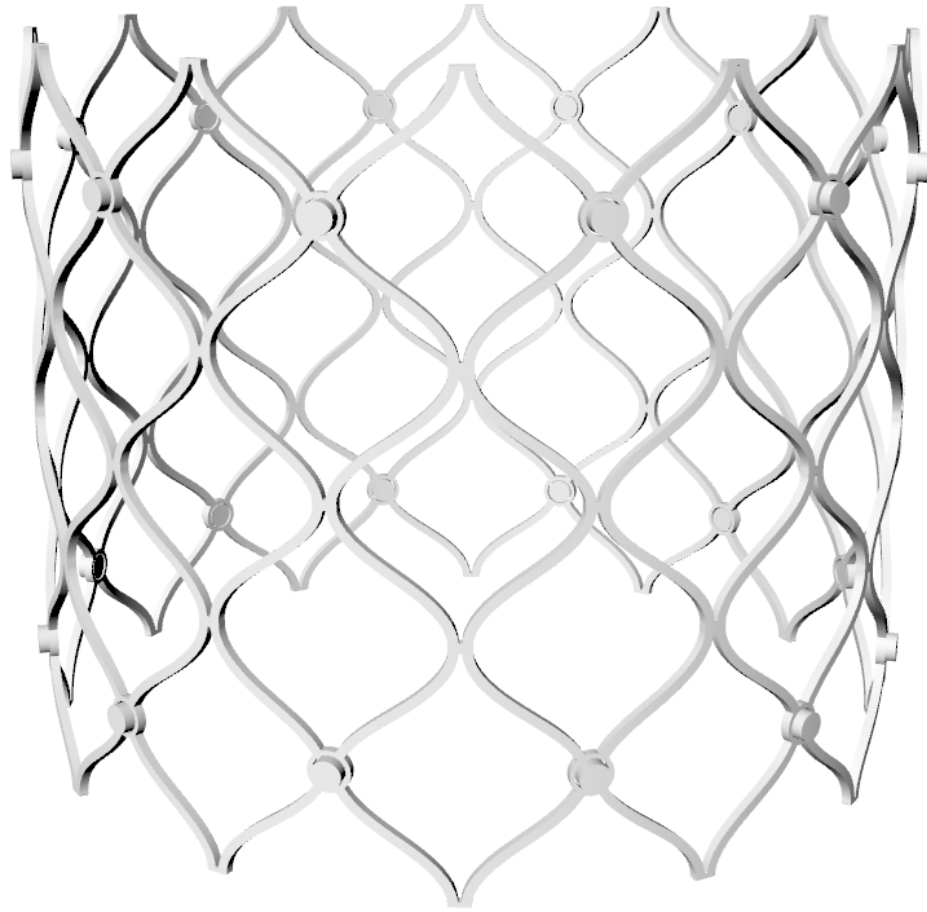
FIGURE 8.3: The magnetic exchangeable valve frame model with ferromagnetic regions.

The main design goals for the magnetic exchangeable valve frame were:

- determine the optimal number, size, and position of the ferromagnetic regions to ease removal, resist dislodging, ensure crimpability and deployment;

- exert enough COF after deployment to achieve sufficient friction force between itself and the holding member for axial anchoring;

- have low enough radial strength such that the frame can be collapsed and re-sheathed *in vivo* via the catheter.

8.2 Nitinol Material Modelling

All current self-expanding bioprosthetic valves are made of a nickel titanium alloy called Nitinol. The properties of this material and how these properties were modelled for the FEA simulations of the exchangeable valve frame are described below.

8.2.1   Properties of Nitinol

The two important and closely related properties of Nitinol are its shape memory and superelasticity. Shape memory refers to Nitinol's ability to return to its original shape, after undergoing deformations, when the ambient temperature is increased above a threshold value [164]. Superelasticity is the ability of a metal to undergo large strains under constant stress which are recoverable when the stress is removed [164]. Nitinol exhibits both properties depending on whether the ambient temperature is above or below a threshold value.

These properties are exhibited due to the phase transformation of Nitinol between temperatures. At high temperatures Nitinol is in its austenite phase and at low temperatures it is in the martensite phase. In its martensite phase, the material can undergo deformations and change its shape under stress. However, if the temperature is then increased and Nitinol undergoes phase transformation to the austenite phase, the material forms back into its original shape. This way, the martensite-austenite phase transformation causes the shape memory effect. When a mechanical strain is imposed on the material in its austenite phase, local regions in the material undergo a stress-induced phase transformation to the martensite phase. With these transformations, the material can accommodate large strains up to 10% [165]. The proportion of the material that has transformed into martensite increases with increased strain, without too much of an increase needed in the applied stress. This discrepancy between the applied stress and increased strain can be seen in the plateau present in the stress-strain curve of Nitinol shown in Figure 8.4. When the applied load to the material is removed, the material reverts back to its austenite phase. With this reverse phase transformation, the strain accommodated by the localised martensite phase transformation is recovered and the material reverts back to its original shape prior to the application of mechanical strain. In this way, through the stress-induced, localised austenite-martensite phase transformations, Nitinol exhibits superelasticity.

The temperature at which phase transformation occurs is dependent on the alloy percentage between nickel and titanium [164]. For SE prosthetic valve applications, this temperature is set around 37° C, the healthy human body temperature. This allows the valve to be in the austenite phase in the body. Hence, Nitinol exhibits superelastic properties in the body.

8.2.2   Nitinol Material Properties in the Literature

A typical stress-strain curve of a superelastic material is shown in Figure 8.4. The points labelled on the curve show the material properties that need to be defined to model the material. The inbuilt superelasticity model in ABAQUS 2018, based on Auricchio and
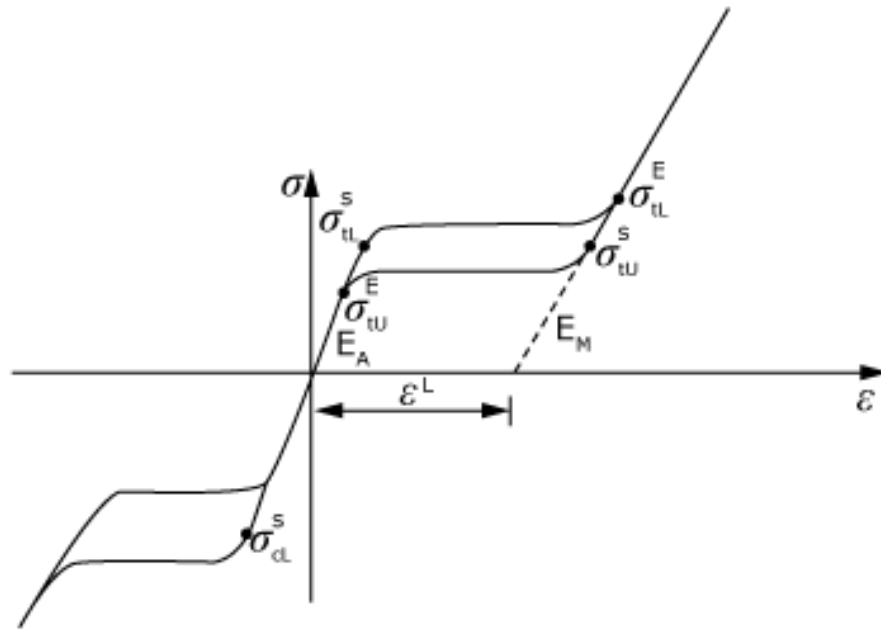
FIGURE 8.4: A typical superelastic material uniaxial stress-strain curve showing the parameter inputs to the ABAQUS superelastic material routine
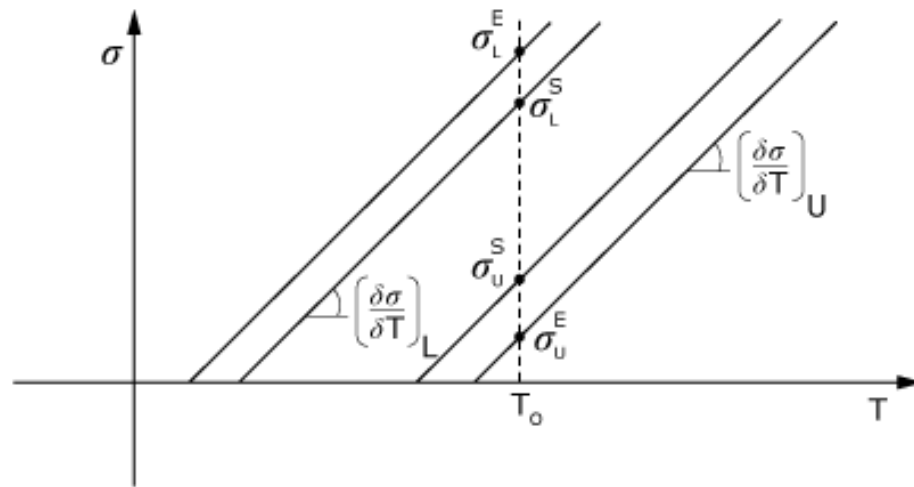
FIGURE 8.5: Relationship between temperature and stress for superelastic materials, also showing the rest of ABAQUS superelastic material routine parameters [166]. See Table 8.3 for parameter definitions.

Taylor's work that takes the parameters in Table 8.3 as arguments, was used in this PhD research [166, 167].

Different values for the Nitinol parameters are abundant in the literature. As seen in Tables 8.4 and 8.5, some of these material properties, in particular transformation stresses and Young's moduli, vary wildly between articles. This is because the determination of these variables are based on bench testing of various Nitinol samples such

TABLE 8.3: Nitinol material model parameters, also labelled in Figure 8.4 and 8.5.

Material Parameter	Symbol
Young's modulus of martensite	E_M
Young's modulus of austenite	E_A
Poisson's ratio of martensite	v_M
Poisson's ratio of austenite	v_A
Uniaxial transformation strain	ϵ^L
Stress at which the transformation begins during loading in tension	σ_{tL}^S
Stress at which the transformation ends during loading in tension	σ_{tL}^E
Stress at which the reverse transformation begins during unloading in tension	σ_{tU}^S
Stress at which the reverse transformation ends during unloading in tension	σ_{tU}^E
Stress at which the transformation begins during loading in compression	σ_{cL}^S
Reference temperature	T_0
Slope of the stress versus temperature curve for loading	$\left(\dfrac{\delta\sigma}{\delta T}\right)_L$
Slope of the stress versus temperature curve for unloading	$\left(\dfrac{\delta\sigma}{\delta T}\right)_U$

TABLE 8.4: Nitinol material model parameters from literature for non-cardiovascular applications.

	Vidal et al. *(2008)*[168]	Fu et al. *(2012)*[169]	Cao et al. *(2020)* [170]
E_M (MPa)	32000	42900	26500
E_A (MPa)	37000	42300	71300
v_M	0.33	0.30	0.30
v_A	0.33	0.30	0.30
ϵ^L	0.012	0.020	0.046
σ_{tL}^S (MPa)	250	600	407
σ_{tL}^E (MPa)	540	1200	427
σ_{tU}^S (MPa)	290	500	180
σ_{tU}^E (MPa)	1	200	175
σ_{cL}^S (MPa)	0	600	540
T_0	115°C	22°C	37°C
$\left(\dfrac{\delta\sigma}{\delta T}\right)_L$ $(MPaT^{-1})$	3.2	0	7.34
$\left(\dfrac{\delta\sigma}{\delta T}\right)_U$ $(MPaT^{-1})$	2.0	0	7.64

as wires, springs, stents and actuators. The results of the bench tests are compared against predictions through FEA simulations to validate the material properties. The

TABLE 8.5: Nitinol material model parameters from literature for stents and heart valves.

	Kleinstreuer et al. (2008) [171]	Nematzadeh et al. (2012) [156]	Finotello et al. (2021)[155]
E_M (MPa)	47800	18554	20000
E_A (MPa)	51700	40000	44000
v_M	0.30	0.46	0.30
v_A	0.30	0.46	0.30
ϵ^L	0.063	0.040	0.055
σ_{tL}^S (MPa)	600	390	460
σ_{tL}^E (MPa)	670	425	465
σ_{tU}^S (MPa)	288	140	360
σ_{tU}^E (MPa)	254	135	260
σ_{cL}^S (MPa)	900	585	900
T_0	$37°C$	$37°C$	$37°C$
$\left(\frac{\delta\sigma}{\delta T}\right)_L$ $(MPaT^{-1})$	6.527	6.527	6.527
$\left(\frac{\delta\sigma}{\delta T}\right)_U$ $(MPaT^{-1})$	6.527	6.527	6.527

type of validation tests also vary across different publications including uniaxial tensile tests, radial strength tests, crushing tests, and stress-strain comparisons. These differences between verification methodology partly explains the difference in values. Another contributing factor is the lack of information of alloy composition of Nitinol in different devices. Different percentages of Nickel and Titanium would be expected to exhibit different material properties, in addition to the change in the phase transformation temperature. This is reflected when comparing the two tables where the parameters of vascular application samples are closer in value compared to non-vascular samples since the Nitinol alloy compositions must be similar to achieve the same phase transformation temperature.

Kleinstreuer et al. compared two sets of material properties, claimed to represent two different real-life stent materials, in terms of fracture resistance. Within this analysis, the material models were validated through the radial force produced by a single half-cell [171]. Nematzadeh et al. used the better performing material model from the Kleinstreuer study and analysed its accuracy in terms of stress during loading and unloading, comparing it to another Auricchio model and a Lagoudas model. The conclusion was that the model from the Kleinstreuer study (listed under Nematzadeh et al. in Table 8.5) had the best accuracy compared to bench testing of an identical short stent frame. Nematzadeh et al. also showed that both Auricchio models performed better compared to the Lagoudas model [156].

The Nitinol material composition in the e-TAVI system was not predetermined. Furthermore, the literature has an evidence gap in the relationship between material composition

and the parameters of the Auricchio model. Consequently, even if the alloy composition of the exchangeable valve frame was selected to be a specific nickel-titanium ratio, the superelasticity model parameters (Table 8.3) specific for such a composition would require the manufacturing of the frame to determine. Hence, the aim was to use a material model that represented a generic Nitinol composition for cardiovascular use with a reference temperature of 37° C. Since it had been validated in two separate studies using different validation methods, the Nematzadeh model values were used to model Nitinol in ABAQUS.

8.2.3   Effect of Nitinol Material Properties on Simulation Results

Although the material model was chosen in accordance with evidence in the literature to represent Nitinol, the effect of different material models on simulation outcomes was investigated.

8.2.3.1   Methodology of Nitinol Material Property Comparison

To determine the effect of different Nitinol material properties, the same simulation was performed with the Kleinstreuer and Nematzadeh material models. The simulation was the crimping and expansion of the basic Nitinol frame shown in Figure 8.1. There were two steps in the simulation consisting of the crimping of the frame via the boundary condition on the crimping cylinder, and the expansion of the frame via the reverse boundary condition on the crimping cylinder. The setup of this simulation was the same as the crimping and unsheathing simulation described in Chapter 6, with the unsheathing step replaced with an expansion step. The reason for this change was to be able to extract the outward radial force exerted by the frame during expansion via the reaction force on the cylinder. The boundary condition on the crimping cylinder was 3 mm directed radially inwards in the first crimping step and -3 mm in the final expansion step. Hard and frictionless contact was defined between the frame surface and the cylinder surface. The target time increment, step duration, mesh resolution and mesh element types were the same as described in Chapter 6

The outward radial force and stress data from the crimping and expansion simulations of the basic frame was extracted for the Kleinstreuer and Nematzadeh material models for comparison.

8.2.3.2   Results of Nitinol Material Property Comparison

Figures 8.6 and 8.7 show the results of this analysis. Towards the conclusion of this PhD research, Finotello et al. published a new Nitinol material model (Table 8.5) based

on the bench testing of the CoreValve Evolut heart valve [155]. While this data was not available to the author during the PhD research, the same basic frame simulations were performed using this new model and retroactively added to Figure 8.6 and 8.7 for comparison.
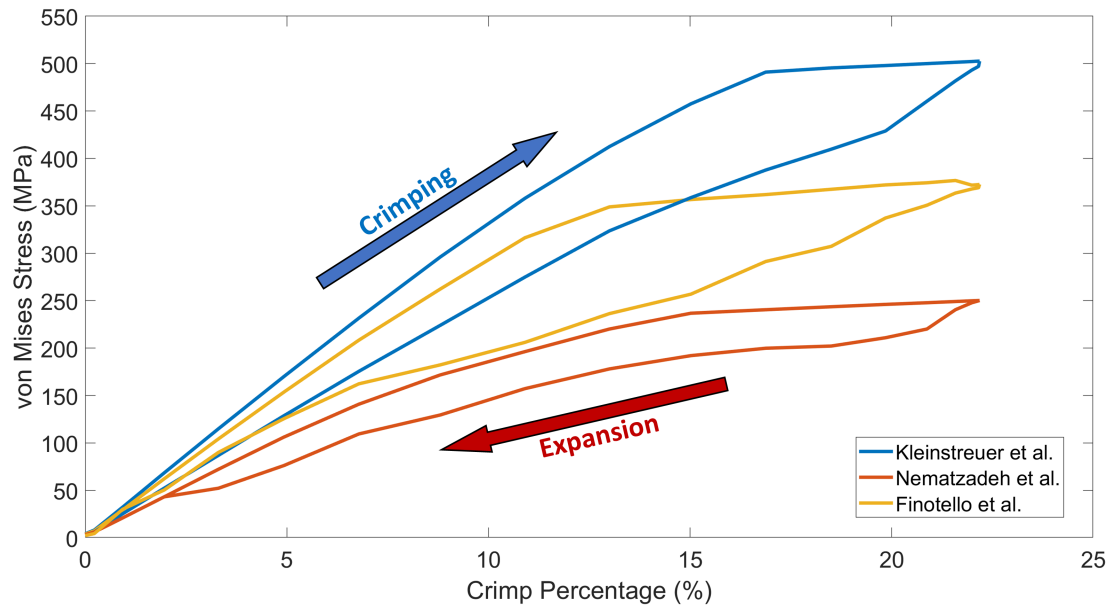
FIGURE 8.6: von Mises Stress values for three different Nitinol material models during crimping and expansion.
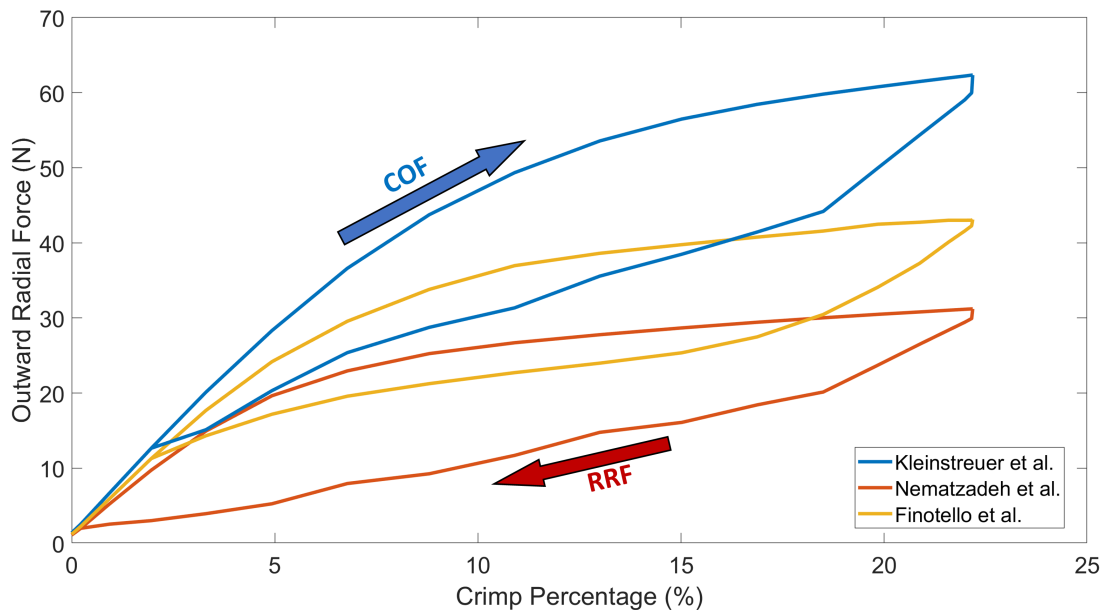
FIGURE 8.7: Radial force values for three different Nitinol material models during crimping and expansion. COF = chronic outward force, RRF = radial resistive force.

8.2.3.3   Discussion on Nitinol Material Property Comparison

As expected, the Nitinol model parameters do have a large effect on the calculated stresses and radial force during simulations. The differences in the values of martensite and austenite Young's Moduli along with the start and end of transformation limits reflect the variance in the results. The Kleinstreuer model has the highest values for these variables, and the calculated values for both the radial force and stress are the highest in Figures 8.6 and 8.7. Similarly, the Finotello model predicts intermediate values and the Nematzadeh model the lowest. As explained in the previous section, the Nematzadeh values were used throughout this thesis due to its better validation results. However, this effect of the chosen material model must be noted when discussing the numerical values in this thesis as a different choice can obviously have different results. Hence, the analysis in this thesis will be comparative in terms of design parameter effects rather than absolute. Table 8.6 summarises the percentage differences between models averaged below and above 5% reduction in frame diameter. The difference in results grew more pronounced as the frame was crimped further.

TABLE 8.6: Percentage differences between the radial force and stresses predicted by the three Nitinol material models

	Radial Force ($< 5\%$)	Radial Force ($> 5\%$)	Stress ($< 5\%$)	Stress ($> 5\%$)
Kleinstreuer vs Nematzadeh	44.1%	95.6%	21.1%	75.2%
Finotello vs Nematzadeh	23.1%	38.5%	10.4%	32.4%

8.3   Ferromagnetic Region Placement

As discussed in Section 8.1.2, the ferromagnetic regions were designed to be placed on the connection points between cells and/or the crowns on the exchangeable valve frame to preserve the strut and cell shapes of the basic frame as much as possible. Including the crowns at either end of the frame, this amounted to 84 possible positions. There were seven possible positions across the height of the device and 12 positions at each height. The placement of these regions effected the crimpability and removal of the exchangeable valve frame, and hence different positions were evaluated in terms of the effects they had on these two aspects of the frame.

8.3.1 Placement Across the Height of the Frame

Initially, the number of ferromagnetic regions around the circumference was kept at the maximum of 12, placed between each cell around a ring. This left 7 possible positions of rings of ferromagnets across the height of the frame. To evaluate the optimal of these positions, the ability to crimp the frame solely through their radially inward movement was investigated.

8.3.1.1 Methodology of Ferromagnetic Region Placement Across the Height of the Frame

Separate node sets were defined on the basic frame of Figure 8.1, grouping each ring of connectors across the frame height. Radially inward displacement boundary conditions were then defined on the node sets in each simulation and the final crimped shape was evaluated. The magnitude of the boundary conditions were set to 8 mm in the radial direction while motion of these nodes were constrained in the axial and circumferential directions. There was a single step in these simulations with mesh, step, and material model parameters as described in Chapter 6.

A total of four ferromagnetic placements were investigated, depicted in Figure 8.8:

1. Middle ring (*yellow* in Figure 8.8).

2. Top and bottom end crowns (*blue* in Figure 8.8).

3. Top and bottom cell rows (*red* in Figure 8.8).

4. Above and below middle ring cell rows (*green* in Figure 8.8).

The direction of the boundary conditions and the location of each node set for the four ferromagnetic placements are shown in Figure 8.9.

8.3.1.2 Results of Ferromagnetic Region Placement Across the Height of the Frame

Figure 8.10 shows the final crimped shape of each combination. The envelope radius of each was also quantified, relating to the largest diameter, axial cross-section of the resulting shape. The minimum diameter was achieved with combination 3, where the boundary conditions were on the bottom and top row of cells.
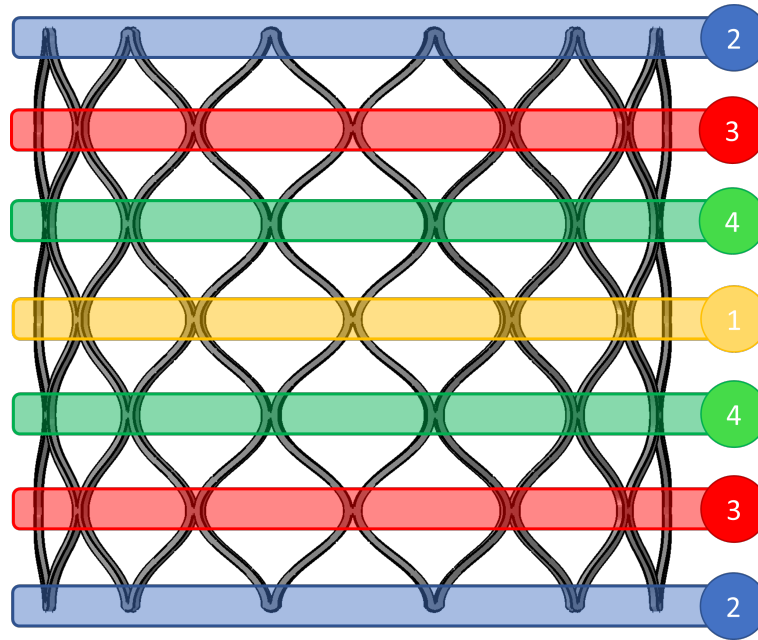
FIGURE 8.8: Representation of the placement of boundary conditions on the basic frame for the 4 different combinations: (1)(yellow) middle ring, (2)(blue) top and bottom end crowns, (3)(red) top and bottom cells, (4)(green) above and below middle ring.

8.3.1.3 Discussion of Ferromagnetic Region Placement Across the Height of the Frame

A single ring of ferromagnetic regions in combination 1 were unfeasible as the resultant envelope diameter increased above the initial diameter of 26 mm due to flaring of the ends of the frame. Similar flaring was observed in combination 4, although to a lesser extent such that there still was an overall decrease in diameter. Considering that the exchangeable valve frame needed to undergo re-sheathing following crimping, flaring at the ends were unacceptable due to the possibility of the end crowns of the frame getting caught in the sheath material and causing tears. Placing the ferromagnetic regions closer to the ends of the frame considerably decreased this flaring behaviour but resulted in a bulging mid section. This bulging, while not ideal, could be tolerated by the re-sheathing process. Additionally, placing the ferromagnetic regions nearer to the ends of the device made the potential engagement between the catheter and the frame during removal easier. The easiest engagement scenario would be combination 2 where the regions were placed at either end; but the decrease in envelope diameter through this placement was too small to feasibly retrieve the device. Hence, due to the superior decrease in envelope diameter and relatively easier engagement via the catheter, combination 3 was chosen.
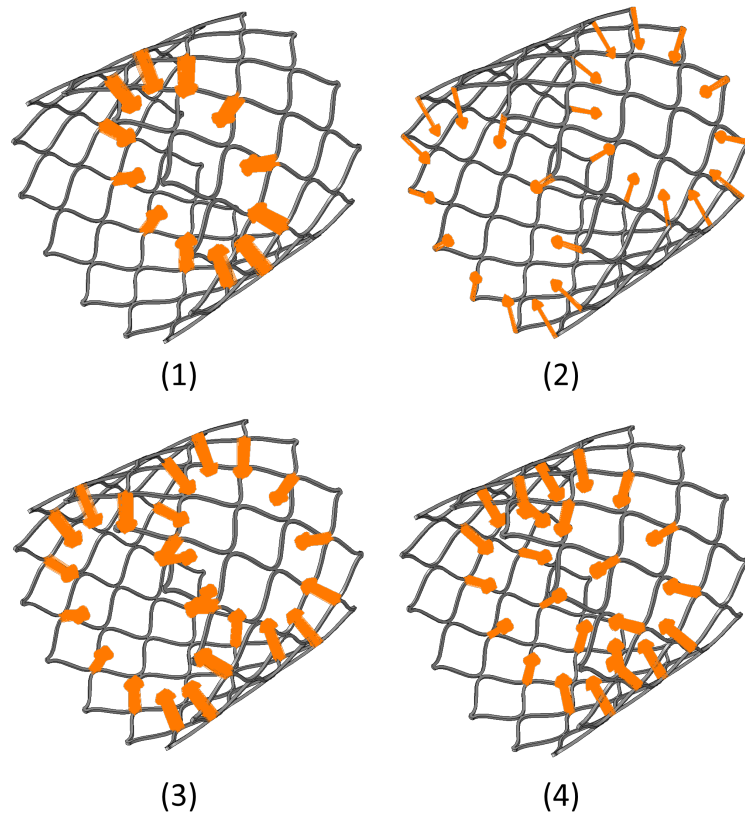
FIGURE 8.9: The node sets and corresponding boundary conditions on the basic frame for the 4 different combinations: (1) middle ring, (2) top and bottom end crowns, (3) top and bottom cells, (4) above and below middle ring. The orange arrows portray the radially inward boundary conditions acting on each set of nodes.
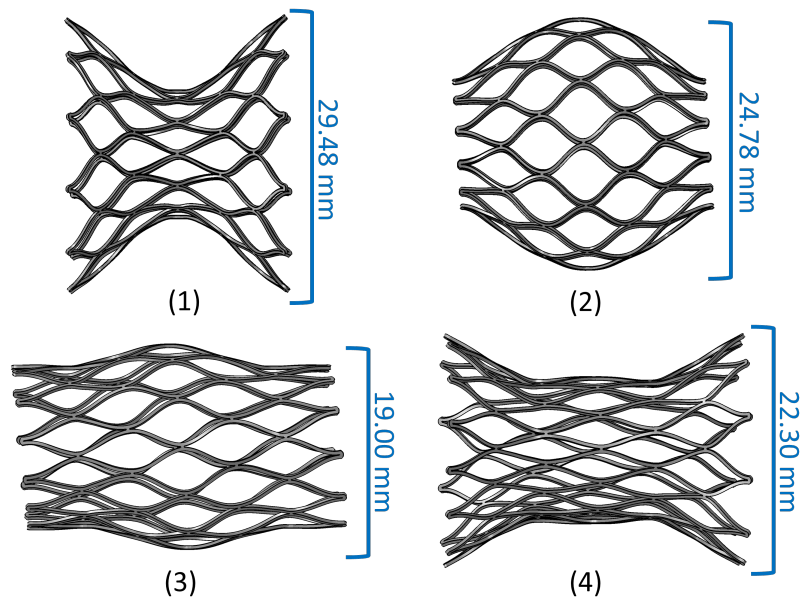
FIGURE 8.10: Results of the crimping simulations with ferromagnets placed at (a) middle ring (b) top and bottom end crowns (c) top and bottom cells (d) above and below middle ring. The resultant envelope diameter of each case is also shown.

8.3.2 Removal Crimping Force

Following the identification of the ideal ferromagnetic region placement across the height of the frame, the frame design was updated to include circular elements in these regions to hold the ferromagnets. Then, the crimpability of the exchangeable frame design through solely applying forces on the ferromagnetic regions was investigated.

8.3.2.1 Methodology of Removal Crimping Force

The exchangeable valve frame holding circular ferromagnetic regions of 1 mm diameter and 0.5 mm thickness was added to the assembly. Tie constraints were defined between the ferromagnetic regions and the frame as described in Chapter 6. Concentrated force loads increasing up to 1 N through a smooth step amplitude curve were defined on these circular regions in the radially inward direction to mimic the *in vivo* crimping of the devices via the catheter. The assembly of this simulation is shown in Figure 8.11. The arrows on the image portray the loads defined on the magnetic regions, directed radially inward, which are also shown in Figure 8.12 in the axial view. The simulation consisted of two steps where the loads on the ferromagnetic regions were increased upto their maximum value of 1 N in the first step and then kept constant through the second step. Contact was defined between the ferromagnetic regions and the frame alongside self contact for each. The material properties of the parts, mesh, step size and contact formulation were as described in Chapter 6.
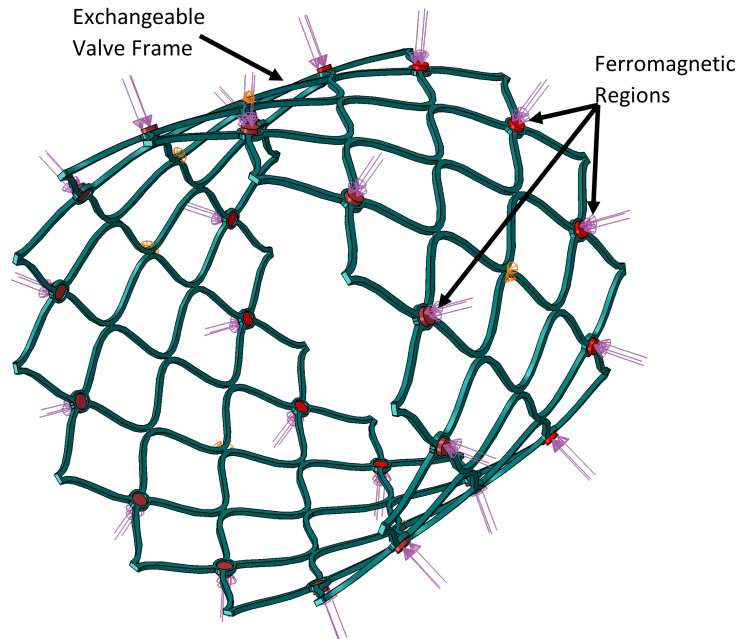
FIGURE 8.11: The assembly of the removal crimping force simulation of a magnetic exchangeable valve frame with loads defined on the ferromagnetic regions.

8.3.2.2 Results of Removal Crimping Force
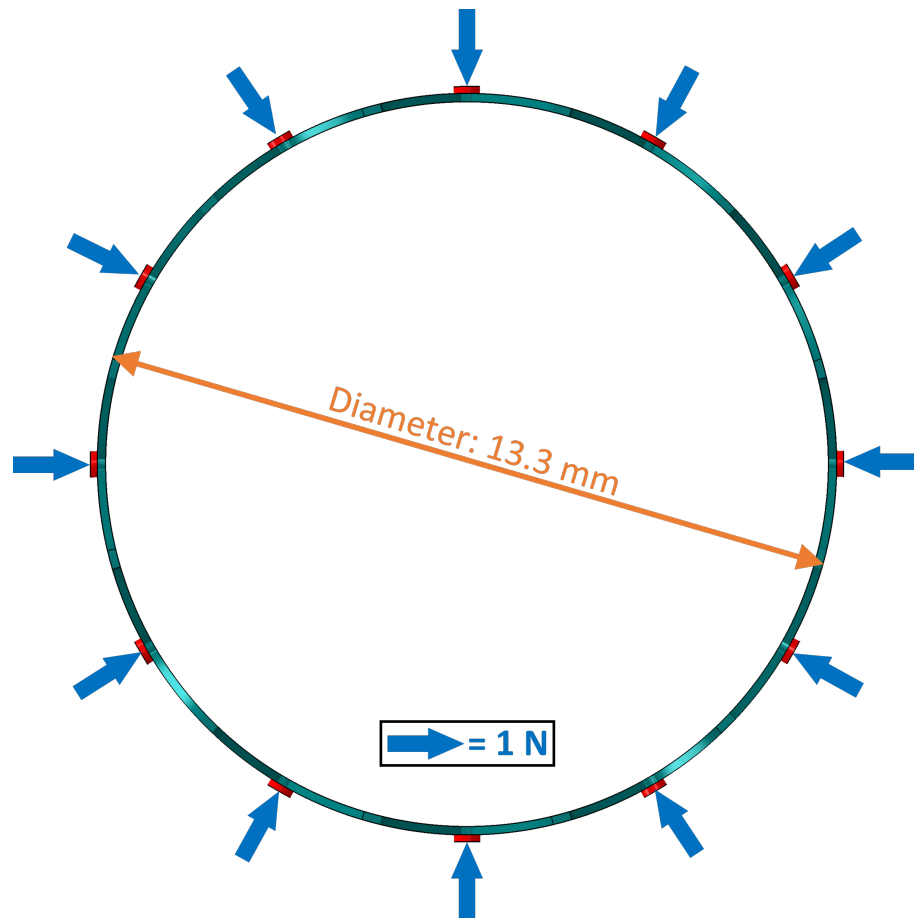
FIGURE 8.12: Axial view of the start of the exchangeable frame removal simulation. Loads on all ferromagnetic regions acting radially inwards are shown as blue arrows. The magnitude of each load was 1 N. The orange line depicts the starting envelope diameter of the frame which was 13.3 mm.

Figure 8.13 shows the collapsed frame following a sustained radially inward load on the ferromagnetic regions of magnitude 1 N. Although the same magnitude of force was applied on each magnet, and the expanded position in Figure 8.12 was symmetrical, the frame collapsed into a triangular shape. Note that all the magnetic regions have moved radially inward, achieving a smaller envelope radius (from 13.3 mm to 12.5 mm), but some have moved further inward than others, resulting in this triangular profile.

8.3.2.3 Discussion of Removal Crimping Force

In the initial steps of the simulation, the frame followed an expected crimping pattern where each cell closed the same amount and the diameter decrease was uniform across the circumference of the frame. At a certain intermediate crimp diameter, however, the force required to close the cells exceeded buckling force. In other words, because the crimping force was applied in discrete points some distance away from each other, the
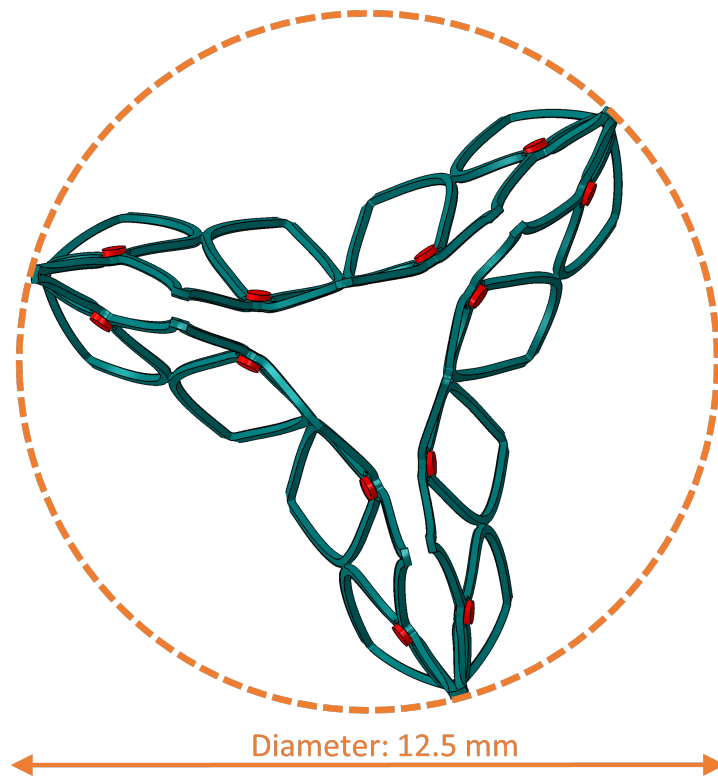
FIGURE 8.13: Axial view of the end of the exchangeable frame removal simulation. Although the same magnitude force was acting on all the ferromagnets, the frame collapsed down to a triangular profile. The orange dashed circle represents the circular envelope of the final crimped shape which had a diameter of 12.5 mm.

force required to bend the struts between two force points became lower than the force required to further deform the cells between them. This resulted in the triangular profile in Figure 8.13.

Although the triangular profile was not a circular reduction to a small diameter for the exchangeable valve frame, a circular reduction was not necessary for retrieval as the removed frame would be discarded. The main purpose was to reduce the diameter of the exchangeable valve enough to overcome the mating to the holding member and be able to axially move it out of the aortic annulus. Since this decrease was achieved with the resultant frame in Figure 8.13, the triangular crimp profile was not an issue.

An important result of this triangular profile was also the fact that there were only three vertical slices of the frame that had moved radially inward the most. This led to the idea of having only three engagement points per ferromagnetic ring between the frame and the catheter. If applying radially inward forces on all twelve regions per ring amounted to a triangular crimp, the same shape could be achieved by only applying radially inward forces on three regions per ring. Decreasing the number of magnets on the catheter could then allow for larger magnets able to deliver larger forces, and a lower catheter profile.

8.3.3   Placement Across the Circumference of the Frame

With the idea of having less than 12 engagement points per ring between the catheter and the exchangeable frame, the possibility of decreasing the number of ferromagnetic regions per ring on the frame was also captured. While the advantage of having less ferromagnets would be less material, lower crimp profile, and less deviation from the original cell structure, the disadvantage would be the higher required precision while engaging via the catheter *in vivo*.

8.3.3.1   Methodology of Ferromagnet Placement Across the Circumference of the Frame

To evaluate this, the *ex vivo* crimping and unsheathing of two identical frames holding 12 and 6 ferromagnets per ring respectively, was simulated. This corresponded to a ferromagnet between every cell (Figure 8.14) and a ferromagnet between every other cell (Figure 8.15). The diameter of the ferromagnetic regions in both designs were set to 1 mm as a starting point.
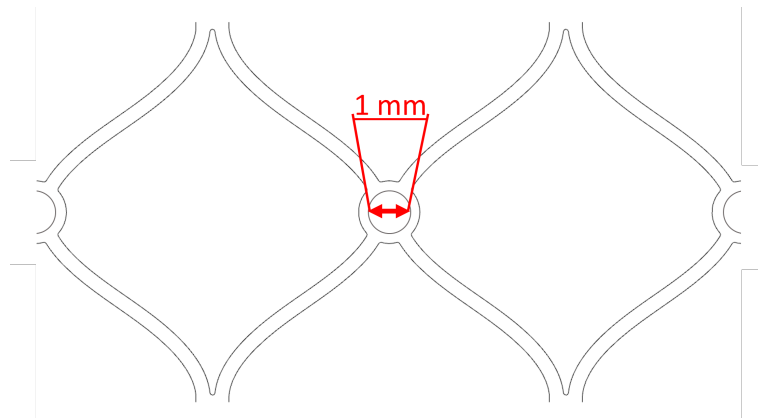
FIGURE 8.14: Ferromagnetic regions between each cell. The diameter of the ferromagnetic regions, 1 mm, is annotated in red.
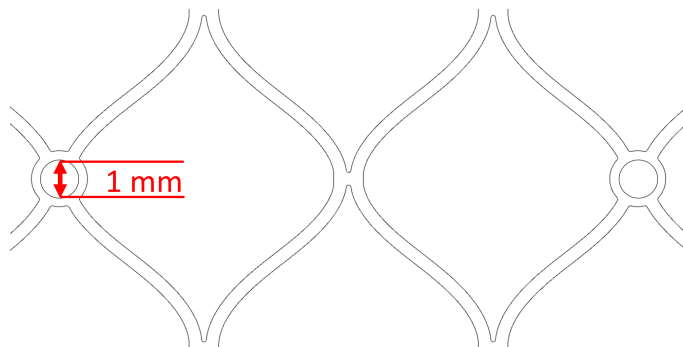
FIGURE 8.15: Ferromagnetic regions between every other cell. The diameter of the ferromagnetic regions, 1 mm, is annotated in red.

The setup of the crimping and unsheathing simulations of the exchangeable valve were described in Chapter 6. This simulation only included the crimping step of these simulations but were otherwise identical with a final crimp diameter of 8 mm.

8.3.3.2   Results of Ferromagnet Placement Across the Circumference of the Frame

Figure 8.16a and 8.16b show the crimped state of the two designs.
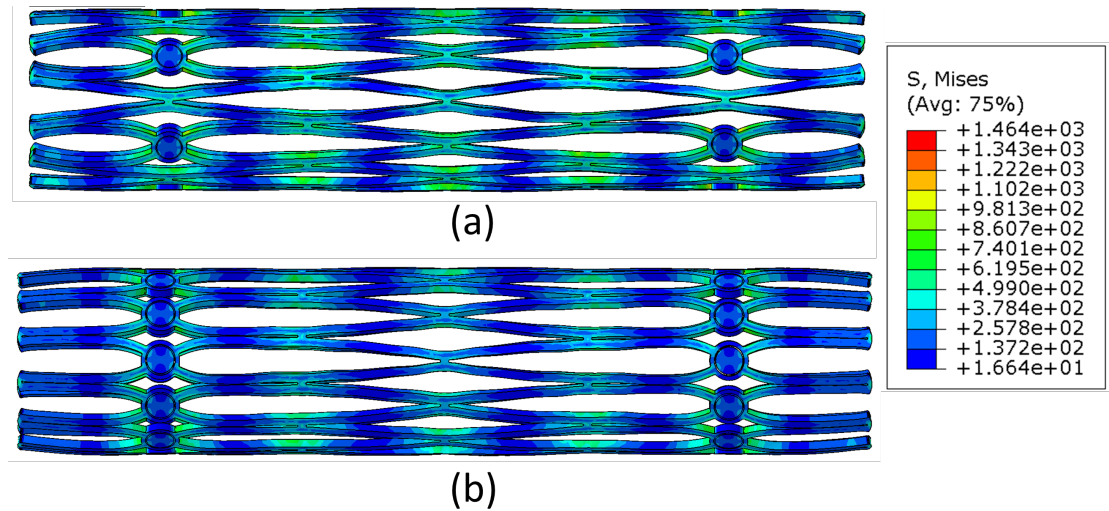
FIGURE 8.16:   (a) Exchangeable valve frame with 6 ferromagnets per ring crimped down to 8 mm diameter. (b) Exchangeable valve frame with 12 ferromagnets per ring crimped down to 8 mm diameter. Both images show the von Mises stress contours across the frames with colour band limits shown on the right.

In both cases the crimped shape of the cells adjacent to the ferromagnet positions differed from the shape of the other cells. In Figure 8.16a this difference was amplified due to having ferromagnetic regions every other cell. In other words, the design with more asymmetry across the frame crimped more non-uniformly. Following unsheathing, both frames were able to expand to their initial shapes even from a non-uniform crimped shape.

8.3.3.3   Discussion of Ferromagnet Placement Across the Circumference of the Frame

In terms of crimpability and expansion, designs with asymmetrical ferromagnet positions were feasible. However, the asymmetric crimp shape also caused localised high stress points, particularly around cells that were not adjacent to a ferromagnet because they underwent larger deformation. These higher stress points can be seen in Figure 8.16a at either end of the frame, between the ferromagnetic regions. The maximum von Mises stress on the frame of Figure 8.16a was 1464 MPa compared to 1260 MPa of

Figure 8.16b. As self-expanding valves are usually packaged in a crimped state on their delivery systems, they stay in the crimped position for a long amount of time where further deformation due to creep can occur [39]. This can, in turn, affect the expanded frame shape. Additionally, although they were not included in these simulations, the exchangeable valve would hold animal leaflets attached which could also undergo high stress and even tears due to an improper crimp shape [172]. Therefore, frame designs with ferromagnetic regions at every cell connection around a ring were preferred.

8.4 Number of Cells Around the Circumference

Based on the previous analyses, the position of the rings of ferromagnetic regions across the height of the frame was determined. In addition, the number of ferromagnetic regions per ring was set to equal the number of cells around the circumference of the frame. Following these, an analysis on the effect of the number of cells around the circumference (and hence the number of ferromagnetic regions) on the removal force and crimped envelope diameter was made.

Three exchangeable valve frame designs were considered, differentiated only by the number of cells on a single ring of the frame: 12 cells, 9 cells and 8 cells. The choices reflected existing TAVI valves with the minimum number of cells where the Acurate Neo valve has 12 cells across a single ring and the Portico valve has 9 cells, as detailed previously in Figure 3.17 [39, 63]. The 8-cell design was investigated for comparison of forces against the 12 cell configuration, even though it lacked the symmetry required to accommodate a tri-leaflet valve. The rationale behind using designs that reflected the structure of existing TAVI valves was described in Chapter 7, pointing out that these frames had clinically proven performance in terms of their crimpability, expansion and radial strength. The minimum number of circumferential cells were preferred since frames with coarser cells exhibit lower radial strength and hence are advantageous for removal.

The number of engagement points between the frames and the catheter was another design parameter in this study. To ensure a symmetric crimped shape that achieved the minimum envelope diameter, the number of cells per ring had to be divisible by the number of engagement points. The lower limit of the number of engagement points was three since a lower number would not achieve any reduction in envelope diameter. The upper limit was four due to the limited volume in the catheter. Hence, the cell number-engagement point combinations investigated were:

- 8 cell frame design with 4 engagement points per ring;

- 9 cell frame design with 3 engagement points per ring;

- 12 cell frame design with 3 engagement points per ring;

- 12 cell frame design with 4 engagement points per ring.

8.4.1 Methodology of Number of Cells Around the Circumference

The frame designs were modelled starting from a deployed position without leaflets or skirts. Engagement points were also modelled as cylinders representing magnets, with their starting position 0.1 mm away from corresponding ferromagnetic regions on the frame. The catheter magnet size was kept constant at 0.5 mm radius and 0.5 mm thickness for all four designs in this investigation. Tie constraints were defined between the ferromagnetic regions and the frame as described in Chapter 6. A VUAMP subroutine was used to apply force on the ferromagnetic regions dependant on their distance from the catheter magnets, and a boundary condition was defined on each catheter magnet moving them radially inward over the course of the simulation. Further description of this subroutine is given in Chapter 7. A cylinder of 6 mm diameter was included in the assembly – representing an 18 Fr catheter – solely to compare the crimped profile with the desired catheter diameter, but there was no contact defined between the catheter and any of the other parts to allow the catheter magnets and frame to crimp the furthest distance.

The simulations consisted of two steps. In the initial step the catheter magnets were kept stationary via an encastre boundary condition on each cylinder. The VUAMP subroutine was activated to allow for contact to be made between the catheter magnets and their corresponding ferromagnets. The step duration in this case was 0.1 s with a target time increment of 4×10^{-7} s. In the second step, the catheter magnets had a radially inward boundary condition of 12 mm with constraints in the axial and circumferential directions, shown by the orange arrows in Figure 8.17. The amplitude curve was defined as a smooth step. The step duration for this step was increased to 0.3 s with the same time increment. Hard, frictionless contact was defined between the ferromagnetic regions, catheter magnets, and the frame throughout the simulation alongside self contact for all. The catheter magnets were meshed with hexahedral (C3D8R) elements with a target global seed size of 0.1 mm to match the mesh resolution of the ferromagnets. The catheter magnets were also modelled as neodymium magnets with material properties listed in Table 6.2. The meshes and material properties of the frame designs and the ferromagnets were as described in Chapter 6.

An example assembly for this investigation is shown in Figure 8.17. The minimum force per catheter magnet and the envelope diameter of the resultant crimped frame profile were recorded.
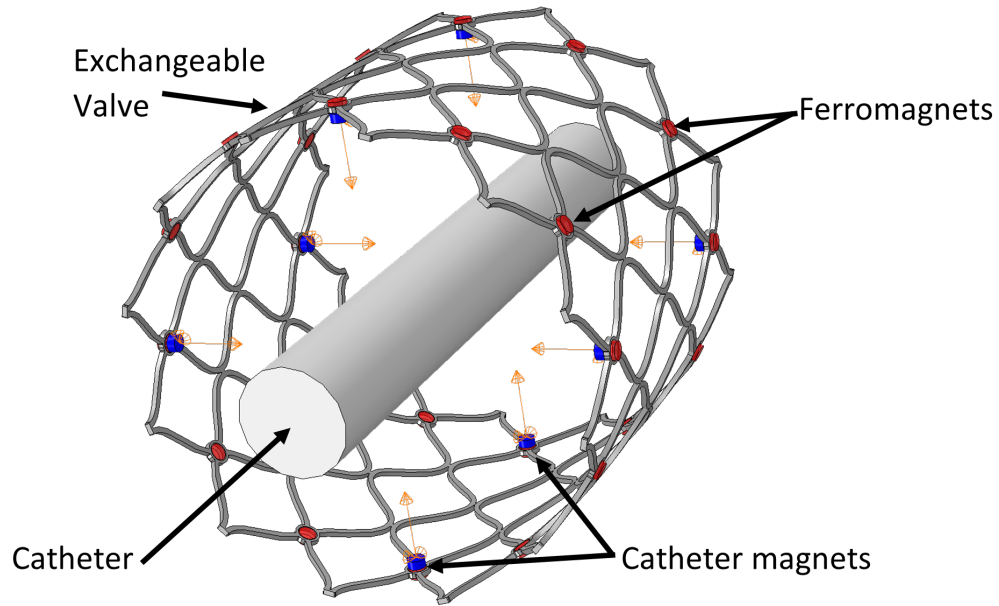
FIGURE 8.17: Assembly for crimping simulations using four magnets (in blue) per ring in a 12 cell frame. The inner diameter of the frame is 26 mm and the cylinder representing the catheter is 18 Fr (6 mm) in diameter. The orange arrows show the direction of the boundary condition on the catheter magnets. The ferromagnetic regions on the frame are in red.

8.4.2   Results of Number of Cells Around the Circumference

As seen in Figure 8.18, four engagement points were required to achieve a meaningful amount of crimping of the 8-cell and 12-cell frames. For the cases with three points, the envelope diameter of the crimped frame was higher than that of the initial deployed frame, with the inwardly bending points protruding beyond the initial diameter. Hence, four magnets on the catheter was necessary for a feasible removal process.

8.4.3   Discussion of Number of Cells Around the Circumference

Between the two frames crimped through four magnets, the 8-cell design achieved a slightly smaller radius at 10.5 mm compared to 11 mm for the 12 cell design. However, the 12-cell design required less force per catheter magnet to crimp at 2.57 N compared to 3.18 N. The reason for this difference was partly due to the presence of ferromagnetic regions equidistant from the four engagement points in the 8-cell design. The added material of these regions increased the bending stiffness between each of the four prongs on the crimped frame, requiring greater force to deform. Since the force requirement determined the sizes of catheter magnets and ferromagnetic regions on the frame, the design requiring the least amount of force while still achieving a decrease in envelope diameter – the 12-cell design with 4 electromagnets – was selected as the optimal configuration.
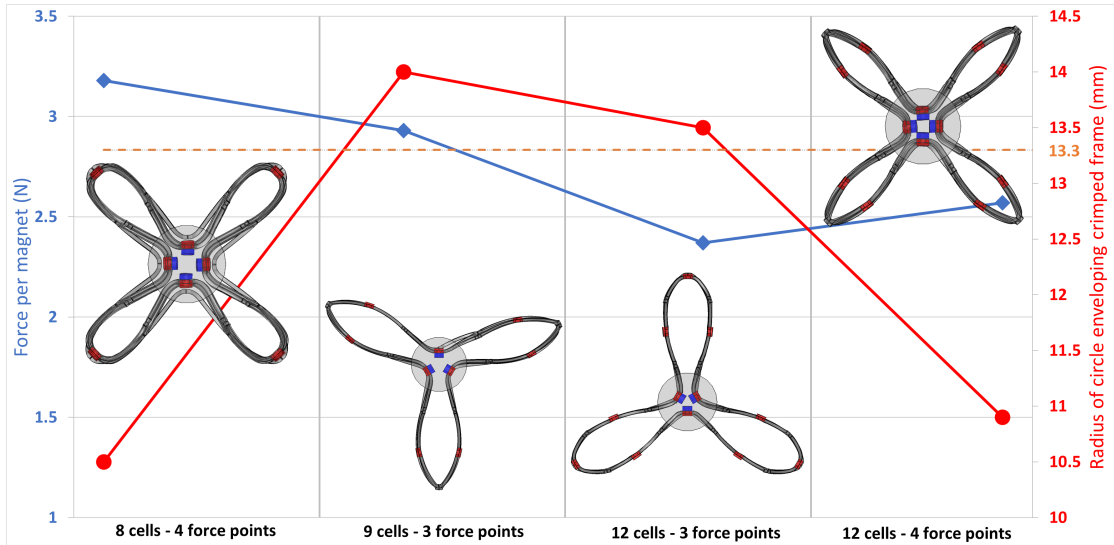
FIGURE 8.18: **Left axis (blue):** Force (N) per magnet required to crimp (i) an 8 cell frame with 4 catheter magnets, (ii) a 9 cell frame with 3 catheter magnets, (iii) a 12 cell frame with 3 catheter magnets, and (iv) a 12 cell frame with 4 catheter magnets. **Right axis (red):** Radius (mm) of circle enveloping the entire final crimped frame for i,ii,iii and iv. A top-down view of the crimped frame for each investigation is shown corresponding with the horizontal axis labels. The dashed orange line shows the 13.3 mm point on the right vertical axis which is the radius of the circle enveloping the frame prior to crimping.

8.5 Ferromagnetic Region Radius

Having established the number of ferromagnetic regions and catheter magnets above, the purpose of this analysis was to determine the relationship between removal force per catheter magnet and ferromagnetic region size on the frame.

8.5.1 Methodology of Ferromagnetic Region Radius

The same setup to the previous investigation was used with catheter magnets moving radially inward and magnetic force being applied to nodes on ferromagnetic regions of the frame through the VUAMP subroutine. The two scenarios considered both had a total of 24 ferromagnetic regions and a thickness of 0.5 mm, with radii of 0.5 mm and 1 mm respectively. The setup of these simulations with each frame scenario are shown in Figure 8.19. The size of the ferromagnetic regions in each case is labelled on the figure and the radially inward boundary condition on the electromagnets is shown. The load defined on the ferromagnetic regions dependant on their distance from their corresponding electromagnets via the VUAMP subroutine is not shown.
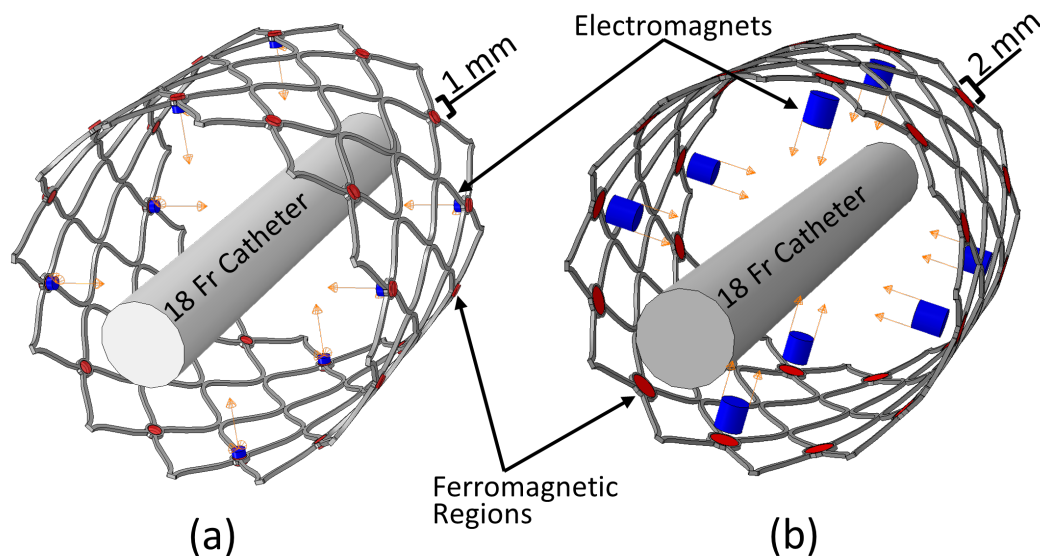
FIGURE 8.19: The setup of the ferromagnetic region radius simulations with (a) the frame with 0.5 mm radius ferromagnets and, (b) the frame with 1 mm radius ferromagnets. The orange arrows depict the direction of the boundary conditions on each electromagnet. The load that was applied on the ferromagnetic regions through the VUAMP subroutine is not shown in the image.

8.5.2 Results of Ferromagnetic Region Radius

As can be seen in Figure 8.20, larger ferromagnetic regions resulted in a larger force requirement per catheter magnet. This was due to the struts connecting into the ferromagnetic regions being shorter for designs with larger ferromagnetic regions. The shorter struts required more force at one end to deform compared to the longer struts and hence the total force required to crimp increased with ferromagnetic region size.

8.5.3 Discussion of Ferromagnetic Region Radius

While larger ferromagnetic regions provide a bigger target for the catheter magnets to engage with, they increase the force required to achieve a diameter reduction in the frame. The size of the ferromagnets also influence the force of their attraction to the catheter magnets as discussed later in Chapter 9. Hence, the determination of the optimum size depends on the design of the magnetic elements on the catheter. In other words, while in terms of the required removal force to achieve a sufficient reduction in frame diameter smaller ferromagnets are advantageous, larger ferromagnets can allow the catheter magnets to exert a higher force for a given design. Selection of the appropriate size, then, was left to the investigations into the catheter design in Chapter 9.
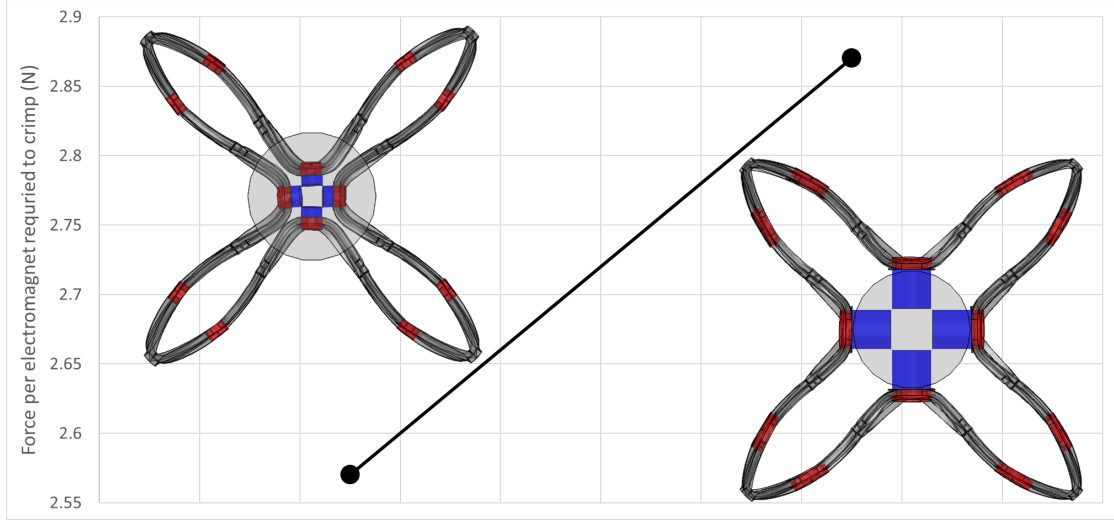
FIGURE 8.20: Force required to achieve a four-pronged crimp of the exchangeable valve frame with (left) ferromagnetic region radius of 0.5 mm and, (right) ferromagnetic region radius of 1 mm. The force values reported are for a single electromagnet and all 8 electromagnets exert this same force on corresponding ferromagnetic regions. The ferromagnetic regions on the frames are coloured in red, and the electromagnets are coloured in blue. The light grey circle in the middle of both frame images represents a 18 Fr catheter.

8.6   Strut Width and Cell Height

After determining the size and position of the ferromagnetic regions on the frame, an analysis was undertaken to determine the optimal strut width and cell height of the exchangeable valve in terms of the force required to remove and the outward radial force it exerts. In the literature, the strut width, cell density and valve height were found to affect the outward radial force of the frame the most [52]. Wider struts, coarser cells and longer valve frames were found to have higher radial force, as could be predicted with there being an increased amount of material on the frame in all three cases. The cell density is defined through the number of cells around a circumferential slice of the frame and the number of cells on a vertical slice of the frame. In the case of the e-TAVI valve, the number of cells around the circumference was determined by the number of ferromagnetic regions on the frame. Hence, the strut width and cell height were determined as the variables of interest for this investigation.

Typical values of strut width in commercial self-expanding heart valve frames is approximately 0.3 mm [45, 49]. In general, thinner struts are preferred in industry due to less overall inorganic material on the frame and hence higher biocompatibility. However, the frame needs to exert enough radial force to anchor into the aorta. While the cell shape and frame parameters also have an effect on the radial strength, a value much thinner than the current standard is unlikely to be sufficient; especially since the e-TAVI frame is considerably less cell-dense than its counterparts such as CoreValve. Hence, the lower limit of strut width was determined as 0.25 mm in this analysis. The upper limit was set

to 0.4 mm as thicker frames were infeasible in terms of the force that would be required to remove them.

Many commercial designs make use of varying cell heights, both for conforming to the aortic root and allowing access to the coronary ostia. The cell height for CoreValve ranges from 6 mm to 10 mm. The same range for cell height was used in this investigation.
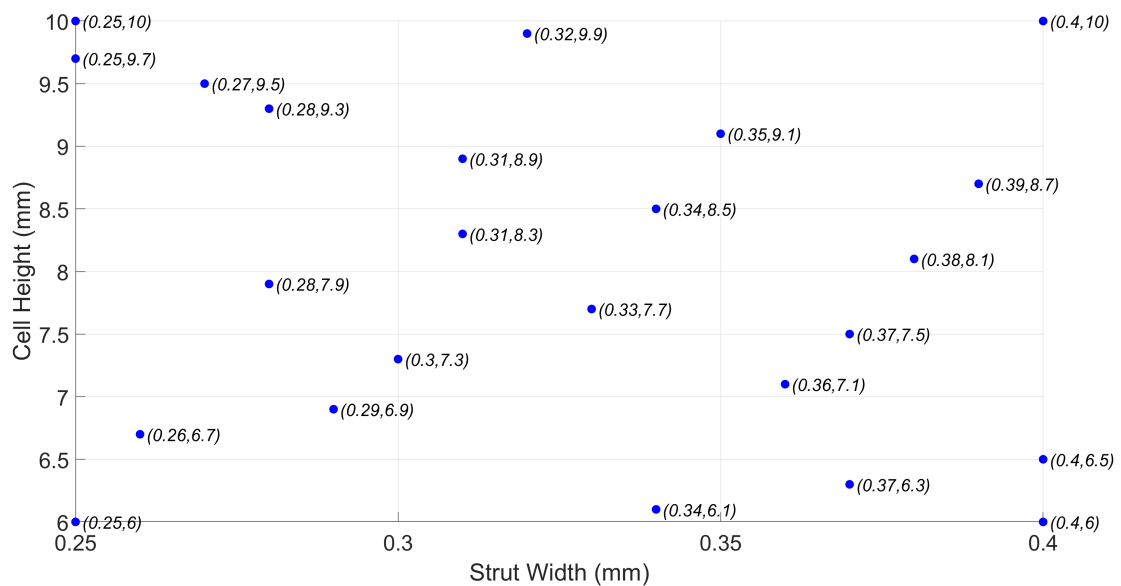
FIGURE 8.21: Strut width and cell height design space with the Latin Hypercube samples.

In order to investigate the effects of strut width and cell height, a Latin Hypercube sampling method was used to populate the design space with 20 sample points. Figure 8.21 shows the positions of these points along with the four corners of the design space, to better cover the entire space, bringing the total to 24 designs.
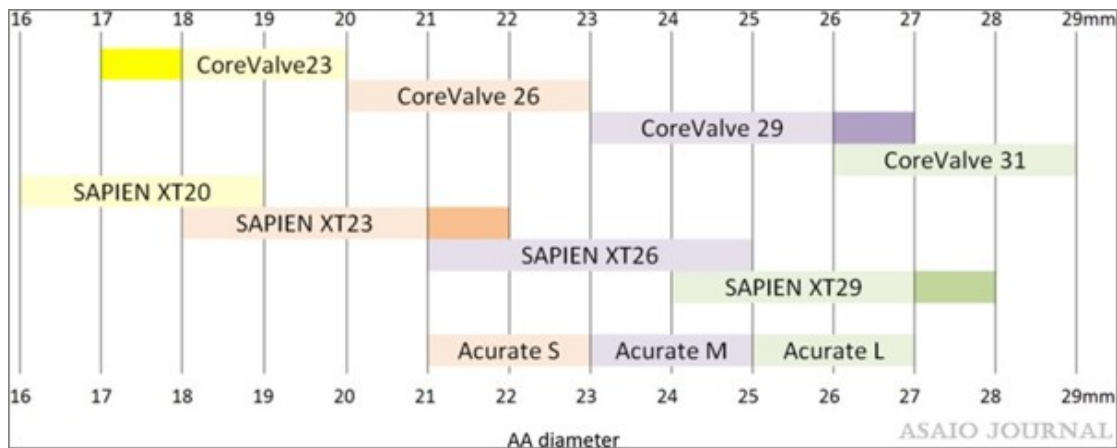
FIGURE 8.22: Commercial prosthetic valve sizes and their recommended annulus sizes [53]

8.6.1   Methodology of Strut Width and Cell Height

In this analysis, the assembly consisted of a crimping cylinder, exchangeable valve frame, ferromagnetic regions and the catheter magnets. The material and mesh properties of the exchangeable valve, ferromagnets and the crimping cylinder were as described in Chapter 6. These properties for the catheter magnets were as described in Section 8.4.1.

The simulation consisted of three steps:

- In the first step the crimping cylinder had a radial displacement boundary condition to crimp the frame down to 10 mm outer diameter. The cylinder was also constrained not to move in the axial and circumferential directions. Frictionless, hard contact was defined between the cylinder, frame and the ferromagnets.

- In the second step the radial boundary condition on the cylinder was reversed in direction to expand the frame back to 5% of its full outer diameter.

- In the third step, contact was defined between the catheter magnets and the frame and ferromagnets. The VUAMP subroutine was activated via which a distance dependant load was applied on the ferromagnetic regions towards the catheter magnets. A radially inward boundary condition of 12 mm was defined on the catheter magnets and their motion in the axial and circumferential directions were constrained.

The step duration of all steps were 0.3 s with a target time increment of 4×10^{-7} s, as described in Chapter 6. This time increment was such that contact between the expanding cylinder and the frame was not lost between time increments. This way, the chronic outward force (COF) of the frame at different underexpansion amounts up until 5% could be extracted from the same simulation. The general contact algorithm was used to model contact interactions between the cylinder and the frame, as described in Chapter 6, with hard contact and no friction. The ferromagnets were attached to the exchangeable valve frame via tie constraints, also as discussed in Chapter 6.

As the frames were designed to have an inner diameter of 26 mm with 0.3 mm strut thickness, expanding to 5% of their full diameter equated to the frame expanding into a diameter of 25.3 mm. In practice, the underexpansion amount of TAVI frames after deployment is variable. Obviously, some underexpansion is necessary to exert an outward radial force and anchor into the aorta. The range of underexpansion in practice can be estimated by observing the different sizes of commercial valves and which aorta sizes they are recommended for. The CoreValve Evolut series have 23, 26, 29 and 34 mm sizes. The recommended aortic sizes for each are shown in Figure 8.22. Taking the 26 mm design as an example, since the e-TAVI model was also 26 mm, it is recommended

for aortic diameters ranging between 20-23 mm. This translates to an underexpansion range of 11.5-23.1%.

The COF of the frames through the second step and the force per catheter magnet necessary to partially crimp the frame in the final step was evaluated.

8.6.2   Results of Strut Width and Cell Height
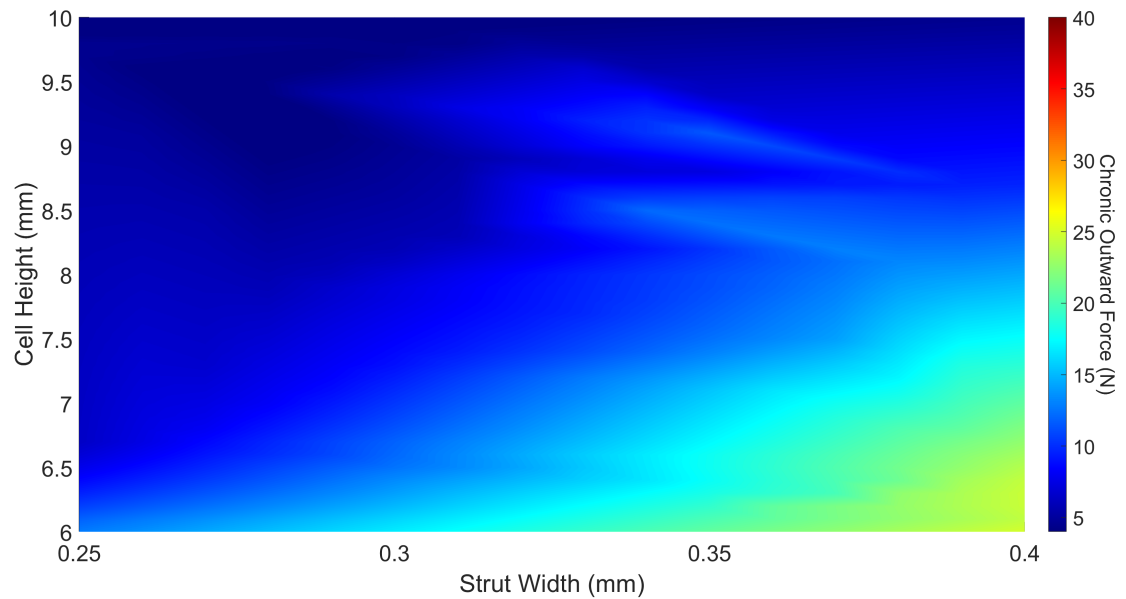
FIGURE 8.23: 5% underexpansion COF values versus cell height and strut width.
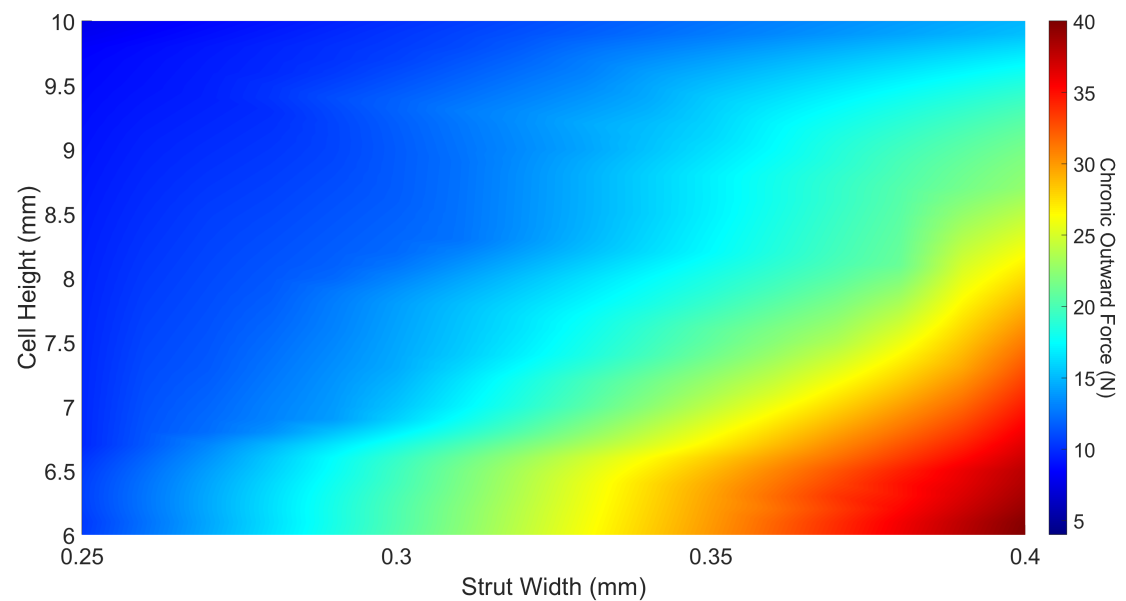
FIGURE 8.24: 10% underexpansion COF values versus cell height and strut width.

As evinced by the similarity in the contour regions in Figures 8.23 and 8.24, the effect of both strut width and cell height on the COF was very similar at 5% and 10% underexpansion. Wider struts (correlation coefficient (r) = 0.53, p-value = 0.0155) and shorter cells ($r = -0.37, p = 0.106$), represented at the bottom right corner in both figures, resulted in higher COF values. The range of values in Figure 8.24 is approximately twice that of Figure 8.23, showing a linear relationship between COF and underexpansion between 5%-10%.
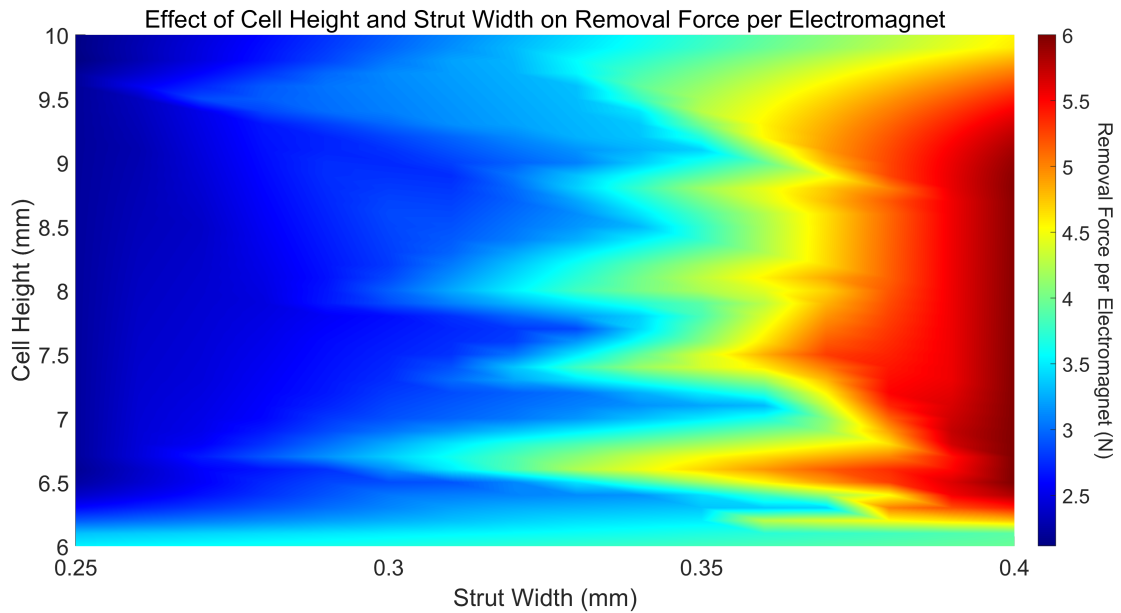
FIGURE 8.25: Removal force per catheter magnet values versus cell height and strut width.

Figure 8.25 shows the relationship between the force per catheter magnet required to crimp the frame into the four-pronged shape, and strut width and cell height. Wider struts required a higher force, as represented on the right-hand side of the figure (correlation coefficient (r) = 0.84, p-value = $1.37E - 6$). Interestingly, the effect of cell height on the removal force was minimal (correlation coefficient (r) = -0.19, p-value = 0.417), as opposed to its effect on radial force.

8.6.3   Discussion of Strut Width and Cell Height

The results of this analysis implied that the cell height of the frame could be changed to achieve higher radial strength while keeping the removal force at similar values. Consequently, reduction in frame diameter for re-sheathing could be achieved by forces lower than the COF of the frame for certain strut width and cell height combinations. To identify these regions, Figure 8.26 plots the difference between the chronic outward force (COF) and total removal force within the design space. The plot is colored according to negative and positive values of this difference, portraying the designs where the COF was larger than the total force required to crimp the frame, coloured in pink.

Hence, the pink regions defines the boundary where the reduction in frame diameter for re-sheathing could be achieved by forces lower than the chronic outward force. This boundary was approximately below 8 mm cell height. Designs with narrow strut widths (< 0.3 mm) did not reliably exhibit this advantage as the COF decreased more rapidly than the removal force with respect to strut width.
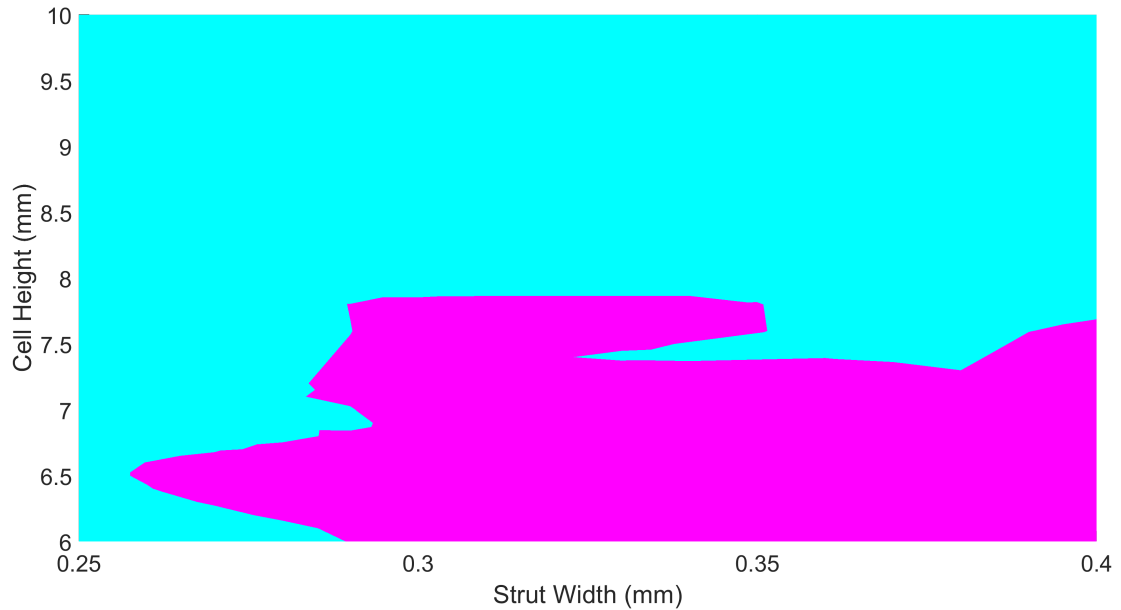
FIGURE 8.26: Difference between the COF and total magnetic force required to remove the exchangeable valve frame designs. Pink regions show positive values and blue regions show negative values.

8.7 Skirt and Leaflets

The lack of leaflets and skirts in the exchangeable valve model represented one of the limitations in this study. While the effect of including the leaflets in a TAVI deployment simulation were found to be minimal by Bailey et al., in the removal investigation here, the space taken up by the leaflets could increase the minimum feasible crimp diameter [49, 172]. The skirt could also have some effect on the radial strength of the frame and hence require a larger amount of force per electromagnet to crimp.

Structurally, the skirt and the leaflets could be sutured around cell connectors without ferromagnetic regions, as it is in the case of CoreValve devices. Both an outer and an inner skirt could be attached to encompass and hold the ferromagnetic regions in addition to preventing paravalvular leakage. This would alleviate the need for melding/binding the ferromagnets to the frame after manufacture. Figure 8.27 represents how a complete e-TAVI valve could look like with skirts, leaflets and ferromagnetic regions.
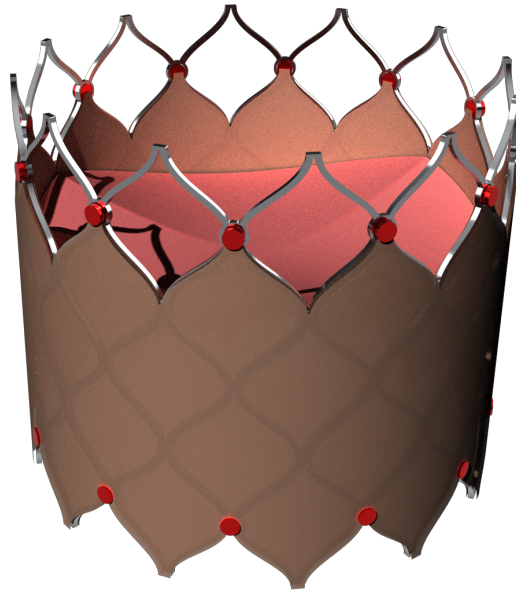
FIGURE 8.27: Representative exchangeable valve with leaflets and skirt.

8.8 Summary

In this chapter, the exchangeable valve frame of the e-TAVI system was designed and developed, mainly in terms of the position and size of its ferromagnetic regions. The feasibility of these additions were evaluated in terms of the crimpability of the frame and ease of magnetic removal. The results of the magnetic removal simulations influenced the design of the magnetic catheter of the e-TAVI system in terms of number and size of magnetic elements, and the results of the radial force investigations informed the design of the holding member in terms of anchoring requirements. Further points from the chapter are summarised below.

- The exchangeable valve frame was designed as a basic SE valve frame with circular ferromagnetic regions to engage with the removal catheter.

- The optimum ferromagnetic region placement was found to be two rings across the height of the frame with regions between each cell on both rings.

- Applying radially inward forces on all the ferromagnetic regions resulted in a three-pronged crimped profile as opposed to a proper circular crimp.

- The largest decrease in envelope diameter per removal force was achieved by the frame with 12 cells across its circumference and four catheter magnets per ferromagnet ring.

- Larger ferromagnetic region radii on the frame resulted in higher removal forces per catheter magnet.

- Wider struts and shorter cells resulted in larger radial forces.

- The four-pronged crimping of the e-TAVI frame required less force than the COF of certain frame designs with cell height lower than 8 mm.

Chapter 9

Catheter Design

This chapter details the analyses performed relating to the development of the dedicated e-TAVI catheter. The VUAMP subroutine validation is discussed and the analysis on magnetic engagement feature size on the catheter is described.

The removal investigations on the exchangeable valve frame had determined the number of magnetic engagement points per ferromagnetic ring as four, between the catheter and the valve frame. Since the regions on the frame were ferromagnetic, the elements on the catheter had to be magnetic to engage with the valve. These elements were designed as electromagnets. The reason for this choice was two-fold: for the given volume, an electromagnet can deliver a higher magnetic force than a permanent magnet; and an electromagnet can be controlled remotely to turn it on and off [173]. Since there were size constraints on the magnetic elements in the catheter, the higher force to volume ratio of electromagnets was advantageous. The electromagnets would be powered through an external source with power wires connecting to the electromagnets through the catheter. With the ability to control the current supply to the electromagnets, the magnetic attraction between the catheter and the exchangeable valve could be turned on and off. This would allow for the catheter to be positioned in close proximity to the dysfunctional exchangeable valve in the aortic root prior to removal, and prevent erroneous attraction between them during this process. When the catheter position is satisfactory, the current could be turned on to begin the removal of the valve.

The design parameters for the electromagnets were:

- thickness;
- core radius;
- number of windings;
- current.

Additionally, the general design objectives for the catheter were:

- contain magnetic elements able to move radially outwards, securely engage to the valve frame, move radially inward maintaining engagement to the valve and, move axially into a tapered sheath;

- hold a controllable sheath that could open up into a tapered shape with a larger diameter facing the removal elements to receive the partially crimped valve, and close down to fully re-sheath the valve;

- have the lowest profile possible;

- optionally, contain a delivery module proximal to the removal elements to allow for full exchange process via a single catheter.

9.1 Modelling Magnetic Force

For removal simulations using electromagnets, the magnetic attraction force between the catheter and exchangeable valve frame had to be modelled. Calculating the force between an electromagnet and a magnetised surface is not straightforward [174]. Firstly, the magnetic field of an electromagnet must be modelled. This magnetic field is the total of all magnetic dipole fields on the atomic level, and a three-dimensional integral would be required to sum these dipole fields to determine the magnetic field of a single magnet [175, 176]. As there were a total of 8 electromagnets on the catheter, coupled with 24 ferromagnetic regions on the frame, solving for the magnetic field of each through integration over volume elements would be too costly in computation time. Hence, some approximations of this field were necessary.

9.1.1 Simplified Magnetic Force Calculation

The magnetic flux density of an electromagnet, also known as the B-field, describes the strength of the magnetic field per area generated around it [175]. For cylindrical electromagnets, the magnetic flux density (B) along its axis can be simplified to:

$$B = \frac{N \times I \times \mu \times \mu_r}{2} \left(\frac{\frac{D}{2} - z}{D \times \sqrt{R^2 + (\frac{D}{2} - z)^2}} + \frac{\frac{D}{2} + z}{D \times \sqrt{R^2 + (\frac{D}{2} + z)^2}} \right) \quad (9.1)$$

where N is the number of windings, I is the current through the wire, z is the distance away from the electromagnet pole, D is the thickness of the electromagnet, R is the radius of the electromagnet and μ_r is the relative magnetic permeability of the medium

[173]. From this, the force, F, acting on a magnetized area of size A perpendicular to the same axis is given by

$$F = \frac{B^2 A}{2\mu} \tag{9.2}$$

where μ is the magnetic permeability of the environment [173]. This simplification is described in APPENDIX C.

The force value calculated through these equations was equivalent to the maximum value that could be exerted on a surface A that was z distance away from the electromagnet. This was because the equations assumed that the surface was oriented perfectly with the electromagnet pole face and was exactly on the face axis. At any position out of this plane at distance z the force would be lower [175]. However, calculating this difference was non-trivial so the magnetic attraction in the simulations were modelled as if they were always on the same axis, with poles facing each other.
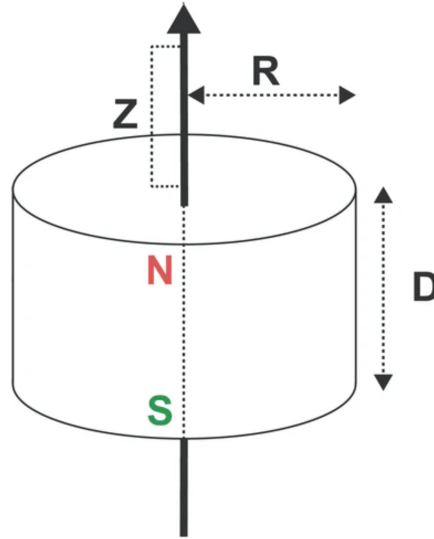
FIGURE 9.1: Representation of a cylindrical magnet showing the parameters used in the approximation of magnetic flux density [177].

Another drawback to these approximations was that the force magnitude became unrealistically large as z tended to zero [175]. This was handled in the VUAMP subroutine by limiting the maximum value of the force to an experimentally determined maximum pull force value for each electromagnet size [177].

9.1.2 VUAMP Subroutine Development

Following the simplified calculation of the magnetic force, it had to be applied on the appropriate node during simulations. In ABAQUS 2018 this could be done through an amplitude subroutine, VUAMP [178]. This allowed the user to write a subroutine that

can then pass a value into the simulation as an amplitude value. The direction of the force, however, could not be controlled through this subroutine. To get around this, three unit loads were defined on each ferromagnetic region on the frame such that the direction of each force was either in the global x, y or z direction. A different amplitude was defined for each load. These amplitudes were then calculated in the subroutine, using Eq. 9 and Eq. 10 for each.

Most parameters in the equations were set as constants in the VUAMP subroutine throughout the simulations. I, N, D, and R were set in the setup in accordance with the electromagnet sizes used in the simulation. μ was set as 1.257×10^{-6} Tm/A, which is the magnetic permeability of water, to most closely represent blood. The z variable, however, changed throughout the simulations as the distance between electromagnets and ferromagnets varied. Hence, history output request in the simulations were used, defined on a single node in each electromagnet and ferromagnet, that exported the global coordinates of that node at each time interval. Each electromagnet was paired up with a ferromagnetic region and the x, y and z components of the distance between them was calculated in the subroutine. For each distance, Eq. 8.1 and Eq. 8.2 were used to calculate the force in that global direction and this value was then imported to the appropriate amplitude definition in the simulation. This process updated at every time interval for all electromagnet and ferromagnet pairs.

9.1.3   Magnetostatic Simulations

The force per catheter magnet required to remove the exchangeable valve with 0.5 mm and 1 mm radius ferromagnetic regions were determined in Chapter 8. For the catheter design the electromagnet parameters required to exert these forces needed to be calculated.

Magnetostatic simulations were set up in the Electromagnetic model in ABAQUS/Standard to simulate the magnetic field produced by electromagnets of different sizes and currents. Magnetostatic analysis in ABAQUS can be used in applications where the magnitude of direct current can be assumed to be constant over time, allowing the coupling between magnetic and electric fields to be neglected [179]. The analysis solves for the static magnetic field produced by a direct current in the space around the current carrying region. The governing field equations of this analysis is based on the magnetostatic approximation to Maxwell's equations describing electromagnetism. This approximation is:

$$\nabla \times (\mu^{-1} \cdot B) = J \qquad (9.3)$$

where μ is the magnetic permeability tensor, B is the magnetic flux density vector and, J is the direct volume current density distribution [179]. The magnetic permeability (μ) relates the magnetic flux density (B) to the magnetic field (H) through $B = \mu \cdot H$. For the numerical solution, ABAQUS introduces a magnetic vector potential (A) where $B = \nabla \times A$. With this, the variational form of Eq 8.3 is:

$$\int_V \nabla \times \delta A \cdot (\mu^{-1} \cdot \nabla \times A) dV = \int_V (\delta A \cdot J) dV + \int_S (\delta A \cdot K) dS \qquad (9.4)$$

where δA is the variation of the magnetic vector potential, and K is the tangential surface current density. ABAQUS solves Eq 9.4 for the components of A and derives the other field quantities from it [179].

9.1.3.1 Assumptions in Modelling Magnets

In modelling magnets there were several assumptions made in both the above magnetic force calculation and the magnetostatic analyses in this thesis. Firstly, the electromagnets and ferromagnetic parts were treated as continuous bodies with a uniform magnetic field along the entirety of the part. In reality, impurities in the material of the magnets and misaligned dipole moments within their structure can result in differences in the magnetic properties of these magnets in different sections [180]. Hence, the magnetic field produced by the electromagnets and the force exerted on the ferromagnets could be less than predicted in the simulations. Secondly, the magnetic field strength produced by the electromagnets were assumed to be directly proportional to the magnetization of the electromagnet core. In other words the H-B curve of the magnets in this thesis were assumed to be linear [180]. The limitation of this assumption was that the magnetic field strength of the electromagnet could be overestimated at very high current values. Thirdly, the magnetic properties of both the ferromagnetic regions and the electromagnets were assumed to be constant over time [180]. While this assumption did not have a direct effect on the simulations performed in this thesis, it must be taken into account when considering that the catheter and exchangeable valve might be kept in storage for some time following manufacture before they are used in deployment. Fourthly, the medium surrounding the magnets were assumed to have no effect on the magnetic behaviour [180]. This assumption neglected the effect of the electrical components in a clinical setting and the associated magnetic fields they produced. It also neglected the effect that the electromagnets on the catheter have on each other which can effect their properties particularly when they are in close proximity at the end of the removal process. Finally, the magnet was assumed to be isotropic, meaning that its magnetic properties are the same in all directions and the magnet exhibits the same behaviour regardless of its orientation [180]. This assumption had minimal effect on the results in

this thesis as the assemblies always positioned the electromagnets and the ferromagnets in the same orientation relative to each other.

9.1.4   VUAMP Subroutine Verification

The simplified expression overestimated the magnetic force at separation distances comparable to the radii of the electromagnets. However, the change in force with respect to the distance was captured correctly. This was verified by a series of magnetostatic simulations where the distance between an electromagnet and a ferromagnet on the same axis was increased from 0.1 mm to 0.45 mm, and the Lorentz force experienced by the ferromagnet in each case was recorded.

9.1.4.1   Methodology of VUAMP Subroutine Verification

The assembly of the magnetostatic simulations to verify the VUAMP subroutine included a single ferromagnetic region of 0.5 mm radius and 0.5 mm thickness, and an electromagnet with 0.5 mm radius and 0.5 mm thickness, where the core radius was 0.25 mm. The assembly of this simulation is shown in Figure 9.2. The electromagnet was modelled by a cylinder, representing the core, surrounded by a hollow cylinder representing the winding. The material for the core and the ferromagnetic region was defined as iron. The winding was modelled as copper and the medium surrounding the ferromagnet and electromagnet was defined as blood. The electrical and magnetic properties of these materials are listed in Table 9.1.

The distinct parts in the simulation and the medium surrounding them, as shown in shown in Figure 9.2, were merged in ABAQUS to form a single part consisting of four domains: ferromagnet, electromagnet core, electromagnet winding, medium. This part was meshed with tetrahedral electromagnetic elements (EMC3D4). There was a single time-harmonic step in the simulation with a frequency of 50 Hz. Boundary conditions were defined on each outer face of the medium cylinder, setting the magnetic vector potential of all component to zero at these boundaries. A body current density load of 2.89×10^{10} A/m^3 was defined on the electromagnet ring.

The same magnetostatic simulation was performed where the distance between the electromagnet and the ferromagnet was increased from 0.1 mm to 0.45 mm with a resolution of 0.05 mm. This resulted in the force profile that the electromagnet exerted on the ferromagnet within this distance.

TABLE 9.1: Electrical and magnetic material properties used in the magnetostatic finite element simulations.

Material Parameter	Value
Electrical Conductivity (Iron)	10^7 S/m ([181])
Magnetic Permeability (Iron)	6.3×10^{-3} H/m ([182])
Electrical Conductivity (Copper)	5.96×10^7 S/m ([183])
Magnetic Permeability (Copper)	1.256629×10^{-6} H/m ([182])
Electrical Conductivity (Blood)	1.5 S/m ([184])
Magnetic Permeability (Blood)	1.256627×10^{-6} H/m ([185])
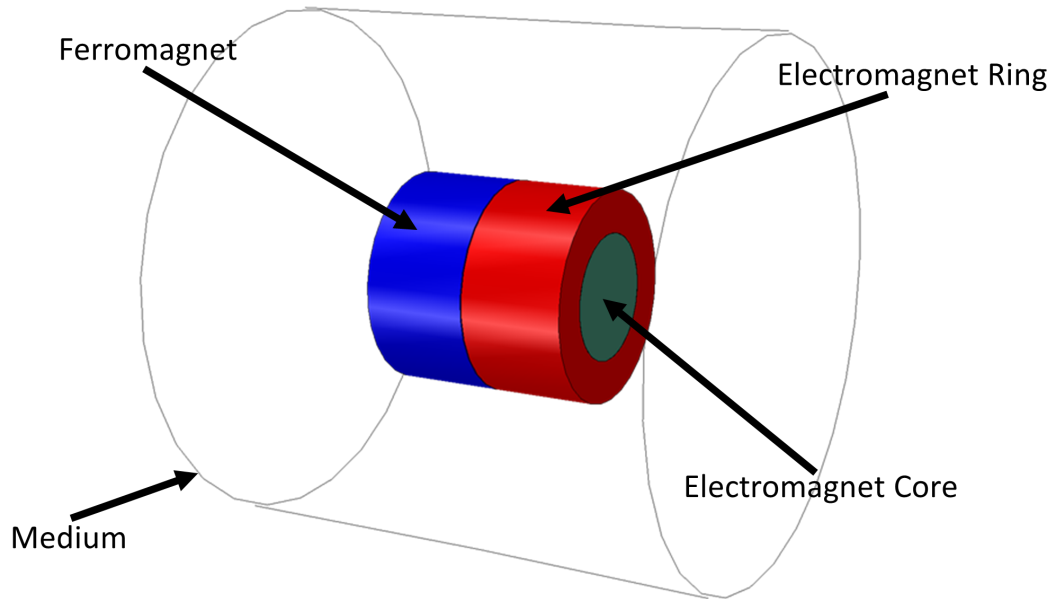
FIGURE 9.2: Assembly of magnetostatic simulations investigating the body current density required to exert the required crimping force. The electromagnet core is in green, the ring representing the windings in red and the ferromagnetic region in blue. The wireframe cylinder surrounding the magnets represents the medium.

9.1.4.2 Result of VUAMP Subroutine Verification

When the parameters in the VUAMP subroutine equation (current and number of windings) were set such that the calculated force at 0.1 mm was equal to the Lorentz force at the same distance, the calculated force at higher distance values agreed with the magnetostatic simulations to within 6.15%. This agreement is shown in Figure 9.3.

9.1.4.3 Discussion of VUAMP Subroutine Verification

The force calculated at 0.1 mm distance was set as the maximum pull force of the electromagnets because for smaller distance values, the magnetostatic simulations returned lower force values. This lower force was due to the core of the electromagnet and the entire ferromagnet being computed as a single part because of the minuscule distance
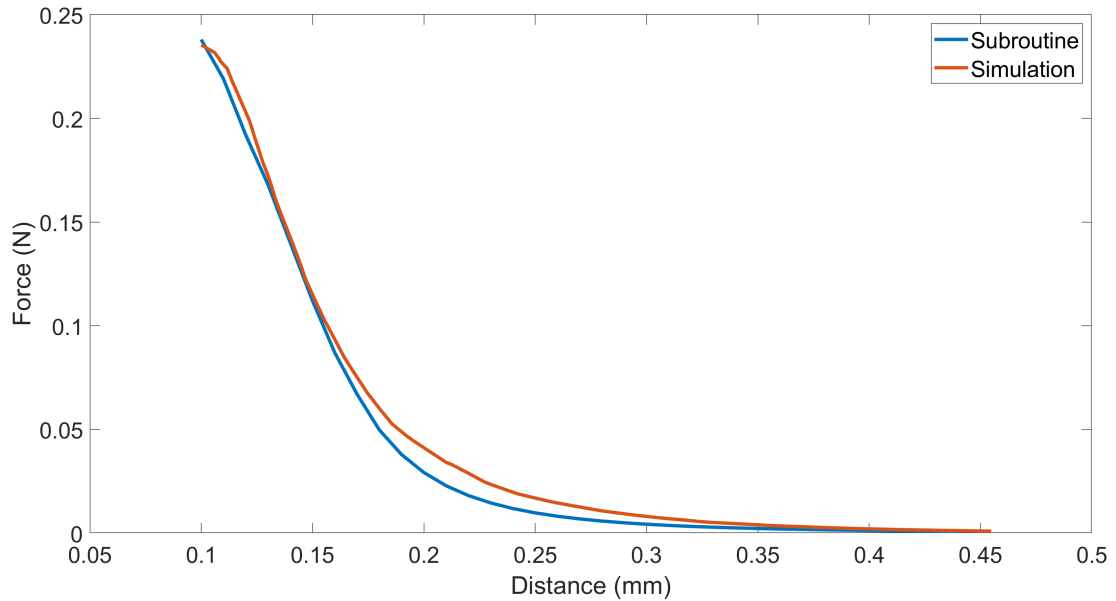
FIGURE 9.3: Comparison between the change in magnetic force between 0.1 mm and 0.45 mm separation predicted by finite element simulations (red) versus the change calculated by the VUAMP subroutine (blue).

between, and the resultant force became equivalent to the force exerted by a solenoid on a ferromagnetic cylinder within it rather than an electromagnet with an iron core.

It should be noted that Equation 8.1 and 8.2 were not used to calculate the maximum force exerted by the electromagnet but, instead, were used to determine the force at greater distances, given that at 0.1 mm distance the calculated force agreed with the results of the magnetostatic simulations.

9.2 Size of Electromagnets

The electromagnet parameters of interest were electromagnet size (radius and thickness), number of windings (N) and current (I). The size of the electromagnet was constrained at a maximum of 1 mm radius and 2 mm thickness due to the limited volume in the catheter. From this, the following electromagnet sizes (radius, thickness) were included in the investigation:

- 0.5 mm x 0.5 mm;

- 0.5 mm x 1 mm;

- 1 mm x 1 mm;

- 1 mm x 2 mm.

All electromagnet sizes paired with both the small and large ferromagnetic region sizes from the previous investigation were included in the analysis. The body current density (A/m^3) applied to the ring around the electromagnetic core that resulted in the required force on the ferromagnet was determined for each pair. The determined body current density values were multiplied by the volume of the electromagnet ring representing the windings. This resulted in a total current value, given by current on a single winding multiplied by the number of windings. The number of windings for each electromagnet size was determined by calculating the volume of a single winding, dividing the total volume of the ring by the single winding volume and rounding down to the nearest integer. To calculate the volume of a single winding, the wire radius had to be determined.

For a single electromagnet design, the surface current density (A/mm^2) for wire radii ranging from 0.01 mm to 0.45 mm was analysed to obtain the optimum wire radius. It was identified that the lower the wire radius, the lower the surface current density in Figure 9.4 (correlation coefficient (r) = 0.83, p-value < 0.001). Since the decrease in current density reduces as the wire radius is decreased, and that the wire will need to withstand a certain amount of stress as the catheter is manoeuvred through blood vessels, a wire radius of 0.1 mm was chosen.
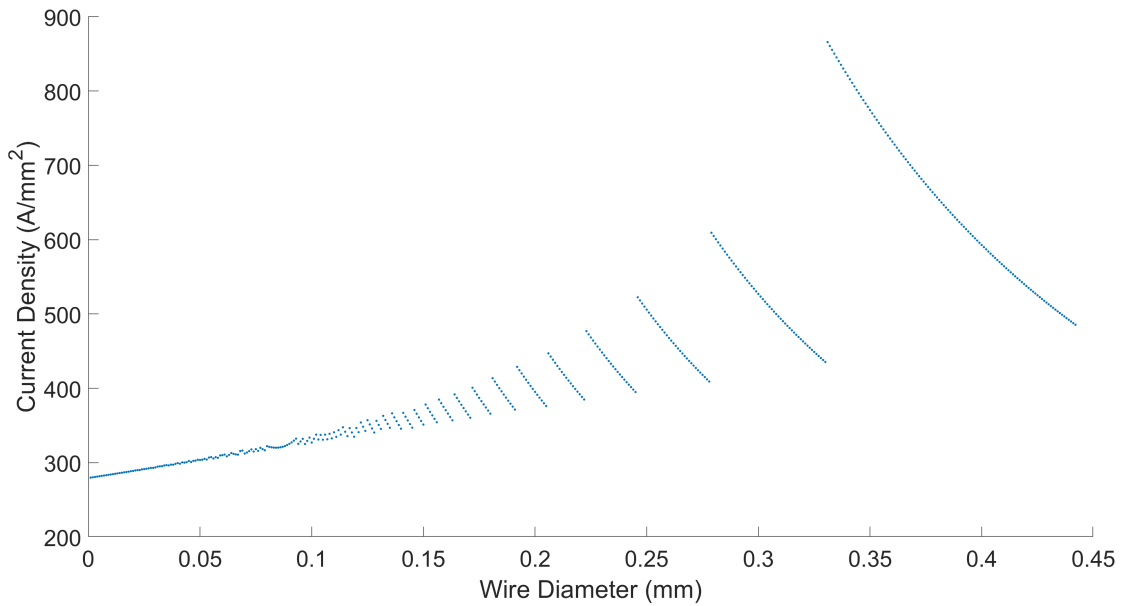
FIGURE 9.4: The relationship between wire radius and surface current density. The surface density tends to increase as wire diameter increases. The discontinuities in the curve occur when the increase in wire diameter causes a decrease in the number of windings that can fit in the given volume.

9.2.1 Core Ratio

The core to winding ratio also had an effect on the force exerted by an electromagnet. A series of magnetostatic simulations were performed to determine the core-to-winding

ratio that resulted in the highest force.

9.2.1.1 Methodology of Core Ratio

The same magnetostatic simulation setup described in section 9.1.4.1 was performed to investigate the size ratio between the ring and core of the electromagnet and its effect on the maximum pull force while keeping current density constant. The electromagnet and ferromagnet sizes were 1 mm diameter and 1 mm thickness respectively with a body current density of 2.89×10^{12} A/m^3 applied to the electromagnet ring. The ratio that resulted in the highest force was used in all electromagnet designs. Figure 9.5 shows electromagnet models with differing core-to-ring ratios that were a part of this investigation.
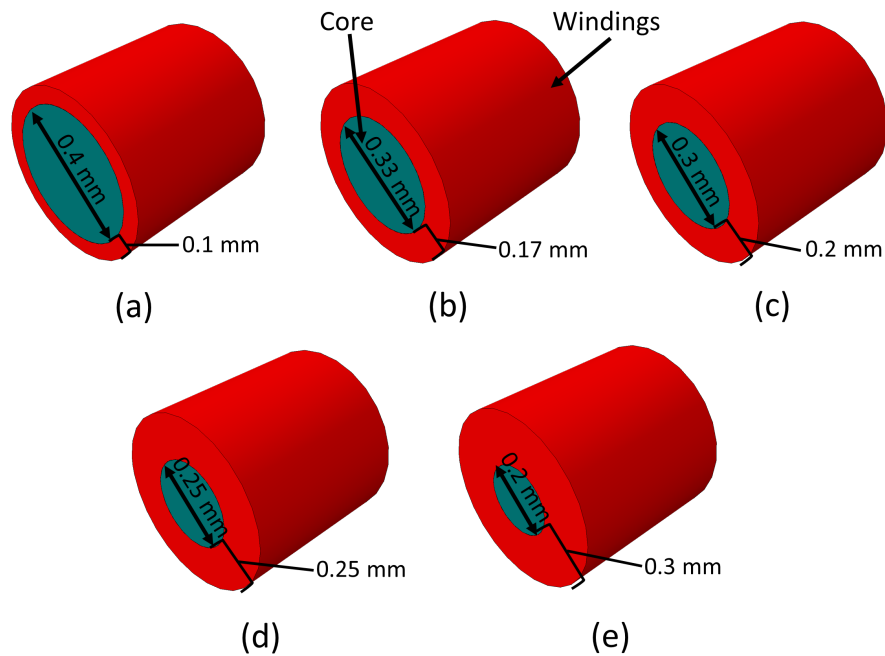
FIGURE 9.5: Electromagnets with differing core-to-ring ratios used in the magnetostatic simulations investigating the ratio that resulted in the highest force exerted on a ferromagnet. The rings are coloured in red and the cores are green. The ratios shown are (a) 0.25, (b) 0.52, (c) 0.67, (d) 1.0, (e) 1.5.

9.2.1.2 Results of Core Ratio

It was determined that a 2/3 ratio between the ring and core resulted in the maximum force exerted on the ferromagnet for a given current (Figure 9.6) and this this ratio was upheld in all electromagnet models. Figure 9.5c depicts this ratio for an electromagnet with 1 mm diameter and thickness.
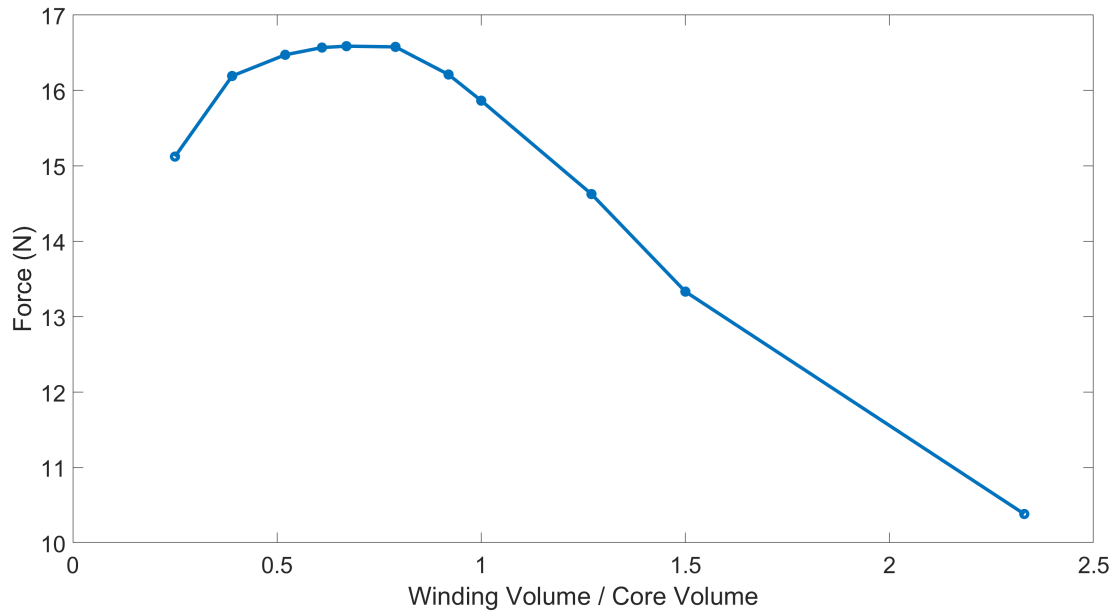
FIGURE 9.6: The relationship between exerted force and core to ring ratio for an electromagnet.

9.3 Electromagnet Current

The current and number of windings necessary to exert sufficient force was determined for each electromagnet and ferromagnet design pairing to identify the ideal electromagnet size.

9.3.1 Methodology of Electromagnet Current

The same magnetostatic simulation setup described in section 9.1.4.1 was used to determine the body current density on the electromagnet winding to achieve the required force. For each electromagnet and ferromagnet pair, several magnetostatic simulations were performed with differing body current density values until the force exerted on the ferromagnet was the required force to remove the exchangeable valve with the ferromagnetic sizes in question. This required force was either 2.57 N for the 0.5 mm ferromagnetic regions or 2.87 N for the 1 mm radius regions.

The number of windings for each electromagnet was calculated by keeping the core to wire ratio at 2/3. This allowed the calculation of the volume of the hollow cylinder that housed the wiring. The volume of a single winding of 0.1 mm was calculated and the hollow cylinder volume was divided by the winding volume to determine the number of windings for each case in Table 9.2. Figure 9.7 shows the pairs of electromagnet and ferromagnet sizes that were used in the magnetostatic simulations.
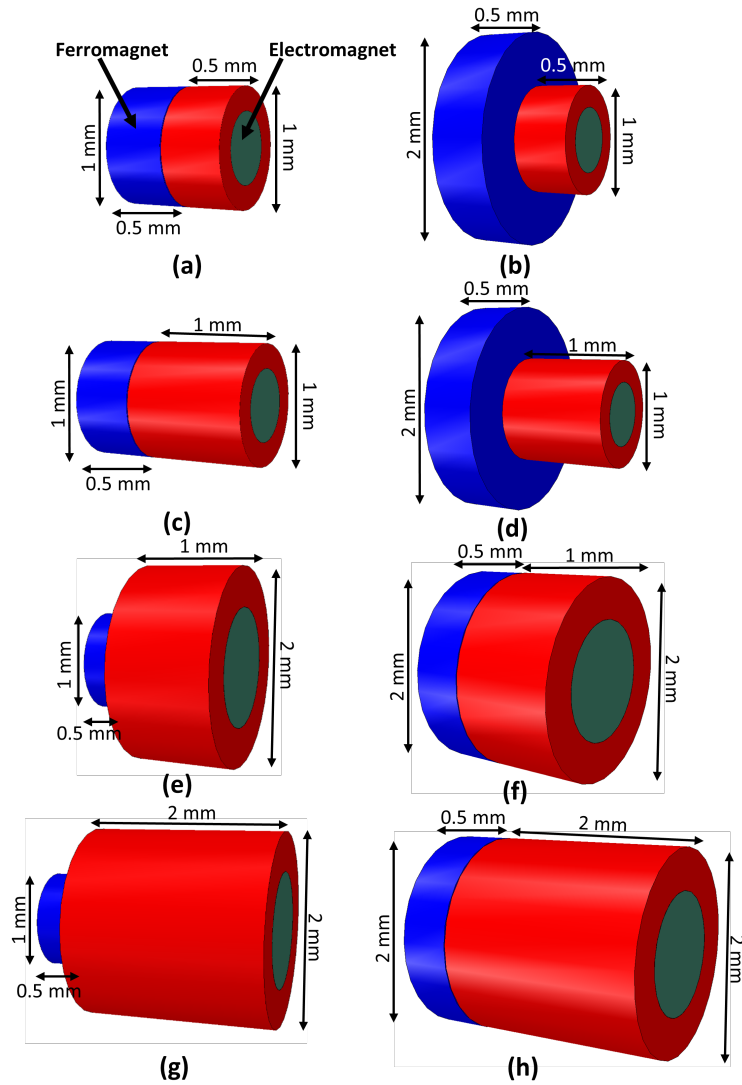
FIGURE 9.7: The electromagnet and ferromagnet pairs used in the magnetostatic simulations investigating the current required to exert the required removal force. The diameter and thickness of each pair are annotated on the image. The order of the images reflect the order in Table 9.2 which reports the results.

9.3.2 Results of Electromagnet Current

For the required force values identified for each ferromagnetic region size, the electromagnet design parameters that would exert that force on the regions were identified in Table 9.2. The lowest current requirement was for the pairing between 1 mm x 2 mm electromagnets and 1 mm x 0.5 mm ferromagnetic regions. The current requirement in this case was 2.52 A which resulted in a wire current density of 320.9 A/mm^2.

TABLE 9.2: Electromagnet parameters to exert the threshold force per electromagnet for different combinations of electromagnet and ferromagnetic region sizes. The force requirement to crimp the frame for each ferromagnetic region size is shown in parentheses next to their dimensions. The value labelled density refers to the surface current density of the wire. The minimum current value is highlighted in green.

		Ferromagnetic Region Size (Radius x Thickness) (mm)			
		0.5 x 0.5 (2.57 N)		1 x 0.5 (2.87 N)	
Electromagnet Size (Radius x Thickness) (mm)	0.5 x 0.5	Core Radius (mm)	0.3	Core Radius (mm)	0.3
		Number of Windings	14	Number of Windings	14
		Current (A)	**26.43**	Current (A)	**15.36**
		Density (A/mm^2)	3365.2	Density (A/mm^2)	1955.3
	0.5 x 1	Core Radius (mm)	0.3	Core Radius (mm)	0.3
		Number of Windings	29	Number of Windings	29
		Current (A)	**12.24**	Current (A)	**6.42**
		Density (A/mm^2)	1558.4	Density (A/mm^2)	816.6
	1 x 1	Core Radius (mm)	0.6	Core Radius (mm)	0.6
		Number of Windings	62	Number of Windings	62
		Current (A)	**14.76**	Current (A)	**4.50**
		Density (A/mm^2)	1879.3	Density (A/mm^2)	573.0
	1 x 2	Core Radius (mm)	0.6	Core Radius (mm)	0.6
		Number of Windings	125	Number of Windings	125
		Current (A)	**8.48**	Current (A)	**2.52**
		Density (A/mm^2)	1079.7	Density (A/mm^2)	320.9

9.3.3 Discussion of Electromagnet Current

To evaluate the feasibility of transmitting the required current, the fusing surface current density of copper for a wire diameter of 0.1 mm was compared with the required current density. The fusing current depends on the temperature reached in the wire. The widely used equation for calculating this fusing current is based on Preece's experiments in 1888:

$$I = a \times d^{3/2} \tag{9.5}$$

where I is the current, d is the diameter of the wire, and a is a material dependant constant which is 80.0 A/mm$^{3/2}$ for copper [186]. This equation predicts a fusing current of 2.53 A and a surface current density of 322.1 A/mm^2 for a wire diameter of 0.1 mm. In a lesser cited paper by Schwartz and James in 1905, a piecewise fit to the experimental data of copper fusing current was suggested to be a better fit [187, 188]:

$$
\begin{aligned}
I &= 52.4 \times d^{1.195} \quad d < 0.25 \ mm, \\
I &= 69.9 \times d^{1.403} \quad d > 0.25 \ mm.
\end{aligned}
\tag{9.6}
$$

This equation predicts a fusing current of 3.34 A and a surface current density of 425.8 A/mm^2 for the same wire diameter.

The electric current required for the e-TAVI catheter electromagnets was only slightly lower than the fusing currents for the diameter of copper. This showed that it was theoretically possible to transmit the required force through the electromagnets, but the current required was very close to the failure point of the copper wire. It should be noted that these estimates do not consider the sheathing of the wire or any manner of heat sink, so design improvements such as these on the copper wiring could improve the safety margin [187].

9.4   Re-sheathing

Following the analyses on the ferromagnetic regions and electromagnet sizes, the crimping and re-sheathing of the exchangeable valve frame was simulated.

9.4.1   Methodology of Re-sheathing

A tapered sheath was modelled with the proximal end to the frame at 24 mm diameter and the distal end at 8 mm. This mimicked a 24 Fr sheath as preliminary investigation showed that the frame design comprising the larger (1 mm) radius ferromagnetic regions could not fit inside a smaller (i.e. 18 Fr) sheath in its crimped shape. Following the partial crimping of the frame through the VUAMP subroutine and boundary conditions on the electromagnets, the electromagnets were moved axially, pulling the crimped frame into the tapered sheath. The sheath was modelled as a hard, rigid part. Hard contact definitions were defined between the frame and the sheath with a range of friction coefficients: 0.1, 0.2 and 0.3. The friction coefficient range was based on metal-polymer sliding experiments in the literature which reported values within that range [189–191]. The different coefficients were observed to have no effect in the success of the re-sheathing.

The re-sheathing simulations consisted of three steps: Crimp, Sheathe-1, and Sheathe-2. In the Crimp step, the electromagnets had boundary conditions of 10 mm directed radially inwards to crimp the valve frame via the VUAMP subroutine which applied a concentrated load on the ferromagnetic regions directed towards their corresponding electromagnets. In the Sheathe-1 step, the boundary condition on the electromagnets were changed to the axial direction with magnitude of 40 mm, moving the frame within the tapered sheath. This resulted in the frame completely entering the tapered sheath and moving halfway within the smaller diameter region of the sheath. Finally, in the Sheathe-2 step, the axial boundary condition had a magnitude of 10 mm and the frame was fully pulled in to the small diameter region of the sheath. This two-step sheathing

was necessary to avoid distorted elements and wave speed errors. The time increment of all steps were 4×10^{-7} s with a step duration of 0.3 s, as explained in Chapter 6. The sheathe was modelled as a 3D solid part and meshed with reduced-integration hexahedral elements (C3D8R) with a global seed size of 1 mm. The mesh for the other parts and material properties were as reported in Chapter 6.

9.4.2 Results of Re-sheathing

Figure 9.8 shows the results of the re-sheathing simulation. The re-sheathing simulation showed that the 4-pronged shape of the exchangeable valve frame following partial crimping by the electromagnets could be re-sheathed into a 24 Fr sheath, achieving a proof of concept for the removal of an e-TAVI exchangeable valve. However, the axial movement of the frame towards the sheath, or the movement of the sheath towards the frame, could not be achieved through purely magnetic attraction between the exchangeable valve frame and the removal catheter. This was due to the weak shear holding force of the electromagnets where the frame would be detached from the electromagnets and spring back into a fully deployed state as it made contact with the sheath. The full re-sheathing was achieved by defining a tie constraint between the electromagnets and ferromagnetic regions.

9.4.3 Discussion of Re-sheathing

The necessity of defining tie constraints between the electromagnets and the ferromagnets in the re-sheathing simulations indicates that a further physical mechanism to attach the frame to the removal catheter is needed to realise the e-TAVI concept. In such a scenario, the attraction between the electromagnets and ferromagnetic regions would be used to achieve alignment and coupling to said physical mechanism on the catheter. Through this physical coupling, the exchangeable valve frame would be crimped and re-sheathed. The coupling would also exert much of the force required for crimping the frame and thus a weaker magnetic attraction between the electromagnets and ferromagnets could be tolerated, decreasing the required current.

9.5 On the Generalisation of the Results

The conclusions drawn from the analyses in this chapter in terms of the current requirements and the infeasibility of the re-sheathing process with the force delivered by the electromagnets may be specific to the frame design considered. Indeed, as discussed in section 8.6, different frame designs can result in lower force requirements for removal while still achieving a sufficient COF to anchor the exchangeable valve in place. Future
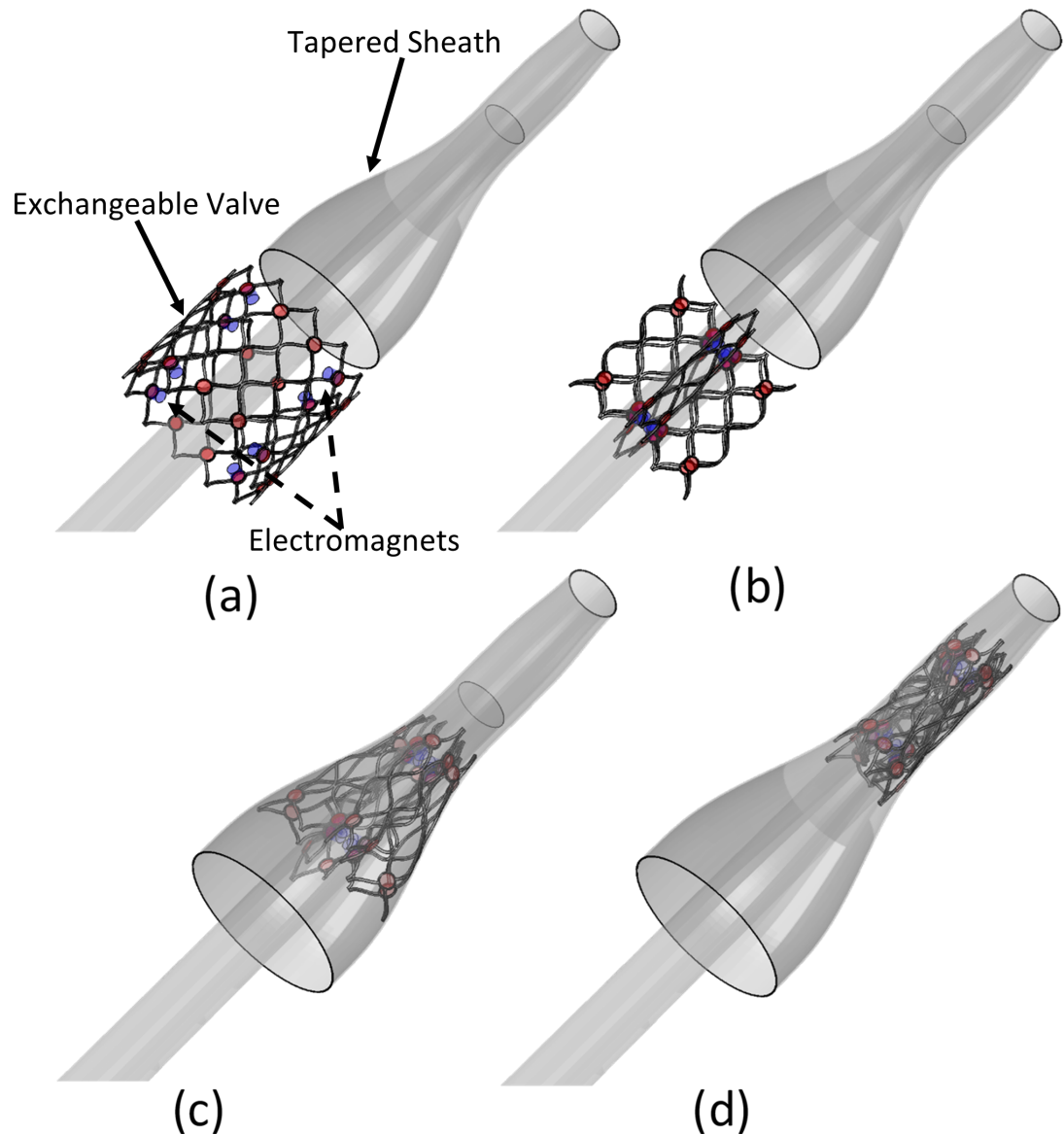
FIGURE 9.8: Series of images showing the partial crimping and re-sheathing of the 12 cell exchangeable frame, holding 1 mm x 0.5 mm ferromagnetic regions, and using 4 electromagnets per ring. (a) Initial deployed position, (b) frame crimped via electromagnets, (c) frame is pulled halfway into the sheath, and (d) frame is fully re-sheathed.

work for the development of the e-TAVI system in section 11.1 proposes updating the design of the exchangeable valve to solve the problems identified with the removal and re-sheathing of the frame designs in this thesis. Hence the conclusions drawn from the analyses in this chapter, which may be specific to the design considered, will influence the design of future prototypes. Through the testing of these new designs the results can be generalised further. The aim of this research was not to draw conclusions about the e-TAVI system that could be generalised for any and all designs imaginable, but rather investigate the feasibility of such a system, starting from a basic frame design based on existing TAVI valves, and identify paths of further development to fully achieve the

design requirements of the system.

9.6 Summary

The magnetic elements of the e-TAVI catheter was designed in this chapter in terms of the force required to remove the exchangeable valve, which was identified in the previous chapter. This was done in terms of the size and current of eight electromagnets. The re-sheathing of the exchangeable valve frame via the electromagnets was also simulated, demonstrating the removal process of e-TAVI. The main results in this chapter are listed below.

- The magnetic elements on the catheter were chosen to be electromagnets due to higher magnetic force and ability to control polarity.

- A subroutine was developed and validated to model magnetic attraction in dynamic FEA simulations.

- Magnetostatic simulations on the pairing of electromagnet and ferromagnet designs determined 1 mm x 0.5 mm ferromagnets and 1 mm x 2 mm electromagnets required the least current to achieve sufficient attraction force amongst the simulated pairings with 2.52 A.

- The current requirement for the best electromagnet and ferromagnet pairing was still too close to the fusing current of the windings.

- In the partial crimping and re-sheathing simulations of the exchangeable valve frame via electromagnets, the engagement between the catheter and the valve was not strong enough to resist the shear force during re-sheathing.

Chapter 10

Holding Member Design

This chapter describes the design and development of the holding member of the e-TAVI system. Surgical and transcatheter cases are considered and the friction needed for axial anchoring is quantified.

The two main design considerations for the holding member were:

- provide sufficient anchoring to the exchangeable valve to resist dislodging against blood flow;

- limit contact between the exchangeable valve and the aortic wall to minimise tissue growth on the exchangeable valve.

Anchoring was dependant on the chronic outward force of the exchangeable valve frame exerted on the holding member and the static friction coefficient of the holding member surface. With high enough values for both, the friction force would resist the axial force exerted on the valve during diastole. Further, the anchoring of the exchangeable valve within the holding member could be improved through the addition of magnetic regions to the holding member to attract the ferromagnetic regions on the exchangeable valve. This would ensure conformed expansion into the holding member during deployment and could allow for under-sized exchangeable valve frames where over-expansion of the frame would be achieved through magnetic attraction.

10.1   Anchoring and Friction

For a holding member design without any magnetic regions, the anchoring force depended on the radial strength of the exchangeable valve and the friction coefficient between the valve and the holding member. In this case, the exchangeable valve would

be deployed over-sized relative to the holding member to exert a non-zero radial force. The contact between the radially inward face of the holding member and the radially outward face of the exchangeable valve was important in this analysis in terms of the anchoring force. The general contact algorithm was used to model this interaction. The hard contact property was defined to model the normal forces between the two parts.

The default Coulomb friction model was used to model the friction between the holding member and the exchangeable valve. The Coulomb friction model relates the maximum allowable shear stress across an interface to the contact pressure between the bodies in contact [192]. The surfaces in contact between the bodies stick together until this maximum shear stress is reached at which point they start sliding relative to one another. This sliding movement is referred to as slipping. The value of the critical shear stress, τ_{crit}, after which slipping occurs is calculated from:

$$\tau_{crit} = \mu \cdot p \qquad (10.1)$$

where μ is the coefficient of friction and p is the contact pressure [192]. The value of the coefficient of friction was user-specified to reflect the tribological properties of the holding member. In reality, these surface properties would be set by the manufacturing process where the surface roughness of the holding member could be controlled.

The friction in the simulations was set as isotropic which allowed the slip rate, γ, to be expressed in the form:

$$\frac{\tau_i}{\tau_{eq}} = \frac{\gamma_i}{\gamma_{eq}} \qquad (10.2)$$

where τ_i is the frictional stress in the i direction, τ_{eq} is the equivalent frictional stress between the two orthogonal components of shear stress, γ_i is the slip rate in the i direction, and γ_{eq} is the magnitude of the slip velocity [193]. The penalty contact algorithm was used in ABAQUS/Explicit to model the above behaviour where relative motion between the contacting bodies in the absence of slip is equal to the friction force divided by the penalty stiffness [193].

Figure 10.1 shows the outward radial force profile of the exchangeable frame designs with varying cell height and strut width. The orange curves portraying the radial force during unloading was the variable of interest for anchoring. The maximum crimped radius was 9.75 mm, corresponding to an underexpansion of 25%, in line with commercial sizing ranges.
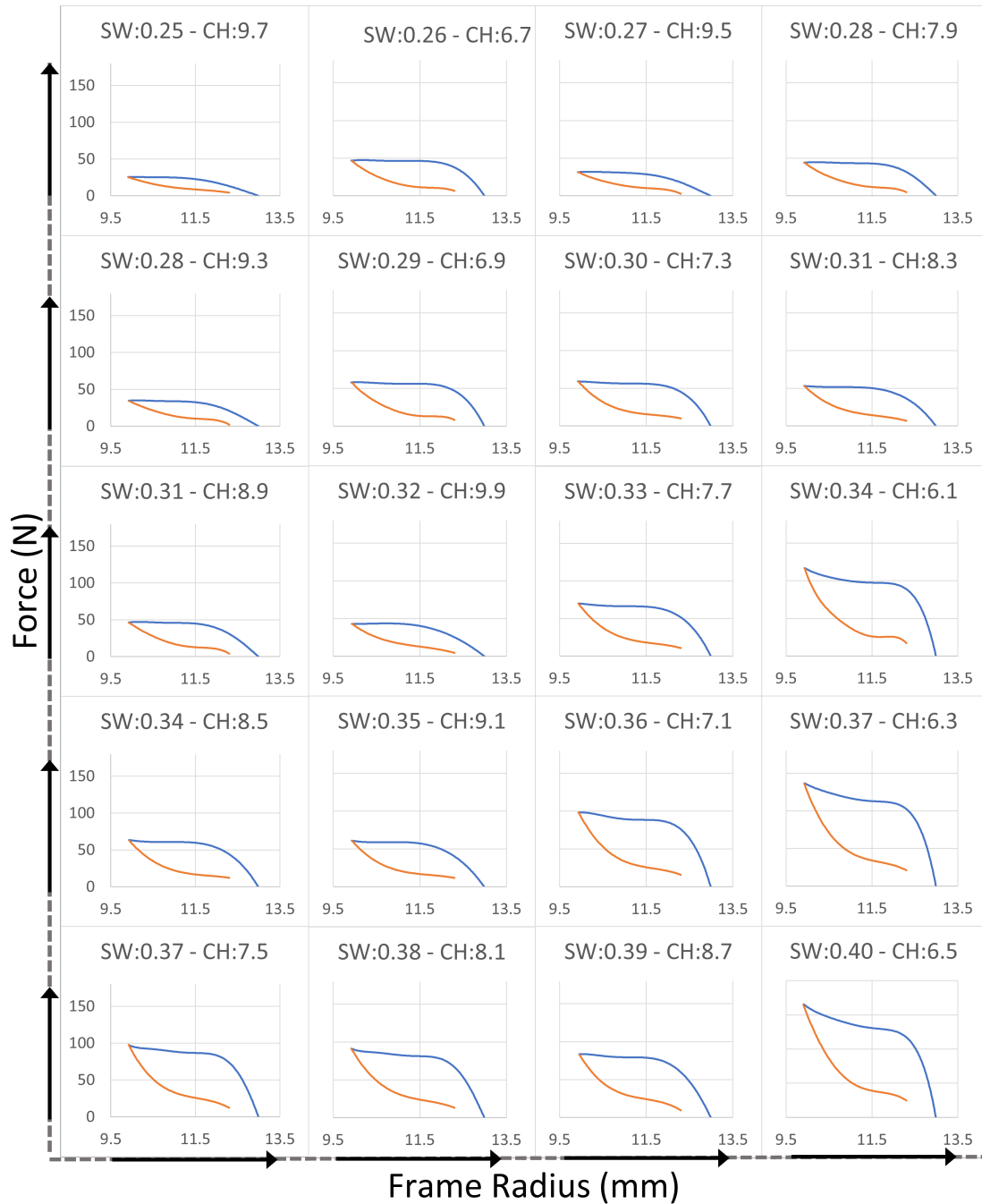
FIGURE 10.1: Radial force profiles of exchangeable valve frame designs. SW = strut width, CH = cell height. Blue curves represent the RRF and orange curves represent the COF.

The ranges of COF produced across the designs at different underexpansion amounts is summarised in Table 10.1. The pull force value describes the amount of axial force that the valve can resist before dislodging. One value that could be used for this force was the force on the valve by blood flow, which was at its maximum during diastole. This has been shown to be approximately 6 N in a normal functioning heart [19]. However, commercial TAVI valves exhibit significantly higher values of pull force, both due to a safety factor and the fact that heart valve patients may develop further hypertension

increasing the force on the valve. Consequently, the friction values of the holding member were determined such that the resulting axial anchoring was similar in magnitude to the pull force of a 26 mm CoreValve in ViV deployment at 11.5% underexpansion [194].

TABLE 10.1: Ranges for COF produced by exchangeable valve frames at 5%, 10%, and 20% underexpansion. Calculated friction values to achieve sufficient anchoring for a given COF is also shown.

	Minimum	Maximum	Pull Force	Friction
COF (5%)	2.1 N	23.7 N	11 N	0.46 - 5.24
COF (10%)	8.53 N	37.5 N	11 N	0.29 - 1.29
COF (20%)	18.2 N	94.6 N	11 N	0.12 - 0.60

As can be seen, underexpansion above 10% resulted in more realistic friction coefficient values due to the higher COF. This finding reflects the commercial valves which are recommended to be deployed at 10-20% underexpansion [195]. For the holding member, friction coefficients as low as 0.12 could be tolerated through strut width and cell height design choices and a minimum underexpansion of 20% in deployment. Conversely, friction coefficients around 0.6 would allow for less underexpansion and frames with narrower struts and higher cells.

10.2 Delivery Method

The holding member could either be implanted surgically or via a catheter. A surgical deployment would ensure precise placement of a uniformly circular holding member and remove the native valve to achieve larger EOA. Delivery via a catheter would result in a less precise and non-uniform area for subsequent exchangeable valve deployment but would remove the need for open-heart surgery in the primary e-TAVI procedure.

Both the surgical and the transcatheter holding member designs were considered. The surgical design consisted of a hollow cylinder with magnetic regions facing radially inward. Extrusions on the inner cylindrical face existed to constrain the axial movement of the exchangeable valve under blood flow. There were also suture rings connected to the cylinder that allowed for the suturing of the member to the aortic root. The transcatheter holding member could have been SE or BE but the SE case was chosen due to prior experience with strut deformation in BE frame designs. The cell shape of the SE frame design was based on the industry leader in self-expanding valves, the CoreValve series. Between certain cells (depending on the position and number of magnets) were cylindrical features to hold magnets. Figures 10.2 and 10.3 shows different designs for both holding members.

The requirement for crimpability of the transcatheter member was the defining difference in the two holding member designs. The transcatheter member had to hold significantly smaller magnetic areas for the exchangeable valve to engage. This size difference can be
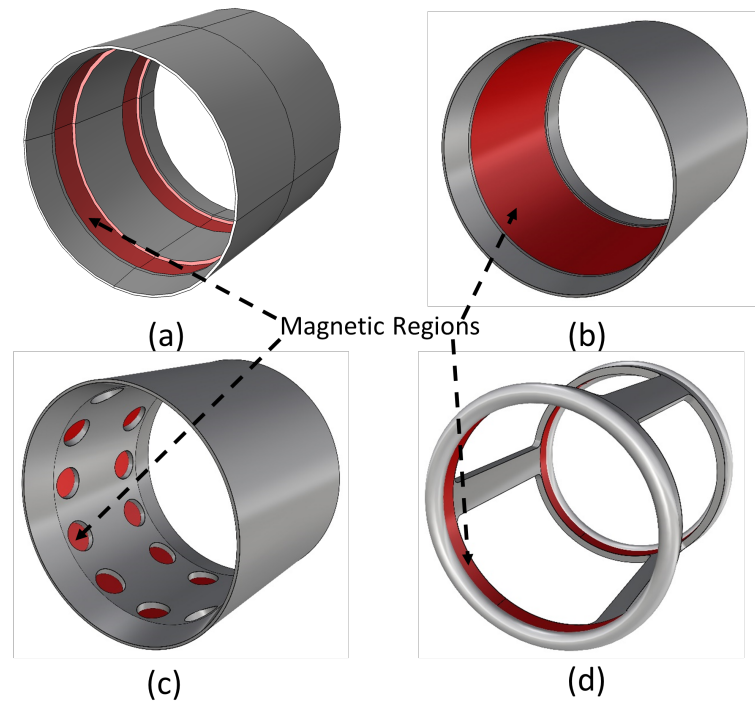
FIGURE 10.2: Different designs of the surgical magnetic holding member. (a) Two magnetic bands corresponding to each ferromagnet ring on the exchangeable valve, (b) one large magnetic band covering the entire inner surface, (c) circular magnetic regions for the ferromagnets on the exchangeable valve to fit into, (d) two magnetic bands with hollow regions across the height of the member.

seen in general when comparing the magnetic regions in Figure 10.2, highlighted in red, to the magnetic regions in Figure 10.3

Both of these designs had to satisfy the following conditions:

- the total magnetic force exerted by the holding member must be large enough to conform the exchangeable valve and anchor it in place;

- the total magnetic force exerted by the holding member must be weak enough to overcome when the exchangeable valve needs to be replaced;

- the features on the inner surface of the member must extend radially inward enough such that axial movement of the exchangeable valve is prevented.

Additionally, the transcatheter design must satisfy the following:

- the magnetic regions must be positioned and be limited in number such that the frame can still be crimped to a low enough profile for the catheter;

- the COF and RRF of the member must be high enough to not only pin the native leaflets and anchor in the aortic root but also to anchor the exchangeable valve.
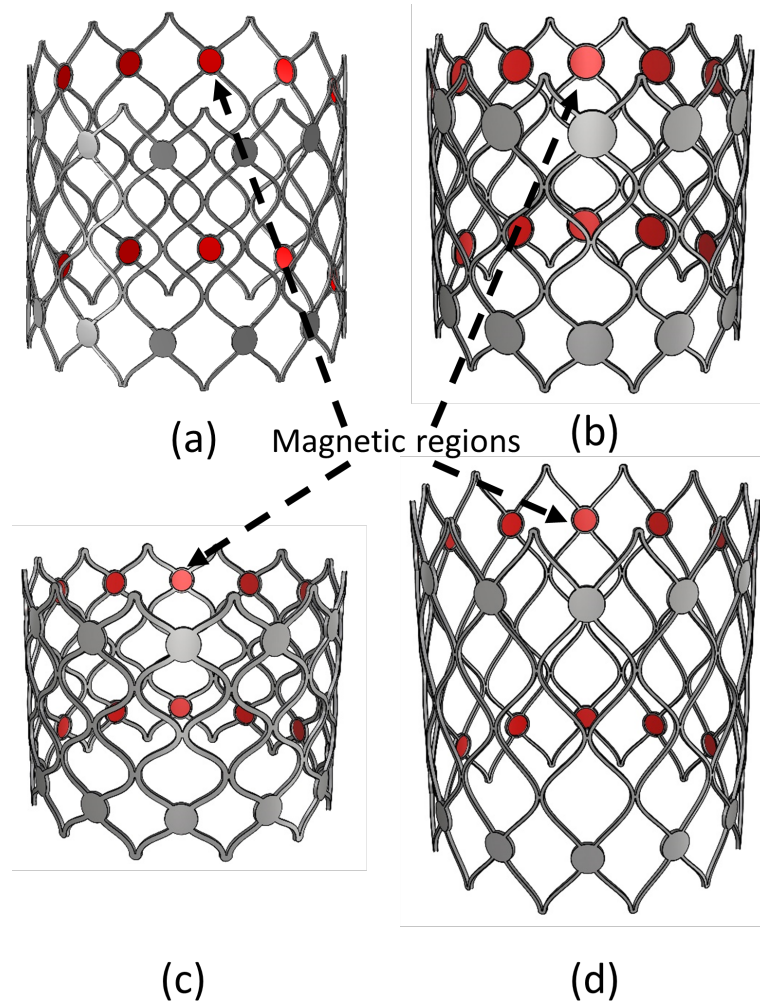
FIGURE 10.3: Different designs of the transcatheter magnetic holding member. The frame shapes in all designs reflected that of the exchangeable valve frame to cover the valve circumferentially and minimise its contact with the aortic wall. (a) Magnetic regions radius: 1 mm, strut width: 0.3 mm, cell height: 8 mm; (b) Magnetic regions radius: 1.5 mm, strut width: 0.3 mm, cell height: 8 mm; (c) Magnetic regions radius: 1 mm, strut width: 0.4 mm, cell height: 6.5 mm; (d) Magnetic regions radius: 1 mm, strut width: 0.25 mm, cell height: 9.5 mm.

10.3 Deployment into the Holding Member Designs

The deployment and engagement of the exchangeable valve frame to both the surgical and transcatheter holding members using the magnetism subroutine was simulated to assess anchoring performance.

10.3.1 Methodology of Deployment into the Holding Members

In the assembly, the exchangeable valve frame was placed axially above the holding member. There were five steps in the simulation: Crimp, Move, Unsheathe, Relax and Pull. The simulation steps are depicted in Figure 10.4. The outer surface of the holding

member had an encastre boundary condition over all steps. The target time increment in each step was 4×10^{-7} s and the step duration was 0.3 s.

Step 1 (Crimp): Radially inward displacement boundary condition on the cylinder to crimp the exchangeable valve.

Step 2 (Move): Axial displacement boundary condition on the cylinder and frame to move the crimped frame into the holding member.

Step 3 (Unsheathe): Axial displacement boundary condition on the cylinder while constraining twelve nodes on the middle of the frame to move only in radial direction to deploy the exchangeable valve.

Step 4 (Relax): The boundary condition on the twelve nodes of the frame is deactivated to allow the frame to fully expand.

Step 5 (Pull): A concentrated load increasing up to 25 N is applied on all nodes on the exchangeable valve frame in the axial direction.

FIGURE 10.4: Flowchart of the exchangeable valve deployment into the holding member simulations. The five steps are described in order. The holding member model is the surgical version but the same steps applied for the transcatheter holding member simulations as well. The boundary conditions are portrayed with orange arrows. The concentrated load applied in the final step is shown with a light blue arrow. The constrained nodes on the exchangeable valve frame are shown in red.

1. In the Crimp step, the cylinder had a radially inward displacement boundary condition of 10 mm to crimp the exchangeable frame.

2. In the Move step, this boundary condition became an axial displacement of 32 mm to move the crimped cylinder inside the holding member. The same axial displacement condition was also put on twelve nodes between each cell around the middle of the exchangeable frame.

3. In the Unsheathe step, the three nodes were constrained in the axial direction and the cylinder was moved axially (40 mm) to unsheathe the frame.

4. In the Relax step, the boundary condition on the frame was deactivated.

5. In the final Pull step, a ramping load up to 25 N was applied on the exchangeable frame in the axial direction.

Both the surgical and transcatheter holding members were meshed with C3D8R elements with a target global seed size of 0.5 mm and 0.1 mm respectively. The transcatheter holding member was assigned the Nitinol material definition and the ferromagnets were modelled as N52 neodymium, as described in Chapter 6. The entirety of the surgical holding member was modelled as a neodymium magnet with the parameters stated in Chapter 6.

Hard, frictionless contact was defined between the crimping cylinder and the exhcangeable valve frame including the ferromagnets. Contact was not defined between the cylinder and the holding member. Contact was also defined between the holding member and the exchangeable valve frame including the ferromagnets. The interaction properties for this contact were hard contact with a friction coefficient of 0.1. The details of the friction model used was described in section 9.1.

The VUAMP subroutine was defined through the generation of user amplitudes. For each magnet in the simulation, three amplitudes were defined representing the three coordinate directions. Each of these amplitudes were then used in the generation of three concentrated forces on each magnet, each of those three being a unit vector towards x, y or z. The VUAMP subroutine also needed the position information of all magnets and all targets for magnets on the holding member. This was done through defining three history output requests for a single node on all magnets and their corresponding targets. The current (I) multiplied by the number of windings (N) in the electromagnetic subroutine equation was replaced by the magnetic remanence (B_r) of a permanent magnet. The target regions within the VUAMP subroutine were defined as nodes on the ferromagnetic regions of the transcatheter holding member facing ferromagnets on the exchangeable valve, and nodes on the magnetic band sections of the surgical holding member facing ferromagnets.

In initial simulations, the expanded diameter of the exchangeable valve frame was the same as the inner diameter of the holding members. This did not exhibit an interesting result as the frames expanded perfectly into the holding members and the effect of the magnetic attraction could not be determined. Following this, the diameter of the exchangeable frame was set to be undersized by 2 mm. In this case the COF of the frame was irrelevant to the anchoring.
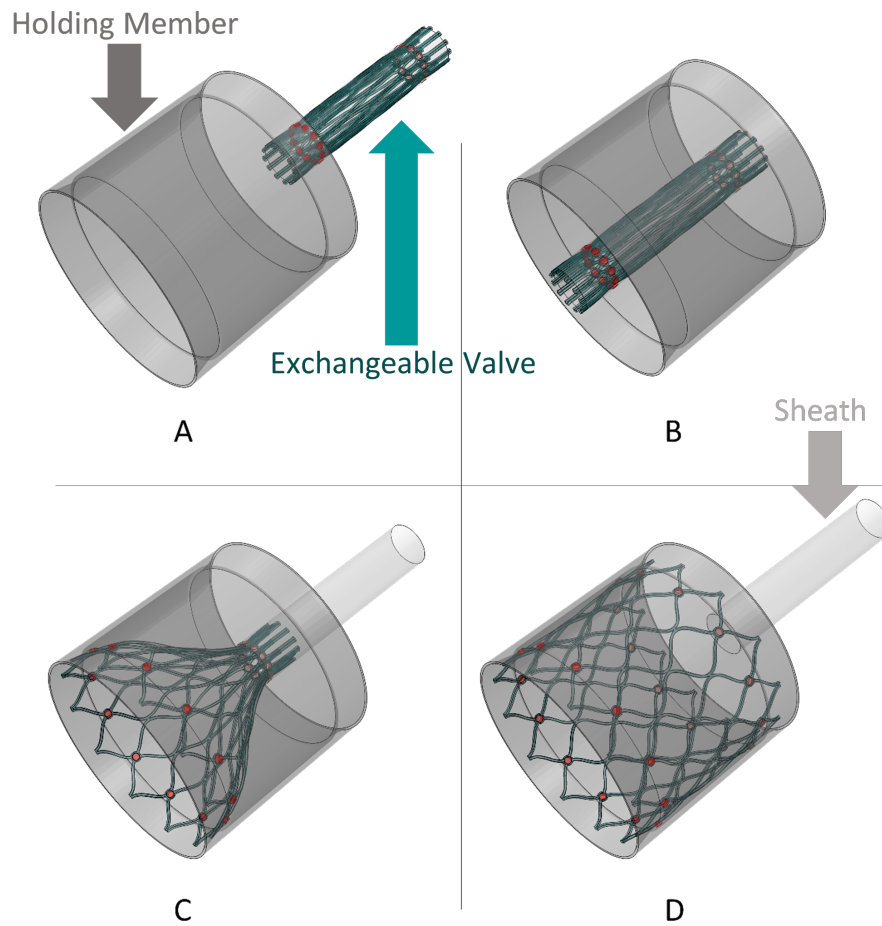
FIGURE 10.5: Steps of the deployment of an exchangeable valve frame into the surgical holding member.

10.3.2 Results of Deployment into the Holding Members

Figures 10.5 and 10.6 show the result of the deployment when the magnetic strength of the holding member regions was equivalent to 2 mm diameter magnets. In this case correct deployment was achieved and the exchangeable valve was mated fully to the holding member. The magnetic strength was able to over-expand the exchangeable valve. Contrary to this, the ends of the exchangeable valve frame moved radially inward. This was because the half-cells above both rings of ferromagnetic regions landed on top of the extrusions on the holding member. Decreasing the thickness of these extrusions

in accordance with the results of the axial magnetic mating strength investigation can remedy this movement. The resistance to axial force in this case was 13 N.

(a) (b)
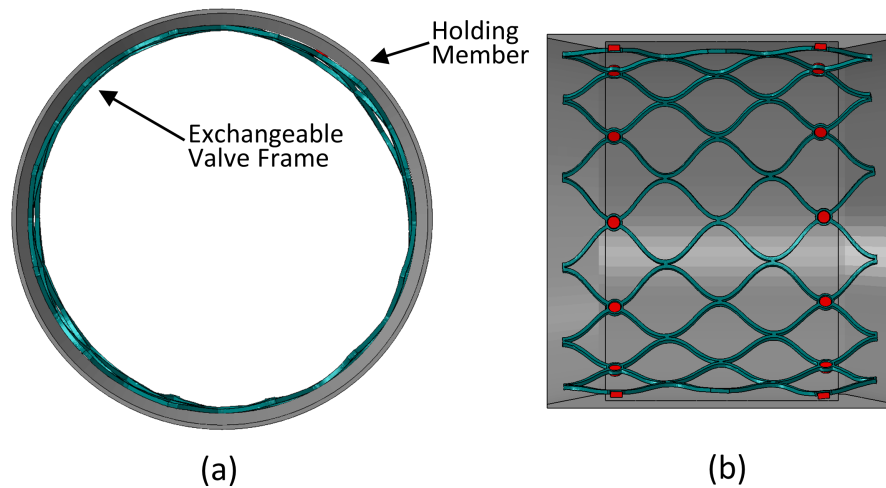
FIGURE 10.6: (a) Axial and (b) side view of the under-sized exchangeable valve frame after deployment into the surgical holding member.

Different from the surgical case, Figures 10.7 and 10.8 show some struts of the exchangeable valve frame stuck within the cells of the transcatheter holding member. This happened as the exchangeable frame was unsheathed where the end uncovered first expanded to a diameter close to that of the holding member. The ends of these expanding cells pushed out through the holding member's cells and got stuck, even as the frame was fully unsheathed and some recoil was experienced. The presence of an aortic root around the holding member - alongside fabric covering and/or skirts mounted to the member - would decrease the likelihood of this happening as the expanding cells would not be pushed too far through the cells of the holding member. However, the nature of the magnet subroutine also affected this where the components of the magnetic force on each ferromagnet was calculated separately, as described in Chapter 9. This caused scenarios where some ferromagnetic regions on the exchangeable valve moved radially outward from the holding member during unsheathing and then encountered a large magnetic force sticking them in place, dominated by a single coordinate component.

Although proper mating was mostly achieved, there were still gaps visible between the members in Figure 10.8 which showed that not all ferromagnets on the exchangeable valve had settled into the appropriate holes on the holding member. This was caused by two main reasons. The first was the independent calculation of magnetic force for each coordinate axis. When a ferromagnet got close to its target in any of the global axes, the magnetic force in that axis became large enough to mate the ferromagnet in that position even if the other axes were not aligned. The second was that the target areas were only slightly larger than the ferromagnetic regions on the exchangeable valve frame and hence they were just less likely to hit the target. The resistance to axial force in this case was 10 N.
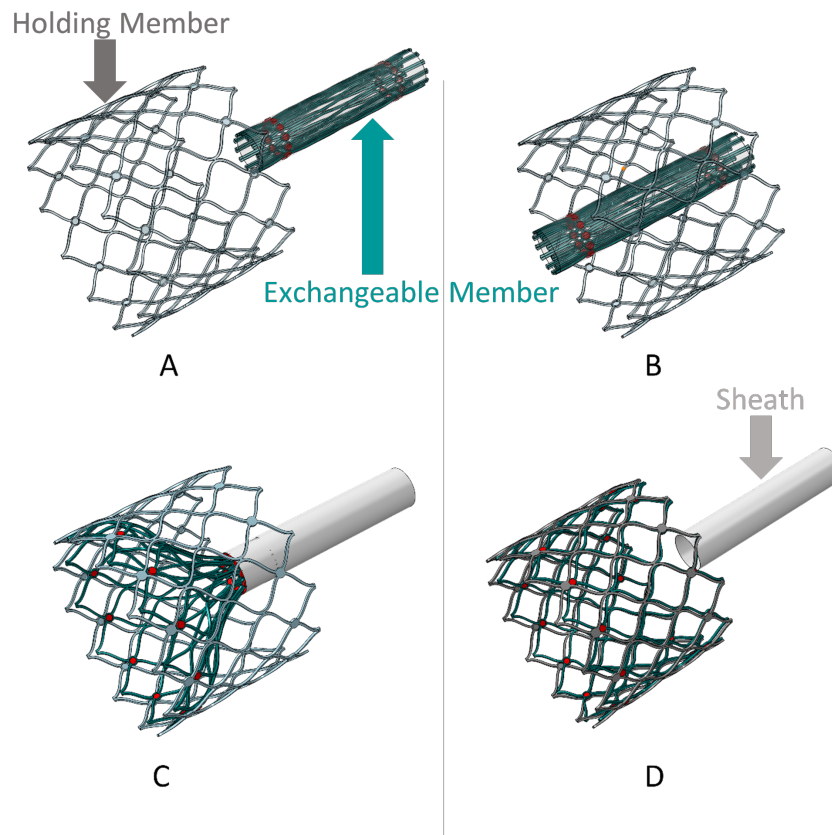
FIGURE 10.7: Perspective view of the undersized exchangeable valve frame after deployment into the transcatheter holding member.

10.3.3 Discussion of Deployment into the Holding Members

As a result, undersizing of the exchangeable valve could be used to make the removal process easier. If the removal catheter could exert enough force to overcome the magnetic attraction of the holding member, the exchangeable valve would collapse back from its over-expanded position, reducing its diametric profile. The removed valve could then be moved out from inside the holding member more easily and quickly, allowing the deployment of a new valve. The further crimping and re-sheathing of the removed valve could then be achieved without a time constraint caused by pacing.

10.3.3.1 Limitations

Complex interactions between the heart valve prosthetic and the biological environment in the aorta have not been accounted for in this thesis. The main body of work was focused on the mechanical properties of the e-TAVI components and their effect on the deployment and removal of the exchangeable valve frame minimally invasively. In the future development of the e-TAVI system, the interactions occurring at the blood/material and tissue/material interface of the implanted components (i.e. the holding member
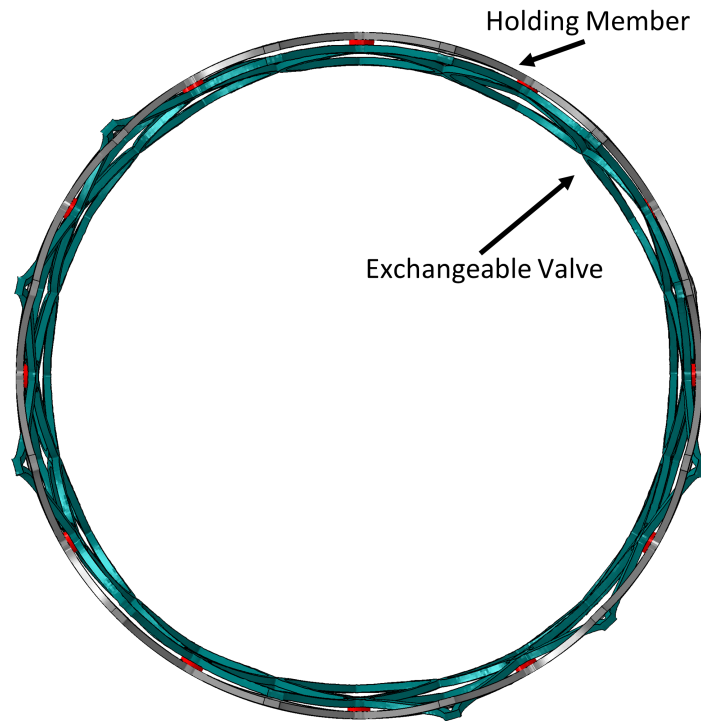
FIGURE 10.8: Axial view of the under-sized exchangeable valve frame after deployment into the transcatheter holding member.

and the exchangeable valve) should be considered as these can effect the clinical efficacy of the device. Depending on the chemical composition, electrical charge, surface texture, elastic modulus, and porosity of the prosthetic, responses such as the deposition of plasma proteins, platelets, leukocytes, monocytes and the migration of endothelial and smooth muscle cells can occur [196]. These responses can then affect further changes to the behaviour of the entities in these interactions. These tissue reactions regulate thrombogenecity [196]. Further to these, reactions between biomolecules in the aortic wall and the prosthetic surface can lead to temporary or permanent bond formations which can be weak (van der Waals or hydrogen bonds) or strong (ionic or covalent) [197]. These bonds mostly form due to hydration and protein layers which cover the inorganic prosthesis material in a biological environment where cells interact with these layers [197]. Consequently, the microscopic bond formations can have an effect on the macro scale where the anchoring between the components of the e-TAVI system can be affected.

10.4   Summary

This chapter detailed the investigations into the holding member of the e-TAVI system in terms of the anchoring it must provide to the exchangeable valve, based on the COF magnitudes of different frame designs identified in Chapter 8. Although a range of

friction coefficients was identified to successfully anchor the exchangeable valve, a holding member that would provide this friction coefficient was not explicitly designed. The possibility of adding radially-inward-facing, magnetic regions on the holding member was also discussed but an optimum design with or without these magnets was not identified due to the need of an additional, physical mating mechanism between the catheter and the exchangeable valve for removal. Through this addition, the COF of the exchangeable member could be greatly increased, changing the design requirements on the holding member. Other main points from this chapter are listed below.

- The required friction coefficient of the holding member was a function of the COF of the exchangeable valve.

- Below 10% underexpansion, a friction coefficient between 0.12 - 1.29 was needed to resist 11 N of axial force, for all exchangeable valve designs.

- The holding member could be delivered surgically or via a catheter.

- Anchoring of an undersized exchangeable valve was possible through addition of magnetic elements on the holding member.

Chapter 11

Future Potential of e-TAVI

This chapter combines the results from the previous three chapters to asses the development of the e-TAVI system as a whole.

The main aim of the e-TAVI system was to provide an alternative to the current state-of-the-art in redo valve replacements through allowing the removal of a dysfunctional heart valve. This was achieved through the development of the magnetic exchangeable valve and the e-TAVI catheter. The feasibility of achieving a reduction in diameter of a deployed valve frame via a catheter using magnetic attraction was shown in this thesis. The most exciting result in the removal of this exchangeable valve was the identification of the advantageous trade-off between the COF of the frame and the required removal force in terms of the strut width and cell height of the device. It was identified that the cell height of the frame greatly influenced the COF but only minimally changed the force required to crimp the frame. For the frame designs in this thesis, frames with cell height values below 8 mm exhibited higher COF compared to the total force required to decrease their diameter.

The final design of the e-TAVI system is shown in Figure 11.1. The exchangeable valve frame had a strut width of 0.37 mm and cell height of 6.3 mm which was the design that had the largest difference between the force required to remove and its COF at 14.79 N. The sizes of the ferromagnetic regions and the electromagnets reflect the results of the analysis in Chapter 9 with 1 mm radius and 2 mm thickness electromagnets facing 1 mm radius and 0.5 mm thickness ferromagnets. The holding member did not contain any magnetic elements for engagement with the exchangeable valve but its radially inner surface must have a friction coefficient larger than 0.32 to anchor the exchangeable valve up to 11 N of axial force as the COF produced by the exchangeable valve frame was 33.6 N at 10% underexpansion.

The e-TAVI system presents an exciting prospect for minimally invasive redo valve replacements, the need for which is continuously increasing. Indeed, throughout the
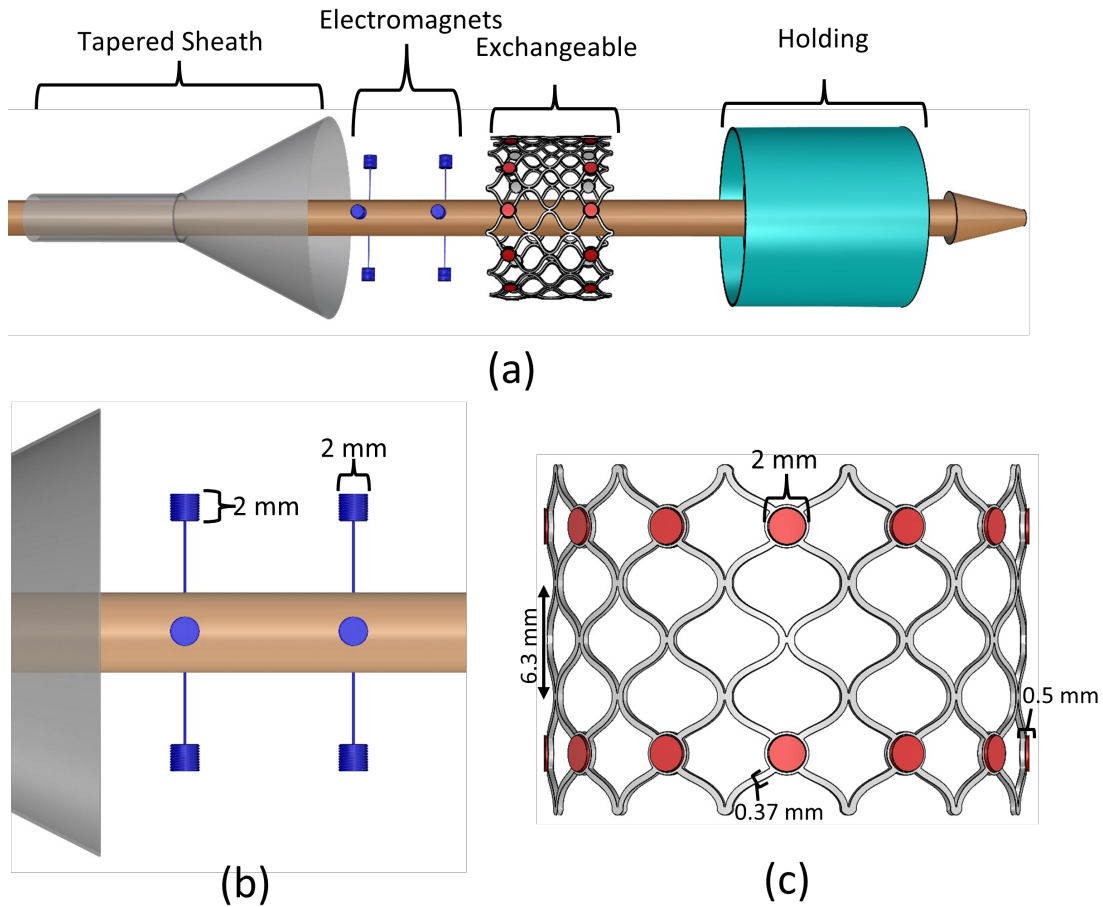
FIGURE 11.1: The components of the final e-TAVI system design showing: (a) the entire system including the catheter, exchangeable valve and the holding member; (b) close up view of the electromagnets; (c) close up view of the exchangeable valve. The size parameters determined in this thesis is annotated on the images, namely the electromagnet and ferromagnet sizes with the strut width and cell height of the exchangeable valve.

duration of this PhD research, many new articles and presentations were published regarding the future issues facing valvular heart disease treatment with the increased use of bioprosthetic valves in younger patients. The lack of studies regarding the long-term durability of TAVI valves was a common problem identified in these articles with most concluding that early and midterm durability being comparable to that of SAVR valves. There is consensus in the literature that there will be an increase in the number of redo valve replacements in the coming years. [198–203]

The durability of prostheses implanted via ViV and TAV-in-TAV operations is another common topic of discussion with even fewer long term studies assessing their function. The fact that these procedures have been performed on older, higher risk patient to date, is a confounding factor in these studies, where there is evidence of higher SVD of bioprosthetic valves in younger patients. The main issue with ViV and TAV-in-TAV is identified as patient-prothesis mismatch, exhibited through a low EOA and high post-operative, transvalvular gradients.[121, 200, 202, 204, 205]

With the identification of these problems, there is great focus on the lifetime treatment pathway of valvular heart disease. Relating mostly to younger patients, this puts great importance on valve choice for the first valve replacement since this determines the available choices to the patient if this replacement dysfunctions within their lifetime [199, 205, 206]. Some authors suggest TAVI implantation for patients aged 40 - 60, who could then under go SAVR aged 60 - 80 with the explantation of the TAVI valve, and then receive ViV aged 80 - 100 [200]. While this seems feasible, it assumes that a VHD patient aged 40 - 60 would be at a low enough risk of open-heart surgery above the age of 60. Conversely, receiving a SAVR valve at the age of 40 - 60 with the expectation of ViV at 60 - 80 and subsequent TAV-in-TAV above 80 would require a large enough aortic annulus area to avoid patient-prothesis mismatch with three concentric prostheses. Hence, the current suggestions include case by case assessment of patients and even allowing the patient to choose which pathway they prefer [140, 201, 207].

Through the removal of the dysfunctional exchangeable valve, the e-TAVI system provides a solution to this patient pathway conundrum where effectively a dysfunctional valve is removed without the need for open heart surgery. Providing the best of both worlds, the e-TAVI system removes the need for open-heart surgery for redo operations while retaining a clinically satisfactory EOA and preventing patient-prothesis mismatch. This exciting and novel method could be the answer to the potential redo valve replacement pandemic predicted by many professionals in literature.

Although the e-TAVI system was successfully designed and developed in this PhD research, there remains challenges and need for further development of its components.

11.1 Frame Design for Removal

The exchangeable valve frames in this thesis were based on commercial SE valves rather than being developed to achieve the maximum difference between COF and the force required to remove. However, having identified the feasibility of crimping and removing a valve frame via discrete force-points around its circumference, a very exciting path of future development lies in the complete re-design of the frame with consideration to the method of removal. The Acurate Neo valve frame is a great example of a drastically different frame design to other commercial valves while retaining clinically satisfactory function. Variable cell sizes across the exchangeable valve frame could allow for the ferromagnetic regions on the frame to be positioned in such geometries that the force required to achieve enough reduction in diameter to sheathe the valve is lower than the values in this thesis, while still achieving a similar COF. Also, as previously discussed in Chapter 8, the Nitinol material properties had a significant effect on the results of the simulation. Thus, different Nitinol compositions could be investigated to achieve increased COF for a given design.

11.2   Physical and Magnetic Mating

The re-sheathing investigation concluded the need for a physical mating between the catheter and the exchangeable valve frame, at the very least in the axial direction. This was because the magnetic attraction, between the ferromagnets on the frame and electromagnets on the catheter, was weaker against shear force. Dedicated exchangeable valve frame designs for removal could reduce the force requirement on the magnetic elements of the catheter, even allowing for permanent magnets rather than electromagnets, but this would not provide an improvement to the axial mating during re-sheathing. Hence, a physical mating between the catheter and the exchangeable frame has to be designed. This could allow for the complete removal of any magnetic regions on the e-TAVI components, but the alignment and engagement of any physical mating mechanism will be difficult *in vivo*, as seen in this thesis for the slotting exchange concept. Consequently, the addition of physical mating that is aligned and engaged through magnetic attraction is a feasible solution. This addition would change the force requirement of magnetic attraction from being able to achieve a reduction in frame diameter to being able to achieve physical mating between the catheter and the frame. Through this, smaller ferromagnets on the exchangeable valve, and smaller electromagnets on the catheter could be tolerated. Making these features smaller reduces both the removal force on the frame and allows for a smaller profile of catheter. Further, the method of attaching these ferromagnetic regions to the frame must be determined. This could be through welding after manufacture, a biocompatible bonding agent, or skirts encompassing the ferromagnets.

11.3   Minimising Tissue Growth

The holding member was initially designed to provide anchoring to an exchangeable valve that did not have sufficient chronic outward force. The reason for this was to achieve an exchangeable valve that was easy to reduce in diameter due to its lower radial strength. However, the identification of the four-pronged crimp profile and its lower removal force requirement compared to the COF removed the need for anchoring. This could have resulted in the complete removal of the holding member from the e-TAVI system, except for the issue of tissue growth around the exchangeable valve. For all commercial TAVI valves, whether BE or SE, tissue growth around the valve is advantageous for increased anchoring strength and reduction of paravalvular leakage. Figure 11.2 shows explanted valves and the tissue buildup around them.

For the e-TAVI system, however, tissue growth around the exchangeable valve had to be minimised to allow for the eventual removal of the valve without damaging the aortic wall. This could theoretically be accomplished without a holding member. One method would be to have an outer skirt on the entirety of the exchangeable valve frame to minimise contact between the frame struts and aortic wall. The main problem with
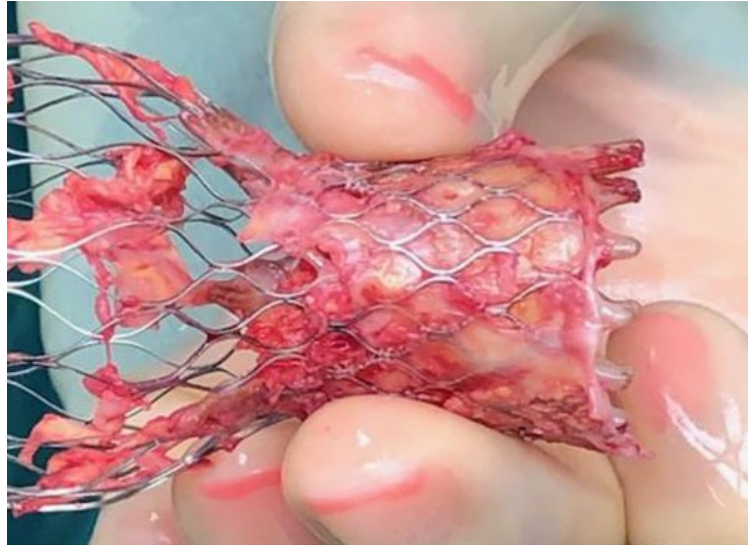
FIGURE 11.2: Explanted CoreValve Evolut device demonstrating the tissue growth around the frame [208].

this would be access to the coronaries where current commercial valves hold larger cells and no skirt to maintain this access. If the height of the frame was lower than the distance between the left ventricular outflow track (LVOT) and the coronary ostia, this outer skirt could be a solution. This distance, however, is approximately 15 mm with great variance amongst the population, particularly between women and men [209]. All current commercial valves are much higher than this value, as shown previously in Table 3.17. Further, the variance between patients makes a set height that would definitely leave the ostia uncovered in all patients unfeasible to determine. Consequently, a holding member that will minimise tissue contact while allowing coronary access is necessary. The height of the holding member must also be limited to fit between the LVOT and coronary ostia. Hence, there will be portions of the exchangeable valve that, when deployed, protrude above and below the holding member. The contact with the aortic wall for these regions would be minimised if the exchangeable valve frame retained a constant diameter across its height after deployment, since the aortic root diameter increases in the supraannular regions containing the coronary ostia. This way, the height of the exchangeable valve frame could be comparable to the commercial valves while still minimising tissue contact.

11.4 Axial Anchoring

With the positioning of the holding member between the exchangeable valve and the aortic wall, the COF of the valve is exerted on the inner surface of the holding member. In the absence of tissue growth over the exchangeable valve, the axial anchoring of the frame is purely dependant on the friction force between the two components. The range of friction coefficients that would result in sufficient axial anchoring for the exchangeable

valve frame designs in this thesis were identified in Chapter 10. These values assume that the entire outer surface of the exchangeable valve is in contact with the holding member. In practice, this contact surface area will depend on the height of the holding member since it will need to be shorter than the exchangeable valve. The friction coefficient of the inner surface of the holding member must be maximised to tolerate as low COF of the exchangeable valve as possible to decrease the removal force requirement. The contact area between the two components must also be maximised, through maximising the height of the holding member. Due to the variability of the distance between LVOT and the coronary ostia, a holding member that could be shortened in accordance with patient-specific aortic geometry would be ideal. This could be achieved by a fabric such as the ones used in SAVR valves for suturing. In this case, the length of fabric sutured around the aortic root could be measured to fit the patient's aortic root geometry during the first surgical implantation of the e-TAVI valve. The fabric would conform to the natural shape of the aortic root in this instance, which could result in a non-circular deployment area for the exchangeable valve, resulting in different COF values after deployment for the same frame across its height. An alternative would be to have a more rigid holding member, possibly made from a polymer, that could produce a perfectly cylindrical deployment area. While this would be advantageous for the predictable deployment of the exchangeable valve, the holding member would need to be thicker to retain the required rigidity. This would result in the decrease of the EOA of the valve, increasing the transvalvular pressure drop.

11.5   Simultaneous Removal and Deployment

A very important aspect of the e-TAVI system is the time between the removal of an exchangeable valve and the deployment of a new one. Effectively, the patient is without an aortic valve in this duration and cannot survive for long. In fact, the recommend pacing duration where the patient's aortic valve is kept open by fluttering the heart is 30 seconds during TAVI [43]. This gives the e-TAVI procedure 30 seconds to:

1. reduce the diameter of the dysfunctional exchangeable valve;

2. move it completely out of the holding member and;

3. deploy a new exchangeable valve.

The reduction in diameter of the exchangeable valve firstly requires the engagement of the catheter to the valve. An important consideration in this is whether the dysfunctional valve can continue its function after this engagement. Depending on the placement of the engagement points on the exchangeable valve frame relative to the position of the leaflets, and the size of the removal features (e.g. electromagnets) on the catheter the valve may

continue to function. For example, consider ferromagnetic regions that are placed at far ends of the exchangeable valve. The catheter can then be pushed through the leaflets such that the engagement points at either end is aligned with the removal features on the catheter. With small enough removal features, these can then move radially outward and "grab" the exchangeable valve without interfering with the opening and closing of the leaflets. This would allow the interventionist to assess whether the mating is secure enough to achieve diameter reduction without a time constraint. Unfortunately, this is very unlikely due to the difficulty in achieving diameter reduction of the frame by exerting force at the extreme ends of the device, as portrayed in Figure 8.10. The other option is to ensure that the engagement between the catheter and the exchangeable valve is securely achieved 100% of the time. For a mating mechanism consisting of both physical and magnetic elements, this would most likely require a big safety margin in mating strength. The magnetic force required to engage the physical mating would need to be higher than the minimum force required. Similarly, the strength of the physical mating must be higher than the required removal force of the valve. The design of such a reliable, accurate and precise mating system represents the biggest challenge for the e-TAVI system moving forward.

Once the reduction in exchangeable valve diameter is achieved, the catheter must translate its removal features - along with the dysfunctional valve - in the direction of the arching aorta to move out of the holding member and leave space for the deployment of a new valve. This movement represents an opportunity where, simultaneously, the new exchangeable valve could be moved out of its sheath by the same motion, effectively deploying the new valve. Such a mechanism would combine the steps 2 & 3 that must occur within the pacing window, saving valuable time.

11.6   Tapered Sheath

The sheathe to receive and fully crimp a dysfunctional exchangeable valve was modelled as a rigid cone in this thesis. The implication of this is that the sheathe material must be stiff enough to collapse the Nitinol frame down to the catheter diameter (24 Fr, in the case of current designs). The tapering of the sheath must also be controllable such that it can be closed down to fully encompass the removed valve and move it out of the body without damaging the vessel of access. The design of such a sheath and its control mechanism is another future challenge of the e-TAVI system. Existing technologies such as retrievable vena cava filters and emboli protection devices indicate the possibility of such a controllable sheath, usually through the use of Nitinol struts forming an umbrella-like device [210, 211].

11.7   Additional Simulations

The simulations in this thesis focused on the mechanical aspects of the e-TAVI system. The crimping, expansion, anchoring, and removal of the exchangeable valve mostly depend on the frame of the valve in terms of its structure and material properties. Hence, the exchangeable valve modelled only included its frame in this thesis. The function of the exchangeable valve, however, is dependant on the leaflets and skirts which were lacking in the simulations. Moving forward, the leaflets and skirts must be added to the models to assess the effects of the crimping, expansion and removal processes on the stresses in these elements. Any damage to the leaflets of the exchangeable valve during its crimping and unsheathing could compromise its function after its deployment. During removal, the leaflets can be damaged to compromise their function as the valve will not need to function beyond that point but tears resulting in parts of the leaflet ripping out and becoming emboli within the vessels must be avoided. Hence, the effect of the exchange procedure on the leaflets and skirt must be simulated.

Additionally, the e-TAVI valve system will function within a fluid environment. The way in which blood will interact with the exchangeable valve and holding member compound must be simulated via a fluid-structure interaction (FSI) simulation. Again, the exchangeable valve should include leaflets and skirts in this simulation to assess the opening and closing of the leaflets and the paravalvular leakage between the holding member and the exchangeable valve. The paravalvular leakage must then be minimised by updating the design, thickness, and position of the skirt on the exchangeable valve. Frame design must also be updated if necessary to ensure the leaflets function properly as this is crucial for valve function. The exchangeable valve frame and the holding member must also be assessed in terms of the flow around them and whether regions of blood stasis can form. Blood stasis must be avoided as much as possible to reduce the risk of thrombosis.

Finally, bench test verification of all the simulations must be performed to validate the numerical results of the simulations in this thesis. This would likely involve the manufacture of the exchangeable valve frame and performing a bench crimping of the frame extracting the outward radial force of the frame through crimping and expansion. These results can then be compared to the forces predicted in the crimping and expansion simulations performed in this thesis. Similarly, the FSI simulations proposed previously should lead to the manufacture of a complete exchangeable valve, including leaflets and skirt, and flow testing of this valve in a pulse duplicator test system.

11.8   Summary

The potential of the e-TAVI system poses a very exciting opportunity in the redo treatment of valvular heart disease. The next step in the future development of this system must be the method of physical engagement between the catheter and the exchangeable valve. This method will then inform the required strength of the magnetic attraction between the two components to securely achieve engagement. Through this, the shape and size of the engagement regions on both the catheter and the exchangeable valve can be determined. Following this, a dedicated exchangeable valve frame design that can hold these features and take full advantage of the star-shaped crimping to minimise removal force and maximise COF could be developed. The required COF of the frame will be informed by the possible friction coefficient of the inner surface of the holding member. Finally, the catheter mechanism capable of radially and axially moving the removal elements, simultaneously unsheathing the new valve to be deployed, and opening and closing a rigid, tapered sheath to receive and fully crimp the removed valve must be designed. Further points from this chapter are listed below.

- The increasing future need for multiple, minimally invasive aortic valve replacements have proliferated the literature through the duration of this PhD research.

- A dedicated exchangeable valve frame design could further increase the advantage of the star-shaped crimping profile captured in this thesis.

- The main purpose of the holding member should be to limit tissue contact with the exchangeable valve and provide sufficient friction.

- The duration between the removal of an exchangeable valve and the deployment of a new one must be below 30 seconds for the e-TAVI system to be clinically feasible.

Chapter 12

Conclusion

The e-TAVI valve system described in this thesis was devised and developed to address the growing need of minimally invasive, multiple valve replacements of the aortic valve. The purpose of the system was to allow the removal of a dysfunctional valve prior to the deployment of a new one. Through this removal, concurrent valve replacements would be possible without decreasing the EOA of the valve or the need for open heart surgery.

Through this research, major contributions were made in the following areas:

- design of a novel valve replacement system named e-TAVI comprising an exchangeable valve deployed within a holding member which could be removed via a dedicated catheter;

- design and development of a novel SE valve frame holding ferromagnetic regions for engagement with the e-TAVI catheter;

- identification of the ideal placement of ferromagnetic regions on this exchangeable valve to achieve sufficient diameter reduction and crimping;

- analysis on the effect of circumferential cell number, ferromagnetic regions size, strut width and cell height on the reduction of frame diameter achieved by crimping via electromagnets;

- design of a catheter with electromagnets capable of engaging with the exchangeable valve magnetically, reduce its diameter through this engagement *in vivo*, and remove the valve;

- identification of the size, current, and number of electromagnets necessary to achieve diameter reduction;

- design of a holding member that minimises tissue contact with the exchangeable valve and provide sufficient friction force for axial anchoring;

- identification of the range of friction values for the holding member in relation to the COF of the exchangeable valve.

The numerical findings that relate to these contribution were:

- a 12-cell exchangeable valve frame crimped via four electromagnets per ferromagnet ring;

- circular ferromagnetic regions of 1 mm radius and 0.5 mm thickness on the exchangeable valve frame;

- 2.87 N per ferromagnetic region to reduce the diameter of an exchangeable valve frame with 0.3 mm strut width and 8 mm cell height;

- 1 mm radius and 2 mm thickness electromagnets on the catheter with 2.52 A of current to prove this removal force;

- friction coefficients between 0.12 - 1.29 to on the inner surface of the holding member to resist 11 N of axial force.

The novel e-TAVI system comprises three components:

- an exchangeable valve;

- a catheter;

- a holding member.

The engagement between the three components were designed to be magnetic, which alleviated the need for precise manoeuvring of the catheter during the exchange process. The design of this magnetic engagement was the main aim of the analyses in this thesis.

The exchangeable valve was designed as a self-expanding TAVI frame with ferromagnetic regions on the frame to engage with the catheter and the holding member. These regions were designed as circular regions in between the cells of the frame. The effect of the size and position of these ferromagnets on the crimping and expansion of the frame was investigated.

The most interesting result from the design of the exchangeable valve was the collapse of the frame into a 3-pronged structure when 12 radially inward force vectors were applied around the frame. Collapsing the frame into such a structure required much less force compared to fully crimping the frame by uniformly closing all cells. Furthermore, shorter cells on the frame were associated with an increase in outward radial strength of the frame while the force required to remove was less dependant on cell height. This showed

that the strut width and cell height of the exchangeable valve frame could be optimised to deliver high radial force while keeping removal force within tolerable magnitudes for the catheter.

In terms of the minimum achieved crimp radius per magnitude of force, a 12-cell exchangeable frame model holding 1 mm radius and 0.5 mm thickness ferromagnet regions, crimped by 4 force points per ring was the best among the simulated designs. Larger radii of ferromagnetic regions required more force per ferromagnet to achieve crimping but required less current on the catheter electromagnets to apply the same force.

1 mm radius and 2 mm thickness catheter electromagnets with a current of 2.52 A was necessary to apply the required force of 2.87 N on the ferromagnet regions of the exchangeable frame. While this coupling was sufficient to crimp the frame, re-sheathing could not be performed due to the weaker magnetic force in shear. Hence, a further mechanical mating between the catheter and the exchangeable valve was found to be necessary to achieve full removal. Since the current requirement for crimping was also dangerously close to the fusing current of the power wire, the additional force delivered via the mechanical coupling would be advantageous. The magnetic force requirement in such a case would be to align and achieve the mechanical mating. Then, the additional strength provided by the mechanical mating would need to be able to crimp the frame and re-sheathe it. Considering a mechanical coupling where engagement requires less force than disengagement, the force requirement on the magnetic attraction could be lower than the calculated 2.87 N for the same frame design.

With the radial strength values calculated for the exchangeable valve designs and the further scope of tolerating a high radial strength with the addition of mechanical mating during removal, the main purpose of the holding member becomes the prevention of contact between the exchangeable valve and the aortic tissue. The axial anchoring aspect of the holding member could purely depend on its inner surface roughness and the resulting friction coefficient. The surgical holding member was superior in terms of preventing tissue contact due to its structure. The transcatheter holding member had to be crimpable and hence had open cells in its expanded state where some struts of the exchangeable valve frame deployed within expanded through these cells. Due to this, a surgically delivered holding member was preferred to limit tissue contact. The main problem with a surgical holding member was that the patient must undergo an open heart surgery in the first e-TAVI deployment. Since the advantage of e-TAVI was mostly towards low-risk patients who would be expected to survive a long time with the prosthetic valve as to require multiple valve replacements, these patients most likely could survive open heart surgery in their first implantation.

In conclusion, the e-TAVI system is a very exciting new valve replacement method that has the potential of addressing the growing need of minimally invasive redo valve replacements without sacrificing EOA. This PhD research has served as the starting

point in the future development of this novel valve system with promising results moving forward.

References

[1] J. L. d'Arcy *et al.*, "Large-scale community echocardiographic screening reveals a major burden of undiagnosed valvular heart disease in older people: The oxvalve population cohort study," *Eur Heart J*, vol. 37, no. 47, pp. 3515–3522, 2016. DOI: `10.1093/eurheartj/ehw229`.

[2] J. E. Hall. and A. C. Guyton, *Textbook of medical physiology.* Philadelphia, PA: Saunders Elsevier, 2011.

[3] R. McMorrow *et al.*, "Assessing the safety and efficacy of tavr compared to savr in low-to-intermediate surgical risk patients with aortic valve stenosis: An overview of reviews," *Int J Cardiol*, vol. 314, pp. 43–53, 2020. DOI: `10.1016/j.ijcard.2020.04.022`.

[4] V. Mauri *et al.*, "Temporal trends of tavi treatment characteristics in high volume centers in germany 2013–2020," *Clin Res Cardiol*, vol. 111, pp. 881–888, 2022. DOI: `10.1007/s00392-021-01963-3`.

[5] N. Cote, P. Pibarot, and M. Clavel, "Incidence, risk factors, clinical impact, and management of bioprosthesis structural valve degeneration," *Curr Opin Cardiol*, vol. 32, no. 2, pp. 123–129, 2017. DOI: `10.1097/HCO.0000000000000372`.

[6] T. Bourguignon *et al.*, "Very long-term outcomes of the carpentier-edwards perimount aortic valve in patients aged 60 or younger," *Ann Thorac Surg*, vol. 100, no. 3, pp. 853–859, 2015. DOI: `10.1016/j.athoracsur.2015.03.105`.

[7] J. D. Carroll *et al.*, "Sts-acc tvt registry of transcatheter aortic valve replacement," *J Am Coll Cardiol*, vol. 76, no. 21, pp. 2492–2516, 2020. DOI: `10.1016/j.jacc.2020.09.595`.

[8] S. Y. Ho, "Structure and anatomy of the aortic root," *Eur J Echocardiogr*, vol. 10, no. 1, pp. i3–i10, 2009. DOI: `10.1093/ejechocard/jen243`.

[9] S. Lin *et al.*, "Intraventricular conduction disturbances after transcatheter aortic valve implantation," *Interv Cardiol Rev*, vol. 15, no. e11, pp. 1–7, 2020. DOI: `10.15420/icr.2020.07`.

[10] A. H. Chester, I. El-Hamamsy, J. T. Butcher, N. Latif, S. Bertazzo, and M. H. Yacoub, "The living aortic valve: From molecules to function," *Glob Cardiol Sci Pract*, vol. 11, pp. 52–77, 2014. DOI: `10.5339/gcsp.2014.11`.

[11] F. Robicsek and M. J. Thubrikar, "Role of sinus wall compliance in aortic leaflet function," *Am J Card*, vol. 84, no. 8, pp. 944–946, 1999. DOI: `10.1016/S0002-9149(99)00475-0`.

[12] S. Katayama, N. Umetani, S. Sugiura, and T. Hisada, "The sinus of valsalva relives abnormal stress on aortic valve leaflets by facilitating smooth closure," *J Thorac Cardiovasc*, vol. 136, no. 6, pp. 1528–1535, 2008. DOI: `10.1016/j.jtcvs.2008.05.054`.

[13] E. Lansac *et al.*, "Aortic root dynamics are asymmetric," *J Heart Valve Dis*, vol. 14, no. 3, pp. 400–407, 2005.

[14] J. R. Mitchell and J. Wang, "Expanding application of the wiggers diagram to teach cardiovascular physiology," *Adv Physiol Educ*, vol. 38, no. 2, pp. 170–175, 2014. DOI: `10.1152/advan.00123.2013`.

[15] M. A. Silver and W. C. Roberts, "Detailed anatomy of the normally functioning aortic valve in hearts of normal and increased weight," *Am J Cardiol*, vol. 55, no. 4, pp. 454–461, 1985. DOI: `10.1016/0002-9149(85)90393-5`.

[16] M. J. Thubrikar, *The aortic valve*. Boca Raton, FL: CRC Press, 1989.

[17] K. Balachandran, P. Sucosky, and A. P. Yoganathan, "Hemodynamics and mechanobiology of aortic valve inflammation and calcification," *Int J Inflam*, vol. 2011:263870, pp. 1–15, 2011. DOI: `10.4061/2011/263870`.

[18] S. Arjunon, S. Rathan, H. Jo, and A. P. Yoganathan, "Aortic valve: Mechanical environment and mechanobiology," *Ann Biomed Eng*, vol. 41, no. 7, pp. 1331–1346, 2013. DOI: `10.1007/s10439-013-0785-7`.

[19] H. A. Dwyer, P. B. Matthews, A. Azadani, L. Ge, T. S. Guy, and E. E. Tseng, "Migration forces of transcatheter aortic valves in patients with noncalcific aortic insufficiency," *J Thorac Cardiovasc Surg*, vol. 138, no. 5, pp. 1227–1233, 2009. DOI: `10.1016/j.jtcvs.2009.02.057`.

[20] A. Pick. "Aortic stenosis prognosis: What 6 facts should you know?" (2020), [Online]. Available: `https://www.heart-valve-surgery.com/aortic-stenosis-prognosis.php` (visited on 12/13/2020).

[21] C. M. Otto and B. Prendergast, "Aortic-valve stenosis – from patients at risk to severe valve obstruction," *N Engl J Med*, vol. 371, no. 8, pp. 744–756, 2014. DOI: `10.1056/NEJMra1313875`.

[22] F. J. Schoen and R. J. Levy, "Calcification of tnumber heart valve substitutes: Progress toward understanding and prevention," *Ann Thorac Surg*, vol. 79, no. 3, pp. 1072–1080, 2005. DOI: `10.1016/j.athoracsur.2004.06.033`.

[23] P. Pibarot and J. G. Dumesnil, "Prosthetic heart valves selection of the optimal prosthesis and long-term management," *Circulation*, vol. 119, no. 7, pp. 1034–1048, 2009. DOI: `10.1161/CIRCULATIONAHA.108.778886`.

[24]   K. Maganti, V. H. Rigolin, M. E. Sarano, and R. O. Bonow, "Valvular heart disease: Diagnosis and management," *Mayo Clin Proc*, vol. 85, no. 5, pp. 483–500, 2010. DOI: `10.4065/mcp.2009.0706`.

[25]   C. Koo, J. Shim, N. Kim, Y. Ki, J. Park, and J. Kim, "Anesthetic considerations for a patient with situs inversus totalis undergoing cardiac surgery - a case report," *Anesth Pain Med*, vol. 14, no. 2, pp. 193–196, 2019. DOI: `10.17085/apm.2019.14.2.193`.

[26]   NHS UK. "Aortic valve replacement." (2018), [Online]. Available: `https://www.nhs.uk/conditions/aortic-valve-replacement` (visited on 12/13/2020).

[27]   P. Rajashekar, "Development of mechanical heart valves - an inspiring tale," *J Pract Cardiovasc Sci*, vol. 1, no. 3, pp. 289–293, 2015. DOI: `10.4103/2395-5414.177309`.

[28]   CryoLife Inc., *On-x heart valves*, 2020. [Online]. Available: `https://www.cryolife.com/products/on-x-heart-valves/` (visited on 12/13/2020).

[29]   K. Vahidkhah *et al.*, "Valve thrombosis following transcatheter aortic valve replacement: Significance of blood stasis on the leaflets," *Eur J Cardiothorac Surg*, vol. 51, no. 5, pp. 927–935, 2017. DOI: `10.1093/ejcts/ezw407`.

[30]   Edwards Lifesciences Corporation. "Surgical aortic pericardial valves." (2020), [Online]. Available: `https://www.edwards.com/gb/devices/heart-valves/aortic-pericardial` (visited on 12/13/2020).

[31]   J. Ennker, A. Albert, and I. C. Ennker, "Stentless aortic valves. current aspects," *HSR Proc Intensive Care Cardiovasc Anesth.*, vol. 4, no. 2, pp. 77–82, 2012.

[32]   T. E. David, J. Bos, and H. Rakowski, "Aortic valve replacement with the toronto spv bioprosthesis," *J Heart Valve Dis.*, vol. 1, no. 2, pp. 244–248, 1992.

[33]   C. M. Young, M. Buchbinder, and J. C. Giacomini, "Transcatheter corevalve valve-in-valve implantation in a stentless porcine aortic valve for severe aortic regurgitation," *Clin Case Rep*, vol. 2, no. 6, pp. 281–285, 2014. DOI: `10.1002/ccr3.113`.

[34]   H. Eltchaninoff, E. Durand, M. Barbanti, and M. Abdel-Wahab, "Tavi and valve performance: Update on definitions, durability, transcatheter heart valve failure modes and management," *EuroIntervention*, vol. 14, no. AB, AB64–AB73, 2018. DOI: `10.4244/Eij-D-18-00653`.

[35]   B. Ramlawi, M. Ramchandani, and M. J. Reardon, "Surgical approaches to aortic valve replacement and repair - insights and challenges," *Interv Cardiol*, vol. 9, no. 1, pp. 32–36, 2014. DOI: `10.15420/icr.2011.9.1.32`.

[36]   C. Spadaccio, K. Alkhamees, and N. Al-Attar, "Recent advances in aortic valve replacement," *F1000Res*, vol. 8, no. F1000 Faculty Rev-1159, pp. 1–9, 2019. DOI: `10.12688/f1000research.17995.1`.

[37] M. Abdel-Wahab, J. Jose, and G. Richardt, "Transfemoral tavi devices: Design overview and clinical outcomes," *EuroIntervention*, vol. 11, no. Suppl W, W114–W118, 2015. DOI: `10.4244/EIJV11SWA33`.

[38] MSI. "Disposable heart valve crimping tool." (2020), [Online]. Available: `https://msi.equipment/product/hv500/` (visited on 12/13/2020).

[39] U.S. Food Drug Administration (FDA). "Medtronic corevalve system - p130021/s033." (2019), [Online]. Available: `https://www.fda.gov/medical-devices/recently-approved-devices/medtronic-corevalve-system-medtronic-corevalve-evolut-r-system-medtronic-corevalve-evolut-pro-system` (visited on 12/13/2020).

[40] GHHM. "Medtronic's corevalve tavr system displays great long-term performance in clinical trials." (2019), [Online]. Available: `https://cardiology2.com/edwards-sapien-3-valve-shows-excellent-results-at-2-years/` (visited on 12/13/2020).

[41] A. Giordano, G. Biondi-Zoccai, and G. Frati, *Transcatheter aortic valve implantation: clinical, interventional and surgical perspectives*. Gewerbestrasse 11, 6330 Cham, Switzerland: Springer Nature Switzerland AG, 2019. DOI: `10.1007/978-3-030-05912-5`.

[42] Mayo Foundation. "Transcatheter aortic valve replacement (tavr)." (2020), [Online]. Available: `https://www.mayoclinic.org/tests-procedures/transcatheter-aortic-valve-replacement/about/pac-20384698` (visited on 12/13/2020).

[43] P. Fefer *et al.*, "Impact of rapid ventricular pacing on outcome after transcatheter aortic valve replacement," *J Am Heart Assoc*, vol. 7, no. 14, e009038, 2018. DOI: `10.1161/JAHA.118.009038`.

[44] University Hospital Southampton NHS Foundation Trust. "Post tavi care." (2014), [Online]. Available: `https://www.uhs.nhs.uk/OurServices/Bloodandcirculation/Transcatheter-aortic-valve-implantation/Diagnosis-and-treatment-TAVI/Post-TAVI-care.aspx` (visited on 12/13/2020).

[45] R. S. Rao, H. Maniar, and A. Zajarias, "Sapien valve: Past, present, and future," *Cardiac Interb Today*, vol. 9, pp. 35–41, 2015.

[46] Edwards Lifesciences. "Transcatheter sapien 3." (2020), [Online]. Available: `https://www.edwards.com/gb/devices/Heart-Valves/Transcatheter-Sapien-3` (visited on 12/13/2020).

[47] Cardiology 2.0. "Edwards sapien 3 valve shows excellent results at 2 years." (2020), [Online]. Available: `https://cardiology2.com/edwards-sapien-3-valve-shows-excellent-results-at-2-years/` (visited on 12/13/2020).

[48] T. Rheude *et al.*, "Transcatheter aortic valve replacement with balloon-expandable valves comparison of sapien 3 ultra versus sapien 3," *JACC Cardiovasc Interv*, vol. 13, no. 22, pp. 2631–2638, 2020. DOI: `10.1016/j.jcin.2020.07.013`.

[49] J. Bailey, N. Curzen, and N. W. Bressloff, "Assessing the impact of including leaflets in the simulation of tavi deployment into a patient-specific aortic root," *Comput Methods Biomech Biomed Engin*, vol. 19, no. 7, pp. 733–744, 2016. DOI: `10.1080/10255842.2015.1058928`.

[50] J. M. Bailey, "Implications for leaflet behaviour in heavily calcified patient specific aortic roots: Simulation of transcatheter aortic valve implantation," Ph.D. dissertation, University of Southampton, 2015.

[51] C. Marchand, F. Heim, B. Durand, and N. Chafke, "Nitinol stent for percutaneous heart valve implantation: Material shape setting," *Mater Manuf Process*, vol. 26, no. 2, pp. 181–187, 2011. DOI: `10.1080/10426914.2010.491695`.

[52] M. S. Cabrera, C. W. J. Oomens, and F. P. T. Baaijens, "Understanding the requirements of self-expandable stents for heart valve replacement: Radial force, hoop force and equilibrium," *J Mech Behav Biomed Mater*, vol. 68, pp. 252–264, 2017. DOI: `10.1016/j.jmbbm.2017.02.006`.

[53] S. Egron *et al.*, "Radial force: An underestimated parameter in oversizing transcatheter aortic valve replacement prostheses: In vitro analysis with five commercialized valves," *ASAIO J.*, vol. 64, no. 4, pp. 536–543, 2018. DOI: `10.1097/MAT.0000000000000659`.

[54] Y. Sun *et al.*, "Outcomes of evolut r versus corevalve after transcatheter aortic valve implantation: A meta-analysis," *Heart Lung Circ*, vol. 29, no. 2, pp. 288–294, 2020. DOI: `10.1016/j.hlc.2018.12.013`.

[55] S. Noble *et al.*, "Comparison of procedural and clinical outcomes with evolut r versus medtronic corevalve: A swiss tavi registry analysis," *EuroIntervention*, vol. 12, no. 18, e2170–e2176, 2017. DOI: `10.4244/EIJ-D-16-00677`.

[56] U. Landes *et al.*, "Comparative matched outcome of evolut-r vs corevalve transcatheter aortic valve implantation," *J Invasive Cardiol*, vol. 29, no. 2, pp. 69–74, 2017.

[57] G. Rao *et al.*, "Early real-world experience with corevalve evolut pro and r systems for transcatheter aortic valve replacement," *J Interv Cardiol*, vol. 2019:1906814, pp. 1–8, 2019. DOI: `10.1155/2019/1906814`.

[58] K. E. O'Sullivan, A. Gough, R. Segurado, D. S. M. Barry, and J. Hurley, "Is valve choice a significant determinant of paravalvular leak post-transcatheter aortic valve implantation? a systematic review and meta-analysis," *Eur J Cardiothoracic Surg.*, vol. 45, no. 5, pp. 826–833, 2013. DOI: `10.1093/ejcts/ezt515`.

[59] M. Barbanti *et al.*, "Anatomical and procedural features associated with aortic root rupture during balloon-expandable transcatheter aortic valve replacement," *Circulation*, vol. 128, no. 3, pp. 244–253, 2013. DOI: `10.1161/CIRCULATIONAHA.113.002947`.

[60] W. Kim *et al.*, "The savi-tf registry: 1 year outcomes of the european post-market registry using the acurate neo transcatheter heart valve under real world conditions in 1,000 patients," *JACC: Cardiovasc Interv*, vol. 11, no. 14, pp. 1368–1374, 2018. DOI: `10.1016/j.jcin.2018.03.023`.

[61] P. Wenaweser *et al.*, "Transcatheter aortic valve implantation with the nvt allegra transcatheter heart valve system: First-in-human experience with a novel self-expanding transcatheter heart valve," *EuroIntervention*, vol. 12, no. 1, pp. 71–77, 2016. DOI: `10.4244/EIJV12I1A13`.

[62] D. Jagielka *et al.*, "Transfermoral aortic valve implantation using self-expanding new valve technology (nvt) allegra bioprosthesis: A pilot prospective study," *Cardiol J.*, vol. 28, no. 3, pp. 384–390, 2021. DOI: `10.5603/CJ.a2019.0019`.

[63] A. Denegri *et al.*, "Real-world procedural and 30-day outcome using the portico transcatheter aortic valve prosthesis: A large single center cohort," *Int J Cardiol*, vol. 253, pp. 40–44, 2018. DOI: `10.1016/j.ijcard.2017.10.101`.

[64] M. Weferling, C. W. Hamm, and W. Kim, "Percutaneous coronary intervention in transcatheter aortic valve implantation patients: Overview and practical management," *Front Cardiovasc Med*, vol. 8, no. 653768, pp. 1–13, 2021. DOI: `10.3389/fcvm.2021.653768`.

[65] Abbott Vascular International. "Portico transcatheter aortic heart valve implantation system." (2019), [Online]. Available: `https://www.cardion.cz/file/1306/portico-spec-sheet.pdf` (visited on 07/18/2022).

[66] K. H. Yap, R. Murphy, M. Devbhandari, and R. Venkateswaran, "Aortic valve replacement: Is porcine or bovine valve better?" *Interact Cardiovasc Thorac Surg*, vol. 16, no. 3, pp. 361–371, 2013. DOI: `10.1093/icvts/ivs447`.

[67] M. A. Borger, F. Nette, M. Maganti, and C. M. Feindel, "Carpentier-edwards perimount magna valve versus medtronic hancock ii: A matched hemodynamic comparison," *Ann Thorac Surg*, vol. 83, no. 6, pp. 2054–2058, 2007. DOI: `10.1016/j.athoracsur.2007.02.062`.

[68] I. M. Wagner *et al.*, "Influence of completely supra-annular placement of bioprostheses on exercise hemodynamics in patients with a small aortic annulus," *J Thorac Cardiovasc Surg*, vol. 133, no. 5, pp. 1234–1241, 2007. DOI: `10.1016/j.jtcvs.2006.10.074`.

[69] R. M. Suri *et al.*, "Left ventricular mass regression after porcine versus bovine aortic valve replacement: A randomized comparison," *Ann Thorac Surg*, vol. 88, no. 4, pp. 1232–1237, 2009. DOI: `10.1016/j.athoracsur.2009.04.128`.

[70] M. J. Dalmau *et al.*, "Hemodynamic performance of the medtronic mosaic and perimount magna aortic bioprostheses: Five year results of a prospectively randomized study," *Eur J Cardiothorac Surg*, vol. 39, no. 6, pp. 844–852, 2011. DOI: `10.1016/j.ejcts.2010.11.015`.

[71] M. Constable, H. E. Burton, B. M. Lawless, V. Gramigna, K. G. Buchan, and
      D. M. Espino, "Effect of glutaraldehyde based crosslinking on the viscoelasticity
      of mitral valve basal chordae tendineae," *BioMed Eng Online*, vol. 17, no. 93,
      pp. 1–14, 2018. DOI: `10.1186/s12938-018-0524-2`.

[72] E. A. Talman and D. R. Boughner, "Glutaraldehyde fixation alters the internal
      shear properties of porcine aortic heart valve tissue," *Ann Thorac Surg*, vol. 60,
      no. 2, pp. 369–373, 1995. DOI: `10.1016/0003-4975(95)00250-o`.

[73] P. Singhal, A. Luk, and J. Butany, "Bioprosthetic heart valves: Impact of im-
      plantation on biomaterials," *Int Sch Res Notices*, vol. 2013, pp. 1–14, 2013. DOI:
      `10.5402/2013/728791`.

[74] A. Cribier *et al.*, "Percutaneous transcatheter implantation of an aortic valve
      prosthesis for calcific aortic stenosis: First human case description," *Circulation*,
      vol. 106, no. 24, pp. 3006–3008, 2002. DOI: `10.1161/01.CIR.0000047200.36165.`
      `B8`.

[75] T. Umegaki, S. Kunisawa, Y. Nakajima, T. Kamibayashi, K. Fushim, and Y.
      Imanaka, "Comparison of in-hospital outcomes between transcatheter and surgi-
      cal aortic valve replacement in patients with aortic valve stenosis: A retrospective
      cohort study using administrative data," *J Cardiothorac Vasc Anesth*, vol. 32,
      no. 3, pp. 1281–1288, 2018. DOI: `10.1053/j.jvca.2017.06.047`.

[76] R. Sarmento-Leite and G. E. de Oliveira Jr., "Transcatheter aortic valve implan-
      tation: Where are we in 2020?" *Int J Cardiovasc Sci*, vol. 33, no. 5, pp. 537–549,
      2020. DOI: `10.36660/ijcs.20200089`.

[77] N. Ali *et al.*, "Valve for life: Tackling the deficit in transcatheter treatment of
      heart valve disease in the uk," *Open Heart*, vol. 8, no. 1, pp. 1–7, 2021. DOI:
      `10.1136/openhrt-2020-001547`.

[78] M. Mariathas, J. Rawlins, and N. Curzen, "Transcatheter aortic valve implanta-
      tion: Where are we now?" *Future Cardiol*, vol. 13, no. 6, pp. 551–566, 2017. DOI:
      `10.2217/fca-2017-0056`.

[79] D. Capodanno *et al.*, "Standardized definitions of structural deterioration and
      valve failure in assessing long-term durability of transcatheter and surgical aor-
      tic bioprosthetic valves: A consensus statement from the european association of
      percutaneous cardiovascular interventions (eapci) endorsed by the european so-
      ciety of cardiology (esc) and the european association for cardio-thoracic surgery
      (eacts)," *Eur J Cardiothorac Surg*, vol. 52, no. 3, pp. 408–417, 2017. DOI: `10.`
      `1093/ejcts/ezx244`.

[80] G. Costa, E. Criscione, D. Todaro, C. Tamburino, and M. Barbanti, "Long-term
      transcatheter aortic valve durability," *J Interv Cardiol*, vol. 14, no. 2, pp. 62–69,
      2019. DOI: `10.15420/icr.2019.4.2`.

[81] A. E. Kostyunin, A. E. Yuzhalin, M. A. Rezvova, E. A. Ovcharenko, T. V. Glushkova, and A. G. Kutikhin, "Degeneration of bioprosthetic heart valves: Update 2020," *J Am Heart Assoc*, vol. 9, no. 19, pp. 1–19, 2020. DOI: `10.1161/JAHA.120.018506`.

[82] S. Bleiziffer and T. K. Rudolph, "Patient prosthesis mismatch after savr and tavr," *Front. Cardiovasc. Med.*, vol. 9, no. 761917, pp. 1–10, 2022. DOI: `10.3389/fcvm.2022.761917`.

[83] D. Dvir *et al.*, "Standardized definition of structural valve degeneration for surgical and transcatheter bioprosthetic aortic valves," *Circulation*, vol. 137, no. 4, pp. 388–399, 2018. DOI: `10.1161/CIRCULATIONAHA.117.030729`.

[84] A. C. Egbe *et al.*, "Bioprosthetic valve thrombosis versus structural failure: Clinical and echocardiographic predictors," *J Am Coll Cardiol*, vol. 66, no. 21, pp. 2285–2294, 2015. DOI: `10.1016/j.jacc.2015.09.022`.

[85] R. Guenzinger, K. Fiegl, M. Wottke, and R. S. Lange, "Twenty-seven-year experience with the st. jude medical biocor bioprosthesis in the aortic position," *Ann Thorac Surg*, vol. 100, no. 6, pp. 2220–2226, 2015. DOI: `10.1016/j.athoracsur.2015.06.027`.

[86] J. Forcillo *et al.*, "Carpentier-edwards pericardial valve in the aortic position: 25-years experience," *Ann Thorac Surg*, vol. 96, no. 2, pp. 486–493, 2013. DOI: `10.1016/j.athoracsur.2013.03.032`.

[87] T. E. David, C. M. Feindel, J. Bos, J. Ivanov, and S. Armstrong, "Aortic valve replacement with toronto spv bioprosthesis: Optimal patient survival but suboptimal valve durability," *J Thorac Cardiovasc Surg*, vol. 135, no. 1, pp. 19–24, 2008. DOI: `10.1016/j.jtcvs.2007.04.068`.

[88] P. S. U. Myken and O. Bech-Hansen, "A 20-year experience of 1712 patients with the biocor porcine bioprosthesis," *J Thorac Cardiovasc Surg*, vol. 137, no. 1, pp. 76–81, 2009. DOI: `10.1016/j.jtcvs.2008.05.068`.

[89] C. A. Yankah *et al.*, "Aortic valve replacement with the mitroflow pericardial bioprosthesis: Durability results up to 21 years," *J Thorac Cardiovasc Surg*, vol. 136, no. 3, pp. 688–696, 2008. DOI: `10.1016/j.jtcvs.2008.05.022`.

[90] W. R. E. Jamieson *et al.*, "Carpentier-edwards supra-annular aortic porcine bioprosthesis: Clinical performance over 20 years," *J Thorac Cardiovasc Surg*, vol. 130, no. 4, pp. 994–1000, 2005. DOI: `10.1016/j.jtcvs.2005.03.040`.

[91] T. Christ, B. Claus, R. Borck, W. Konertz, and H. Grubitzsch, "The st. jude toronto stentless bioprosthesis: Up to 20 years follow-up in younger patients," *Heart Surg Forum*, vol. 18, no. 4, E129–E133, 2015. DOI: `10.1532/hsf.1252`.

[92] D. S. Bach and N. D. Kon, "Long-term clinical outcomes 15 years after aortic valve replacement with the freestyle stentless aortic bioprosthesis," *Ann Thorac Surg*, vol. 97, no. 2, pp. 544–551, 2014. DOI: `10.1016/j.athoracsur.2013.08.047`.

[93] S. Mohammadi *et al.*, "Long-term clinical and echocardiographic follow-up of the freestyle stentless aortic bioprosthesis," *Circulation*, vol. 126, no. 11, S198–S204, 2012. DOI: `10.1161/CIRCULATIONAHA.111.084806`.

[94] A. Repossini *et al.*, "Pericardial stentless valve for aortic valve replacement: Long-term results," *Ann Thorac Surg*, vol. 102, no. 6, pp. 1956–1965, 2016. DOI: `10.1016/j.athoracsur.2016.05.080`.

[95] L. Sondergaard *et al.*, "Durability of transcatheter and surgical bioprosthetic aortic valves in patients at lower surgical risk," *J Am Coll Cardiol*, vol. 73, no. 5, pp. 546–553, 2019. DOI: `10.1016/j.jacc.2018.10.083`.

[96] D. R. Johnston *et al.*, "Long-term durability of bioprosthetic aortic valves: Implications from 12,569 implants," *Ann Thorac Surg*, vol. 99, no. 4, pp. 1239–1247, 2015. DOI: `10.1016/j.athoracsur.2014.10.070`.

[97] T. Senage *et al.*, "Early structural valve deterioration of mitroflow aortic bioprosthesis: Mode, incidence, and impact on outcome in a large cohort of patients," *Circulation*, vol. 130, no. 23, pp. 2012–2020, 2014. DOI: `10.1161/CIRCULATIONAHA.114.010400`.

[98] D. J. Blackman *et al.*, "Long-term durability of transcatheter aortic valve prostheses," *J Am Coll Cardiol*, vol. 73, no. 5, pp. 537–545, 2019. DOI: `10.1016/j.jacc.2018.10.078`.

[99] H. Eltchaninoff *et al.*, "Assessment of structural valve deterioration of transcatheter aortic bioprosthetic balloon-expandable valve using the new european consensus definition," *EuroIntervention*, vol. 14, no. 3, e264–e271, 2018. DOI: `10.4244/EIJ-D-18-00015`.

[100] E. W. Holy *et al.*, "Long-term durability and haemodynamic performance of a self-expanding transcatheter heart valve beyond five years after implantation: A prospective observational study applying the standardised definitions of structural deterioration and valve failure," *EuroIntervention*, vol. 14, no. 4, e390–e396, 2018. DOI: `10.4244/EIJ-D-18-00041`.

[101] L. Testa *et al.*, "Long-term clinical outcome and performance of transcatheter aortic valve replacement with a self-expandable bioprosthesis," *EuroIntervention*, vol. 41, no. 20, pp. 1876–1886, 2020. DOI: `10.1093/eurheartj/ehz925`.

[102] M. Deutsch *et al.*, "Beyond the five-year horizon: Long-term outcome of high-risk and inoperable patients undergoing tavr with first-generation devices," *EuroIntervention*, vol. 14, no. 1, pp. 41–49, 2018. DOI: `10.4244/EIJ-D-17-00603`.

[103] M. Barbanti *et al.*, "5-year outcomes after transcatheter aortic valve implantation with corevalve prosthesis," *JACC Cardiovasc Interv*, vol. 8, no. 8, pp. 1084–1091, 2015. DOI: `10.1016/j.jcin.2015.03.024`.

[104] R. A. Panico *et al.*, "Long-term results and durability of the corevalve transcatheter aortic bioprosthesis: Outcomes beyond five years," *EuroIntervention*, vol. 14, no. 16, pp. 1639–1647, 2019. DOI: `10.4244/EIJ-D-18-00779`.

[105] E. Durand *et al.*, "Assessment of long-term structural deterioration of transcatheter aortic bioprosthetic valves using the new european definition," *Circ Cardiovasc Interv*, vol. 12, no. 4, pp. 1–8, 2019. DOI: `10.1161/CIRCINTERVENTIONS.118.007597`.

[106] R. Didier *et al.*, "Five-year clinical outcome and valve durability after transcatheter aortic valve replacement in high-risk patients," *Circulation*, vol. 138, no. 23, pp. 2597–2607, 2018. DOI: `10.1161/CIRCULATIONAHA.118.036866`.

[107] T. G. Gleason *et al.*, "5-year outcomes of self-expanding transcatheter versus surgical aortic valve replacement in high-risk patients," *J Am Coll Cardiol*, vol. 72, no. 22, pp. 2687–2696, 2018. DOI: `10.1016/j.jacc.2018.08.2146`.

[108] A. P. Durko, R. L. Osnabrugge, and A. P. Kappetein, "Long-term outlook for transcatheter aortic valve replacement," *Trends Cardiovasc Med*, vol. 28, no. 3, pp. 174–183, 2018. DOI: `10.1016/j.tcm.2017.08.004`.

[109] R. A. Meneguz-Moreno *et al.*, "Progression and prognosis of paravalvular regurgitation after transcatheter aortic valve implantation," *Arq Bras Cardiol*, vol. 109, no. 6, pp. 590–598, 2017. DOI: `10.5935/abc.20170172`.

[110] S. Katsanos *et al.*, "Position of edwards sapien transcatheter valve in the aortic root in relation with the coronary ostia: Implications for percutaneous coronary interventions," *Catheter Cardiovasc Interv*, vol. 85, no. 3, pp. 480–487, 2015. DOI: `10.1002/ccd.25718`.

[111] J. P. Fanning, D. G. Platts, D. L. Walters, and J. F. Fraser, "Transcatheter aortic valve implantation (tavi): Valve design and evolution," *Int J Cardiol*, vol. 168, no. 3, pp. 1822–1831, 2013. DOI: `10.1016/j.ijcard.2013.07.117`.

[112] T. M. Nazif *et al.*, "Clinical implications of new-onset left bundle branch block after transcatheter aortic valve replacement: Analysis of the partner experience," *Eur Heart J*, vol. 35, no. 24, pp. 1599–1607, 2014. DOI: `10.1093/eurheartj/eht376`.

[113] E. Lansac and L. de Kerchove, "Aortic valve repair techniques: State of the art," *Eur J Cardiothorac Surg*, vol. 53, pp. 1101–1107, 2018. DOI: `10.1093/ejcts/ezy176`.

[114] G. E. Khoury and L. de Kerchove, "Principles of aortic valve repair," *J Thorac Cardiovasc Surg*, vol. 145, pp. 26–29, 2013. DOI: `10.1016/j.jtcvs.2012.11.071`.

[115] A. Mazine *et al.*, "Ross procedure in adults for cardiologists and cardiac surgeons," *J Am Coll Cardiol*, vol. 72, no. 22, pp. 2761–2777, 2018. DOI: `10.1016/j.jacc.2018.08.2200`.

[116] I. El-Hamamsy *et al.*, "Propensity matched comparison of the ross procedure and prosthetic heart valve replacement in adults," *J Am Coll Cardiol*, vol. 79, no. 8, pp. 805–815, 2022. DOI: `10.1016/j.jacc.2021.11.057`.

[117] Z. Shao *et al.*, "Recent progress in biomaterials for heart valve replacement: Structure, function, and biomimetic design," *View*, vol. 2, pp. 1–17, 2021. DOI: `10.1002/VIW.20200142`.

[118] C. D. Resor and D. L. Bhatt, "Polymeric heart valves: Back to the future?" *Matter*, vol. 1, pp. 17–38, 2019. DOI: `10.1016/j.matt.2019.06.003`.

[119] F. Inc. "Tria heart valves." (2022), [Online]. Available: `https://foldax.com/` (visited on 11/29/2022).

[120] M. Silaschi *et al.*, "Transcatheter valve-in-valve implantation versus redo surgical aortic valve replacement in patients with failed aortic bioprostheses," *Interact Cardiovasc Thorac Surg*, vol. 24, no. 1, pp. 63–70, 2017. DOI: `10.1093/icvts/ivw300`.

[121] A. Thandra *et al.*, "Valve-in-valve transcatheter aortic valve replacement versus redo surgical valve replacement for degenerated bioproshetic aortic valve: An updated meta-analysis comparing midterm outcomes," *Catheter Cardiovasc Interv*, vol. 97, no. 7, pp. 1481–1488, 2021. DOI: `10.1002/ccd.29541`.

[122] A. H. Malik *et al.*, "Valve-in-valve transcatheter implantation versus redo surgical aortic valve replacement," *Am J Cardiol*, vol. 125, no. 9, pp. 1378–1384, 2020. DOI: `10.1016/j.amjcard.2020.02.005`.

[123] Shin Tokyo Hospital. "Transcatheter aortic valve implantation." (2017), [Online]. Available: `https://www.shin-tokyohospital.or.jp/tavi/` (visited on 12/13/2020).

[124] H. Hatoum, S. Lilly, P. Maureira, J. Crestanello, and L. P. Dasi, "The hemodynamics of transcatheter aortic valves in transcatheter aortic valves," *J Thorac Cardiovasc Surg*, vol. 161, no. 2, pp. 565–576, 2021. DOI: `https://doi.org/10.1016/j.jtcvs.2019.09.174`.

[125] M. Spaziano *et al.*, "Transcatheter aortic valve implantation versus redo surgery for failing surgical aortic bioprostheses: A multicentre propensity score analysis," *EuroIntervention*, vol. 13, no. 10, pp. 1149–1156, 2017. DOI: `10.4244/EIJ-D-16-00303`.

[126] N. Nalluri *et al.*, "Valve in valve transcatheter aortic valve implantation (viv-tavi) versus redo-surgical aortic valve replacement (redo-savr): A systematic review and meta-analysis," *J Interv Cardiol*, vol. 31, no. 5, pp. 661–671, 2018. DOI: `10.1111/joic.12520`.

[127] T. Stankowski *et al.*, "Femoral transcatheter valve-in-valve implantation as alternative strategy for failed aortic bioprostheses: A single-centre experience with long-term follow-up," *Int J Cardiol*, vol. 306, pp. 25–34, 2020. DOI: `10.1016/j.ijcard.2020.02.035`.

[128] F. J. Woitek *et al.*, "Treatment of failed aortic bioprostheses: An evaluation of conventional redo surgery and transfemoral transcatheter aortic valve-in-valve implantation," *Int J Cardiol*, vol. 300, pp. 80–86, 2020. DOI: `10.1016/j.ijcard.2019.09.039`.

[129] A. F. Sedeek, K. L. Greason, G. S. Sandhu, J. A. Dearani, D. R. H. Jr, and H. V. Schaff, "Transcatheter valve-in-valve vs surgical replacement of failing stented aortic biological valves," *Ann Thorac Surg*, vol. 108, no. 2, pp. 424–430, 2019. DOI: `10.1016/j.athoracsur.2019.03.084`.

[130] P. Deharo *et al.*, "Transcatheter valve-in-valve aortic valve replacement as an alternative to surgical re-replacement," *J Am Coll Cardiol*, vol. 76, no. 5, pp. 489–499, 2020. DOI: `10.1016/j.jacc.2020.06.010`.

[131] S. A. Hirji *et al.*, "Comparison of in-hospital outcomes and readmissions for valve-in-valve transcatheter aortic valve replacement vs. reoperative surgical aortic valve replacement: A contemporary assessment of real-world outcomes," *Eur Heart J*, vol. 41, no. 29, pp. 2747–2755, 2020. DOI: `10.1093/eurheartj/ehaa252`.

[132] J. G. Webb, D. Murdoch, and D. Dvir, "Will transcatheter replacement become the new default therapy when bioprosthetic valves fail?" *J Am Coll Cardiol*, vol. 72, no. 4, pp. 383–385, 2018. DOI: `10.1016/j.jacc.2018.04.073`.

[133] H. Eggebrecht *et al.*, "Valve-in-valve transcatheter aortic valve implantation for degenerated bioprosthetic heart valves," *JACC Cardiovasc Interv*, vol. 4, no. 11, pp. 1218–1227, 2011. DOI: `10.1016/j.jcin.2011.07.015`.

[134] D. Dvir *et al.*, "Transcatheter aortic valve replacement for degenerative bioprosthetic surgical valves results from the global valve-in-valve registry," *Circulation*, vol. 126, no. 19, pp. 2335–2344, 2012. DOI: `10.1161/Circulationaha.112.104505`.

[135] P. T. L. Chiam *et al.*, "Percutaneous transcatheter aortic valve implantation for degenerated surgical bioprostheses: The first case series in asia with one-year follow-up," *Singapore Med J*, vol. 57, no. 7, pp. 401–405, 2016. DOI: `10.11622/smedj.2016097`.

[136] H. B. Riberiro *et al.*, "Incidence, predictors, and clinical outcomes of coronary obstruction following transcatheter aortic valve replacement for degenerative bioprosthetic surgical valves: Insights from the vivid registry," *Eur Heart J*, vol. 39, no. 8, pp. 687–695, 2018. DOI: `10.1093/eurheartj/ehx455`.

[137] H. B. Ribeiro *et al.*, "Predictive factors, management, and clinical outcomes of coronary obstruction following transcatheter aortic valve implantation insights from a large multicenter registry," *J Am Coll Cardiol*, vol. 62, no. 17, pp. 1552–1562, 2013. DOI: 10.1016/j.jacc.2013.07.040.

[138] M. J. Hoyt, J. Hathaway, R. Palmer, and M. Beach, "Predictors of permanent pacemaker implantation after transcatheter aortic valve replacement," *J Cardiothorac Vasc Anesth*, vol. 29, no. 5, pp. 1162–1166, 2015. DOI: 10.1053/j.jvca.2015.06.001.

[139] A. Duncan, C. Quarto, and S. Davies, "Midterm degeneration of transcatheter heart valve device following valve-in-valve transcatheter aortic valve replacement requiring repeat transcatheter aortic valve replacement," *CASE*, vol. 4, no. 4, pp. 291–298, 2020. DOI: 10.1016/j.case.2020.04.008.

[140] G. Tarantini and L. N. Fovino, "Lifetime strategy of patients with aortic stenosis: The first cut is the deepest," *JACC Cardiovasc Interv*, vol. 14, no. 15, pp. 1727–1730, 2021. DOI: 10.1016/j.jcin.2021.06.029.

[141] A. Kalra *et al.*, "Aortic valve replacement in bioprosthetic failure: Insights from the society of thoracic surgeons national database," *Ann Thorac Surg*, vol. 110, no. 5, pp. 1637–1642, 2020. DOI: 10.1016/j.athoracsur.2019.08.023.

[142] D. Dvir *et al.*, "Novel strategies in aortic valve-in-valve therapy including bioprosthetic valve fracture and basilica," *EuroIntervention*, vol. 14, no. AB, AB74–AB82, 2018. DOI: 10.4244/EIJ-D-18-00667.

[143] J. T. Saxon, K. B. Allen, D. J. Cohen, and A. K. Chhatriwalla, "Bioprosthetic valve fracture during valve-in-valve tavr: Bench to bedside," *Interv Cardiol*, vol. 13, no. 1, pp. 20–26, 2018. DOI: 10.15420/icr.2017:29:1.

[144] World Bank. "Life expectancy at birth, total (years)." (2018), [Online]. Available: http://data.worldbank.org/indicator/SP.DYN.LE00.IN (visited on 09/09/2018).

[145] M. C. Raschpichler *et al.*, "Valve-in-valve for degenerated transcatheter aortic valve replacement versus valve-in-valve for degenerated surgical aortic bioprostheses: A 3-center comparison of hemodynamic and 1-year outcome," *J Am Heart Assoc*, vol. 9, no. 14, pp. 1–15, 2020. DOI: 10.1161/JAHA.119.013973.

[146] I. Vesely, *U.s. patent 2006/0136052: Cardiovascular valve assembly*, 2006.

[147] M. T. Alonso, *U.s. patent us5032128a: Heart valve prosthesis*, 1988.

[148] M. Garrison, H. Gifford, and F. S. Goar, *U.s. patent us20020151970a1: Methods and devices for implanting cardiac valves*, 1999.

[149] A. Sharkawy, M. Foley, D. Gittings, D. Cole, and S. Crews, *U.s. patent us7503930b: Prosthetic cardiac valves and systems and methods for implanting thereof*, 2009.

[150] T. R. R. J. M. Revuelta J. D. Lemmon, *U.s. patent us8591570b2: Prosthetic heart valve for replacing previously implanted heart valve*, 2004.

[151] N. W. Bressloff, N. Curzen, and O. C. Eren, *Wipo patent wo2022185063a1: A catheter*, 2022.

[152] R. Hopf, M. Gessat, V. Falk, and E. Mazza, "Reconstruction of stent induced loading forces on the aortic valve complex," in *Proceedings of medical image computing and computer assisted intervention society (MICCAI-STENT'12)*, (Nice, France), Nice, France, Oct. 2011, pp. 104–111. [Online]. Available: http://campar.in.tum.de/STENT2012/WebHome.

[153] G. Luraghi *et al.*, "On the modeling of patient-specific transcatheter aortic valve replacement: A fluid-structure interaction approach," *Cardiovasc Eng Technol*, vol. 10, no. 3, pp. 437–455, 2019. DOI: 10.1007/s13239-019-00427-0.

[154] M. Bianchi *et al.*, "Patient-specific simulation of transcatheter aortic valve replacement: Impact of deployment options on paravalvular leakage," *Biomech Model Mechanobiol*, vol. 2019, pp. 435–451, 2019. DOI: 10.1007/s10237-018-1094-8.

[155] A. Finotello, R. Gorla, N. Brambilla, F. Bedogni, F. Auricchio, and S. Morganti, "Finite element analysis of transcatheter aortic valve implantation: Insights on the modelling of self-expendable devices," *J Mech Behav Biomed Mater*, vol. 123, no. 104772, pp. 1–8, 2021. DOI: 10.1016/j.jmbbm.2021.104772.

[156] F. Nematzadeh and S. K. Sadrnezhaad, "Effects of material properties on mechanical performance of nitinol stent designed for femoral artery: Finite element analysis," *Scientia Iranica B*, vol. 19, no. 6, pp. 1564–1571, 2012. DOI: 10.1016/j.scient.2012.10.024.

[157] A. Grujic *et al.*, "Mechanical and magnetic properties of composite materials with polymer matrix," *J Min Metall Sect B-Metall*, vol. 46, no. 1, pp. 25–32, 2010. DOI: 10.2298/JMMB1001025G.

[158] Dassault Systeme Simulia Corp. "Explicit dynamic analysis." (2017), [Online]. Available: http://130.149.89.49:2080/v6.9/books/usb/default.htm?startat=pt03ch06s03at08.html (visited on 07/29/2022).

[159] Dassault Systeme Simulia Corp. "About general contact in abaqus/explicit." (2017), [Online]. Available: https://abaqus-docs.mit.edu/2017/English/SIMACAEITNRefMap/simaitn-c-contactgeneral.htm (visited on 12/20/2022).

[160] Dassault Systeme Simulia Corp. "Contact pressure-overclosure relationships." (2017), [Online]. Available: https://abaqus-docs.mit.edu/2017/English/SIMACAEITNRefMap/simaitn-c-normalinteraction.htm (visited on 12/20/2022).

[161] Dassault Systeme Simulia Corp. "Mesh tie constraints." (2017), [Online]. Available: https://abaqus-docs.mit.edu/2017/English/SIMACAECSTRefMap/simacst-c-tiedconstraint.htm (visited on 12/20/2022).

[162] S. Tzamtzis, J. Viquerat, J. Yap, M. J. Mullen, and G. Burriesci, "Numerical analysis of the radial force produced by the medtronic-corevalve and edwards-sapien after transcatheter aortic valve implantation (tavi)," *Med Eng Phys*, vol. 35, no. 1, pp. 125–130, 2013. DOI: 10.1016/j.medengphy.2012.04.009.

[163] S. B. Capps, R. C. Elkins, and D. M. Fronk, "Body surface area as a predictor of aortic and pulmonary valve diameter," *J Thorac Cardiovasc Surg*, vol. 119, no. 5, pp. 975–982, 2000. DOI: 10.1016/S0022-5223(00)70092-4.

[164] D. Stoeckel, A. Pelton, and T. Duerig, "Self-expanding nitinol stents: Material and design considerations," *Eur Radiol*, vol. 14, no. 2, pp. 292–301, 2004. DOI: 10.1007/s00330-003-2022-5.

[165] T. W. Duerig, K. N. Melton, D. Stockel, and C. M. Wayman, *Engineering aspects of shape memory alloys*. Elsevier Ltd., 1990. DOI: 10.1016/C2013-0-04566-5.

[166] Dassault Systeme Simulia Corp. "Superelasticity." (2017), [Online]. Available: https://abaqus-docs.mit.edu/2017/English/SIMACAEMATRefMap/simamat-c-superelasticity.htm#simamat-c-superelasticity (visited on 12/13/2020).

[167] F. Auricchio and R. L. Taylor, "Shape-memory alloys: Modelling and numerical simulations of the finite-strain superelastic behavior," *Comput Methods Appl Mech Eng*, vol. 143, no. 1-2, pp. 175–194, 1997. DOI: 10.1016/S0045-7825(96)01147-4.

[168] N. Vidal, E. Asua, J. Feuchtwanger, A. Garcia-Arribas, J. Gutierrez, and J. Barandiaran, "Fem simulation of the nitinol wire," *Eur Phys J Spec Top*, vol. 158, pp. 39–44, 2008. DOI: 10.1140/epjst/e2008-00651-9.

[169] C. H. Fu, Y. B. Guo, J. McKinney, and X. T. Wei, "Process mechanics of low plasticity burnishing of nitinol alloy," *J Mater Eng Perform*, vol. 21, no. 12, pp. 2607–2617, 2012. DOI: 10.1007/s11665-012-0313-1.

[170] H. Cao, M. H. Wu, F. Zhou, R. M. McMeeking, and R. O. Ritchie, "The influence of mean strain on the high-cycle fatigue of nitinol with application to medical devices," *J Mech Phys Solids*, vol. 143, no. 104057, pp. 1–29, 2020. DOI: 10.1016/j.jmps.2020.104057.

[171] C. Kleinstreuer, Z. Li, C. A. Basciano, S. Seelecke, and M. Farber, "Computational mechanics of nitinol stent grafts," *J Biomech*, vol. 41, no. 11, pp. 2370–2378, 2008. DOI: 10.1016/j.jbiomech.2008.05.032.

[172] N. W. Bressloff, "Leaflet stresses during full device simulation of crimping to 6 mm in transcatheter aortic valve implantation, tavi," *Cardiovasc Eng Tech*, 2022. DOI: 10.1007/s13239-022-00614-6.

[173] E. P. Furlani, *Permanent magnet and electromechanical devices*. Academic Press, 2001, pp. 97–205. DOI: 10.1016/B978-0-12-269951-1.X5000-1.

[174] E. G. Loukaides, S. K. Smoukov, and K. Seffec, "Magnetic actuation and transition shapes of a bistable spherical cap," *Int J Smart Nano Mater*, vol. 5, no. 4, pp. 270–282, 2014. DOI: 10.1080/19475411.2014.997322.

[175] M. McCraig and A. G. Clegg, *Permanent magnets in theory and practice*. New York: John Wiley and Sons, 1987.

[176] S. Blinder. "Magnetic field of a cylindrical bar magnet." (2011), [Online]. Available: https://demonstrations.wolfram.com/MagneticFieldOfACylindricalBarMagnet/ (visited on 12/13/2020).

[177] KL Magnetics Inc. "How much will a magnet hold?" (), [Online]. Available: https://www.kjmagnetics.com/blog.asp?p=how-much-will-a-magnet-hold (visited on 12/13/2020).

[178] SIMULIA. "Vuamp." (2017), [Online]. Available: https://abaqus-docs.mit.edu/2017/English/SIMACAESUBRefMap/simasub-c-vuamp.htm (visited on 12/13/2020).

[179] Dassault Systeme Simulia Corp. "Magnetostatic analysis." (2017), [Online]. Available: https://abaqus-docs.mit.edu/2017/English/SIMACAEANLRefMap/simaanl-c-magnetostatic.htm (visited on 12/20/2022).

[180] I. Perugia, V. Simoncini, and M. Arioli, "Linear algebra methods in a mixed approximation of magnetostatic problems," *SIAM J Sci Comput*, vol. 21, no. 3, pp. 1085–1011, 1999. DOI: 10.1137/S1064827598333211.

[181] R. A. Serway, *Principles of physics*. Saunders College Pub., 1998.

[182] W. F. Brown, *Handbook of chemistry and physics*. McGraw-Hill, 1958.

[183] R. A. Matula, "Electrical resistivity of copper, gold, palladium, and silver," *J Phys Chem Ref Data*, vol. 8, no. 4, pp. 1147–1148, 1979. DOI: 10.1063/1.555614.

[184] S. Abdalla, S. Al-ameer, and S. Al-Magaishi, "Electrical properties with relaxation through human blood," *Biomicrofluidics*, vol. 4, no. 034101, pp. 1–16, 2010. DOI: 10.1063/1.3458908.

[185] L. Pauling and C. D. Coryell, "The magnetic properties and structure of hemoglobin, oxyhemoglobin and carbonmonoxyhemoglobin," *Proc Natl Acad Sci USA*, vol. 22, no. 4, pp. 210–216, 1936. DOI: 10.1073/pnas.22.4.210.

[186] W. H. Preece, "On the heating effects of electric currents," *Proc R Soc*, vol. 36, pp. 464–471, 1883. DOI: 10.1098/rspl.1883.0133.

[187] V. Babrauskas and I. S. Wichman, "Fusing of wires by electrical current," *Conf Proc - Fire Mater*, vol. 12, pp. 769–780, 2011.

[188] A. Schwartz and W. H. N. James, "Low tension thermal cut-outs," *Proc IEEE*, vol. 35, pp. 364–420, 1905. DOI: 110.1049/jiee-1.1905.0060.

[189] E. O. Filippova, A. V. Filippov, and I. A. Shulepov, "Experimental study of sliding friction for pet track membranes," *IOP Conf Ser Mater Sci Eng*, vol. 125, no. 012020, pp. 1–7, 2016. DOI: 10.1088/1757-899X/125/1/012020.

[190] V. Quaglini and P. Dubini, "Friction of polymers sliding on smooth surfaces," *Adv Tribol*, vol. 2011, no. 178943, pp. 1–9, 2011. DOI: 10.1155/2011/178943.

[191] F. Khoffi, N. Khenoussi, O. Harzallah, and J. Y. Drean, "Mechanical behaviour of polyethylene terephthalate/copper composite filament," *Phys Procedia*, vol. 21, pp. 240–245, 2011. DOI: 10.1016/j.phpro.2011.11.001.

[192] Dassault Systeme Simulia Corp. "Frictional behaviour." (2017), [Online]. Available: https://abaqus-docs.mit.edu/2017/English/SIMACAEITNRefMap/simaitn-c-friction.htm (visited on 12/20/2022).

[193] Dassault Systeme Simulia Corp. "Coulomb friction." (2017), [Online]. Available: https://abaqus-docs.mit.edu/2017/English/SIMACAETHERefMap/simathe-c-coulombfric.htm (visited on 12/20/2022).

[194] J. Mummert, E. Sirois, and W. Sun, "Valve type, size, and deployment location affect hemodynamics in an in vitro valve-in-valve model," *JACC Cardiovasc Interv*, vol. 9, no. 15, pp. 1618–1628, 2016. DOI: 10.1016/j.jcin.2016.05.030.

[195] G. D'Ancona, M. Dißmann, and H. Heinze, "Transcatheter aortic valve replacement with the 34 mm medtronic evolut valve," *Neth Heart J*, vol. 26, no. 7-8, pp. 401–408, 2018. DOI: 10.1007/s12471-018-1122-4.

[196] H. P. Greisler, "Interactions at the blood/material interface," *Ann Vasc Surg*, vol. 4, no. 1, pp. 98–103, 1990. DOI: 10.1007/BF02042699.

[197] B. Kasemo and J. Lausmaa, "Material-tissue interfaces: The role of surface properties and processes," *Environ Health Perspect*, vol. 5, no. Suppl 5, pp. 41–45, 1994. DOI: 10.1289/ehp.94102s541.

[198] I. Belluschi, N. Buzzatti, A. Castiglionni, M. de Bonis, F. Maisano, and O. Alfieri, "Aortic and mitral bioprosthetic valve dysfunction: Surgical or percutaneous solutions?" *Eur Heart J*, vol. 23, no. Supplement E, E6–E12, 2021. DOI: 10.1093/eurheartj/suab083.

[199] M. Casenghi, A. P. Rubbio, L. Menicanti, F. Bedogni, and L. Testa, "Durability of surgical and transcatheter aortic bioprostheses a review of literature," *Cardiovasc Revasc Med*, pp. 1–10, 2022. DOI: 10.1016/j.carrev.2022.03.006.

[200] A. G. Chatfield *et al.*, "Transcatheter solutions for transcatheter aortic valve replacement dysfunction: Is redo transcatheter aortic valve replacement a durable option?" *Ann Cardiothorac Surg*, vol. 10, no. 5, pp. 571–584, 2021. DOI: 10.21037/acs-2021-tviv-85.

[201] N. A. Clarizia, V. N. Bapat, and M. Ruel, "Current surgical bioprostheses: Looking to the future," *Prog Cardiovasc Dis*, vol. 72, pp. 21–25, 2021. DOI: 10.1016/j.pcad.2022.06.005.

[202] M. Ibrahim, J. Grimm, M. Woods, P. N. Fiorilli, and W. Y. Szeto, "Self-expandable transcatheter aortic valve for surgical prosthetic aortic valve dysfunction," *Ann Cardiothorac Surg*, vol. 10, no. 5, pp. 689–691, 2021. DOI: `10.21037/acs-2021-tviv-16`.

[203] G. Marengo *et al.*, "Durability of transcatheter aortic valves, current evidence and future perspective," *Vessel Plus*, vol. 5, no. 12, pp. 1–12, 2021. DOI: `10.20517/2574-1209.2020.58`.

[204] M. Gallo *et al.*, "Transcatheter valve-in-valve implantation for degenerated bioprosthetic aortic and mitral valves - an update on indication, techniques, and clinical results," *Expert Rev Med Devices*, vol. 18, no. 7, pp. 597–608, 2021. DOI: `10.1080/17434440.2021.1939009`.

[205] S. Tom, E. Perdoncin, and K. J. Grubb, "Balloon expandable transcatheter aortic valve for degenerative prior prosthetic valve dysfunction," *Ann Cardiothorac Surg*, vol. 10, no. 5, pp. 686–688, 2021. DOI: `10.21037/acs-2021-tviv-12`.

[206] G. Tarantini and L. N. Fovino, "Treatment of degenerated surgical aortic valve: The importance of having a lifetime strategy in younger patients with severe aortic disease," *Catheter Cardiovasc Interv*, vol. 97, no. 7, pp. 1489–1491, 2021. DOI: `10.1002/ccd.29766`.

[207] S. O. Oyetunji, "Transcatheter aortic valve implantation or replacement? valve durability in the context of patient life expectancy," *Eur Heart J*, vol. 42, no. 30, pp. 2920–2923, 2021. DOI: `10.1093/eurheartj/ehab393`.

[208] S. Fukuhara, A. A. Brescia, and G. M. Deeb, "Surgical explantation of transcatheter aortic bioprostheses: An analysis from the society of thoracic surgeons database," *Circulation*, vol. 142, no. 23, pp. 2285–2287, 2020. DOI: `10.1161/CIRCULATIONAHA.120.050499`.

[209] L. Buellesfeld *et al.*, "Aortic root dimensions among patients with severe aortic stenosis undergoing transcatheter aortic valve replacement," *JACC Cardiovasc Interv*, vol. 6, no. 1, pp. 72–83, 2013. DOI: `10.1016/j.jcin.2012.09.007`.

[210] R. Al-Hakim, S. T. Kee, K. Olinger, E. E. Lee, J. H. Moriarty, and J. P. McWilliams, "Inferior vena cava filter retrieval: Effectiveness and complications of routine and advanced techniques," *J Vasc Interv Radiol*, vol. 25, no. 6, pp. 933–939, 2014. DOI: `10.1016/j.jvir.2014.01.019`.

[211] M. Roffi and D. Mukherjee, "Current role of emboli protection devices in percutaneous coronary and vascular interventions," *Am Heart J*, vol. 157, no. 2, pp. 263–270, 2009. DOI: `10.1016/j.ahj.2008.09.008`.

Appendix A: CAD Modelling

The CAD software Rhinoceros3D 5 (McNeel, 2012) was used to model all designs. The functionality of writing python scripts to control the generation of the model was utilised to define a number of design parameters for each part. Detailed below for each design concept, these parameters afforded the ability to make quick and easy design changes to the models.

12.1 Holding Member

12.1.1 Slot Concept

TABLE 12.1: Design parameters for the slot holding member modelling script.

Design Parameter	Symbol
Valve height (Fig. 12.1)	h_v
Valve radius (Fig. 12.1)	r_v
Number of horizontal cells (Fig. 12.2)	N_{hor}
Number of vertical cells (Fig. 12.2)	N_{ver}
Strut thickness (Fig. 12.1)	t_{st}
Strut width (Fig. 12.2)	w_{st}
Fillet radius	r_f
Slot width (Fig. 12.5)	w_{slot}
Crown height (Fig. 12.6)	h_c
Crown gap width (Fig. 12.6)	w_c

The steps of the script to build the holding member model for the slot exchange concept began with the formation of a rectangular prism from which the cells were cut out. As shown in Figure 12.1 the dimensions of the prism was linked to the three design parameters: h_v, r_v and t_{st}.

The cell profile was drawn next, which was a simple rhombus, like the cells on the SAPIEN valves. The height and length of the cells were scaled according to four intermediate parameters: cell height(h_{cell}), cell width(w_{cell}), gap between vertically adjacent cells (Δh), and gap between horizontally adjacent cells (Δw):
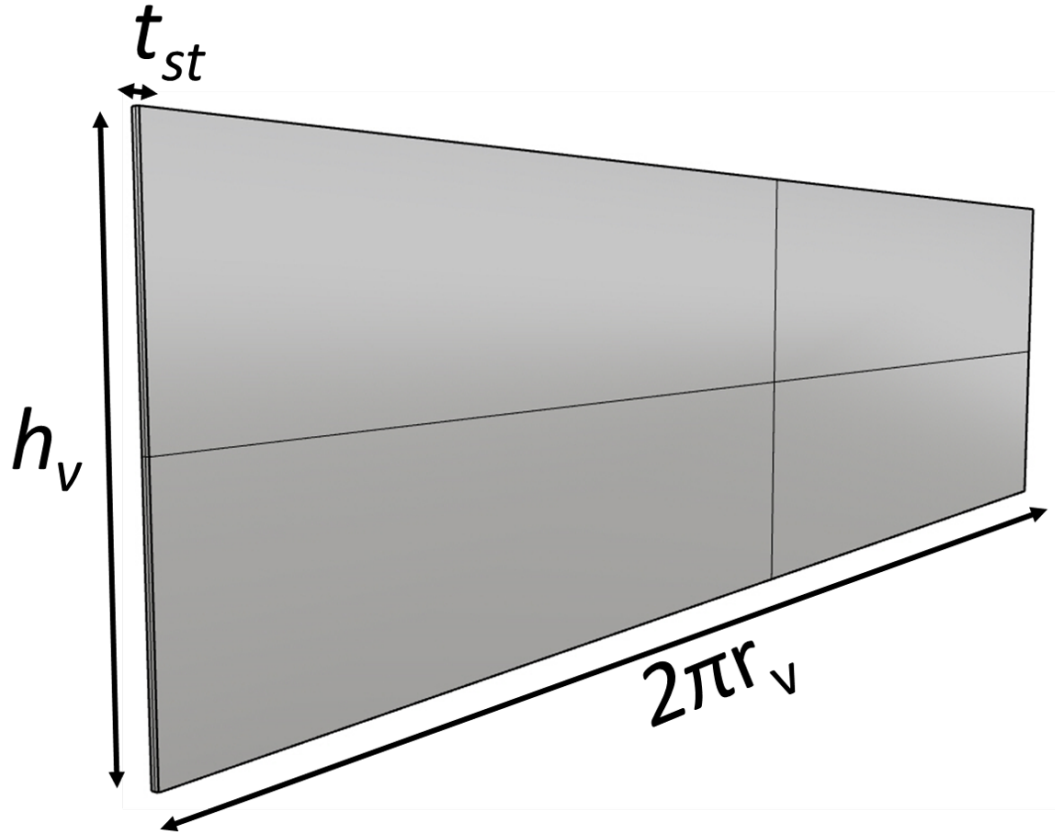
FIGURE 12.1: The rectangular prism from which the slotted holding member was modelled and the design parameters relating to the prism.

$$h_{cell} = \frac{h_v}{N_{ver}} - \Delta h \tag{12.1}$$

$$w_{cell} = \frac{2 \times \pi \times r_v}{N_{hor}} - \Delta w \tag{12.2}$$

where;

$$\Delta h = \frac{w_{st}}{\sin\left(\tan^{-1}\left(\dfrac{2 \times \pi \times r_v \times N_{ver}}{h_v \times N_{hor}}\right)\right)} \tag{12.3}$$

$$\Delta w = \frac{w_{st}}{\cos\left(\tan^{-1}\left(\dfrac{2 \times \pi \times r_v \times N_{ver}}{h_v \times N_{hor}}\right)\right)} \tag{12.4}$$

How the N_{ver}, N_{hor} and w_{st} variables related to the script is shown in Figure 12.2. The horizontal and vertical gap values related to the distance between the corners of two

(vertically or horizontally) adjacent cells. The equations above were used to calculate the necessary gap between cells to ensure constant strut width across the frame, given the number of vertical and horizontal cells. These equations were specific to the case of a rhombus cell profile and would not give correct results for any other shape. The corners of the profile were then filleted to prevent sharp edges in the final structure according to the r_f value.
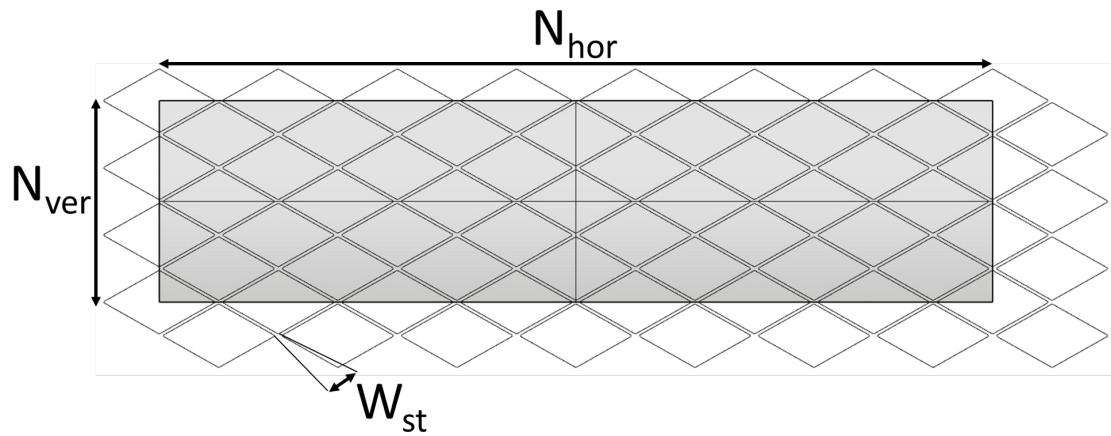

FIGURE 12.2: The cell profiles patterned across the rectangular prism in accordance to the strut width and number of cells parameters.

The next step was to pattern the appropriate number of cell profiles across the prism, extrude the profiles such that they intersect with the prism and use boolean difference to form the cells. This resulted in an unfolded frame as shown in Figure 12.3. This was followed by a flow operation where the planar frame was bent around a circle of radius equal to the r_v parameter, resulting in the final cylindrical frame.
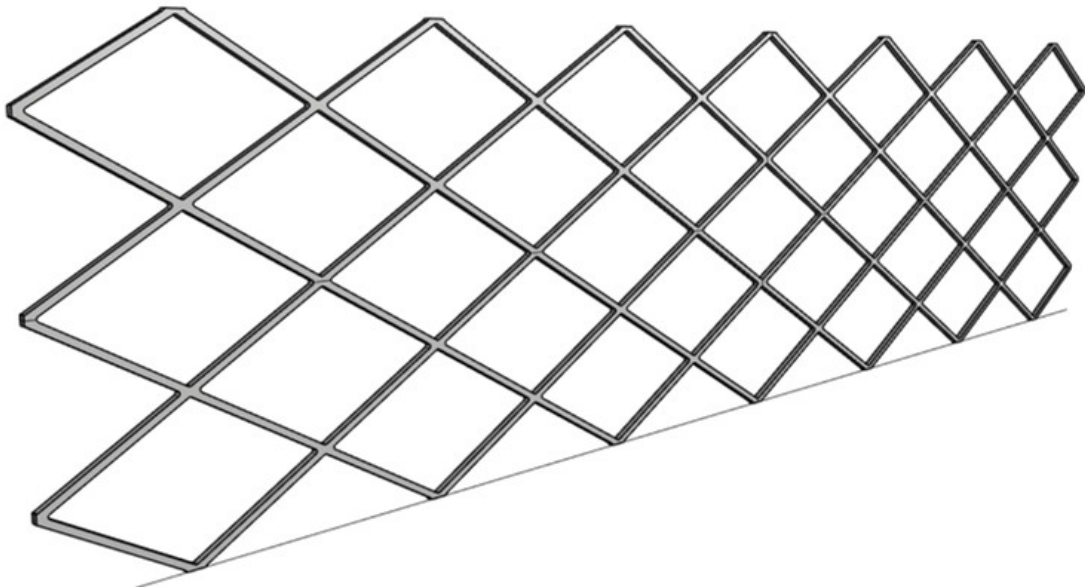

FIGURE 12.3: The planar slotted holding member after the extruded cell profile were cut out.

With the balloon-expendable frame ready, next was to add the slots for the mating process. This was done by splitting an entire strut path across the planar frame and extending it to form a series of planes as shown in Figure 12.4. Slots were then created by cutting rectangular holes in these planes, in accordance with the design parameter w_{slot}, determining the size of the slot gaps. (Figure 12.5).
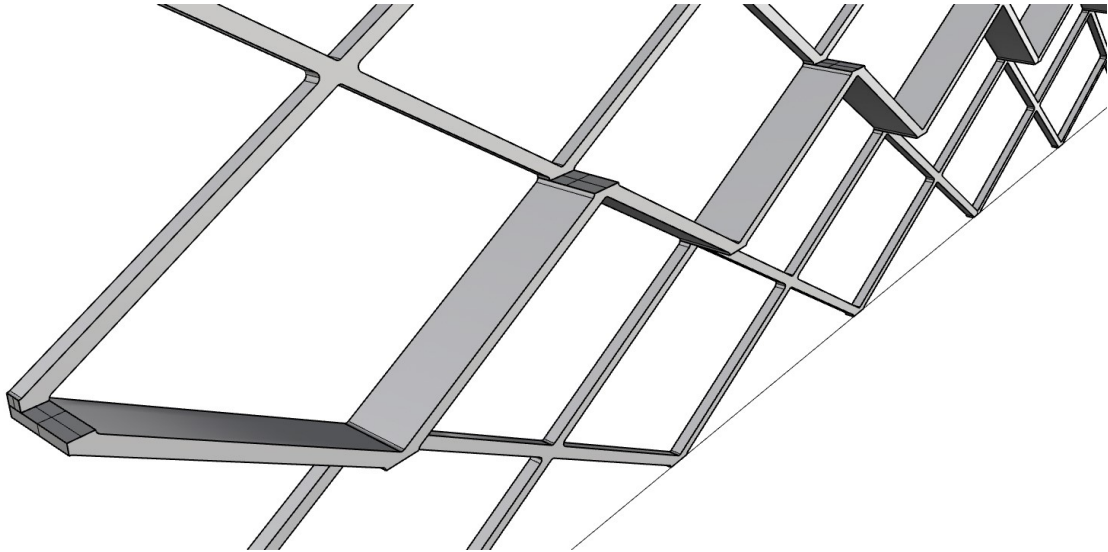

FIGURE 12.4: Planes extruded from struts for the slots.
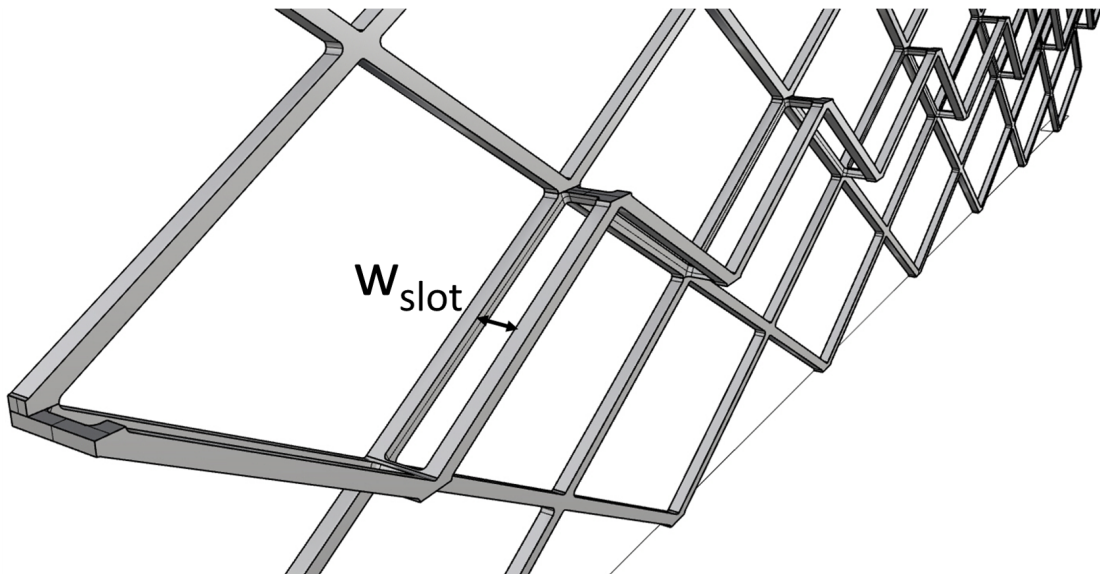

FIGURE 12.5: The slots formed after Boolean Difference, showing the SlotGap design parameter.

As can be seen in Figure 12.3 there were planar faces along the top and bottom of the member along with the ones on the slot structure in Figure 12.5. These were located at top and bottom corners of cells which were expected to experience the highest stresses during crimping and expansion. These planar faces contain nipple-like crowns on the SAPIEN models to handle higher stresses and these were added to the model as well. The crowns were formed in two steps where the same crown structure was scaled by two

different factors and their boolean difference was taken to form the final shape. The length of the bigger crown structure's base was equal to the Δh variable calculated in Eq. 9.3, plus the additional distance caused by the fillet operation on the cell profile corners. This additional distance (Δw_f) was calculated through:

$$\Delta w_f = 2 \times \left(\frac{r_f}{\sin(\alpha)} - r_f \right) \tag{12.5}$$

where;

$$\alpha = \tan^{-1} \left(\frac{2 \times \pi \times r_v \times N_{ver}}{h_v \times N_{hor}} \right) \tag{12.6}$$
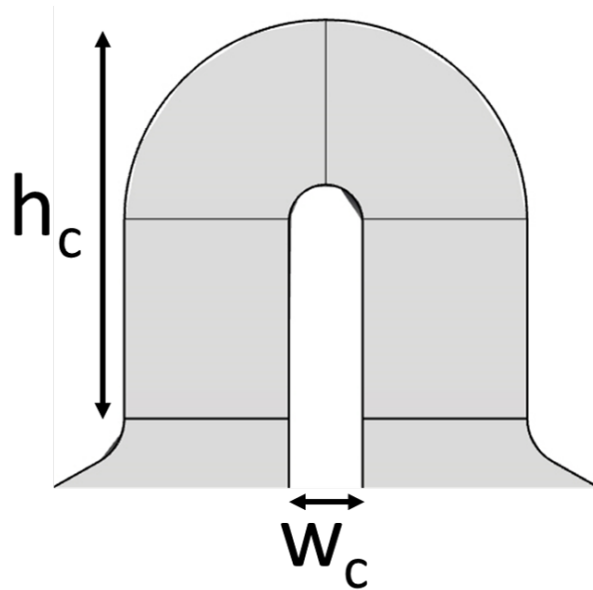

FIGURE 12.6: The crowns formed to replace the planar faces on the slotted holding member.

The height of the crown and the width of the gap inside the crown (Figure 12.6) were set to reflect the design parameters: h_c and w_c.
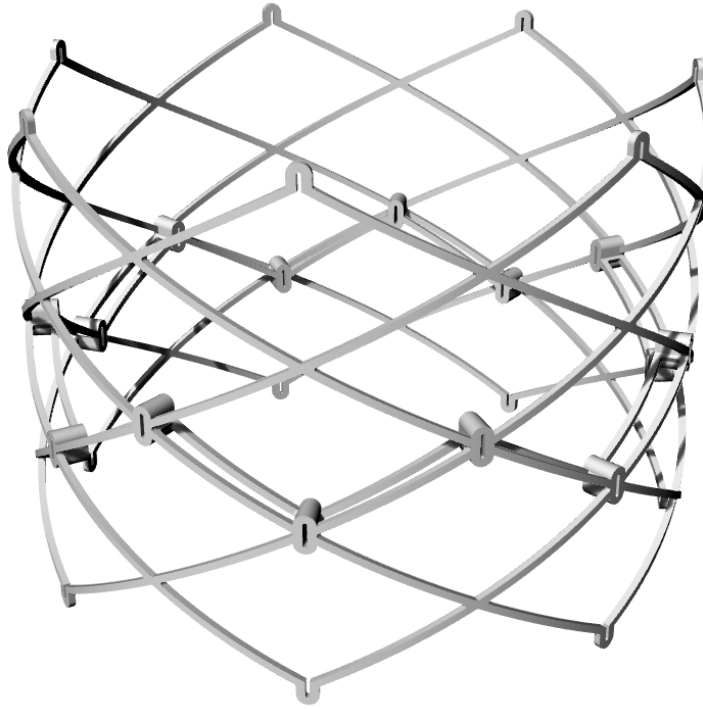
FIGURE 12.7: The holding member for the slot exchange concept.

The final holding member model for the slot exchange concept, generated following the steps above, is shown in Figure 12.7. The design parameter values for this member are shown in Table 12.2.

TABLE 12.2: Values of design parameters used to generate the slotted holding member.

Design Parameter	Value
h_v	20 mm
r_v	13 mm
N_{hor}	7
N_{ver}	3
t_{st}	0.3 mm
w_{st}	0.3 mm
r_f	0.1 mm
w_{slot}	0.8 mm
h_c	0.4 mm
w_c	0.15 mm

12.1.2 Magnetic Concept

The magnetic engagement method had two different holding member designs: the surgical and the transcatheter holding member.

12.1.2.1 Surgical Holding Member

TABLE 12.3: Design parameters for surgical magnetic holding member modelling script.

Design Parameter	Symbol
Valve height (Fig. 12.8)	h_v
Valve radius	r_v
Valve thickness (Fig. 12.8)	t_v
Suture ring thickness (Fig. 12.8)	t_{ring}
Suture ring width (Fig. 12.8)	w_{ring}
Thickness of extrusions on inner face (Fig. 12.8)	t_{ext}
Magnet radius (Fig. 12.8)	r_{mag}
Magnet thickness	t_{mag}
Number of magnets	N_{mag}

The surgical magnetic holding member was generated by first sketching a two-dimensional profile of an axial slice of the whole structure. A closed curve was generated with a total width equal to h_v. The axial slice of the suture ring and extrusions were also represented on the longer edge of the closed curve. Figure 12.8 shows this axial slice and how the design parameters influence its shape.
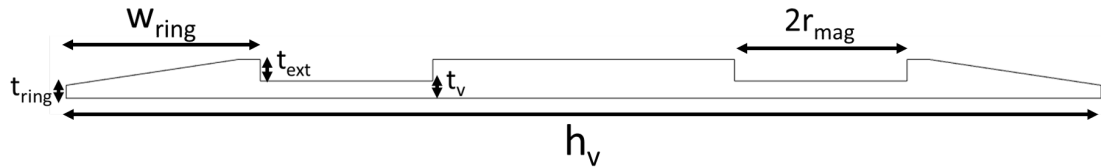

FIGURE 12.8: An axial slice of the magnetic surgical holding member. The features affected by the design parameters are labelled.

A circle was then drawn with a radius equal to r_v, orthogonal to and passing through the middle of the closed slice curve. The curve was swept over this circle, forming the three dimensional holding member (Figure 12.9). In one embodiment, N_{mag} number of cylinders with radius equal to r_{mag} and height equal to t_{mag} were then created and aligned radially inside the holding member, coinciding completely. Boolean difference was then used to form cylindrical holes to serve as the extrusions that constrain the exchangeable valve axially. The values of the design parameters for generating the holding member of Figure 12.9 is given in Table 12.4.
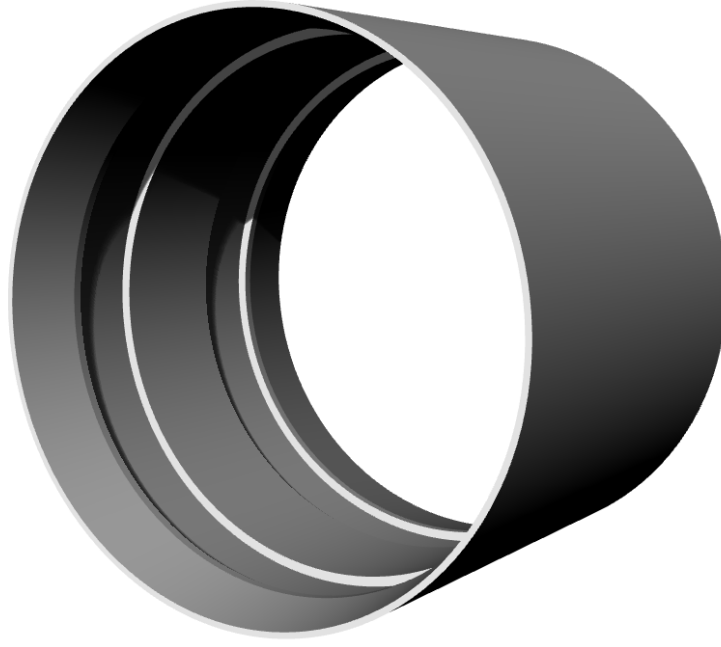
FIGURE 12.9: One embodiment of the surgical magnetic holding member.

TABLE 12.4: Values of design parameters used to generate the surgical magnetic holding member.

Design Parameter	Value
h_v	24 mm
r_v	14.2 mm
t_v	0.4 mm
t_{ring}	0.3 mm
w_{ring}	4 mm
t_{ext}	0.5 mm
r_{mag}	2 mm
t_{mag}	1 mm
N_{mag}	12

12.1.2.2 Transcatheter Holding Member

For the transcatheter holding member the cell profile of the CoreValve series was used. Seven points were drawn and a curve was interpreted through them to form a quarter of the cell shape. A new curve was offset from this interpreted curve by w_{st} to form a strut. Straight lines were added to ends of the resulting curves to achieve the $w_{hgap}/2$ and $w_{vgap}/2$ parameters between cells. Two mirror operations were used to form the complete cell profile.

TABLE 12.5: Design parameters for transcatheter magnetic holding member modelling script.

Design Parameter	Symbol
Valve height	h_v
Valve radius	r_v
Number of horizontal cells	N_{hor}
Number of vertical cells	N_{ver}
Strut thickness	t_{st}
Strut width	w_{st}
Fillet radius	r_f
Width of gap between horizontal cells	w_{hgap}
Width of gap between vertical cells	w_{vgap}
Magnet radius (Fig. 12.10)	r_{mag}
Width of strut around magnets (Fig. 12.10)	w_{mag}
Magnet thickness	t_{mag}
Number of magnets	N_{mag}
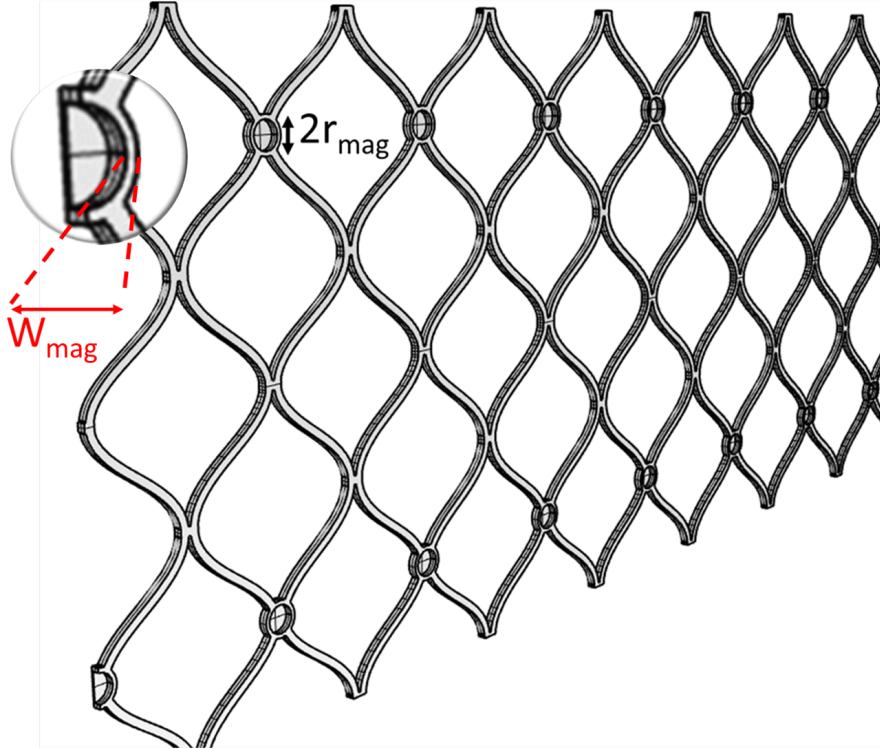
FIGURE 12.10: Planar frame of the magnet transcatheter holding member. The design parameters r_{mag} and w_{mag} are shown on the figure. The w_{mag} variable is marked in red and zoomed in for clarity.

Half circles of radius $r_{mag} + w_{mag}$ were then drawn such that they intersected with the profile. The intersecting sections were trimmed to form a continuous edge around the profile and the circles. Depending on the position and number of magnets, the half circles intersected the profile differently, forming a different frame design. The final profile with the magnets was then patterned horizontally and vertically according to N_{hor} and N_{ver}. The resulting 2D structure was formed into a closed curve and extruded

to form the planar frame in Figure 12.10. Cylinders with height t_{mag} and radius t_{mag} were then used to cut holes on the inside of the circular features in the frame, modelling the magnet holders. Finally, the frame was flowed around a circle of radius r_v and the final model was formed, as shown in Figure 12.11 with the design parameter values used listed in Table 12.6.
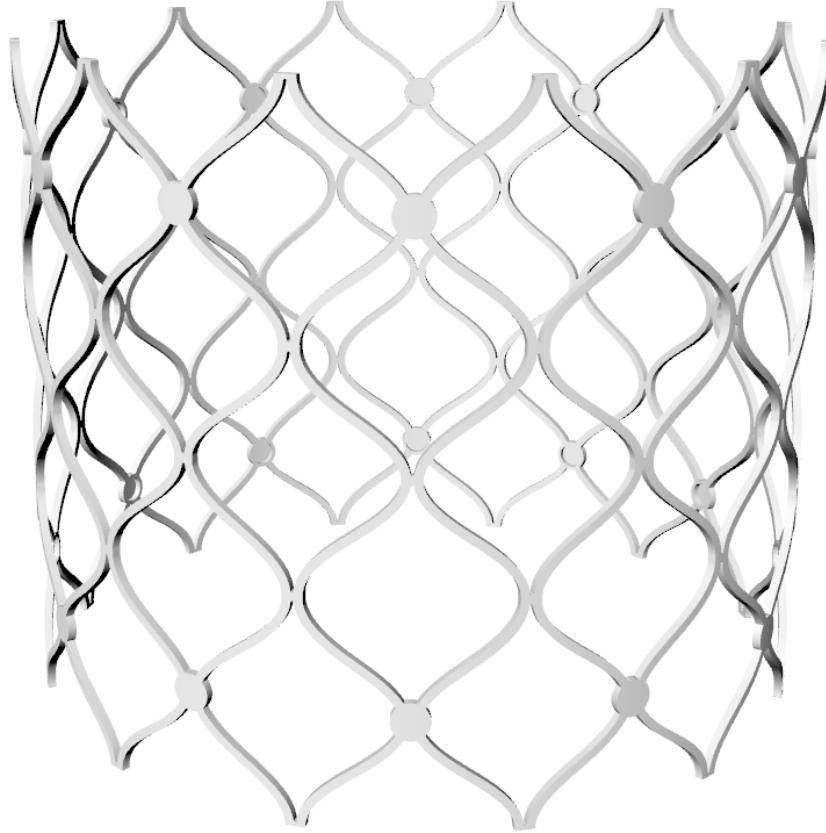

FIGURE 12.11: One embodiment of the transcatheter magnetic holding member.

TABLE 12.6: Values of design parameters used to generate the transcatheter magnetic holding member.

Design Parameter	Value
h_v	24 mm
r_v	14.3 mm
N_{hor}	12
N_{ver}	3
t_{st}	0.3 mm
w_{st}	0.3 mm
r_f	0.05 mm
w_{hgap}	0.1 mm
w_{vgap}	0.15 mm
r_{mag}	0.5 mm
w_{mag}	0.15 mm
t_{mag}	1 mm
N_{mag}	12

12.2 Exchangeable Valve

12.2.1 Slot Exchange Concept

TABLE 12.7: Design parameters for slot exchangeable valve modelling script.

Design Parameter	Symbol
Valve height	h_v
Valve radius	r_v
Number of horizontal cells	N_{hor}
Number of vertical cells	N_{ver}
Strut thickness	t_{st}
Strut width	w_{st}
Fillet radius	r_f
Width of gap between horizontal cells (Fig. 12.12)	w_{hgap}
Width of gap between vertical cells (Fig. 12.12)	w_{vgap}

The modelling script for the exchangeable valve for the slot exchange concept followed the same main steps of its holding member counterpart. Firstly, a rectangular prism was formed in accordance with dimensions h_v, r_v and t_{st}. Then the cell profile reflecting that of CoreValve, which is very different to the rhombus shape of the holding member, was formed. A unit arc was first drawn tangent to the y-axis. A copy of this arc was then mirrored across the y=x line and joined with the first arc. This formed a quarter of the cell profile. This entire curve was then mirrored across a horizontal line to form the left half of the profile. The line over which the quarter curve was mirrored was distanced away from the curve by w_{vgap}. Note that this parameter was independent from the other design parameters, unlike in the rhombus cell case of the slotted holding member.

The two curves now distanced from each other by the vertical gap were connected by a straight line. This entire left half was then mirrored across a vertical line w_{hgap} away from the curves. The left and right halves of the profile were joined with half-circle arcs, rather than straight lines, to prevent sharp edges in the final model. An example cell profile is shown in Figure 12.12.
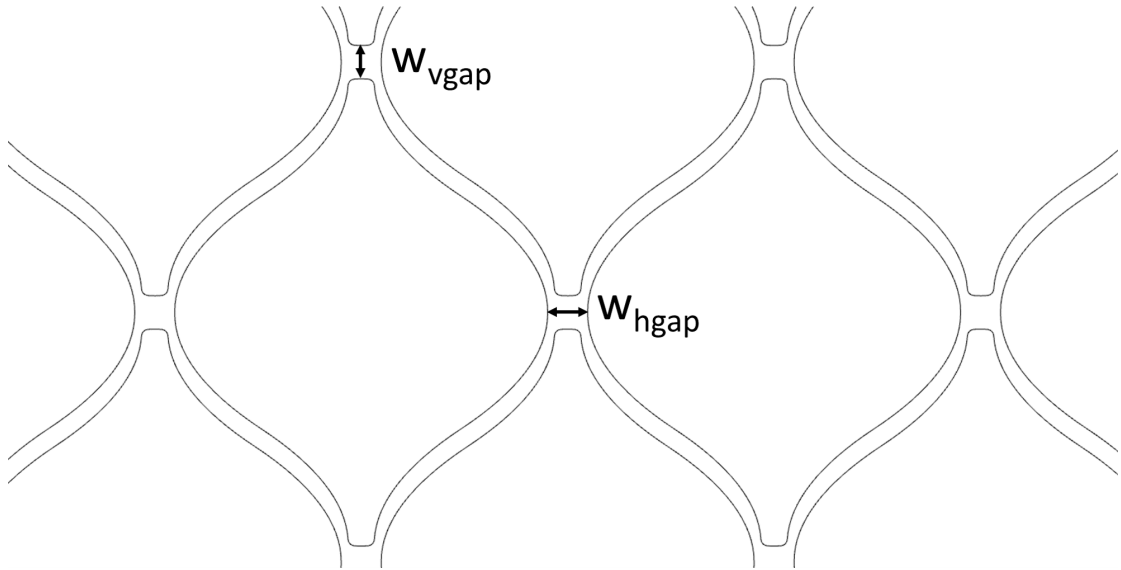
FIGURE 12.12: Patterned cell profiles of the exchangeable valve.

Following the formation of the cell profile, it was scaled to the appropriate cell height (h_{cell}) and cell width (w_{cell}) which were calculated through:

$$h_{cell} = \frac{h_v}{N_{ver}} - w_{st} - w_{vgap} \tag{12.7}$$

$$w_{cell} = \frac{2 \times \pi \times r_v}{N_{hor}} - w_{st} - w_{hgap} \tag{12.8}$$

The corners of the profile were filleted with radius r_f after scaling to ensure there were no sharp corners.
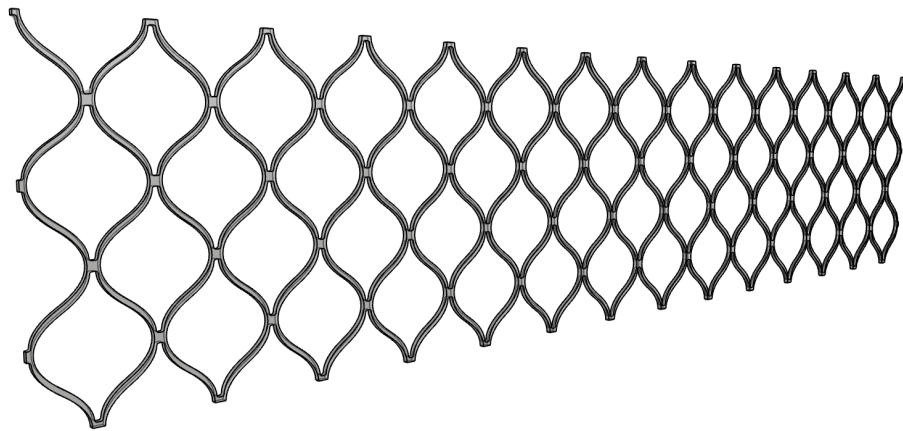

FIGURE 12.13: The planar exchangeable valve following boolean difference.

The profile was then patterned across the rectangular prism, extruded and cut out, leaving the planar frame shown in Figure 12.13. The connectors between the cells on the bottom ring were cut out to allow the bottom cells to be inserted through the

corresponding slots on the holding member. Importantly, the gap between these cells was equal to the design parameter w_{hgap} and hence could be easily changed. Following this, the planar valve was flowed around a circle with radius r_v and the final exchangeable valve was formed, as shown in Figure 12.14, with corresponding design parameter values listed in Table 12.8.
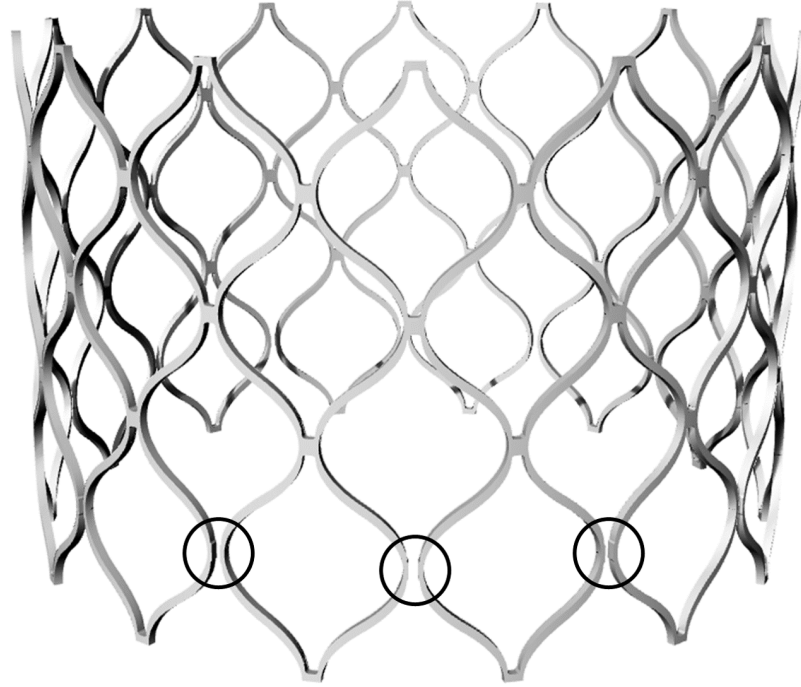

FIGURE 12.14: The exchangeable valve model for the slot exchange concept. The connectors that have been removed to allow mating are circled for emphasis.

TABLE 12.8: Values of design parameters used to generate the slot exchangeable valve.

Design Parameter	Value
h_v	24 mm
r_v	13 mm
N_{hor}	12
N_{ver}	2.5
t_{st}	0.3 mm
w_{st}	0.3 mm
r_f	0.1 mm
w_{hgap}	0.3 mm
w_{vgap}	0.2 mm

12.2.2 Magnetic Exchange Concept

TABLE 12.9: Design parameters for magnetic exchangeable valve modelling script.

Design Parameter	Symbol
Valve height	h_v
Valve radius	r_v
Number of horizontal cells	N_{hor}
Number of vertical cells	N_{ver}
Strut thickness	t_{st}
Strut width	w_{st}
Fillet radius	r_f
Width of gap between horizontal cells	w_{hgap}
Width of gap between vertical cells	w_{vgap}
Magnet radius	r_{mag}
Width of strut around magnets	w_{mag}
Magnet thickness	t_{mag}
Number of magnets	N_{mag}

The steps for generating the model for the magnetic exchangeable valve frame were the same as the transcatheter magnetic holding member script. The same cell profile and magnet holders were used. One difference was that the holes on the magnet holders faced outside the frame for the exchangeable valve rather than inside. The profile of these cells with appropriate design dimensions labelled is shown in Figure 12.15.
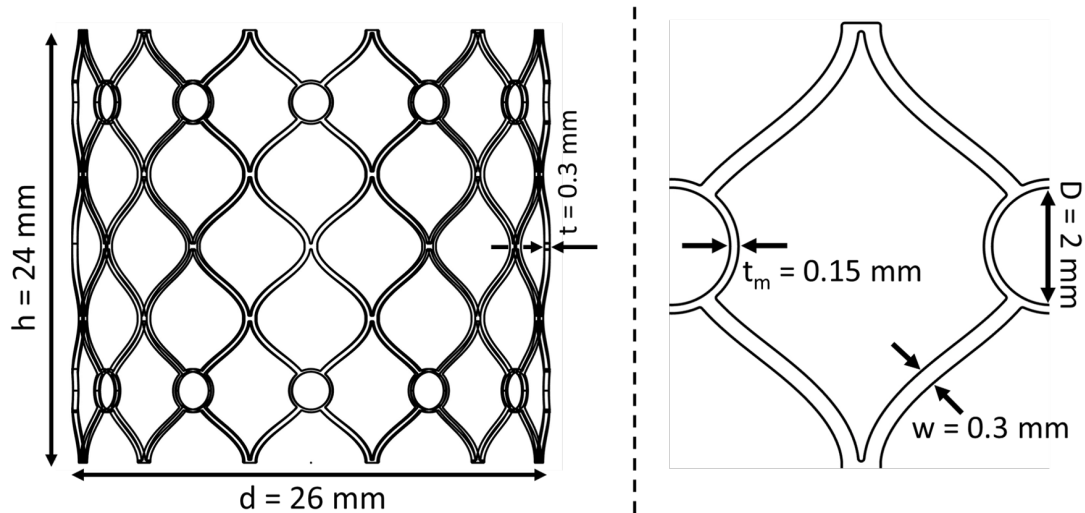

FIGURE 12.15: The profile of the magnetic exchangeable valve frame.

The holes were also shallower than the t_{mag} so that a portion of ferromagnetic material extended beyond the frame diameter. This extension was to provide a complementary shape to the features on the holding member that constrained axial movement after mating. A model of the exchangeable magnetic valve is shown in Figure 12.16 with corresponding design parameter values in Table 12.10.
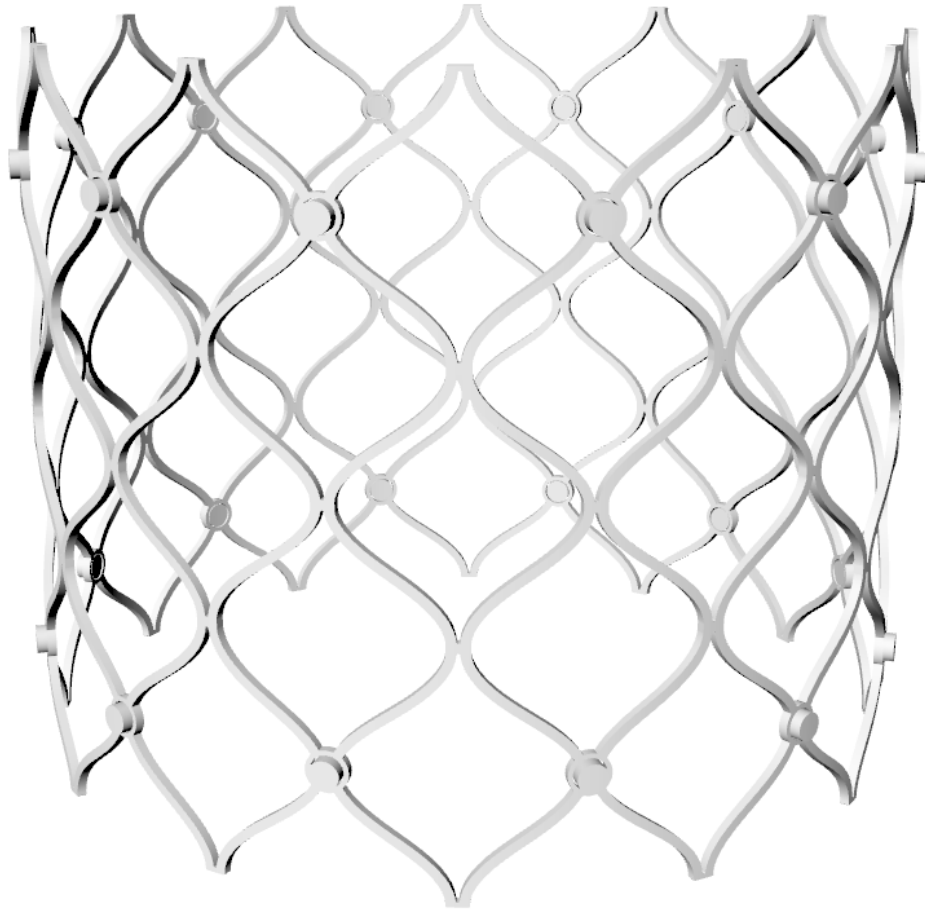
FIGURE 12.16: The magnetic exchangeable valve model with circular magnetic regions.

TABLE 12.10: Values of design parameters used to generate the magnetic exchangeable valve.

Design Parameter	Value
h_v	24 mm
r_v	13.3 mm
N_{hor}	12
N_{ver}	3
t_{st}	0.3 mm
w_{st}	0.3 mm
r_f	0.1 mm
w_{hgap}	0.1 mm
w_{vgap}	0.15 mm
r_{mag}	0.5 mm
w_{mag}	0.15 mm
t_{mag}	1 mm
N_{mag}	12

Appendix B: Mass Scaling Analysis and Mesh Refinement

The crimping and expansion of a basic SE frame (Figure 8.1) was simulated to determine the appropriate mass scaling value. The global seed size was set at 0.1 mm in accordance with data from literature, resulting in 92,313 elements [152, 171]. The same simulation was repeated for four time increments:
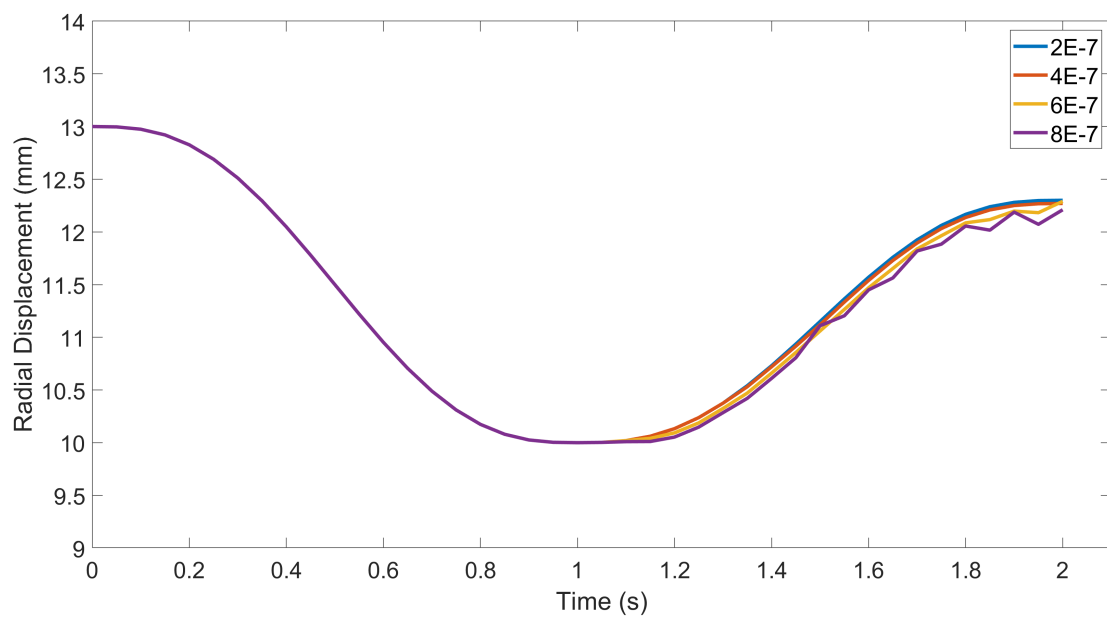
- 2E-7 s

- 4E-7 s

- 6E-7 s

- 8E-7 s

FIGURE 12.17: Displacement of the frame at different time increments: (blue) 2E-7 s, (red) 4E-7 s, (yellow) 6E-7 s, (purple) 8E-7 s.

Smaller time increments resulted in large computation times for the simulations so the largest value that produced an accurate result was preferred. Figure 12.17 shows the radial displacement values of the frame for the four cases. Time increments 8E-7 s and 6E-7 s showed an oscillatory response during the expansion of the frame, showing that the time increment was too large. The kinetic energy of the model was also above the 5% of the total internal energy in these two cases where the frame was energized during unloading. The smaller time increments of 2E-7 s and 4E-7 s did not exhibit this oscillation during unloading. Hence, the target time increment of 4E-7 was used in the simulations.
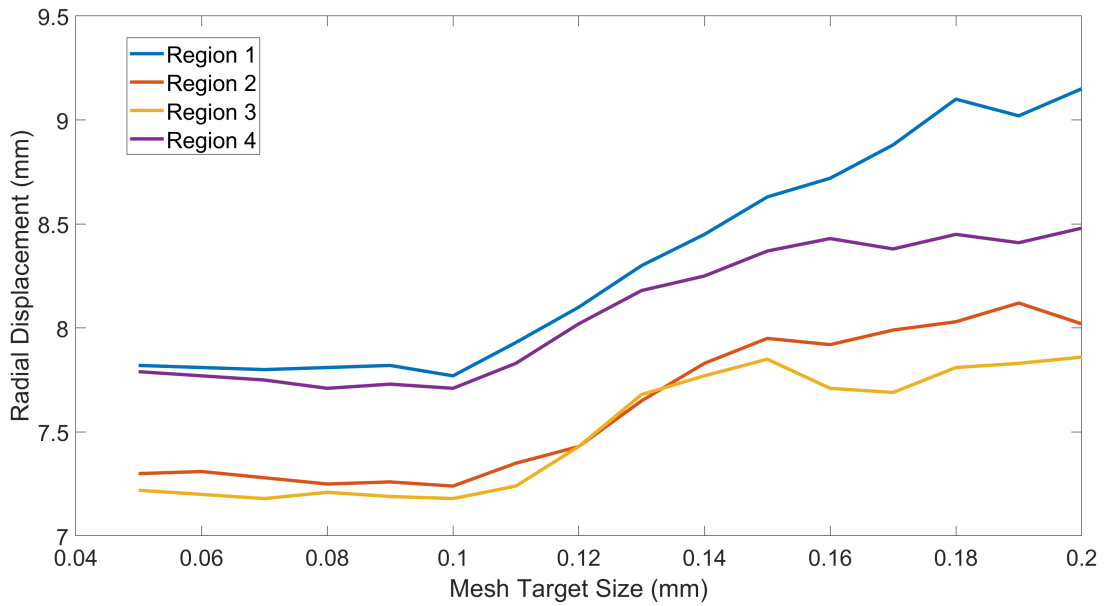

FIGURE 12.18: The radial displacement in four different regions on the frame across different mesh resolutions during crimping.

To investigate the effect of global seed size on the accuracy of results, the crimping of the basic SE frame design was simulated with target mesh element sizes between 0.2 mm and 0.05 mm. A vertical slice of the frame encompassing an entire cell was selected to extract data from. The slice was then divided into four regions across the height of the frame. This selection was done due to the large number of elements, particularly at smaller target seed sizes, which made extracting element output data computationally costly. The average von Mises stress and radial displacement for each region at different mesh resolutions are shown in Figures 12.18 and 12.19.

The ideal target global seed size should result in minimal variation in the displacement and stress outputs compared to that of a smaller seed size. As can be seen in both figures, this precision was achieved for both outputs at 0.1 mm target seed size. This seed size resulted in 3 elements across the strut of the frame which were 0.3 mm x 0.3 mm, further supporting the literature values [171].
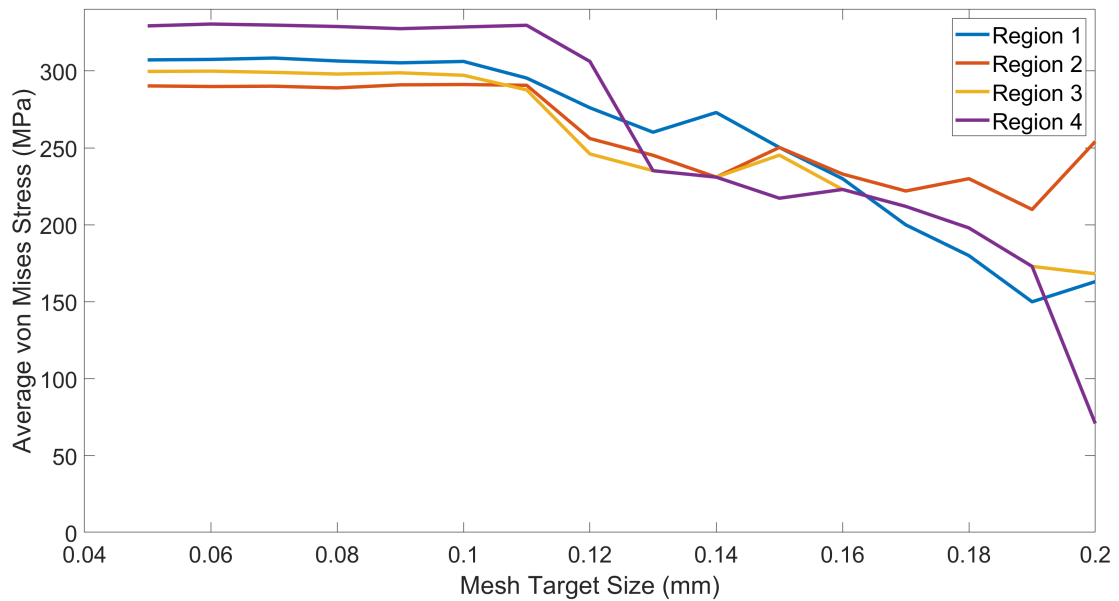
FIGURE 12.19: The average von Mises stress in four different regions on the frame across different mesh resolutions during crimping.

The computational time required to complete the simulations also increased to over 10 hours below 0.1 mm seed size. Considering that the crimping of the frame was a small and simple step within the deployment and removal simulations, a target element size of 0.1 mm was used to keep simulations accurate and run times within reason.

12.3 Comparison Between Full Integration and Reduced Integration Elements

Another choice for the element types was between using full integration elements and reduced integration elements. In literature, TAVI crimping and deployment simulations are extensively performed using reduced integration hexahedral elements (C3D8R) for the less computational cost they require [152–155]. The crimping of the basic frame meshed with both C3D8 and C3D8R elements was performed to evaluate the difference between results in terms of the calculated von Mises stresses. The mesh resolution was three elements across the frame strut, as determined via the mesh refinement analysis. Figure 12.20 depicts the difference in von Mises stress output for the same node between frames meshed with either element type.

There was an average of 8.44% underestimation of stress when using reduced integration elements compared to full integration elements. As can be seen in 12.20 this underestimation was pronounced after 0.075 s in the simulation which corresponded to crimping below 7.8% of the frame diameter. The computation time for the model meshed with
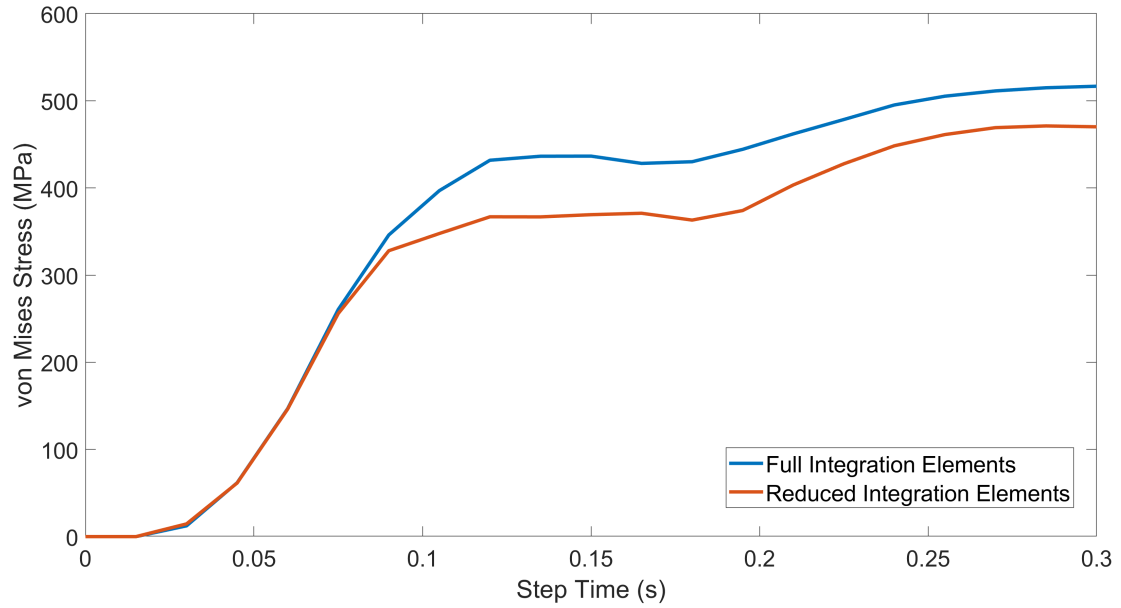
FIGURE 12.20: The von Mises stress of the same node across a crimping step for reduced integration elements and full integration elements.

reduced integration elements was around 45 minutes while the model with full integration elements took 2.5 hours. Due to the increased computational cost of using full integration elements in this simple simulation and the relatively small difference between predicted stress values, reduced integration elements were used in the simulations in this thesis.

Appendix C: Magnetic Force Derivation

The electric potential in classic electromagnetism is used to determine the electric field. The magnetic scalar potential, ϕ of a cylindrical magnet can be calculated through a triple integral in cylindrical coordinates [176]:

$$\phi(r, z) = \frac{\mu}{4\pi} M \int \int \int \frac{(z - Z)RdRd\Phi dZ}{[r^2 - 2Rrcos\Phi + R^2 + (z - Z)^2]^{3/2}} \tag{12.9}$$

where, μ is the permeability of the medium, M is the magnetization field magnitude, (R, Φ, Z) are the global cylindrical coordinates and (r, ϕ, z) are the magnetic field components [174]. This potential can be interpreted as originating from two circular monopoles of radius a and separated by a distance D, defining a cylindrical electromagnet of radius a and thickness D [176]. From this, the global axial component contributing to the magnetic flux density of the cylindrical electromagnet is $B_z = -d\phi/dZ$ which is expressed in terms of elliptic functions with complex arguments [176]. B_z can be evaluated using numerical methods and through Mathematica's *NIntegrate* routine:

$$B_z(r, z, \phi) = -\frac{\mu}{4\pi} M \int_0^{2\pi} \int_0^a \left(\frac{R(D/2 - z)}{(R^2 + (D/2 - z)^2 + r^2 - 2Rrcos\phi)^{3/2}} \right) \tag{12.10}$$
$$+ \left(\frac{R(D/2 + z)}{(R^2 + (D/2 + z)^2 + r^2 - 2Rrcos\phi)^{3/2}} \right) dRd\phi$$

This equation can be further simplified by neglecting the effects of magnet orientation and considering that the z-component of the magnetic field coincides with the global z direction [173]. This leads to:

$$B_z(z) = \frac{\mu}{4\pi} M \int_{-D}^0 \int_0^{2\pi} \frac{R^2 d\phi dz'}{[R^2 + (z - z')^2]^{3/2}} \tag{12.11}$$

where z is the distance from the magnet face and z' is the position of the magnet face in the system. Note that z' is integrated over the thickness of the magnet but the limits of the integral are reversed to remove the negative sign in Eq. 9.10. Performing the integration leads to the definition of magnetic flux density $B_z(z)$ for a cylindrical magnet on its magnetic axis:

$$B(z) = \frac{\mu \times M}{2} \left(\frac{\frac{D}{2} - z}{D \times \sqrt{R^2 + (\frac{D}{2} - z)^2}} + \frac{\frac{D}{2} + z}{D \times \sqrt{R^2 + (\frac{D}{2} + z)^2}} \right) \qquad (12.12)$$

For electromagnets the magnetization field magnitude (M) is approximated as $M = I \times N$ where I is current and N is the number of windings. For a permanent magnet $M = B_r$ where B_r is the magnetic remanence dependant on the magnet material composition.